Author:
Lewis-Borrell, Luke J

Title:
Mapping Synthetically Relevant Photochemical Pathways in Solution by Application of Transient Absorption Spectroscopy

Mapping Synthetically Relevant Photochemical Pathways in Solution by Application of Transient Absorption Spectroscopy

Luke J. Lewis-Borrell

A dissertation submitted to the University of Bristol in accordance with the requirement of the degree of Doctor of Philosophy in the Department of Chemistry, Faculty of Science.

August 2021

~41’000 word

Abstract

Transient electronic and vibrational absorption spectroscopy (TEAS and TVAS, respectively) has been applied to the study of solution phase reactive mixtures relevant to synthetic methodology used in polymerisation and small molecule synthesis.

The photochemical dynamics of three classes of organic photoredox catalysts (OPCs) employed in organocatalysed atom transfer radical polymerisation (O-ATRP) are studied. In total nine catalysts were selected for study with structures that vary around the N-aryl and core-substitution of dihydrophenazine, phenoxazine and phenothiazine scaffolds, each with varying propensities for control of polymerization outcomes. Experiments for both lifetime and photoinduced electron transfer measurements were recorded in three solvents of differing polarity: N'N-dimethylformamide (DMF), dichloromethane (DCM), and toluene.

S_1-state lifetimes are reported and range from 130 ps to 40 ns with considerable dependence on the photocatalyst structure and the solvent. Competition between ground-electronic state recovery and intersystem crossing controls triplet state populations and is a minor pathway in the dihydrophenazine derivatives but is of greater importance for phenoxazine and phenothiazine catalysts. Comparison of these results with previously reported O-ATRP performances of the various photoredox catalysts shows that high triplet-state quantum yields are not a pre-requisite for controlling polymer dispersity. The results call for a re-evaluation of the excited state properties of most significance in governing the photocatalytic behaviour of organic photoredox catalysts in O-ATRP reactions.

Spectroscopic signatures of the OPC excited states, electron acceptors and products of photoinduced electron transfer are tracked over sub-picosecond to nanosecond and microsecond time-intervals. Trends in bimolecular electron transfer rate coefficients are rationalized using a modified Marcus-Savéant theory of dissociative electron transfer and show that the Gibbs energy change is the major determinant of electron transfer rates in OPCs relevant for ATRP.

TVAS is applied to a recently reported reaction involving the addition of an electron-deficient alkyl radical to the strained σ-bond of a bicyclo[1.1.0]butyl boronate complex to form a cyclobutyl boronic ester. The previously proposed single electron transfer mechanism does not adequately account for the observed spectral and kinetic data. Instead, iodine atom transfer is shown to be the preferred pathway for this reaction and is likely to be operative for other reactions of this type.

Acknowledgements

Every person mentioned here has helped me achieve this and I am so happy that I have been able to share this time with you all.

I would first like to thank my wonderful girlfriend and partner Becca. You've been so incredibly supportive and have always been there when life (the PhD) has got me down. I honestly do not know how I would have got through this period of my life without you.

To my two wonderful parents Sue and Peter and equally wonderful brother Henry, thank you for believing in me every step of the way and never asking if I'm finished yet. Also, thank you Dad for inspiring me to follow in your footsteps and pursue chemistry.

Andrew, I remember when I first walked into your office and asked about this project. I was concerned that I didn't have the skills necessary to succeed in a physical chemistry PhD and your answer was so calm, "Well we'll teach you". Since then, you have been such an amazing mentor and supervisor. I truly admire how dedicated and in love with chemistry you are. Thank you so much for taking me on and providing me with such a wonderfully challenging and fun PhD.

Mahima, where to start? You've been like a sister to me since I met you. Not only have you been a fantastic mentor, pushing me to constantly question my own work and do better, but you've always been there to support me when I have doubted myself. I can't wait to welcome you and Sujith back for a Lewis-Borrell Christmas. P.S. You've found a great man in Sujith!

Varinder and Adam, you have both been fantastic supervisors. Always pushing and expecting more, presenting my work in front of you guys has given me the confidence to present anywhere in the world. If you both like it then I know it can't be too bad!

To everyone in the laser group, thank you for making it such a wonderful and welcoming group. It truly upsets me that I won't get to do another Friday pub with everyone because of this stupid pandemic. Mike, Tom, and Colin you have all been excellent friends and mentors throughout these past few years. Mike, I hope you enjoy your retirement and enjoy a thoroughly deserved rest. Tom, thank you for being a great examiner for my APMs, you always have an interesting train of thought and you've been such good fun to talk, joke and gossip with! Colin, I also hope you enjoy a well-deserved retirement! Giordano and Matt you have both been amazing office

buddies and thank you for such an amazing time travelling the US. Finally, to Georgia, Tony, Fab, Victoria, Marta, Stewart, Fred, Connah, Will and every other person who has passed through the group, thank you so much!

I have had the pleasure of visiting the Rutherford Appleton Laboratory multiple times and getting to play with one of the coolest experiments, LIFEtime. To Ian, Emma, Igor, Greg, Paul, Mike thank you so so much for always making our visits work and providing excellent company along the way. This thesis does not exist without you all.

Whenever I have had to do any synthesis it has been in N209, and I want to thank everyone in that lab who is helped me as I flail around trying to get all my samples ready for RAL visits. In particular: Sheenagh, Stevie, Rory, Felix, Kay, Joe and Alex. Furthermore, all the other amazing scientists in the Aggarwal group who are constantly there to offer a smile and a lovely chat. It's been a pleasure being part of such a wonderful group.

I would like to also thank my CDT cohort who have been there from the start but in particular Sbu, Jess, Eliza, Rachel, Ben, Freddy, Sayed, and Danny. I've had so much fun with you all!!

To the computational gang Rhos, Harry, Callum, Helen, Binnie, Zack, Dasha, and Joe you're nowhere near as nerdy as stereotypes may suggest. Thank you so much for being such great fun and so welcoming of me into your group. Especially all the walks over lockdown for which without I would have lost my sanity.

Having a life separate from chemistry has been so helpful and I must thank Steve and Alex for providing that. We've had so much fun, and I'll be back to Bristol for more.

Finally, to SARS-COV-2 thank you for showing me how sometimes the smallest of things can have the largest impact.

Authors Declaration

I declare that the work in this dissertation was carried out in accordance with the requirements of the University's *Regulations and Code of Practice for Research Degree Programmes* and that it has not been submitted for any other academic award. Except where indicated by specific reference in the text, the work is the candidate's own work. Work done in collaboration with, or with the assistance of, others, is indicated as such. Any views expressed in the dissertation are those of the author.

SIGNED: ..... DATE:.....

Table of Contents

1 Introduction

1.1 Photoredox Catalysis

The recent decade has witnessed a surge of interest in photochemistry brought on by the advent of photoredox catalysis in pioneering studies by MacMillan,[1] Yoon,[2] and Stephenson[3]. The method typically uses a transition metal (Ir or Ru) based catalyst which can absorb a photon of light and access a high energy excited state. Before discussing how this excited state may react it is worth spending time on its photochemistry. When an $[Ir(ppy)_3]^{3+}$ or $[Ru(bpy)_3]^{2+}$

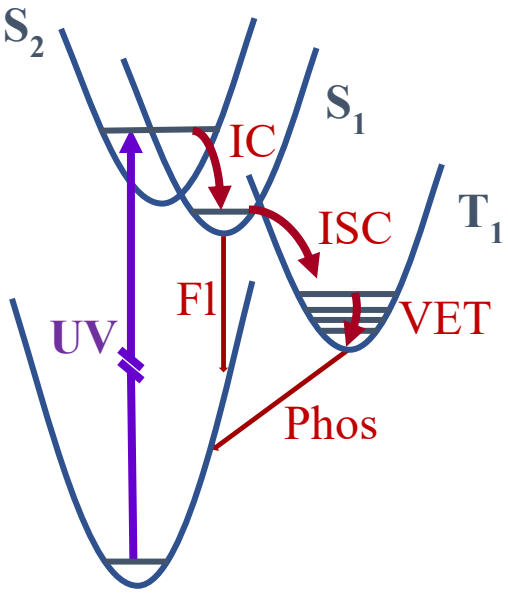

Figure 1.1. *A Jablonksi diagram for the general photophysical processes a molecule may undergo after photoexcitation. Processes are shown from the first UV excitation into the S_2 state followed by internal conversion into the lowest excited singlet state (S_1). From the S_1 state the system may either undergo fluorescence (Fl) back the ground state or intersystem cross (ISC) into the triplet manifold from where it can phosphoresce (Phos) back the ground state. Internally excited molecules will also undergo some vibrational energy transfer (VET) to the solvent as they cool from high lying vibrational states.*

photocatalyst absorbs a photon of light, it is excited to a high lying singlet state (S_n) which can then undergo rapid internal conversion (IC) down to the S_1 state in accordance with Kasha's rule. This S_1 state is localised on the π^* orbital of a bpy or ppy ligand and is called a metal to ligand charge transfer (MLCT) state, resulting in a species where the metal centre has been oxidised and the ligand has been reduced. The singlet MLCT state then undergoes rapid inter system crossing (ISC) into the triplet manifold, which, due to the spin forbidden transition back to the ground state, has an extended lifetime on the order of microseconds. The MLCT excited state may perform a one electron oxidation (reductive quenching) or reduction (oxidative quenching) to start a catalytic cycle, which is then closed by a final redox event. The general

photochemical processes are shown in **Figure 1.1** and a general photoredox mechanism is shown in **Figure 1.2** using the catalyst $[Ru(bpy)_3]^{2+}$ as an example.

This idea has allowed chemists to access an array of reactions including C-H functionalisation,[4] dual catalysed Ni-based $C(sp^3)$-$C(sp^2)$ cross coupling,[5] dual catalysed Cu-based stereoselective reactions,[6] and an enantioselective Minisci-type reaction using a chiral Lewis acid.[7]

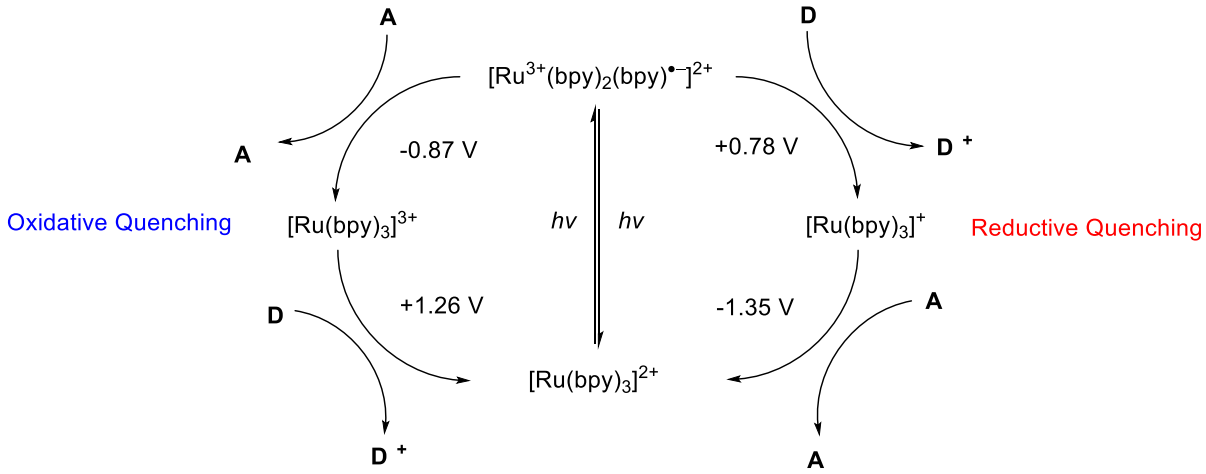

Figure 1.2. *A general mechanism for the oxidative and reductive quenching of the* $[Ru(bpy)_3]^{2+}$ *photocatalyst.*

1.1.1 Photophysical Processes

This section will provide a short introduction to the theory behind the photophysical processes shown in **Figure 1.2**, to provide background of how and why these processes occur. A common distinction made is that between non-radiative (Internal conversion (IC), inter-system crossing (ISC), and vibrational energy transfer (VET)) and radiative (fluorescence and phosphorescence) decay pathways in excited state relaxation. This distinction is typically made both to distinguish pathways that do and do not involve emission of light, and because of the differences in rate between fast non-radiative and slower radiative pathways.

1.1.1.1 Non-Radiative Relaxation

1.1.1.1.1 Internal Conversion

The Born-Oppenheimer approximation states that the wavefunctions of atomic nuclei and electrons may be treated as separate.

$$\Phi_{total} = \phi_{electronic}\Psi_{nuclear} \qquad (1)$$

This approximation is valid in many cases due to the differences in mass of the nuclei and electrons; given an equal amount of kinetic energy, the nuclei will move much more slowly

compared to the lighter electrons. Using the Born-Oppenheimer approximation allows an electronic Schrödinger equation to be solved to obtain the electronic energy (E_e),

$$H_e(\boldsymbol{r}, \boldsymbol{R})\chi(\boldsymbol{r}, \boldsymbol{R}) = E_e\chi(\boldsymbol{r}, \boldsymbol{R}) \quad (2)$$

Where $\boldsymbol{r}$ and $\boldsymbol{R}$ are the electronic and nuclear coordinates, respectively. Varying $\boldsymbol{R}$ and solving for E_e allows a potential energy surface model to be created which maps out the energy landscape in 3N-6 dimensions, where N is the number of nuclei in the molecule. Potential energy surface models are useful for understanding photochemical processes.

IC takes place between electronic states of the same spin multiplicity, e.g., S_2 to S_1 or T_2 to T_1, leading to population of a state which is typically lower in energy. To undergo IC the electronic wavefunctions (ϕ) of the two electronic states must meet at a conical intersection (CI). A CI arises at specific molecular geometries where two potential energy surfaces cross. At such a crossing point the electronic wavefunction are degenerate, $\phi_i = \phi_j$, and the nuclear and electronic motions are strongly coupled leading to a break down of the Born-Oppenheimer approximation.[8]

IC is usually extremely fast, taking place on timescales on the order of femto to pico seconds, and is what gives rise to Kasha's rule in which the radiative state is assumed to be the lowest excited electronic state of a particular spin multiplicity (the S_1 or T_1 state). In some cases, ISC can outcompete IC and the next section looks in more detail at what ISC is and how it happens.

1.1.1.1.2 Inter-System Crossing

ISC is similar to IC in that it is a radiationless transition between electronic states and takes place through a region in which two PE curves cross. The key difference is that the transition takes place between states of *different* spin multiplicity, e.g., S_n to T_n. Transitions between states of different spin multiplicity are forbidden in the absence of spin-orbit coupling (SOC) which is the dominant interaction that induces ISC. Atomic SOC constants, which determine the degree of SOC, increases roughly with the fourth power of the atomic number of an atom.[9] This means molecules containing smaller atoms will typically have weaker SOC and thus slower ISC; conversely, molecules with larger, or heavier, atoms will have stronger SOC and faster ISC which can outcompete IC or radiative decay pathways. This phenomenon is called the "heavy atom effect".[9] Although, the heavy atom effect is the most common mechanism for ISC, in some cases ISC can occur in the absence in heavy atoms. Take for example

benzophenone, a commonly used photocatalyst,[10] which undergoes ISC on timescales of about 200 fs due to near degeneracy of the S_1 and T_2 states.[11]

1.1.1.1.3 Vibrational Energy Transfer

After a molecule has undergone photoexcitation, IC, or ISC it is usually formed in a vibrationally excited level, v_i where $i \neq 0$. From this high vibrational level, rapid VET to the surrounding solvent bath takes place typically within a few picoseconds, depending on the strength of the couplings to the surrounding solvent molecules. In transient spectroscopy experiments, a sign of VET is the appearance of shifting of excited state absorptions to higher wavenumber (shorter wavelength).

1.1.1.2 Radiative Relaxation

1.1.1.2.1 Fluorescence

Fluorescence is a radiative decay pathway back to the ground state which typically takes place from S_1 to S_0 in accordance with Kasha's rule. Compared to IC, fluorescence is slow and commonly takes place over orders of nanoseconds. Fluorescence quantum yields (see section 1.1.2.1) give an indication of the degree of competition between fluorescence and non-radiative decay pathways.

1.1.1.2.2 Phosphorescence

Phosphorescence is another radiative decay pathway, but rather than a singlet excited state it is a pathway from a triplet excited state to the ground state (assumed here to be a closed-shell, singlet state), so takes place with change of spin multiplicity. This process is even slower than fluorescence, with relaxation occurring over micro and milli seconds. Because the T_1 state is generally lower in energy than the S_1 state in a given molecule, phosphorescence bands appear at longer wavelength than fluorescence bands. They are also much weaker because of the spin-forbidden nature of the relaxation pathway.

1.1.2 Photochemical and Electrochemical Aspects

When characterising photocatalysts, it is useful to quantify their behaviour both photophysically (e.g. using quantum yields for ISC and fluorescence) and electrochemically (e.g. by considering redox potentials for electron transfer in the ground state and for photoinduced electron transfer, and Marcus theory for electron transfer rates). Both these features allow a global description of how the excited state may behave after light absorption

and how rates of electron transfer from either the excited or ground electronic states can be understood.

1.1.2.1 Quantum Yield

The simplest definition of a wavelength-dependent quantum yield, equation 3, is that $\Phi_x(\lambda)$ is equal to the number n_x of photochemical or photophysical events x that occurred, divided by the number n_p of photons at the irradiation wavelength λ that were absorbed by the reactant. Both n_x and n_p are measured in moles or Einsteins (1 Einstein = 1 mol of photons) and $\Phi_x(\lambda)$ is dimensionless.

$$\Phi_x(\lambda) = n_x/n_p \quad (3)$$

With regard to photoredox catalysis, quantum yield values can be useful in describing the number of triplet state molecules formed after light absorption, the yield of fluorescence for a catalyst, and the overall efficiency of a photochemical reaction. We can define the quantum yield for ISC ($\Phi_{ISC}(\lambda)$) in terms of fundamental rates of a given process, where the numerator is the rate of inter system crossing and the denominator is the sum of the rates for all the possible non-radiative (v_{nr}) or radiative (v_r) photochemical processes, equation 4 (including the ISC pathway).

$$\Phi_{ISC}(\lambda) = \frac{v_{ISC}}{\sum v_r + \sum v_{nr}} \quad (4)$$

If v_{ISC} is fast enough to compete with other photophysical processes, then T_1 can become the dominant excited state and electron transfer in a photoredox cycle will take place predominantly from/to there. The lifetimes of triplet states tend to be drastically longer (approx. μs to ms) than those of singlet states (typically ns) because the pathway back down to the ground state is spin forbidden from T_1. This leads to two important aspects which can affect reactivity: firstly, it is thought that the long lifetimes of triplet states furnish the photocatalysts with enough time to diffuse and undergo bimolecular electron transfer in dilute solutions; and secondly, back electron transfer from the reactant to the catalyst to repopulate its S_0 state is suppressed due to this being a spin forbidden process.

The quantum yield of fluorescence ($\Phi_f(\lambda)$) is another useful metric as it provides information about other non-radiative pathways of decay to the ground-state. The greater the value of $\Phi_f(\lambda)$, the more likely the reactive excited state will be the S_1 state instead of T_1. Fluorescence

quantum yields approaching unity indicate that decay is almost entirely through fluorescence, while quantum yields close to 0 show that decay pathways are mostly non-radiative. Equation 5 defines this relationship, showing the ratio between the number of photons absorbed ($n_{photons\ in}$) and the number photons emitted ($n_{photons\ out}$).

$$\Phi_f(\lambda) = n_{photons\ out}/n_{photons\ in} \quad (5)$$

1.1.2.2 Lifetimes

Lifetime, τ_x, is defined in equation 6 for any first-order process which can be described with a rate constant, k_x. Lifetimes tend to be used to describe the rate of decay of an intermediate, whether that be an excited state or a short-lived radical.

$$\tau_x = 1/k_x \quad (6)$$

Excited state lifetimes are useful parameters because they gauge whether an excited state will have a lifetime long enough to diffuse and react with a quencher. In a general sense, the longer the lifetime the more likely an excited state will meet a reactant and quench. The lower limit for lifetimes allowing diffusive reactions is about a nanosecond.

1.1.2.3 Electron Transfer in the ground and excited states

The Gibbs energy of electron transfer can be described thus:

$$\Delta G = -\mathcal{F}(\Delta E) = -\mathcal{F}(E_{red} - E_{ox}) \quad (7)$$

$$= -\mathcal{F}\left(E_{1/2}(A/A^{\bullet-}) - E_{1/2}(D^{\bullet+}/D)\right) \quad (7\text{ cont.})$$

$\mathcal{F}$ is the Faraday constant and E_{red} and E_{ox} are the reduction and oxidation potentials, respectively. E_{red} is common shorthand for $E_{1/2}(A/A^{\bullet-})$ which states that an electron acceptor, A, is reduced by a single electron forming, $A^{\bullet-}$. E_{red} values are typically negative (<0 V) for most ground state species as single electron reduction is thermodynamically unfavoured. E_{ox}, which is referred to as the oxidation potential and represents $E_{1/2}(D^{\bullet+}/D)$, refers to the single electron reduction of cationic species $D^{\bullet+}$ to ground state species D. E_{ox} values are generally positive (>0 V) due to the thermodynamic favourability of gaining an electron to form a closed-shell neutral species.

Discussion of *photoinduced* electron transfer (PET) requires use of a different equation, referred to as equation for the Gibbs energy of photoinduced electron transfer, equation 8.

$$\Delta G = -\mathcal{F}(E_{ox}(A/A^{\bullet-}) - E_{red}(D^{\bullet+}/D)) - w - E_{0,0} \quad (8)$$

This equation importantly includes the energy of the excited state ($E_{0,0}$), allowing it to account for differences in excited energies between catalysts. It also includes the electrostatic work term (w) which accounts for solvent-dependent energy differences due to the Coulombic impact of charge separation. By excluding w equation 8 can be simplified, allowing easy estimation of whether a given PET will be thermodynamically favourable. Although important in detailed mechanistic analyses, w can be ignored when quickly judging the thermodynamic feasibility of a given redox event. The Gibbs energy change for a PET involving an excited state (cat*) donating an electron to a substrate (sub) can be quantified using equation 9:

$$\Delta G_{PET} = -\mathcal{F}(E^*_{red}(cat^*/cat^{\bullet-}) - E_{ox}(sub^{\bullet+}/sub)) \quad (9)$$

Where $E^*_{red}(cat^*/cat^{\bullet-})$ is the excited state reduction potential and is calculated by taking into account the redox couple of the ground state reduction and the excited state energy, whether that be singlet or triplet character. The equation for this is shown below.

$$E^*_{red}(cat^*/cat^{\bullet-}) = E_{red}(cat/cat^{\bullet-}) + E_{0,0} \quad (10)$$

For a PET involving oxidation of an excited state (cat*) and reduction of the substrate the equation below may be used.

$$\Delta G_{PET} = -\mathcal{F}(E_{red}(sub/sub^{\bullet-}) - E^*_{ox}(cat^*/cat^{\bullet+})) \quad (11)$$

The oxidation potential ($E_{ox}(cat^*/cat^{\bullet+})$) may be calculated in a similar way to equation 11.

$$E^*_{ox}(cat^*/cat^{\bullet+}) = E_{ox}(cat^{\bullet+}/cat) + E_{0,0} \quad (12)$$

As mentioned above, these equations provide a qualitative understanding of whether a given catalyst will undergo PET with a given substrate. If $\Delta G_{PET} < 0$ then the process is favourable.

1.1.2.4 Marcus Theory

Marcus Theory was proposed by Rudolf Marcus in 1956[12] and states that the rates of electron transfer from both ground and excited states depend on three things:

1) The distance between donor and acceptor, with the electron transfer becoming faster the closer the two species become.

2) The reaction Gibbs energy ($\Delta_r G$), with electron transfer becoming faster the more exergonic a process gets ($\Delta_r G < 0$).

3) The reorganisation energy, the energy required for the solvent to reorganise around the two charged species formed after electron transfer ($D + A \rightarrow D^{\bullet+} + A^{\bullet-}$).

These three points may be visualised using the Gibbs energy surface for the reaction $D + A \rightarrow D^{\bullet+} + A^{\bullet-}$, shown in **Figure 1.3**. This surface represents the free energy space of the donor, acceptor and solvent. Two separate and intersecting parabolas represent the Gibbs energy curves for the solvated reactants and products of the electron transfer reaction **Figure 1.3** highlights the various key points described within Marcus theory. In the figure q^*, the nuclear coordinate at which the two parabolas intersect, is the coordinate at which electron transfer may take place and requires movement of the nuclear geometries of both D and A, so that electron transfer is feasible. $\Delta_r G$ is the thermodynamic driving force for the electron transfer to take place. Outside the inverted region, as this Gibbs energy change grows larger or smaller the Gibbs energy for activation ($\Delta^{\ddagger} G$) will change with it. λ is the energy required for the solvent to reorganise around the now charged species formed after electron transfer ($D^{\bullet+} + A^{\bullet-}$).

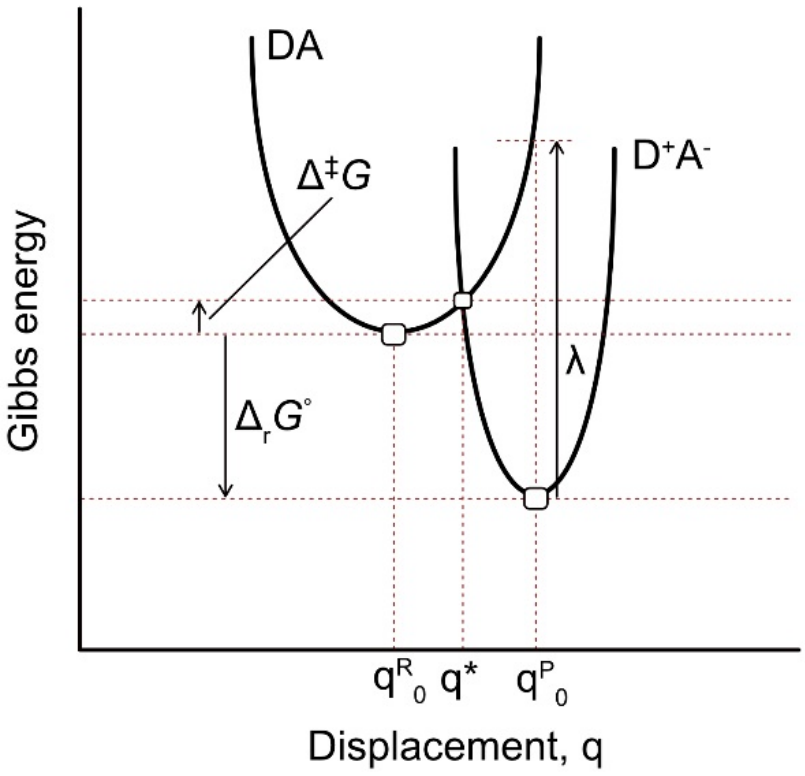

Figure 1.3. *The Gibbs energy surfaces for the complexes DA and D^+A^- involved in an electron transfer process. The displacement parameter (q) represents the change in geometry (including solvent restructuring) from reactant (q^R_0), to transition state (q^*) and products (q^P_0). Gibbs energy of reaction ($\Delta_r G$), Gibbs energy of activation ($\Delta^{\ddagger} G$) and the solvent reorganisation energy (λ) are also shown.*

Each of the key points can be brought together in equations 13 and 14 used to calculate the rate coefficient for electron transfer, k_{et}.

$$k_{et} = \frac{2\langle H_{DA}\rangle^2}{h}\left(\frac{\pi^3}{4\lambda RT}\right)e^{-\Delta^{\ddagger}G/RT} \quad (13)$$

$$\Delta^{\ddagger}G = \frac{(\Delta_r G+\lambda)^2}{4\lambda} \quad (14)$$

The term $\langle H_{DA}\rangle$ is an expectation value of a Hamiltonian which accounts for the coupling of the two electronic wave functions of D and A and incorporates the decrease in rates of electron transfer based on distance between D and A. All other terms are present in **Figure 1.3.**

In systems where $A^{\bullet-}$ dissociates into a radical and an anion, **Scheme 1.1**, traditional Marcus theory cannot be used. Instead Savéant provided a modification which includes the bond dissociation energy for the bond being broken, equation 15.[13,14,15]

$D + A\text{-}X \rightarrow D^{\bullet+} + A^{\bullet} + X^{-}$ (Scheme 1.1)

$$\Delta^{\ddagger}G = \frac{\lambda+E_{BD}}{4}\left(1+\frac{\Delta_r G}{\lambda+E_{BD}}\right)^2 \quad (15)$$

Isse et al. have proposed further additions, here referred to as the Marcus "sticky" model.[16] The "sticky" model accounts for the intermolecular interactions between $A^{\bullet}$ and X^{-} after dissociative electron transfer by addition of D_p, the dissociation energy of the $A^{\bullet}$ and X^{-} pair in the solvent cage. This iteration of Marcus theory is shown in equation 16.

$$\Delta G^{\ddagger} = \frac{\lambda_0+\left(\sqrt{E_{BD}}-\sqrt{D_p}\right)^2}{4}\left(1+\frac{\Delta G_{ET}-D_p}{\lambda_0+\left(\sqrt{E_{BD}}-\sqrt{D_p}\right)^2}\right)^2 \quad (16)$$

1.1.3 Organic Photoredox Catalysis

Within the field of catalysis, there is increasing recognition that the use of the Ir and Ru catalysts is not a sustainable option for the future, and a shift towards alternatives is currently under way.[17,18] One option is the use of carbon-based dyes which can catalyse reactions through the same redox cycles as metal based photocatalysts. A few examples are shown in **Figure 1.4**. Fukuzumi and Nicewicz have pioneered this area of photoredox catalysis with examples such as chlorination,[19] bromination,[20] oxygenation,[21] various forms of anti-Markovnikov additions to alkenes, [22,23,24,25] C-H amination,[26] as well as general strategies for C-H activation of arenes[27] and heteroarenes.[28]

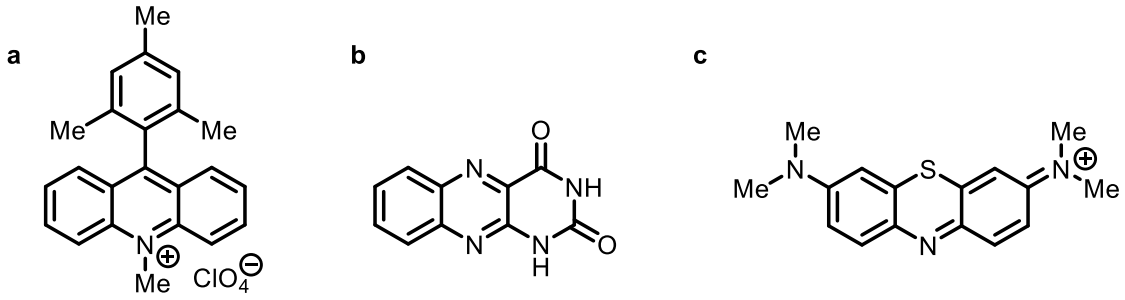

9-Mesityl-10-methyl acridinium perchlorate

alloxazine

Methylene blue

Figure 1.4. *Common organic dyes used to catalyse photoredox reactions.*

1.1.3.1 Singlet vs Triplet States

Due to the large SOC in transition metal photoredox catalysts, the quantum yield for ISC tends to be very high.[29] However for organic photocatalysts the same does not apply due to the absence of heavy atoms. A given catalyst might therefore react through the S_1 or T_1 state. This distinction can have clear effects on reactivity, with singlet states tending to have higher redox potentials than their triplet counterparts, meaning that a singlet state may be able to react with a quencher where a triplet state may fail. Another important difference is the lifetimes of the two species: triplet states tend to have lifetimes on the order of microseconds, whereas singlet states decay much faster, on the order of tens of nanoseconds.

1.1.4 Chain Processes

Photoredox catalysis works through generation of radical species, and chain processes are inherent to radical chemistry. Chain cycles may be thought of as catalytic cycles but without the need for a catalyst. Instead, the initial radical is reformed through a step called propagation where a radical intermediate reacts with the initiator in a product-forming reaction. Propagation reactions may take place through two mechanisms, either: atom transfer, where an atom (typically I, Br, Cl, or H) can be transferred from the initiator to an intermediate in a product-forming step; or electron transfer, where an intermediate may be oxidised or reduced by the initiator to form the product. These two mechanisms may be thought of as inner or outer-sphere electron transfer, respectively.

The efficiency of a propagating chain depends on the magnitude of the rate coefficient of propagation; the lower it is, the more radical-radical termination reactions become competitive. Likewise, in the presence of a catalyst a slow propagation reaction will instead take place through reaction with the catalyst to turn-over the cycle. Conversely this means that if

propagation is fast then the major pathway will **not** be through catalyst turn-over but through chain cycles. Hence, one should be sceptical of any catalytic cycles seen in photo redox catalysis.

1.1.5 Stern-Volmer Quenching

A technique commonly employed throughout photoredox and photochemical studies is Stern-Volmer analysis which provides information about the rates of excited state quenching. The term "quenching" here refers to any process by which the radiative quantum yield of a chromophores is reduced. A typical reaction scheme for a quenching process looks like that shown in **Scheme 1.2**:

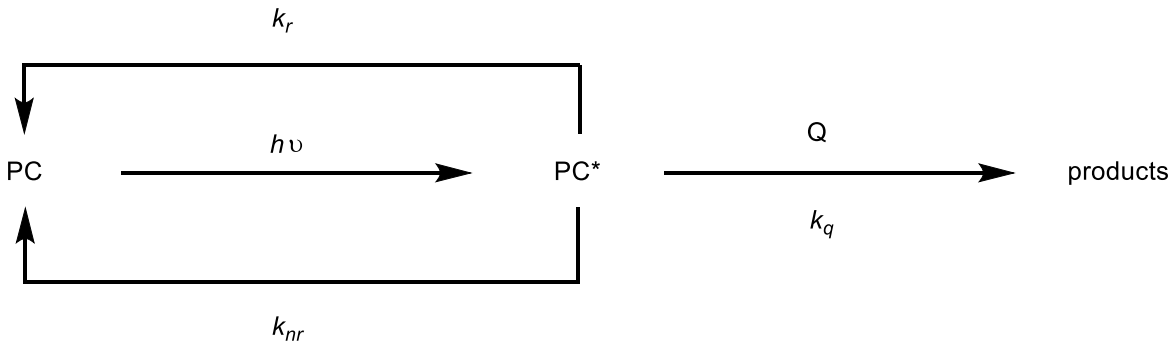

Scheme 1.2. *Reactive pathways in an excited state quenching reaction. A photocatalyst (PC) is photo-excited leading to a reactive excited state (PC*) which can either return to the ground state through radiative (k_r) and non-radiative (k_{nr}) photophysical relaxation pathways or react with a quencher (Q) through either excited state single electron transfer or triplet energy transfer (k_q).*

The corresponding rate equation for this reaction scheme is,

$$\frac{d[PC^*]}{dt} = -(k_r + k_{nr})[PC^*] - k_q[PC^*][Q] \qquad (17)$$

Quenching then refers a situation when $(k_r + k_{nr}) << k_q[Q]$ such that the observed lifetime of PC^* is significantly reduced upon addition of increasing concentrations of Q. When an excited state has a lifetime longer than a nanosecond, it will primarily react through quenching. However, if a new pathway is opened which makes k_{nr} faster, the likelihood of quenching will decrease. In this analysis, there is no explicit differentiation made between singlet and triplet excited states, with the assumption being that quenching occurs only from either the singlet or the triplet state. While this assumption may hold with transition metal photocatalysts, in which k_{ISC} is extremely fast, it is not safe to generalise to organic photocatalysts where k_{ISC} is often much slower due to the absence of heavy atoms. A model is derived in Chapter 2 which allows the competing quenching pathways of singlet and triplet states to be modelled correctly. To

quantify k_q, measurements are made using the pseudo-first order approximation under which equation 17 becomes,

$$\frac{d[PC^*]}{dt} = -(k_r + k_{nr} + k_q[Q])[PC^*] = -k_{obs}[PC^*] \quad (18)$$

$$k_{obs} = k_r + k_{nr} + k_q[Q] = k_d + k_q[Q] \quad (19)$$

Here k_d comes from the measured lifetime of the PC being quenched and is known prior to the experiment. Dividing both sides by k_d gives the equation,

$$\frac{k_{obs}}{k_d} = 1 + \frac{k_q}{k_d}[Q] = 1 + k_q\tau_d[Q] \quad (20)$$

Using the radiative quantum yields without and with the quencher,

$$\frac{\phi_r}{\phi_{rq}} = \frac{\frac{k_r}{k_d}}{\frac{k_r}{k_d+k_q[Q]}} = \frac{k_d+k_q[Q]}{k_d} = \frac{k_{obs}}{k_d} \quad (21)$$

Thus, the Stern-Volmer equation is,

$$\frac{\phi_r}{\phi_{rq}} = 1 + k_q\tau_d[Q] \quad (22)$$

From this, a plot of the ratio of quantum yields determined from fluorescence quenching measurements vs. $[Q]$ will give a straight line with intercept 1 and gradient k_q. Importantly though, this will not reveal what excited state is being quenched, by which mechanism it is being quenched (e.g., electron transfer or triplet energy transfer), or anything about the mechanism beyond this first quenching step. To understand these other processes, time-resolved spectroscopic measurements are required. The most prevalent such method, which is also the key topic of this thesis, is transient absorption spectroscopy, and is discussed in the next section.

1.2 Transient Absorption Spectroscopy in the Mechanistic Study of Photoredox

The pace of publication within photoredox catalysis is at an all-time high, with approximately 1300 publications referencing 'photoredox' in 2020 alone.[30] However, mechanistic study has not kept up with the pace of innovation and there are scarce examples of such studies in the

literature.[31] Scaiano has demonstrated how mechanistic study can influence reaction design:[32] an investigation of the mechanism of an oxidative hydroxylation of arylboronic acids revealed that by switching to the organocatalyst methylene blue (**Figure 1.4c**), the rate of quenching could be increased by up to 40 times compared to the $[Ru(bpy)_3]^{2+}$ catalyst.

One technique which is particularly well suited to study photochemical mechanisms is transient absorption (TA) spectroscopy in which a pump pulse of tuneable wavelength can selectively excite a photocatalyst. The resulting photo products are tracked with a probe pulse in either the UV/Vis wavelength range (200 nm – 700 nm) or IR wavelength range (700 nm – 10 μm), referred to here as transient electronic absorption spectroscopy (TEAS) and transient vibrational absorption spectroscopy (TVAS) respectively. Depending on the set-up, reactions may be tracked from hundreds of femtoseconds up to tens of milliseconds. **Figure 1.5** shows a simple schematic diagram for a TVAS set up with a UV pulse of light passing through a sample followed by an IR probe pulse spanning approximately 200 - 400 cm^{-1}. The transmitted light is dispersed on a grating and spread across a 128-pixel detector array, allowing an IR spectrum to be produced. The advantage of this technique is that it allows real-time tracking of short-lived intermediates, typically with lifetimes on the order of picoseconds. Kinetic analyses can then be performed on species impossible to observe with steady state spectroscopic or other analytical techniques.

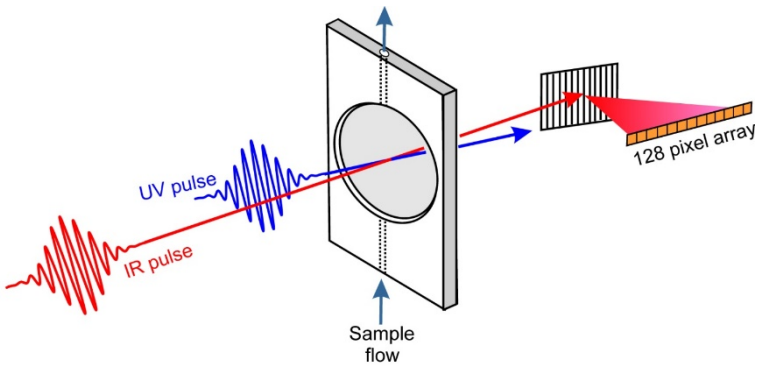

Figure 1.5. *A schematic diagram of a pump-probe transient absorption experiment. A pump pulse of UV light excites the sample, followed by the probe pulse of IR light. The transmitted IR light is frequency dispersed by a grating onto a 128-pixel detector array which provides the spectrum.*

Typically, TA spectra show changes in the absorbance (ΔA) between a sample with the pump (UV pulse) on and pump off. This data processing causes transient spectra to show both positive and negative peaks. The latter are named bleaches and indicate that a ground state species is decreasing in population. In contrast, positive peaks show that new species are being formed.

There are many examples in the literature where TA spectroscopy has been used to understand the mechanism of a reaction, however these studies tend to be limited to showing that the excited state is quenched by reactant. Rarer are studies which lead to a significant change in the understanding of a reaction; lead to improved catalyst or reaction design; or aim to look beyond the first quenching step. The rest of this section will summarise some of these studies.

1.2.1 Nano-Second Transient Absorption Spectroscopy Studies

A seminal example of TA used for the detailed study of photoredox catalysis was by Nicewicz and coworkers, who applied a nanosecond laser set-up to observe the anti-Markovnikov alkene hydrofunctionalization reaction catalysed by 9-mesityl-10-methylacridinium (MesAcr, structure in **Figure 1.4a**).[25] Their aim was to observe, and quantify, each step of the catalytic cycle. Although this was not in the end achieved solely by TA, they did, in combination with other experiments, provide rate coefficients for each step of the cycle. By doing this, they identified the rate determining step (deprotonation) and why this led to an increase in a non-productive catalyst pathway. Although not explicitly stated, it seems likely that these results will have influenced the design of MesAcr analogues used in future work by the group.[33]

Glorious and Guldi used a nanosecond-TA set up to assign the mechanism of a biocompatible hydrothiolation reaction to a Dexter-type triplet-triplet energy transfer.[34] Using this assignment, they showed that by switching to the organic photosensitiser, alloxazine (**Figure 1.4c**), which has higher triplet energy and less steric bulk, both substrate scope and rate of reaction could be increased.

Work by Nocera and coworkers took a different perspective on the optimisation of photoredox reactions. Thinking about these reactions as a fundamental energy flow optimisation problem, they proposed that by understanding the whole mechanism, including competing pathways, inefficient pathways could be 'turned off'. This would increase the overall quantum yield and therefore energy efficiency. To do this, they applied a nanosecond-TA set-up to understand the photoredox catalysed hydroamidation reaction. They found that there were indeed many competing pathways but most important were the unproductive back electron transfer and hydrogen atom transfer from the amidyl radical intermediate to reform starting material. By inclusion of a radical trap reagent (Mes_2S_2) and tuning of the starting material electronics, they could realise an increased quantum yield for reaction.

The Evan group have recently used nanosecond-TA to answer an open question about the mechanism for a photoredox catalysed C-H arylation reaction of activated aryl bromides first published by König.[35,36] This open question lay around the key reductive quenching step between the pyrene excited state (*Pyr) and Hünig's base. It was argued that the single electron transfer (SET) from *Pyr(T_1) would be highly endergonic (ca. -1.0 V vs. SCE). Thus, a triplet-triplet annihilation (TTA) mechanism was proposed in which *Pyr(S_1) is formed after *Pyr(T_1) TTA. The S_1 state would then be oxidising enough to undergo SET (ca. + 2.1 V vs. SCE). By identifying the various reactive intermediates in their spectra and their kinetics, they argued that not only was the TTA mechanism in operation but another competing pathway of SET from *Pyr(T_1) to the $[Ru(bpy)_3]^+$ intermediate was also happening, as shown in **Figure 1.6**.

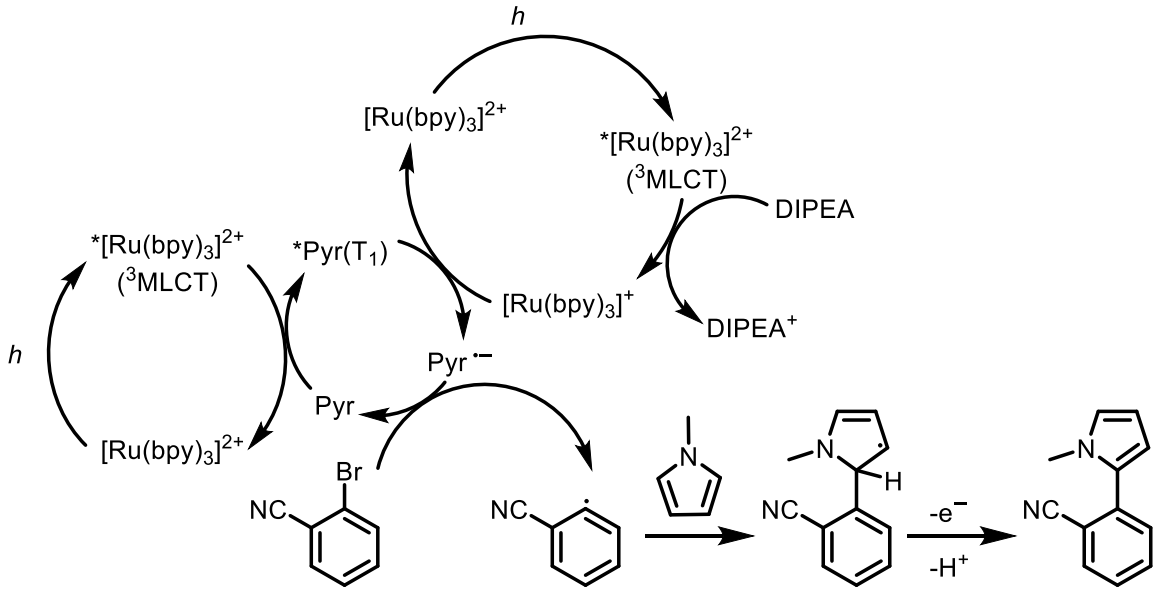

Figure 1.6. *Proposed reaction mechanism for C-H arylation based on TA experiments done by Evans.*

Ellman, Miller and coworkers thought to apply nanosecond-TA to a highly diastereoselective α-amino C-H functionalisation of piperidines they had discovered.[37] They were unsure whether the high diastereoselectivity came about due to thermodynamic or kinetic reasons. If it were to be the latter, the rate of oxidation for the *anti*-piperidine diastereoisomer would be expected to be at least 19 times faster than that of the *syn*-piperidine diastereoisomer to explain the >19:1 diasteroselectivity observed. They were able to see this reductive quenching of the photocatalyst via TA and garner rate coefficients from the experiment. They observed that the rate coefficients for both anti or syn oxidation were the same within error. Therefore, it was argued that the epimerisation is likely to be under thermodynamic control.

Swierk and coworkers took inspiration from Nocera to try to explain the observed quantum yield (QY) measurements in an α-aminoarylation between *N*-phenylpyrrolidine (NPP) and dicyanobenzene (DCB).[38] Their measurements indicated that the external QY (equation 3) started low (0.36) and steadily decreased throughout the course of the reaction. Using TA spectroscopy, they identified key reactive intermediates and created a kinetic model for the reaction. It was also noted that a significant proportion of incident photons were either absorbed by a photochemically inactive ground state complex or scattered by insoluble NaOAc, leading to a lowering of the initial *internal* QY from 1 to an observed *external* QY of 0.36. Using their kinetic model, they showed that throughout the course of the reaction, radical recombination reactions between $DCB^{\bullet-}$ and $NPP^{\bullet+}$, and competitive quenching of the excited state by AcOH (produced in the deprotonation) began to lower the QY over time. Overall, the authors identified the parasitic ground state complex as the area best improved in this reaction, suggesting either use of electrolytes or solvent switches to overcome this problem.

1.2.2 Ultrafast Transient Absorption Spectroscopy Studies

The studies in the previous section highlight how the long time (hundreds of nanoseconds to milliseconds) bimolecular reactions and intermediates can be observed by nanosecond-TA spectroscopy. A drawback to this approach is that chemical dynamics taking place from hundreds of femtoseconds through to the first few nanoseconds tend to be missed. These can be important, especially when trying to assign the identity of excited states as Scholes and Doyle have shown by applying ultrafast-TA to assign the excited state of Ni(II) complexes.[39,40] In a short paper published in 2018, Scholes and Doyle showed that Ni(II) complexes common in photoredox catalytic cycles were also photo active and could access a long-lived excited state (τ = 4 ns) which they assigned to a metal to ligand charge transfer triplet state (^{3}MLCT). Further to this, in a more comprehensive follow up paper, they reassigned this long-lived state to a ^{3}d-d state more common for first row transition metals. They highlighted that the ^{3}MLCT is indeed formed, however this very quickly (in ~5-10 ps) relaxes to the ^{3}d-d state which undergoes bond homolysis to form an aryl radical and Ni(I) species. This assignment was accomplished through a combination of spectroscopies (NMR, EPR, TEAS), but most notable is the TVAS which shows ps growth and ns decay of a ^{3}d-d signature band, as shown in **Figure 1.7**.

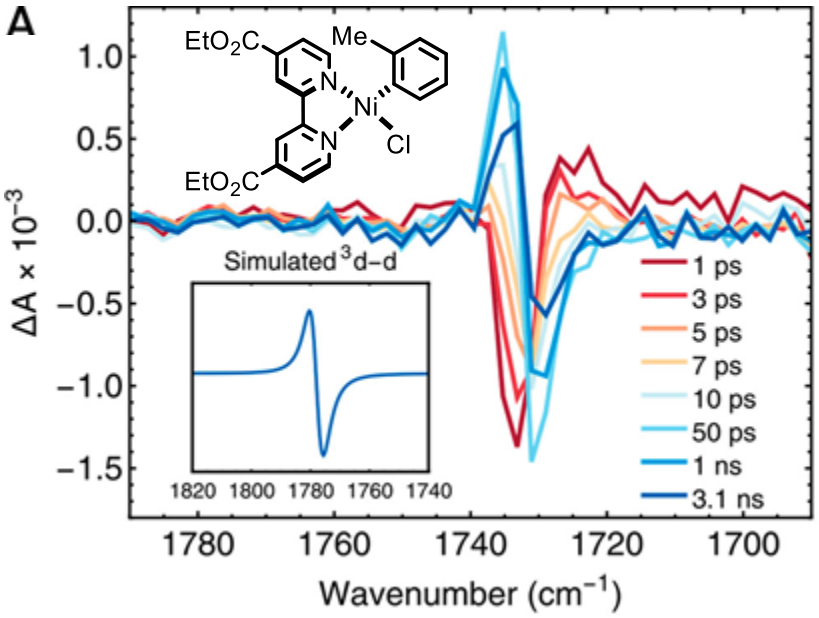

Figure 1.7. *TVA spectra of Ni(CO_2Etbpy)(o-Tol)Cl. The simulated ^{3}d-d spectrum is inset. Recreated from ref: [40].*

Scholes and Doyle argued that the assignment of the Ni(II) excited state has major ramifications for Ni based photochemistry; namely, the possibility that cross-couplings proposed to proceed via photoinduced reductive elimination may actually operate via photoinitiated Ni(I)/Ni(III) cycle.

1.2.3 Wide Timescale TVAS

Preceding sections have discussed how both early and late time dynamics can be useful in assessing the various steps in photoredox catalysed reactions; however, these two timescales tend to be represented in stand-alone experiments (nanosecond-TA or ultrafast-TA). This section will consider how combining both timescales in a single experiment can lead to interesting mechanistic insights.

Although not explicitly about photoredox catalysis, a study by Lynam using this type of wide timescale TVAS spectroscopy showed how powerful it can be in identifying catalytic intermediates which are typically short-lived, of low concentration and appear over dynamic time ranges.[41] Therein, Lynam and co-workers set out to understand the mechanism of a Mn catalysed aryl C-H functionalisation. They were able to identify multiple intermediates within the catalytic cycle and measured how their absorbances changed in real-time leading to a more comprehensive and quantified view of the mechanism.

Orr-Ewing and coworkers applied this wide timescale TVAS to the understanding of a photoredox catalysed decarboxylation shown in **Figure 1.8** and first discovered by Yoshima

and coworkers.[42,43] In this case, it was possible to resolve several intermediates in the catalytic cycle including: phenanthrene (PHEN) excited state; its oxidised radical cation PHEN•+; dicyanobenzene (DCB) radical anion; a carboxyl radical, formed from deprotonation of the carboxylic acid and subsequent oxidation by PHEN•+; and the formation of CO_2 after decarboxylation. From this comprehensive set of observations, they confirmed the proposed mechanism was indeed in operation, and determined the lifetime of the carboxyl radical with respect to unimolecular loss of CO_2. They also showed a possible alternative pathway, photo-excitation of DCB and oxidation of PHEN, was not viable, based on a control experiment in which DCB was selectively excited in the presence of PHEN but no PHEN•+ or DCB•- was observed. Interestingly while Swierk and coworkers identified that DCB•- dimerised in their system, the same was not observed in this study.[38]

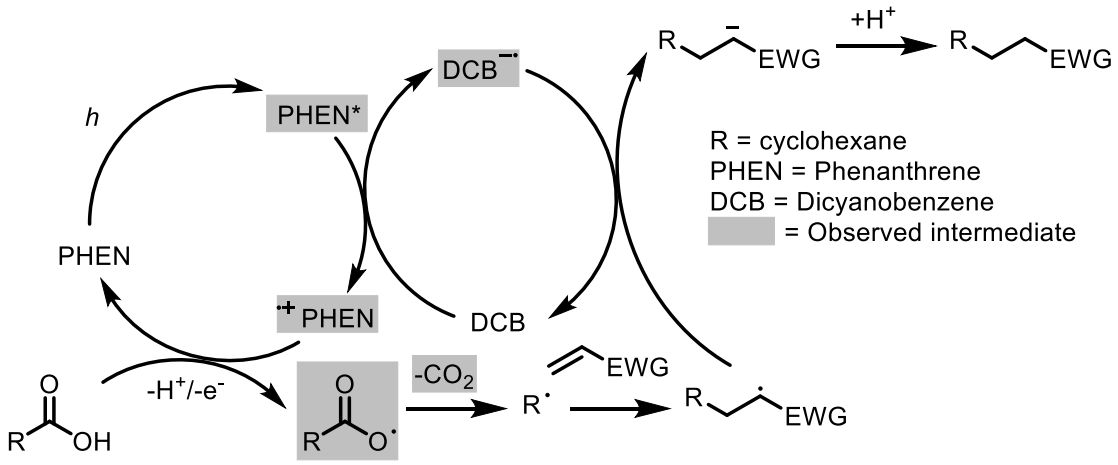

Figure 1.8. *Catalytic cycle for the photoredox catalysed decarboxylation reaction studied by Orr-Ewing and co-workers.*

1.2.4 Outlook

There are many fascinating examples of how TA can help organic chemists better understand the underlying dynamics of their reactions. By allowing observation of intermediates typically invisible by other techniques and by tracking their evolution in time, current understanding of chemical mechanisms can move from a qualitative to a quantitative footing, thereby leading to a more holistic interpretation of the chemistry. There is much more work to be done in this area, with the expectation that application of wide timescale (ps-ms) TVAS will prove to be a powerful new tool for investigation of reaction mechanisms.

1.3 Atom Transfer Radical Polymerisation

Chapters 3 and 4 focus on work done to quantify photocatalysts used in atom transfer radical polymerisation (ATRP). This section discusses key concepts important to this field.

ATRP is a type of controlled radical living polymerisation which exploits a rapid dynamic equilibrium between a minute amount of growing free radicals and a large majority of dormant species, which tend to be alkyl halides. The field began in 1995,[44] with seminal papers by Sawamato,[45] Matyjaszewski,[46] and Percec[47] wherein they found that with careful tuning of catalyst, initiator, and polymerisation conditions unprecedented control over polymerisation attributes could be realised.

Before discussing the mechanism of ATRP, it is worth spending time to define some of the factors used to assess polymer quality. Two commonly used parameters are initiator efficiency (I^*) and molecular weight distribution, or dispersity ($Đ$). I^* provides information on how much of the initial concentration of initiator leads to polymer by comparing the theoretical number average molecular weight ($M_{n(theo)}$) expected for the polymerisation with the experimental number average molecular weight ($M_{n(\mathrm{exp})}$), equation 23. It provides information on how regularly the initiator takes part in non-productive side reactions like termination, with a high I^* indicating most of the initiator ends up in the polymer.

$$I^* = \frac{M_{n(\mathrm{exp})}}{M_{n(theo)}} \qquad (23)$$

$Đ$ is the index of the polymer chain length distribution, equation 24, and includes the weight average molecular weight (M_w) and M_n seen in equation 23. In a well-controlled polymerisation $Đ$ should be approaching one, showing there is a narrow distribution of molecular weights. A $Đ$ of 1.0 would show that every polymer chain is equal in length.

$$Đ = \frac{M_w}{M_n} \qquad (24)$$

Classical ATRP uses a transition metal (TM) catalyst and operates through sequences of activation and deactivation to grow the polymer chain, **Figure 1.10** shows this mechanism. The radical (R•) which is the active polymerisation species is generated through reduction (k_{act}) of the R-X (X is a halide) bond by the TM complex (M_t^n – Y / Ligand, where Y can be another ligand or counterion). The radical can then either terminate through radical-radical coupling and disproportionation or be re-oxidised by the TM catalyst (k_{deact}). K_{eq} (k_{act}/ k_{deact}) determines the polymerisation rate: if K_{eq} is very small, ATRP will not occur or be very slow; conversely if K_{eq} is very large, then a high concentration of radicals will be formed which will lead to a greater number of termination reactions, andlower polymer dispersity and initiator efficiency.

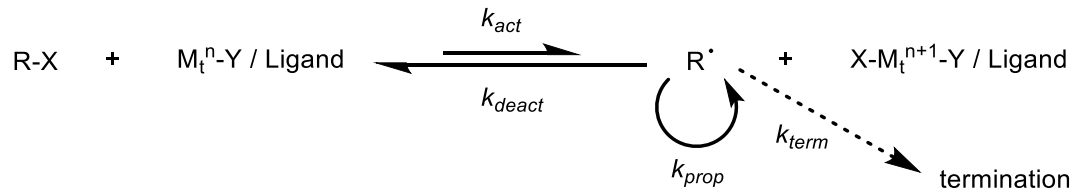

Figure 1.9. *A general mechanism for transition metal catalysed ATRP.*

In ATRP the catalyst is probably the most important component of the reaction, because it allows a chemist to modify the reaction depending on the given reaction parameters (monomers, initiators, solvents, etc.). Modern methods of ATRP are now attempting to modulate catalyst activity through external stimuli. Many of these methods exist to solve the problem of dormant oxidised catalyst taken off-cycle due to termination reaction, however others look to initiate polymerisation through either mechanical force or light absorption. The use of light absorption to activate ATRP will be the focus of Chapters 3 and 4.

1.4 Outlook

This introductory chapter has outlined much of the background important to the mechanistic interrogation of photochemical mechanisms. Most important to this thesis is the application of TA spectroscopy to track reactive intermediates and derive mechanistic insights from their kinetics. The following results chapters of this thesis will look to apply this methodology to organic photocatalysts used in organo-catalysed ATRP (O-ATRP), which harnesses external light stimulus to drive polymerisation. Chapter 3 will detail the quantification of excited state lifetimes of these catalysts and attempt to understand the importance of singlet and triplet states to their reactivity in O-ATRP. Chapter 4 considers the activation step in the O-ATRP cycle and how qualitative catalyst descriptors may be quantified using modified Marcus-Savéant theory. Lessons learnt from Chapters 3 and 4 will be applied to a new chemical system in Chapter 5, where a photochemical chain cycle involving a boronate species is measured and an entire kinetic map of the reaction is derived.

1.5 References

1. Nicewicz DA, MacMillan DWC. Merging Photoredox Catalysis with Organocatalysis: The Direct Asymmetric Alkylation of Aldehydes. *Science* 2008, **322**(5898)**:** 77-80.

2. Ischay MA, Anzovino ME, Du J, Yoon TP. Efficient Visible Light Photocatalysis of [2+2] Enone Cycloadditions. *J Am Chem Soc* 2008, **130**(39)**:** 12886-12887.

3. Narayanam JMR, Tucker JW, Stephenson CRJ. Electron-Transfer Photoredox Catalysis: Development of a Tin-Free Reductive Dehalogenation Reaction. *J Am Chem Soc* 2009, **131**(25)**:** 8756-8757.

4. Perry IB, Brewer TF, Sarver PJ, Schultz DM, DiRocco DA, MacMillan DWC. Direct arylation of strong aliphatic C–H bonds. *Nature* 2018, **560**(7716)**:** 70-75.

5. Zuo Z, Ahneman DT, Chu L, Terrett JA, Doyle AG, MacMillan DWC. Merging photoredox with nickel catalysis: Coupling of α-carboxyl sp³-carbons with aryl halides. *Science* 2014, **345**(6195)**:** 437-440.

6. Wang D, Zhu N, Chen P, Lin Z, Liu G. Enantioselective Decarboxylative Cyanation Employing Cooperative Photoredox Catalysis and Copper Catalysis. *J Am Chem Soc* 2017, **139**(44)**:** 15632-15635.

7. Proctor RSJ, Davis HJ, Phipps RJ. Catalytic enantioselective Minisci-type addition to heteroarenes. *Science* 2018, **360**(6387)**:** 419-422.

8. Retail B, Orr-Ewing AJ. Processes involving multiple potential energy surfaces. In: Brouard M, Vallance C (eds). *Tutorials in Molecular Reaction Dynamics*. Royal Society of Chemistry, 2010.

9. Klán P, Wirz J. Quantum Mechanical Models of Electronic Excitation and Photochemical Reactivity. *Photochemistry of Organic Compounds: From Concepts to Practice*. Wiley, 2009.

10. Dewanji A, Krach PE, Rueping M. The Dual Role of Benzophenone in Visible-Light/Nickel Photoredox-Catalyzed C−H Arylations: Hydrogen-Atom Transfer and Energy Transfer. *Angew Chem Int Ed* 2019, **58**(11)**:** 3566-3570.

11. Venkatraman RK, Kayal S, Barak A, Orr-Ewing AJ, Umapathy S. Intermolecular Hydrogen Bonding Controlled Intersystem Crossing Rates of Benzophenone. *The Journal of Physical Chemistry Letters* 2018, **9**(7)**:** 1642-1648.

12. Marcus RA. On the Theory of Oxidation-Reduction Reactions Involving Electron Transfer. I. *J Chem Phys* 1956, **24**(5)**:** 966-978.

13. Pause L, Robert M, Savéant J-M. Reductive Cleavage of Carbon Tetrachloride in a Polar Solvent. An Example of a Dissociative Electron Transfer with Significant Attractive Interaction between the Caged Product Fragments. *J Am Chem Soc* 2000, **122**(40)**:** 9829-9835.

14. Saveant JM. Dissociative electron transfer. New tests of the theory in the electrochemical and homogeneous reduction of alkyl halides. *J Am Chem Soc* 1992, **114**(26)**:** 10595-10602.

15. Saveant JM. A simple model for the kinetics of dissociative electron transfer in polar solvents. Application to the homogeneous and heterogeneous reduction of alkyl halides. *J Am Chem Soc* 1987, **109**(22)**:** 6788-6795.

16. Isse AA, Bortolamei N, De Paoli P, Gennaro A. On the mechanism of activation of copper-catalyzed atom transfer radical polymerization. *Electrochim Acta* 2013, **110:** 655-662.

17. Hossain A, Bhattacharyya A, Reiser O. Copper's rapid ascent in visible-light photoredox catalysis. *Science* 2019, **364**(6439)**:** eaav9713.

18. Romero NA, Nicewicz DA. Organic Photoredox Catalysis. *Chem Rev* 2016, **116**(17)**:** 10075-10166.

19. Ohkubo K, Mizushima K, Fukuzumi S. Oxygenation and chlorination of aromatic hydrocarbons with hydrochloric acid photosensitized by 9-mesityl-10-methylacridinium under visible light irradiation. *Res Chem Intermed* 2013, **39**(1)**:** 205-220.

20. Ohkubo K, Mizushima K, Iwata R, Fukuzumi S. Selective photocatalytic aerobic bromination with hydrogen bromidevia an electron-transfer state of 9-mesityl-10-methylacridinium ion. *Chem Sci* 2011, **2**(4)**:** 715-722.

21. Ohkubo K, Kobayashi T, Fukuzumi S. Direct Oxygenation of Benzene to Phenol Using Quinolinium Ions as Homogeneous Photocatalysts. *Angew Chem Int Ed* 2011, **50**(37)**:** 8652-8655.

22. Hamilton DS, Nicewicz DA. Direct Catalytic Anti-Markovnikov Hydroetherification of Alkenols. *J Am Chem Soc* 2012, **134**(45)**:** 18577-18580.

23. Nguyen TM, Nicewicz DA. Anti-Markovnikov Hydroamination of Alkenes Catalyzed by an Organic Photoredox System. *J Am Chem Soc* 2013, **135**(26)**:** 9588-9591.

24. Perkowski AJ, Nicewicz DA. Direct Catalytic Anti-Markovnikov Addition of Carboxylic Acids to Alkenes. *J Am Chem Soc* 2013, **135**(28)**:** 10334-10337.

25. Romero NA, Nicewicz DA. Mechanistic Insight into the Photoredox Catalysis of Anti-Markovnikov Alkene Hydrofunctionalization Reactions. *J Am Chem Soc* 2014, **136**(49)**:** 17024-17035.

26. Romero NA, Margrey KA, Tay NE, Nicewicz DA. Site-selective arene C-H amination via photoredox catalysis. *Science* 2015, **349**(6254)**:** 1326-1330.

27. Margrey KA, Czaplyski WL, Nicewicz DA, Alexanian EJ. A General Strategy for Aliphatic C–H Functionalization Enabled by Organic Photoredox Catalysis. *J Am Chem Soc* 2018, **140**(12)**:** 4213-4217.

28. Margrey KA, McManus JB, Bonazzi S, Zecri F, Nicewicz DA. Predictive Model for Site-Selective Aryl and Heteroaryl C–H Functionalization via Organic Photoredox Catalysis. *J Am Chem Soc* 2017, **139**(32)**:** 11288-11299.

29. Kalyanasundaram K. Photophysics, photochemistry and solar energy conversion with tris(bipyridyl)ruthenium(II) and its analogues. *Coord Chem Rev* 1982, **46:** 159-244.

30. *Data taken from web of science using keyword search: 'photoredox'.*

31. Buzzetti L, Crisenza GEM, Melchiorre P. Mechanistic Studies in Photocatalysis. *Angew Chem Int Ed* 2019, **58**(12)**:** 3730-3747.

32. Pitre SP, McTiernan CD, Ismaili H, Scaiano JC. Mechanistic Insights and Kinetic Analysis for the Oxidative Hydroxylation of Arylboronic Acids by Visible Light Photoredox Catalysis: A Metal-Free Alternative. *J Am Chem Soc* 2013, **135**(36)**:** 13286-13289.

33. Romero NA, Margrey KA, Tay NE, Nicewicz DA. Site-selective arene C-H amination via photoredox catalysis. *Science* 2015, **349**(6254)**:** 1326.

34. Teders M, Henkel C, Anhäuser L, Strieth-Kalthoff F, Gómez-Suárez A, Kleinmans R*, et al.* The energy-transfer-enabled biocompatible disulfide–ene reaction. *Nat Chem* 2018, **10**(9)**:** 981-988.

35. Coles MS, Quach G, Beves JE, Moore EG. A Photophysical Study of Sensitization-Initiated Electron Transfer: Insights into the Mechanism of Photoredox Activity. *Angew Chem Int Ed* 2020, **59:** 2-7.

36. Ghosh I, Shaikh RS, König B. Sensitization-Initiated Electron Transfer for Photoredox Catalysis. *Angew Chem Int Ed* 2017, **56**(29)**:** 8544-8549.

37. Walker MM, Koronkiewicz B, Chen S, Houk KN, Mayer JM, Ellman JA. Highly Diastereoselective Functionalization of Piperidines by Photoredox-Catalyzed α-Amino C–H Arylation and Epimerization. *J Am Chem Soc* 2020, **142**(18)**:** 8194-8202.

38. Stevenson BG, Spielvogel EH, Loiaconi EA, Wambua VM, Nakhamiyayev RV, Swierk JR. Mechanistic Investigations of an α-Aminoarylation Photoredox Reaction. *J Am Chem Soc* 2021, **143**(23)**:** 8878-8885.

39. Shields BJ, Kudisch B, Scholes GD, Doyle AG. Long-Lived Charge-Transfer States of Nickel(II) Aryl Halide Complexes Facilitate Bimolecular Photoinduced Electron Transfer. *J Am Chem Soc* 2018, **140**(8)**:** 3035-3039.

40. Ting SI, Garakyaraghi S, Taliaferro CM, Shields BJ, Scholes GD, Castellano FN*, et al.* 3d-d Excited States of Ni(II) Complexes Relevant to Photoredox Catalysis: Spectroscopic Identification and Mechanistic Implications. *J Am Chem Soc* 2020, **142**(12)**:** 5800-5810.

41. Hammarback LA, Clark IP, Sazanovich IV, Towrie M, Robinson A, Clarke F*, et al.* Mapping out the key carbon–carbon bond-forming steps in Mn-catalysed C–H functionalization. *Nat Catal* 2018, **1**(11)**:** 830-840.

42. Bhattacherjee A, Sneha M, Lewis-Borrell L, Tau O, Clark IP, Orr-Ewing AJ. Picosecond to millisecond tracking of a photocatalytic decarboxylation reaction provides direct mechanistic insights. *Nat Commun* 2019, **10**(1)**:** 5152.

43. Yoshimi Y, Washida S, Okita Y, Nishikawa K, Maeda K, Hayashi S*, et al.* Radical addition to acrylonitrile via catalytic photochemical decarboxylation of aliphatic carboxylic acids. *Tetrahedron Lett* 2013, **54**(32)**:** 4324-4326.

44. Matyjaszewski K, Xia J. Atom Transfer Radical Polymerization. *Chem Rev* 2001, **101**(9)**:** 2921-2990.

45. Kato M, Kamigaito M, Sawamoto M, Higashimura T. Polymerization of Methyl Methacrylate with the Carbon Tetrachloride/Dichlorotris-(triphenylphosphine)ruthenium(II)/Methylaluminum Bis(2,6-di-tert-butylphenoxide) Initiating System: Possibility of Living Radical Polymerization. *Macromolecules* 1995, **28**(5)**:** 1721-1723.

46. Wang J-S, Matyjaszewski K. Controlled/"living" radical polymerization. atom transfer radical polymerization in the presence of transition-metal complexes. *J Am Chem Soc* 1995, **117**(20)**:** 5614-5615.

47. Percec V, Barboiu B. "Living" Radical Polymerization of Styrene Initiated by Arenesulfonyl Chlorides and CuI(bpy)nCl. *Macromolecules* 1995, **28**(23)**:** 7970-7972.

2 Spectroscopic Methods

This chapter describes the methods used in the research presented in this thesis for acquisition of transient absorption spectra, analysis of the experimental spectra to extract kinetic information, and interpretation of the resulting data using kinetic models. These methods were used to obtain and analyse the results presented in chapters three – five. The two ultrafast spectroscopy techniques used were transient electronic absorption spectroscopy (TEAS) and transient vibrational absorption spectroscopy (TVAS). In the scientific literature, these techniques are often referred to as transient absorption (TA) and time-resolve infrared (TRIR) spectroscopy, respectively. Specific details about the preparations of samples, and the solutions used for experimental measurements are presented in Chapter 6.

2.1 Ultrafast Laser Systems

The following sections describe the two laser systems used to collect spectroscopic data presented throughout the three main results chapters.

2.1.1 Bristol Ultrafast Laser System

The ultrafast laser system at the University of Bristol was used to record transient electronic absorption spectra covering the early time dynamics of the studied reactions (time delays spanning 100 fs to 1.3 ns). The system was first described by Roberts et al. and a schematic diagram is shown in **Figure 2.1**.[1] An ultrafast Coherent Legend Elite HE+ regenerative amplifier, operating at 1 kHz and configured to produce 40 fs duration pulses at 800 nm (output power 5W) is split into three parts with power ratios of 47:47:2. Two of the resulting laser beams have pulse energies of 2.45 mJ/pulse and the final beam is much weaker at 100 μJ/pulse. The larger components seed two Coherent OPerA Solo optical parametric amplifiers (OPAs). These OPAs generate UV and mid-IR beams via various nonlinear frequency-mixing schemes combining the OPA signal and idler, and 800-nm pump beams. For the experiments reported here, only one OPA is required to generate the pump beam at 340 nm or 370 nm using the fourth harmonic of the OPA signal beam. The lower-energy portion of the 800-nm pump laser beam (100 μJ/pulse) generates a white light continuum (WLC) probe by focusing (using a CaF_2 lens of focal length f = 200 mm) into a 2-mm thick CaF_2 window which is continuously rastered to avoid thermal damage. An off-axis parabolic mirror (f = 100 mm) collimates the resulting WLC probe, which spans wavelengths from ~330 nm to >700 nm.

The WLC probe pulse is reflectively focused into the sample using an f = 75 mm concave aluminium mirror (to avoid achromatic aberrations) to obtain a ~50 μm beam diameter. The pump beam is polarized at magic angle (54.7 degrees) relative to the WLC probe and is focused loosely using a f = 35 mm lens to ensure uniform excitation of the sample in the probed region. The temporal delay (Δt) between the pump and WLC probe beams is controlled by changing the path length of the pump beam with an aluminium retro-reflector (PLX) mounted on a motorized 220-mm delay stage (Thorlabs, DDS220/M), providing a maximum delay of Δt = 1.3 ns. The maximum pump power used is 300 nJ/pulse at the sample to avoid multi-photon excitations. The sample is flowed continuously through a small volume confined between two CaF_2 windows separated by 380 μm PTFE spacers where it is intersected by the pump and probe laser beams. A non-collinear overlap of the pump and probe beams in this sample volume allows their spatial separation after the sample, and the transmitted WLC beam is focused into a spectrograph (Andor, Shamrock 163) fitted with a 1024-element photodiode array (Entwicklungs-büro Stresing). An optical chopper wheel operating at 500 Hz (Thorlabs, MC2000) is used to block every other pump beam pulse to compare pump-on and pump-off spectra at each time delay. The spectra are processed to obtain differential absorbance:

$$\Delta A(t) = -\log\left(\frac{I_{pump\ on}}{I_{pump\ off}}\right)$$

In-house LabVIEW software is used to interface with instruments during data collection; this software controls the motorized delay stage and random sampling of the time-delay *t* to avoid any false spectral kinetics induced by long term drifts in signal intensity. The spectrometer is pixel-to-wavelength calibrated against the electronic spectrum of Holmium oxide. Chirp-correction of recorded TEAS is performed using another LabVIEW software package, KOALA.[2]

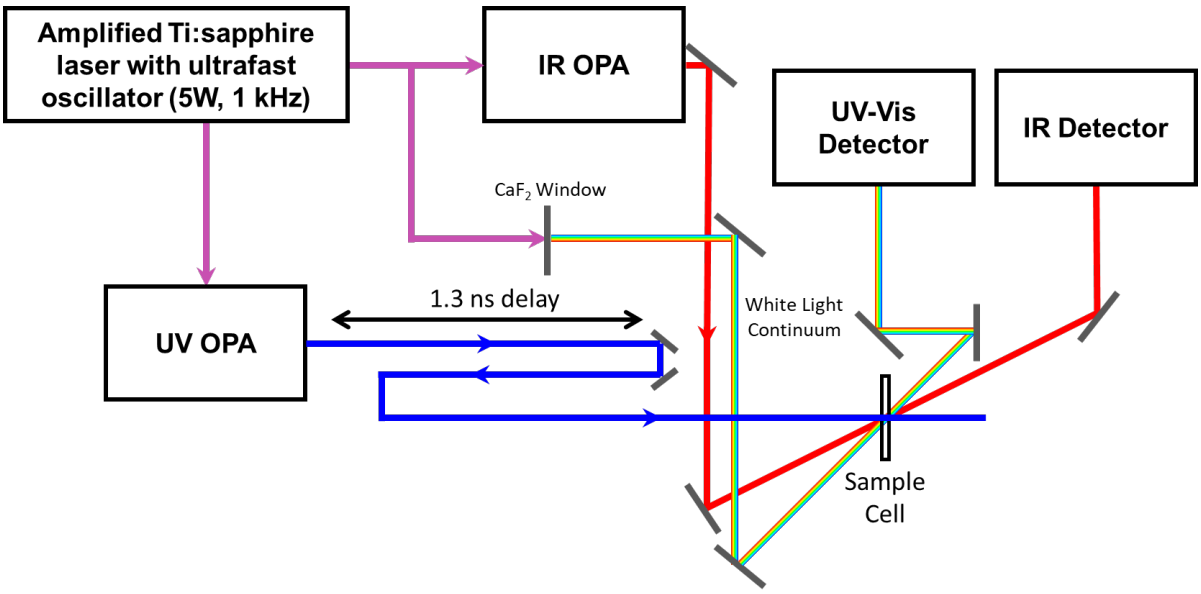

Figure 2.1. *Schematic diagram showing the generation of UV-visible pump, and WLC and IR probes using the Bristol ultrafast laser system.*

2.1.2 Rutherford Appleton Laboratory LIFEtime System

Transient vibrational absorption spectra were recorded using the LIFEtime laser system at the STFC Rutherford Appleton Laboratory, which is capable of an extended range of measurement times from 200 fs to 1 ms.[3,4] The details of the laser system were first described in references [3] and [4], and a schematic diagram is shown in **Figure 2.2.** A single Yb:KGW ultrafast oscillator (80 MHz) seeds two Yb:KGW amplifiers (Light Conversion Ltd., Pharos, 100 kHz, 15 W, 260 fs output pulses and Pharos, 100 kHz, 6W, 180 fs output pulses). The higher power amplifier is used to pump an OPA (Light Conversion Ltd., Orpheus HP) to generate a single pump beam with outputs spanning 21 – 2600 nm, while the 6W amplifier drives two OPAs (Light Conversion Ltd., Orpheus ONE) with difference-frequency generation (DFG) units to generate two separately tuneable mid-IR probe beams (2100 – 13000 nm). The UV pump beam (280 nm, 320 nm, and 370 nm) is collimated and passed along a 0 – 12 ns multi-pass optical delay stage before focusing (120 – 150 µm diameter) at the sample. Pulse-picking reduces the repetition-rate of this pump beam to 1 kHz. Measurements at time delays >12 ns are collected using the time-resolved multiple probe spectroscopy (TRMPS) method first described in reference [3]. TRMPS in the case of LIFEtime uses the repetition rate of the probe amplifier (100 kHz), to give additional time delays every 10 µs up to 1 ms, so for each probe pulse and each setting of the delay stage, a measurement is made at every integer multiple of 10 µs up to a maximum of 1 ms; for example, if a delay of 1 µs is selected then TRMPS delays of 11 µs, 21 µs, 31 µs, 41 µs… up to 1 ms will also be measured in parallel. For time points between 12

ns and 10 μs a combination of optical and electronic delays is used by setting the position of the optical delay stage and pulse picking from the 80 MHz pulse train. This approach allows combinations of the optical delay (200 fs – 12 ns) and the electronic delay; for example, if a delay of 80 ns is desired, the trigger is delayed by an interval corresponding to 6 seed pulses (at 80 MHz repetition rate, or 12.5 ns temporal separation) and an additional 5 ns optical delay is used.

In all the TVAS studies presented here, the dual mid-IR probe beams, each with bandwidth ~200 cm^{-1}, are individually tuned to span the aromatic ring mode (1400-1600 cm^{-1}) and carbonyl stretch (1550-1750 cm^{-1}) regions. Both probe beams operate at a repetition rate of 100 kHz. After transmission through the sample, the probe beams are dispersed into two separate 128-element MCT detector arrays (Infrared Associates).

The pump energy is selected to be 200 nJ/pulse at the sample and both mid-IR probes are set to energies of ~0.05 μJ/pulse to avoid saturation of the detectors. The systematic pattern of noise seen at time delays greater than 9 μs in datasets shown in later chapters is a consequence of electrical pick-up from the probe amplifier and repeats every 10 μs. Three-second averaging with three repeat cycles is performed for each time delay to ensure satisfactory signal-to-noise ratios in acquired spectra. Because of the shot-to-shot stability of the LIFEtime laser system, it is not necessary to normalize spectra to the power of the IR laser pulses (i.e. to divide by a reference spectrum of each pulse) to optimize these signal-to-noise ratios. Changes in optical density as small as 10^{-4} or 10^{-5} can be measured with this set-up.

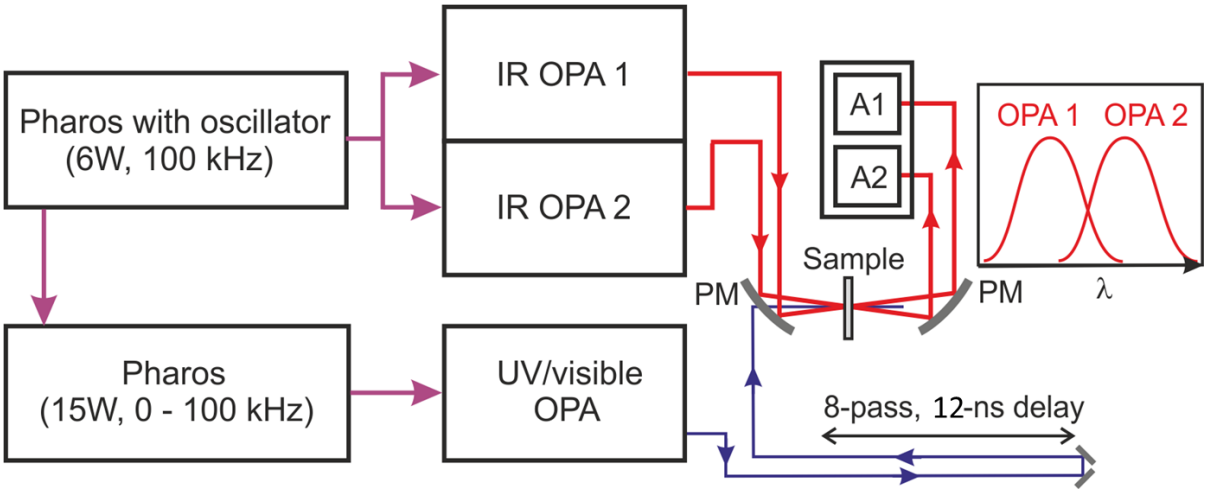

Figure.2.2. *Schematic diagram showing the generation of UV-visible pump and dual IR probe pulses using the LIFEtime system. PM denotes a parabolic mirror used to focus and then recollimated IR laser beams. A1 and A2 are separate MCT array detectors housed in spectrometers. The two IR OPAs can be tuned to give partially overlapping spectra to extend the spectral coverage of the measurements (as shown in the inset) or can be tuned to different IR regions.*

2.2 Kinetic Modelling

Data collected from ultrafast spectroscopy experiments can be analysed in a multitude of ways depending on the given spectroscopic experiment and chemical system under study. This section presents the quantitative models used in Chapters 3 – 5 to interpret the collected data.

2.2.1 Photoexcited-State Models

The decay of a photocatalysts (PC) excited state may be thought of as a unimolecular reaction in which an excited singlet state, $PC^*(S_1)$, decays to reform the ground state, $PC(S_0)$.

$$PC^*(S_1) \xrightarrow{k} PC(S_0) \tag{1}$$

Here, k is the rate coefficient for the decay and determines the rate of this process. The differential equation used to model this decay process is,

$$\frac{d[PC^*(S_1)]}{dt} = -k[PC^*(S_1)] \tag{2}$$

Integration gives

$$\int_{[PC^*(S_1)]_0}^{[PC^*(S_1)]_t} \frac{1}{[PC^*(S_1)]} d[PC^*(S_1)] = \int_0^t -k\, dt \tag{3}$$

$$\ln \frac{[PC^*(S_1)]_t}{[PC^*(S_1)]_0} = -kt \tag{4}$$

$$[PC^*(S_1)]_t = [PC^*(S_1)]_0 e^{-kt} \tag{5}$$

Equation 5 can be used to model the measured time dependent decay of an excited state concentration, $[PC^*(S_1)]_t$, back to the ground state from its initial concentration $[PC^*(S_1)]_0$ with an exponential time dependence given by e^{-kt}. Typically, time constants, τ, are used to describe the lifetimes of excited states, where

$$k = \frac{1}{\tau} \tag{6}$$

Using equation 5, an exponential fit to a given spectroscopic signal obtains a fitted time constant of that photophysical process, for example fluorescence or internal conversion. If the kinetics of transient absorption are deemed to be beyond mono-exponential, as is common

when more than one photophysical process is being measured, then it is appropriate to use a bi- or tri-exponential fit, the integrated kinetic rate equations for which are,

$$[PC^*(S_1)]_t = [PC^*(S_1)]_0(e^{-k_1 t} + e^{-k_2 t}) \quad (7)$$

$$[PC^*(S_1)]_t = [PC^*(S_1)]_0(e^{-k_1 t} + e^{-k_2 t} + e^{-k_3 t}) \quad (8)$$

2.2.2 Bimolecular Electron Transfer Models

The next set of models all attempt to describe electron transfer reactions in solution, which are the subject of Chapter 4. The reactions in question are between various photoexcited PCs and a quencher, methyl 2-bromo propionate (MBP). This section has been taken from the supporting information of A. Bhattacherjee et al.[5] and M. Sneha et al.,[6] with detailed breakdowns of contributions detailed in Chapters 3 and 4, respectively.

2.2.2.1 Pseudo First-Order Kinetics

The text in Chapter 4 shows the kinetic modelling used with single exponential fitting for either PC* decay or MP radical growth arising from the reaction:

$$PC^*(S_1/T_1) + MBP \rightarrow PC^{\bullet+} + MP^{\bullet} + Br^- \quad (9)$$

Within the assumption that $[PC^*(S_1/T_1)] \ll [MBP]$ the rate equation for the growth of $MP^{\bullet}$,

$$\frac{d[MP^{\bullet}]}{dt} = k_{ET}[PC^*(S_1/T_1)][MBP] \quad (10)$$

simplifies to,

$$\frac{d[MP^{\bullet}]}{dt} = k'[PC^*(S_1/T_1)] \quad (11)$$

Where $k' = k_{ET}[MBP]$

This equation can be used to obtain a similar integrated equation as 5,

$$[MP^{\bullet}]_t = [MP^{\bullet}]_0\{1 - e^{-k't}\} \quad (12)$$

Taking measurements at various concentrations of MBP, fitting the resulting traces to equation 12 and then taking the gradient from the plot of k' vs. $[MBP]$ will give k_{ET} for that reaction.

2.2.2.2 Static vs dynamic quenching: the Smoluchowski model

At higher concentrations of MBP, a growing fraction of reactants PC and MBP will be trapped within the same solvent shell. For this reactant fraction, the rate of electron transfer will not be limited by the diffusion rate and in such a case, quenching of the PC* excited states due to electron transfer (ET) is generally referred to as static quenching.[7] In such solutions, the observed rate coefficient will change with time, with the initial fast rate arising from static quenching and a relatively slow component requiring diffusion leading to dynamic quenching of PC* excited states.[8] To model the kinetics of data with higher concentrations of MBP, two approaches have been used.

The first approach is pragmatic: when the kinetic plots do not fit well with a single exponential function, a biexponential fit is used, which gives two rate coefficients, a larger one which is assigned to the static quenching component, and a smaller one which is assigned to the diffusive quenching. Using the rate coefficients for diffusive components at all MBP concentrations, a pseudo first-order kinetic analysis is applied to obtain bimolecular rate coefficients for electron transfer for all PCs and MBP in different solvents. The second approach involves the application of Smoluchowski theory, which considers the time-dependence of the rate coefficient as the reaction changes from the static limit to a diffusional limit.[7,9,10] Further details of both methods are provided below.

As was described earlier, a pseudo first-order analysis can be applied for the reaction between PC* and MBP which gives equations 11 and 12. However, at higher concentrations of MBP, the concentrations of reactants and products can be fitted to biexponential functions with rate coefficients $k_1$and k_2, as shown in equation 16 and 17. k_1 serves as the rate coefficient for static quenching, and k_2 is the slower diffusive dynamic quenching coefficient. This is the pragmatic approach mentioned earlier.

$$[R]_t = [R]_0 \left(exp\,(-k_1 t) + exp(-k_2 t)\right) \quad (13)$$

$$[P]_t = [R]_0 - [R]_t = [R]_0 \left(1 - exp(-k_1 t) - exp(-k_2 t)\right) \quad (14)$$

Instead, in the **Smoluchowski model**, the time dependent change in the rate coefficient is accommodated by replacing equation 13 with:

$$[R]_t = [R]_0 \, exp\left(-\int_0^t k(t')\,dt'\right) exp\left(-\frac{t}{\tau_f}\right) \quad (15)$$

where k is now a time-dependent, pseudo-first-order rate coefficient. The term $exp\left(-\frac{t}{\tau_f}\right)$ accounts for the decay of R, or in this case PC*, by fluorescence or other non-radiative processes (not involving bimolecular ET), where τ_f is the lifetime of the PC*(S_1) state in the absence of MBP.

Under the approximation of Smoluchowski theory that reaction occurs instantaneously when the two reactants diffuse to some critical separation r, this time-dependent rate coefficient can be represented by equation 19:

$$k(t) = 4\pi D N_A r c_0 \left\{1 + \frac{r}{\sqrt{\pi D t}}\right\} \quad (16)$$

where N_A is the Avogadro constant, and D is the sum of the diffusion coefficients for the two reactants. Integrating equation 18 with respect to time and inserting it into equation 19 gives the concentrations of reactant R and product P shown below:

$$[R]_t = [R]_0 \, exp\left(-4\pi D N_A r c_0 \left\{t + \frac{2r\sqrt{t}}{\sqrt{\pi D}}\right\}\right) exp\left(-t/\tau_f\right) \quad (17)$$

$$[P]_t = [R]_0 \left(1 - exp\left(-4\pi D N_A r c_0 \left\{t + \frac{2r\sqrt{t}}{\sqrt{\pi D}}\right\}\right) exp\left(-t/\tau_f\right)\right) \quad (18)$$

In these expressions, $4\pi D N_A r = k_{diffusion}$ which is the bimolecular diffusional rate coefficient. This approach approximates the more complete Smoluchowski-Collins-Kimball (SCK) treatment[9,10,11] but the recorded data do not merit the more involved fitting required by SCK theory. The functional forms of equations 20 or 21 can be applied to the PC* and MBP system by fitting the decay of the PC*(S_1) state, or $MP^{\bullet}$ rise to obtain pseudo-first order $k' = k_{diffusion} c_0$ values. The k' values can then be plotted against c_0 to extract a value for $k_{diffusion}$ from a linear fit. Although some reactions are not fully in the diffusion limit, this value gives an estimate for the rate coefficient for electron transfer through dynamic quenching. Note that for the PCs reported in Chapter 4, there may be no complexation between PC and MBP, because even at high concentrations of MBP, no apparent change in the UV-Vis spectra of PC was observed.

2.2.2.3 Singlet vs. triplet state electron transfer

So far, electron transfer from the PC*(S_1) state to MBP has been the focus for the development of kinetic models. However, as is shown in **Table 4.1** of Chapter 4, some of these catalysts have competitive intersystem crossing rates to populate the T_1 excited triplet state. Miyake and co-workers have calculated reduction potentials of these catalysts which show the T_1 states to be sufficiently reducing to transfer an electron to MBP. [12,13] The reaction between PC*(T_1) and MBP for the N-Aryl phenoxazine catalyst, PC-O2 is discussed in Chapter 4, and here a kinetic model is developed.

The rate of change of PC*(T_1) concentration depends on the following three processes:

$$PC^*(S_1) \xrightarrow{k_{ISC}} PC^*(T_1) \tag{19}$$

$$PC^*(T_1) \xrightarrow{k_T} PC(S_0) \tag{20}$$

$$PC^*(T_1) + MBP \xrightarrow{k_{ET}^T} PC^{\bullet+} + MP^{\bullet} + Br^- \tag{21}$$

PC*(S_1) can also decay by two other pathways as discussed in Chapter 4.

$$PC^*(S_1) \xrightarrow{k_R} PC(S_0) \tag{22}$$

$$PC^*(S_1) + MBP \xrightarrow{k_{ET}} PC^{\bullet+} + MP^{\bullet} + Br^- \tag{23}$$

The three decay pathways for PC*(S_1) give an equation for the rate of decay of PC*(S_1):

$$\frac{d[PC^*(S_1)]}{dt} = -[PC^*(S_1)](k_R + k_{ISC} + k_{ET}[MBP]) \tag{24}$$

Using $k_{S_1} = k_R + k_{ISC} + k_{ET}[MBP]$, and solving for [PC*($S_1$)], gives,

$$[PC^*(S_1)] = [PC^*(S_1)]_0 \exp(-k_{S_1} t) \tag{25}$$

The rate of change of PC*(T_1) is:

$$\frac{d[PC^*(T_1)]}{dt} = k_{ISC}[PC^*(S_1)] - k_T[PC^*(T_1)] - k_{ET}^T[PC^*(T_1)][MBP] \tag{26}$$

Equation 29 can be separated into growth and decay components for PC*(T_1):

$$\frac{d[PC^*(T_1)]\uparrow}{dt} = k_{ISC}[PC^*(S_1)] = k_{ISC}[PC^*(S_1)]_0 e^{-k_{S_1}t} \quad (27)$$

$$\frac{d[PC^*(T_1)]\downarrow}{dt} = -[PC^*(T_1)](k_T + k_{ET}^T[MBP]) \quad (28)$$

Using $k_T + k_{ET}^T[MBP] = k_{decay}$

$$\frac{d[PC^*(T_1)]\downarrow}{dt} = -k_{decay}[PC^*(T_1)] \quad (29)$$

Figure 4.5 in Chapter 4 shows how the triplet kinetic trace can indeed be fitted to a biexponential growth and decay function. As is apparent from equation 30 the rate coefficient for the rising part of the trace is equal to k_{S_1}, i.e., the S_1 state decay rate coefficient. The observed time constant for the exponential decay part of the biexponential gives the constant k_{decay}. As the S_1 decay time constant (4-5 ns) is at least 2 orders of magnitude smaller than the decay time constant for the triplet state, these two can be treated independently. In the absence of MBP, $k_{decay} = k_T$, which is $1/\tau_{lifetime}$ of the PC*(T_1) state. In the presence of MBP, $k_{decay} = k_T + k_{ET}^T[MBP]$. k_{decay} values obtained from the kinetic fits are plotted against the increasing concentration of MBP, with the slope of a linear fit giving the rate coefficient for electron transfer from the PC*(T_1) state.

2.2.2.4 Marcus, Marcus-Savéant, and Marcus "sticky" models

This section will look to derive the equations used in the modelling of experimental data presented in Chapter 4. For a full introduction to Marcus theory the reader is directed Chapter 1 Section 1.1.1.4. To determine the relationship between a rate coefficient for electron transfer and the Gibbs energy of activation for the ET reaction between the PC* excited state (S_1/T_1) and an electron acceptor such as an organohalide RX, the Sticky model of dissociative electron transfer is used. Equation 30 relates the rate coefficient to the Gibbs activation energy.

$$k_{ET} = Ze^{-\frac{\Delta G^\ddagger}{RT}} \quad (30)$$

Here, Z is the collision frequency, R is the gas constant ($8.314\ J\ K^{-1}mol^{-1}$) and T is the temperature (set to 293 K for the studies reported here).

According to the Sticky model of dissociative electron transfer, which is an extension of Marcus theory for electron transfer reactions and Marcus-Savéant theory for the special case of dissociative electron transfer, the activation energy $\Delta G^{\ddagger}$ is given by equation 31.[14,15,16,17]

$$\Delta G^{\ddagger} = \frac{\lambda_0 + \left(\sqrt{E_{BD}} - \sqrt{D_p}\right)^2}{4}\left(1 + \frac{\Delta G_{ET} - D_p}{\lambda_0 + \left(\sqrt{E_{BD}} - \sqrt{D_p}\right)^2}\right)^2 \qquad (31)$$

ΔG_{ET} is the Gibbs energy for electron transfer between PC* and RX, E_{BD} is the C–X bond dissociation energy of RX, and D_p is the interaction energy between R$^{\bullet}$ and X^{-} in a solvent cage. λ_0 is the reorganization energy which is defined by the following equation:

$$\lambda_0 = (N_A e^2/4\pi\epsilon_0)\left(\frac{1}{n^2} - \frac{1}{\epsilon}\right)\left(\frac{1}{2r} + \frac{1}{2r_{PC^*}} - \frac{1}{r + r_{PC^*}}\right) \qquad (32)$$

where $r = (2r_{RX} - r_X)r_X/r_{RX}$; n is the refractive index of the solvent, and ϵ is the dielectric constant.

Isse *et al*. determined the value of the pre-factor $(N_A e^2/4\pi\epsilon_0)\left(\frac{1}{n^2} - \frac{1}{\epsilon}\right)$ in equation 32 by empirical fitting of data in DMF to be 95 kcal mol^{-1} Å.[14,18] Analysis in Chapter 4 is restricted to DMF solutions because most of the experimental values required are only available from the literature for measurements made in either DMF or acetonitrile, and will therefore serve as poor approximations for DCM or toluene solutions (solvents which are also used in Chapter 4). Because of the similarities of the dielectric constants of acetonitrile and DMF, the approximation is made that the oxidation and reduction potentials measured in acetonitrile will be similar to those in DMF. Energies are hereafter specified in kJ mol^{-1} not kcal mol^{-1}.

MBP is the only electron acceptor (radical initiator) used for the studies presented in Chapter 4, and because it is a common electron acceptor organohalide, the required values for this molecule have been previously reported:

$D_p = 0.24\frac{kcal}{mol} = 1.004\frac{kJ}{mol}$ in CH_3CN (Isse *et al.*)[14,19]

$E_{BD} = 220\ kJ/mol$ calculated by Lin *et al.*[20]

$r_{RX} = 3.54$ Å (Isse *et al.*)[14]

$r_X = 1.96$ Å for Br atom (Pan *et al.*)[15]

$r = 1.83$ Å

$E^0(RX/R^\bullet + X^-) = -0.56\,V = 54.0\,\frac{kJ}{mol}$ in DMF (Isse *et al.*)[14,21]

$E^0(RX/R^\bullet + X^-) = -0.68\,V = 65.6\,\frac{kJ}{mol}$ in CH_3CN (Isse *et al.*)

Here, E^0 is the reduction potential of the species shown in parentheses. The quoted values of $E^0(RX/R^\bullet + X^-)$ in DMF or acetonitrile are measured against a saturated calomel electrode (SCE). For ET reactions with all the PCs except PC-S, the $E^0(RX/R^\bullet + X^-)$ value measured in acetonitrile is used because the reported PC oxidation potentials are also measured in acetonitrile solutions (*vide infra*). For each PC, it is assumed that $r_{PC^*} = r_{PC}$, i.e., the radius of the excited state PC is similar to the radius for the ground state geometry. The values of the reorganization energy, λ_0 can then be calculated for each PC in DMF and are shown in **Table 2.1**.

For the PC* + MBP ET reaction, ΔG_{ET} is given by:

$$\Delta G_{ET} = (G_{PC^{\bullet+}} + G_{MP^\bullet} + G_{Br^-}) - (G_{PC} + G_{MBP}) - \frac{N_A e^2}{4\pi\epsilon_0 \epsilon r_{PC^*+MBP}} - E_{00} \qquad (33)$$

$$\Delta G_{ET} = F\{E^0(PC^{\bullet+}/PC) - E^0(RX/R^\bullet X^-)\} - E\left(PC^*(S_1)\right) - \frac{N_A e^2}{4\pi\epsilon_0 \epsilon r_{PC^*+MBP}} \qquad (34)$$

Where the excited-state energy is $E_{00} = E(PC^*(S_1)) = hc/\lambda_{em_0}$, with λ_{em_0} the wavelength of onset of fluorescence at the short-wavelength side of the emission band. To estimate this short-wavelength onset, the wavelength corresponding to an emission that was 10% of the intensity at the wavelength of maximum emission (λ_{em}) is chosen. $\frac{N_A e^2}{4\pi\epsilon_0 \epsilon r_{PC^*+MBP}}$ is the Coulombic attraction term between the reduced acceptor and oxidized donor at a distance, r_{PC^*+MBP}, which is calculated using the above-mentioned r_{MBP} and the r_{PC^*} values reported in **Table 2.1**. Using a dielectric constant value of 36.71 for DMF,[22] the calculated Coulombic attraction values for the products of electron transfer for each PC are listed in **Table 2.1**.

Table 2.2 shows the λ_{em}, λ_{em_0} and ΔG_{ET} values which are either measured or calculated (using equation 37) in DMF solutions. The fluorescence measurements used a Perkin Elmer LS-45 Luminescence spectrometer with 10-nm excitation and 10-nm emission slits. The PC oxidation

potentials were obtained from the references cited in **Table 2.2**. In Chapter 4 nine PCs are studied these are denoted: PC-N1 to PC-N5, for the dihydrophenazines; PC-O1 to PC-O3, for the phenoxazines; and PC-S for the phenthiazine. Their structures are shown in Chapters 3 and 4. For PC-N1 to PC-N5 and PC-O1 to PC-O3, the $E^0(PC^{\bullet+}/PC)$ values reported in these publications derive from cyclic voltammetry experiments using $Ag/AgNO_3$ (0.01 M) as a reference electrode and acetonitrile/DMA as a solvent.[12,13,23] The authors then applied a correction of +0.298 V to convert the reported values obtained using $Ag/AgNO_3$ electrodes (ANE2) to values appropriate for an SCE reference electrode, as shown in measurements by Pavlishchuk and Addison.[24] For these PCs, the reported values of $E^0(\frac{RX}{R^{\bullet}+X^-})$ for a SCE reference electrode in acetonitrile are used. For PC-S, the values are instead reported against SCE for measurements in DMA, and the DMA/DMF values are used for both PC-S and MBP.

Using a D_p value of 1.004 kJ/mol for MBP, $\Delta G^{\ddagger}$ in DMF can now calculated. The test of whether the sticky model of dissociative electron transfer is valid for this analysis comes from comparing experimental with calculated k_{ET} values, and this is done in Chapter 4. To determine k_{ET}, the value of the preexponential factor Z must alsoe be calculated, and can be obtained by:

$$Z = N_A(r_{PC^*} + r_{RX})^2 \left(\frac{8\pi RT}{\mu}\right)^{1/2} \qquad (35)$$

The calculated values of Z are reported in **Table 4.3** of Chapter 4. Thus, using equation 38, the values of the rate coefficients for electron transfer from PC*(S_1) to MBP in DMF may be calculated and are also shown in **Table 4.3** of Chapter 4.

Table 2.1. *Reorganization and Coulomb attraction energies (for the products of the electron transfer reaction) for each of the photocatalysts studied in Chapter 4 and MBP in DMF solution.*

Catalyst	r_{PC^*} (Å)^a	λ_0 ($\frac{kJ}{mol}$)	Coulombic Energy (*kJ/mol*)
PC-N1	6.1	58.3	3.94
PC-N2 [b]	5.1	59.1	4.38
PC-N3 [b]	5.8	58.4	4.05
PC-N4	5.8	58.4	4.06
PC-N5 [e]	5.7	58.5	4.09
PC-O1	4.8	59.5	4.53
PC-O2	5.3	58.8	4.27
PC-O3	8.3	58.5	3.20
PC-S	5.2	58.9	4.33

a. Value reported in ref. [13] **b.** $E^0(\frac{PC^+}{PC})$ value for an SCE reference is obtained by adding 0.298 V to the value measured in $Ag/AgNO_3$ using CH_3CN and DMA as solvents **c.** Value reported in CH_3CN or DMA in ref. [12] **d**. Values taken from ref.[25] **e.** Value reported in DMA against SCE electrode in ref. [15]

Table 2.2. *Thermodynamic parameters for PC* (S_1) + MBP electron transfer reactions studied in Chapter 4 in DMF solution.*

Catalyst	*MW (g/mol)*	*Reduced mass (g/mol)*	λ_{em} (*nm*)	λ_{em_0} (*nm*)	$E^0\left(\frac{PC^+}{PC}\right)$ vs SCE (V)	ΔG_{ET} (*kJ/mol*)
PC-N1	394	117.29	467	422	0.16[a,b]	-206.4
PC-N2 [b]	334	111.33	464	411	0.19 [a,b]	-211.5
PC-N3 [b]	470	123.21	585	494	0.29 [a,b]	-152.7
PC-N4	384	116.38	---	---	0.32 [a,b]	---
PC-N5 [e]	434	120.60	602	501	0.23 [a,b]	-155.1
PC-O1	259.30	101.58	398	341	0.68[b,c]	-224.2
PC-O2	309.35	108.45	511	435	0.69 [b,c]	-147.1
PC-O3	563.68	128.83	470	444[d]	0.66 [b,d]	-143.4
PC-S	325.42	110.36	522	458	0.83[e]	-131.2

a. Value reported in ref. [13] **b.** $E^0(\frac{PC^+}{PC})$ value for an SCE reference is obtained by adding 0.298 V to the value measured in $Ag/AgNO_3$ using CH_3CN and DMA as solvents **c.** Value reported in CH_3CN or DMA in ref. [12] **d**. Values taken from ref.[25] **e.** Value reported in DMA against SCE electrode in ref. [15]

2.2.3 Kinetic Model for the Propagation Reaction Step

The presence of dissolved oxygen in the system introduces a pathway for MP• decay which competes with reaction with isoprene, as is shown in **Figure 3.3**. The MP• + MP• termination reaction is not significant under our conditions because the concentration of MP• is always considerably less than that of the isoprene monomer or dissolved oxygen. This reasoning is confirmed by experimental measurements in the absence of isoprene and following careful removal of dissolved oxygen by nitrogen purging, with a positive nitrogen pressure to prevent further influx of air. Under these conditions, the MP• radical decay time is measured to be ~3 μs, compared to 300 ns for an unpurged solution as can be seen in **Figure E66** from the Experimental Section.

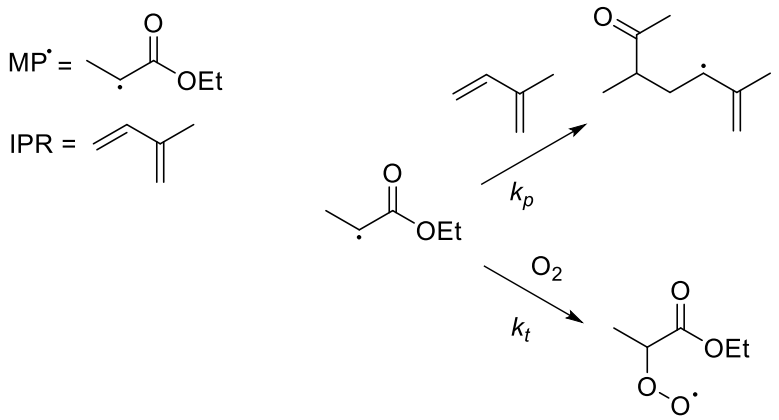

***Figure 2.3**. Competing pathways for the decay of MP• by reaction with the monomer isoprene (with propagation rate coefficient k_p) or with dissolved oxygen (with termination rate coefficient k_t).*

This competitive loss of MP• radicals is considered when fitting the data for decay of the MP• absorption using the kinetic model derived below. In this model, isoprene is abbreviated to IPR.

$$\frac{d[MP^\bullet]}{dt} = -k_p[MP^\bullet][IPR] - k_t[MP^\bullet][O_2] \quad (36)$$

Under our conditions of $[O_2]$, [IPR] >> [MP•]:

$$\frac{d[MP^\bullet]}{dt} = -(k'_p + k'_t)[MP^\bullet] \quad (37)$$

With pseudo-first order rate coefficients:

$$k'_p = k_p[IPR] \quad (38)$$

$$k'_t = k_t[O_2] \quad (39)$$

An exponential fit to a data set of [MP•] vs. time gives a rate coefficient $k = k'_p + k'_t$ for each [IPR]. A linear fit to a plot of $k = k'_p + k'_t$ vs [IPR] then gives k_p from the gradient. Our N_2 purging of solutions minimizes the contribution of the O_2 reaction to the MP• radical loss so that the experimental data mostly reflect loss by reaction with IPR.

2.2.4 Cyclic Kinetic Models

The previous sections have summarized models which can adequately describe fundamental photophysical processes e.g., non-radiative decay, fluorescence, intersystem crossing, triplet state relaxation, and excited state single electron transfer. However, in photochemical and photoredox systems, these models help to explain only part of the overall story. To describe photocatalytic and radical chain cycles a different set of models is required, and deciding between analytical or numerical solutions to rate equations becomes an important question of practicality. This section will look at how an analytical solution to a simple reaction cycle, similar to the one presented in Chapter 5 for a reaction involving a boronate complex radical chain reaction, can be derived and why using a numerical solution may be the preferred method for that study.

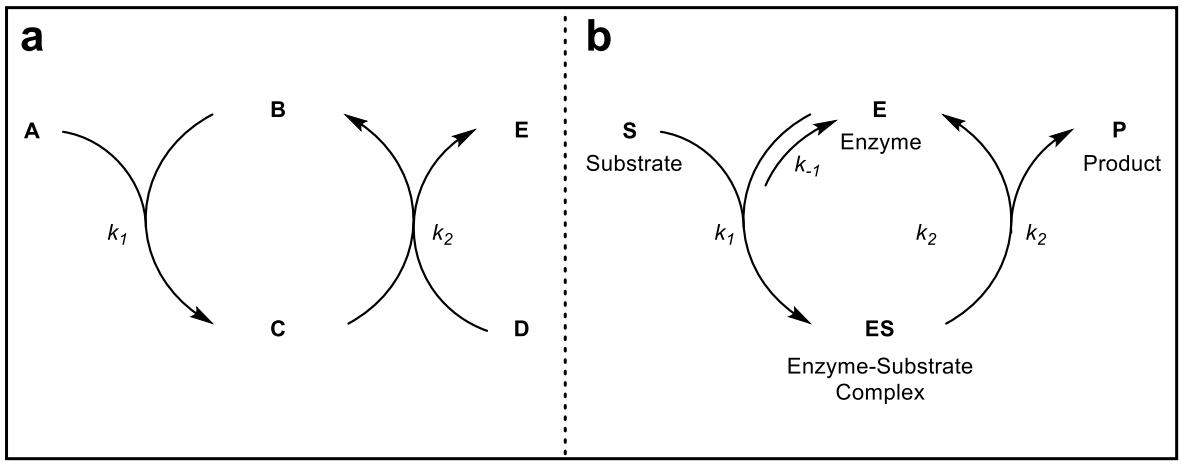

Figure 2.4a. *Mechanism for a catalytic or chain cycle similar to those discussed in Chapter 5.* ***b.*** *Michaelis-Menton enzyme system.*

Figure 2.4a shows a mechanism for a catalytic or chain type cycle, which is similar to a Michaelis-Menton (MM) type system where an enzyme catalyses the reaction of a substrate to product, as shown in **Figure 2.4b**. However, two key differences are apparent in this model: (1) the reaction to form **C** (enzyme-substrate complex in the MM system) is irreversible; and (2) the reaction which forms the product **E** is bimolecular rather than unimolecular. Similar to

the derivation of the analytical solution to MM kinetics, using the steady state approximation an analytical solution can also be found for the boronate system in **Figure 2.4a**.

$$\frac{d[E]}{dt} = k_2[C][D] \quad (40)$$

$$\frac{d[C]}{dt} = k_1[A][B] - k_2[C][D] \quad (41)$$

By the steady state approximation, $\frac{d[C]}{dt} = 0$,

$$k_1[A][B] = k_2[C][D] \quad (42)$$

The law of mass conversion states,

$$[B] = [B]_0 - [C] \quad (43)$$

Taken together,

$$k_1[A]([B]_0 - [C]) = k_2[C][D] \quad (44)$$

$$k_1[A][B]_0 - k_1[A][C] = k_2[C][D] \quad (45)$$

$$k_1[A][C] + k_2[C][D] = k_1[A][B]_0 \quad (46)$$

$$[C] = \frac{k_1[A][B]_0}{k_1[A]+k_2[D]} = \frac{[A][B]_0}{[A]+\frac{k_2}{k_1}[D]} \quad (47)$$

Using eqn. 40 and 47 gives,

$$\frac{d[E]}{dt} = k_2[B]_0 \frac{[A][D]}{[A]+\frac{k_2}{k_1}[D]} \quad (48)$$

This can also be shown in the Michaelis-Menton form,

$$\frac{d[E]}{dt} = V_{Max} \frac{[A][D]}{[A]+K_M[D]} \quad (49)$$

Where $V_{Max} = k_2[B]_0$ and $K_M = \frac{k_2}{k_1}$. While eqn. 49 may still be useful, to derive an integrated form for the time-dependent concentration of product E (or other species) that can be used to fit experimental measurements is in this case challenging, and may even be intractable, although an integrated closed form of the Michaelis-Menton equation is known.[26] Another

problem with using an analytical solution is that addition of new reaction steps is not always straightforward. Thus, to allow the greatest modelling flexibility, numerical integration is chosen to solve the differential equations for the kinetic systems described in Chapter 5, which while obscuring the underlying mathematical relationships, allows quick deployment of multiple models to understand recorded data.

2.3 References

1. Roberts GM, Marroux HJB, Grubb MP, Ashfold MNR, Orr-Ewing AJ. On the Participation of Photoinduced N–H Bond Fission in Aqueous Adenine at 266 and 220 nm: A Combined Ultrafast Transient Electronic and Vibrational Absorption Spectroscopy Study. *J Phys Chem A* 2014, **118**(47)**:** 11211-11225.

2. Grubb MP, Orr-Ewing AJ, Ashfold MNR. KOALA: A program for the processing and decomposition of transient spectra. *Rev Sci Instrum* 2014, **85**(6)**:** 064104.

3. Greetham GM, Sole D, Clark IP, Parker AW, Pollard MR, Towrie M. Time-resolved multiple probe spectroscopy. *Rev Sci Instrum* 2012, **83**(10)**:** 103107.

4. Greetham GM, Donaldson PM, Nation C, Sazanovich IV, Clark IP, Shaw DJ*, et al.* A 100 kHz Time-Resolved Multiple-Probe Femtosecond to Second Infrared Absorption Spectrometer. *Appl Spectrosc* 2016, **70**(4)**:** 645-653.

5. Bhattacherjee A, Sneha M, Lewis-Borrell L, Amoruso G, Oliver TAA, Tyler J*, et al.* Singlet and Triplet Contributions to the Excited-State Activities of Dihydrophenazine, Phenoxazine, and Phenothiazine Organocatalysts Used in Atom Transfer Radical Polymerization. *J Am Chem Soc* 2021, **143**(9)**:** 3613-3627.

6. Sneha M, Bhattacherjee A, Lewis-Borrell L, Clark IP, Orr-Ewing AJ. Structure-Dependent Electron Transfer Rates for Dihydrophenazine, Phenoxazine, and Phenothiazine Photoredox Catalysts Employed in Atom Transfer Radical Polymerization. *J Phys Chem B* 2021.

7. Kumpulainen T, Lang B, Rosspeintner A, Vauthey E. Ultrafast Elementary Photochemical Processes of Organic Molecules in Liquid Solution. *Chem Rev* 2017, **117**(16)**:** 10826-10939.

8. Rosspeintner A, Angulo G, Vauthey E. Bimolecular Photoinduced Electron Transfer Beyond the Diffusion Limit: The Rehm–Weller Experiment Revisited with Femtosecond Time Resolution. *J Am Chem Soc* 2014, **136**(5)**:** 2026-2032.

9. Eads DD, Dismer BG, Fleming GR. A subpicosecond, subnanosecond and steady-state study of diffusion-influenced fluorescence quenching. *J Chem Phys* 1990, **93**(2)**:** 1136-1148.

10. Rini M, Pines D, Magnes B-Z, Pines E, Nibbering ETJ. Bimodal proton transfer in acid-base reactions in water. *J Chem Phys* 2004, **121**(19)**:** 9593-9610.

11. Collins FC, Kimball GE. Diffusion-controlled reaction rates. *J Colloid Sci* 1949, **4**(4)**:** 425-437.

12. McCarthy BG, Pearson RM, Lim C-H, Sartor SM, Damrauer NH, Miyake GM. Structure-Property Relationships for Tailoring Phenoxazines as Reducing Photoredox Catalysts. *J Am Chem Soc* 2018, **140**(15)**:** 5088-5101.

13. Theriot JC, Lim C-H, Yang H, Ryan MD, Musgrave CB, Miyake GM. Organocatalyzed atom transfer radical polymerization driven by visible light. *Science* 2016, **352**(6289)**:** 1082-1086.

14. Isse AA, Bortolamei N, De Paoli P, Gennaro A. On the mechanism of activation of copper-catalyzed atom transfer radical polymerization. *Electrochimica Acta* 2013, **110:** 655-662.

15. Pan X, Fang C, Fantin M, Malhotra N, So WY, Peteanu LA*, et al.* Mechanism of Photoinduced Metal-Free Atom Transfer Radical Polymerization: Experimental and Computational Studies. *J Am Chem Soc* 2016, **138**(7)**:** 2411-2425.

16. Costentin C, Robert M, Saveant J-M. Electron transfer and bond breaking: Recent advances. *Chem Phys* 2006, **324**(1)**:** 40-56.

17. Pause L, Robert M, Saveant J-M. Reductive Cleavage of Carbon Tetrachloride in a Polar Solvent. An Example of a Dissociative Electron Transfer with Significant Attractive Interaction between the Caged Product Fragments. *J Am Chem Soc* 2000, **122**(40)**:** 9829-9835.

18. Kojima H, Bard AJ. Determination of rate constants for the electroreduction of aromatic compounds and their correlation with homogeneous electron transfer rates. *J Am Chem Soc* 1975, **97**(22)**:** 6317-6324.

19. Saveant JM. A simple model for the kinetics of dissociative electron transfer in polar solvents. Application to the homogeneous and heterogeneous reduction of alkyl halides. *J Am Chem Soc* 1987, **109**(22)**:** 6788-6795.

20. Lin CY, Coote ML, Gennaro A, Matyjaszewski K. Ab Initio Evaluation of the Thermodynamic and Electrochemical Properties of Alkyl Halides and Radicals and Their Mechanistic Implications for Atom Transfer Radical Polymerization. *J Am Chem Soc* 2008, **130**(38)**:** 12762-12774.

21. Isse AA, Lin CY, Coote ML, Gennaro A. Estimation of Standard Reduction Potentials of Halogen Atoms and Alkyl Halides. *J Phys Chem B* 2011, **115**(4)**:** 678-684.

22. Marco Montalti AC, Luca Prodi, M. Teresa Gandolfi. *Handbook of Photochemistry*, Third edn. Taylor & Francis Group: Boca Raton, FL, 2006.

23. Corbin DA, Puffer KO, Chism KA, Cole JP, Theriot JC, McCarthy BG*, et al.* Radical Addition to N,N-Diaryl Dihydrophenazine Photoredox Catalysts and Implications in Photoinduced Organocatalyzed Atom Transfer Radical Polymerization. *Macromolecules* 2021.

24. Pavlishchuk VV, Addison AW. Conversion constants for redox potentials measured versus different reference electrodes in acetonitrile solutions at 25°C. *Inorg Chim Acta* 2000, **298**(1)**:** 97-102.

25. Lattke YM, Corbin DA, Sartor SM, McCarthy BG, Miyake GM, Damrauer NH. Interrogation of O-ATRP Activation Conducted by Singlet and Triplet Excited States of Phenoxazine Photocatalysts. *J Phys Chem A* 2021, **125**(15)**:** 3109-3121.

26. Goličnik M. The integrated Michaelis-Menten rate equation: déjà vu or vu jàdé? *J Enzyme Inhib Med Chem* 2013, **28**(4)**:** 879-893.

3 Singlet and Triplet Contributions to the Excited-State Activities of Dihydrophenazine, Phenoxazine, and Phenothiazine Organocatalysts Used in Atom Transfer Radical Polymerization†

3.1 Introduction

Controlled methods for radical polymerization are of great interest for the synthesis of polymers with a desired molecular weight or chain length. Photoredox-catalysed atom transfer radical polymerization (ATRP), in particular, has emerged as an effective approach for the controlled synthesis of polymers with a precise composition and dispersity.[1] Recent developments in organic photoredox catalysis have improved these radical-based polymerization reactions by, most notably, avoiding contamination from metal-containing catalysts.[2,3,4,5] This progress has motivated the development of new classes of organic photocatalyst (PC) molecules based on N-aryl phenothiazines, phenoxazines and dihydrophenazines that have provided the benchmark for organocatalyzed ATRP (denoted O-ATRP).[3,6,7]

---

†Previously published in: A. Bhattacherjee, M. Sneha, L. Lewis-Borrell, G. Amoruso, T. A. A. Oliver, J. Tyler, I. P. Clark, and A. J. Orr-Ewing, *J Am Chem Soc* **2021** *143* (9), 3613-3627.

The writer is the co-first author of the referenced manuscript and: prepared all the samples in the lab of Prof. Varinder Aggarwal (University of Bristol, School of Chemistry) with additional help from Jasper Tyler; collected transient absorption data with Dr. Aditi Bhattacherjee, Dr. Mahima Sneha (University of Bristol, School of Chemistry, Prof. Andrew Orr-Ewing group), and Dr. Ian P. Clark (Central Laser Facility, Research Complex at Harwell, Science and Technology Facilities Council, Rutherford Appleton Laboratory); performed quantum mechanical calculations with Dr. Mahima Sneha and Dr. Aditi Bhattacherjee; analysed the data with Dr. Aditi Bhattacherjee, Dr. Mahima Sneha; interpreted the data and wrote the manuscript in cooperation with Dr. Aditi Bhattacherjee, Dr. Mahima Sneha and the principal investigator, Prof. Andrew Orr-Ewing. Time correlated single photon counting data were collected and analysed by Giordano Amoruso in the lab of Dr. Tom A. A. Oliver (University of Bristol, School of Chemistry).

The redox properties of a molecular photoredox catalyst mainly arise from the higher oxidation or reduction potential of the excited singlet or triplet electronic states of the molecule compared to its ground electronic state.[2] Both synthetically and computationally directed strategies for higher efficiency photoredox catalysts are built on accessing excited electronic states with long lifetimes that enable diffusive bimolecular electron transfer reactions with a radical precursor.[8,9,10] Molecular triplet states are sufficiently long-lived to favour intermolecular single electron transfer to radical initiators over intramolecular deactivation pathways. For this purpose, many early photocatalysts deliberately incorporated transition metal atoms as chromophores to enhance intersystem crossing rates through high spin-orbit coupling.[11]

Seminal research on O-ATRP optimization has placed emphasis on the energy of the lowest-excited triplet state (T_1) of a given photoredox catalyst to predict, rationalize, and tailor photocatalytic activities.[6,9,12] This emphasis derives mainly from three premises: (a) spin-forbidden relaxation to the ground state prolongs the lifetime of a triplet state in comparison to a singlet state;[10] (b) back electron transfer, which quenches photoredox activity, is inhibited in the triplet-spin radical pairs formed by initial electron transfer from the photocatalyst T_1 state (although this is less of a concern for dissociative electron transfer pathways exploited in O-ATRP);[2] (c) organic photocatalyst design should draw on existing knowledge of the photophysical behaviour of organometallic complexes,[11] many of which exhibit ultrafast intersystem crossing (ISC).[13,14,15] This study instead proposes a greater focus on excited state reduction potentials, regardless of the excited state spin multiplicity, as a controlling factor in O-ATRP optimization because of their influence on intermolecular electron transfer rate coefficients.[16] Consequently, molecules with few nanosecond fluorescence lifetimes and low triplet quantum yields may participate in bimolecular electron transfer reactions driving O-ATRP through their S_1 states instead of their triplet states.

Although organic photocatalysts do not contain metal ions, useful analogies may be drawn between the metal-centred or metal-to-ligand charge transfer (CT) states common in photo-excited metal complexes and the locally excited (LE) or CT-character excited states of organic compounds such as dihydrophenazines, phenoxazines and phenothiazines.[10,17,18] This LE vs CT character of the frontier orbitals has been argued to account for large discrepancies in photocatalytic efficiencies of organic compounds that have similar reducing potentials of their triplet states. A LE state descriptor is used when the frontier π and π^* orbitals are both localized over the core (a heterocyclic ring fused between two benzene rings, see **Figure 3.1**); CT instead

describes spatially separated π and π* orbitals that are delocalized over the core and N-aryl groups, respectively. In CT states, electron-withdrawing (donating) groups on the N-aryl rings stabilize (destabilize) the spatially separated π*-SOMOs. This spatial separation between the two SOMO electrons has been proposed to facilitate ISC and intermolecular electron transfer.[7,10,18] Here, direct counter-evidence is presented that one such optimized PC (5,10-di(4-cyanophenyl)-5,10-dihydrophenazine) with an electron-withdrawing nitrile (-CN) functionality on the N-aryl group stabilizing its CT-character S_1 and T_1 states repopulates the S_0 ground electronic state two orders of magnitude faster than the corresponding PC (5,10-bis(4-methoxyphenyl)-5,10-dihydrophenazine) with electron-donating substituents (-OMe), which is detrimental to the efficiencies of both ISC and bimolecular electron transfer reactions.

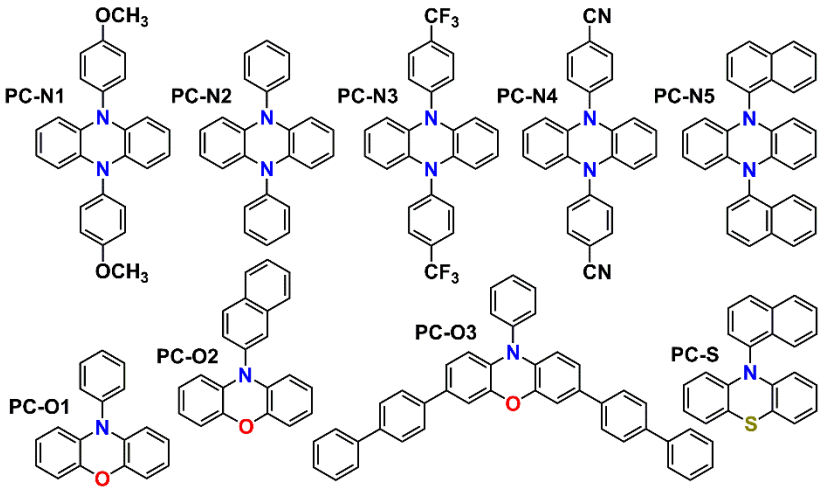

Figure 3.1. *Structures of nine organic photocatalysts studied here. PC-N, PC-O and PC-S nomenclature indicates dihydrophenzine, phenoxazine, and phenothiazine core structures, respectively. The core heteroatoms are emphasized by coloured labels. The PCs N1 to N5, and O1 to O3 further differ in their N-aryl substituents. Only one phenothiazine catalyst is studied. PC-O3 further incorporates core modification by the addition of biphenyl groups.*

In the current work, the solvent-dependent photochemical dynamics of nine PCs based on dihydrophenazine, phenoxazine, and phenothiazine central cores are studied (**Figure 3.1**). Such compounds have been widely applied in the recent development of O-ATRP.[3,6,19,20] These prior works have characterized the steady-state spectroscopies and excited-state redox potentials of these (and other) organic photocatalysts, the latter by combining cyclic voltammetry data with calculated excited state energies, and also tested their polymerization control of the as-grown polymer dispersity.[8,21,22,23,24,25] Design principles have focused on enhanced absorption of near-ultraviolet or visible light for photoinitiation and radical generation to make these polymerization reactions amenable to activation by light emitting diodes or natural sunlight, and to avoid undesirable side reactions.[6]

The PCs chosen for the current study are shown in **Figure 3.1**. They make use of modifications to N-atom and core substituents,[7] and show varying performances in O-ATRP that this work seeks to understand. The selected PCs are five dihydrophenazine (denoted PC-N), three phenoxazine (PC-O), and one phenothiazine (PC-S) derivatives – note that this nomenclature is used specifically in this work to distinguish between the differing heteroatoms. In four of these cases, (PC-N2, PC-N3, PC-N5, PC-O1), prior publications from the Orr-Ewing group have reported the analysis of transient absorption spectroscopy data to determine S_1-state lifetimes.[16,26,27] New solvent-dependent fluorescence lifetime measurements are presented here for all nine PCs, together with previously unreported mid-IR and UV-visible transient absorption spectroscopy studies for five of them, in three solvents chosen for their different polarities. The selected solvents are N,N-dimethylformamide (DMF), dichloromethane (DCM), and toluene. In addition, for the four previously studied PCs (PC-N2, PC-N3, PC-N5, PC-O1), new mid-IR transient absorption spectroscopy measurements are presented which extend over much greater time intervals than prior work from the group. The combined outcomes from the current and prior measurements provide a consolidated picture of the effects of structural modifications and solvent properties on the photodynamics of dihydrophenazine, phenoxazine and phenothiazine PCs.

The structural modifications in the chosen organic PCs explore the effects of changing one central-ring heteroatom in the core dihydrophenazine, phenoxazine or phenothiazine moiety, and of altering the N-aryl substituents, for example by comparing the effects of either electron donating or withdrawing groups. In the literature, PC-N3, PC-N4 and PC-N5 are reported to be promising dihydrophenazine-based photocatalyst with high efficiency and polymer dispersity control.[6] PC-O1 and PC-O2 are both effective phenoxazine-based catalysts with a phenyl or naphthyl substituent at the N atom. PC-O3 additionally involves substitution at the phenoxazine core with biphenyl groups, added to enhance visible light absorption via extended conjugation. Finally, PC-S is a phenothiazine-based catalyst representing a class of organic PCs reported to have superior reducing properties than metal-centred PCs, and high ISC quantum yields.[3,9,12]

3.2 Results and Discussion

Solutions of the organic PCs were first characterized by steady-state absorption and fluorescence spectroscopy. The photochemical dynamics of the PCs were then explored using ultrafast transient absorption spectroscopy, with sub-picosecond time resolution, and time-

resolved fluorescence spectroscopy. The time-resolved spectroscopy methods determined excited state lifetimes, propensities for ISC to triplet states, and timescales for recovery of ground-state molecules by a combination of radiative and non-radiative pathways.

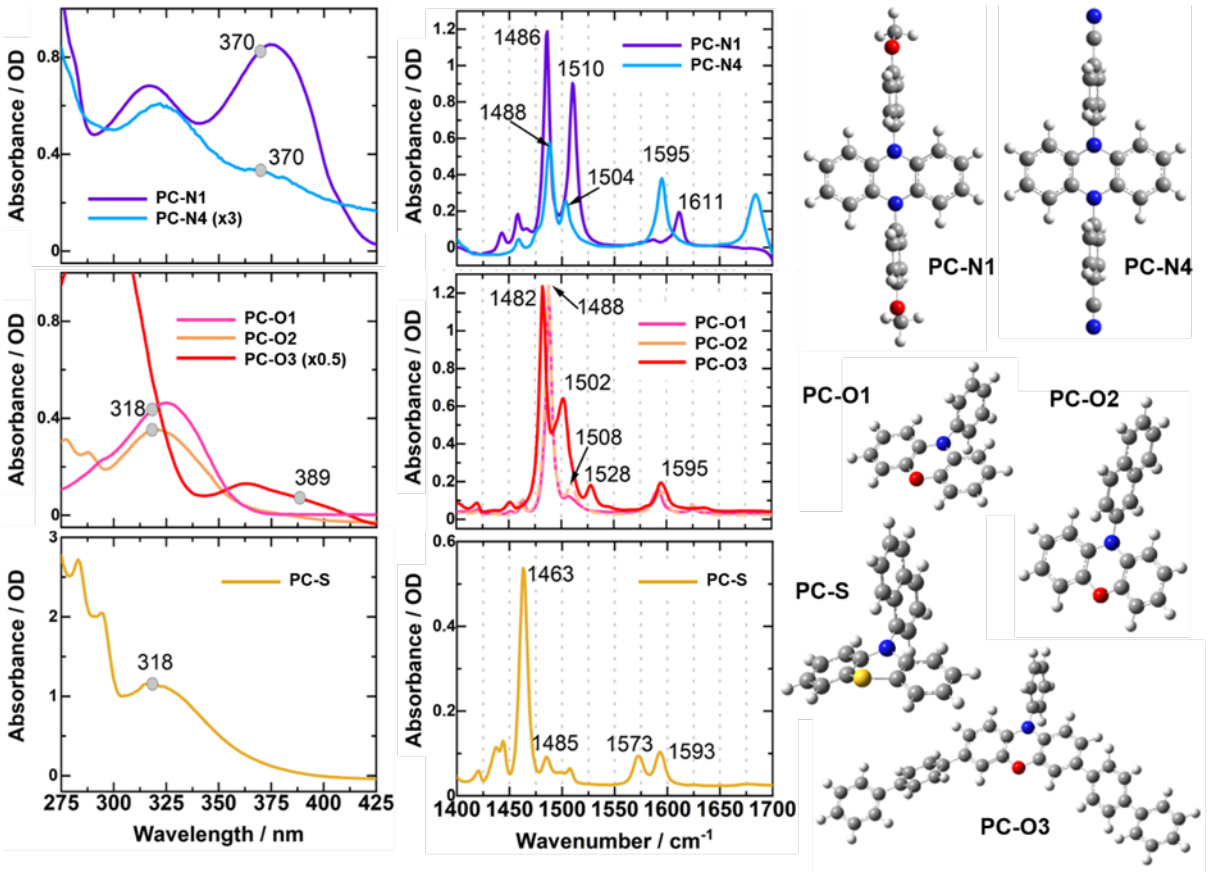

Figure 3.2. *UV-Vis absorption and FTIR spectra of six of the PCs in DCM. Grey circles identify the excitation wavelengths used in the time-resolved spectroscopic investigations. Computed ground-state structures of the organic photocatalysts (PCs) are also shown.*

3.2.1 Steady-State Spectroscopy Data

The UV-Vis absorption spectra of six of the PCs, measured in DCM, are shown in **Figure 3.2** for wavelengths between 275 and 425 nm, together with the optimized geometries of the PCs in their S_0 states. Corresponding data for the other three dihydrophenazine PCs studied have been reported elsewhere.[16,26] In their preferred structures, the N-aryl groups of all the PCs are oriented perpendicularly to the central cores to reduce steric repulsion between the H atoms of the aromatic rings. A similar perpendicular orientation is preferred for the biphenyl core substituents in PC-O3. PC-S differs structurally from all other PCs in that it has a puckered phenothiazine core to accommodate the larger S atom. The UV-vis spectra show that the strongest absorption bands for all PCs lie in the ultraviolet region from 200 to 300 nm; however, this work focuses on photoexcitation via the longer wavelength spectral features in view of their applications in visible / near-UV initiated photoredox catalysis.

The frontier orbitals involved in the long wavelength (>300 nm) photoexcitations of the PCs are predominantly π and π* orbitals. These absorption bands (**Figure 3.2**) may consist of multiple, unresolved, $S_0 \rightarrow S_n$ (n = 1 - 4) electronic excitations. Further details of the contributing orbital excitations, oscillator strengths, LE or CT characters of the S_1 states, and S_1 and T_1 reduction potentials are summarized in **Table 3.1**. These properties are estimated from computed excited state energies and published ground-state cyclic voltammetry data.[6,7,18] The fluorescence emission spectra of all six PCs measured in DMF, DCM, and toluene are shown in **Figure E1** (Figure 1 in Experimental section).

3.2.2 Time-Resolved Spectroscopy of UV-Excited Photocatalysts

Figure 3.3 shows the TVAS spectra of six PCs in three different solvents (DMF, DCM, and toluene-d_8). Similar measurements for PC-N2, PC-N3 and PC-N5 are reported elsewhere.[16,26] The probed IR region from 1400 to 1650 cm^{-1} corresponds mainly to the –C=C– ring stretching / deformation modes of the photocatalysts. For comparison, the FTIR spectra of selected PCs in their ground electronic states in DCM are shown in **Figure 3.2**. The presence of strong absorption bands in DMF restricted the observable spectral window for TVAS to 1525 - 1625 cm^{-1} in this solvent. Toluene-d_8 was chosen in place of protio toluene for these experiments because it has fewer interfering infrared features in this region; however, the TEAS and TCSPC experiments made use of protio toluene.

Figure 3.4 shows the time-dependences of the integrated TVAS band intensities, derived from spectra of the PC solutions in DMF and obtained by fitting the various excited state absorption (ESA) and ground-state bleach (GSB) features to Gaussian functions. The corresponding analyses were also performed for TVAS measurements made with solutions of the PCs in DCM and toluene-d_8. For each combination of a PC and solvent, these types of time-dependent ESA and GSB band intensities were globally fitted to single- or bi-exponential functions to extract the time constants summarized in **Tables 3.2 – 3.3**. The tables also report fluorescence lifetimes for the photoexcited PCs determined from the TCSPC measurements. Fluorescence lifetimes of a few tens of ns reflect the low oscillator strengths for the $S_1 \rightarrow S_0$ transitions in some of these photocatalysts (**Table 3.1**), whereas significantly shorter fluorescence lifetimes, some of which are sub-ns, indicate competing non-radiative decay pathways from S_1 to S_0 or T_1, or perhaps electron transfer reaction with the solvent in the case of measurements made in DCM.[28]

Table 3.1. *Computed and Experimental Photophysical Data for the Studied PCs in DMF.*

Photocatalyst	$S_0 \rightarrow S_n$ wavelength / excitation energy [(a)]	Oscillator strength [(a)]	Reduction potential and electronic LE or CT character [(b)]	
			S_1	T_1
PC-N1	374 nm / 3.3 eV (S_1) 332 nm / 3.7 eV (S_2)	0.0000 0.2056	-2.76 V (LE)	-2.15 V (LE)
PC-N2	376 nm / 3.3 eV (S_1) 333 nm / 3.7 eV (S_2)	0.000 0.206	-2.81 V (LE)	-2.15 V (LE)
PC-N3	374 nm / 3.3 eV (S_1) 337 nm /3.7 eV (S_4)	0.000 0.154	-2.20 V (CT)	-2.08 V (CT)
PC-N4	402 nm / 3.1 eV (S_1) 334 nm / 3.7 eV (S_4)	0.0000 0.1508	--- (CT)[(c)]	-1.89 V (CT)
PC-N5	377 nm / 3.3 eV (S_1) 314 nm / 3.9 eV (S_4)	0.0024 0.2176	-2.23 V (CT)	-1.92 V (CT)
PC-O1	307 nm / 4.0 eV (S_1) 303 nm / 4.1eV (S_2) 290 nm / 4.3 eV (S_3)	0.017 0.056 0.088	-2.93 V (LE)	-2.01 V (LE)
PC-O2	337 nm / 3.7 eV (S_1) 306 nm / 4.1 eV (S_2)	0.0000 0.0303	-2.14 V (CT)	-1.76 V (CT)
PC-O3	354 nm / 3.5 eV (S_1) 303 nm / 4.1 eV (S_2)	0.7692 0.3734	-2.12 V (CT)	-1.72 V (CT)
PC-S	320 nm / 3.9 eV (S_1) 308 nm / 4.0 eV (S_2) 282 nm / 4.4 eV (S_3)	0.0018 0.0165 0.0261	-1.86 V (CT)	-1.65 V (CT)

(a) The $S_0 \rightarrow S_n$ photoexcitation wavelengths (nm) and energies (eV), and the corresponding oscillator strengths were computed by TDDFT methods at the CAM-B3LYP/6-311++g(2d,p)/SCRF=(SMD, solvent, NonEq) level of theory.

(b) The reduction potentials (vs SCE) for the S_1 and T_1 excited electronic states were calculated using $E^{e}(PC^{\cdot+}/PC) - E(PC^*)$, where $E(PC^*)$ denotes the energy (in eV) of the S_1 or T_1 state. S_1 energies were estimated from the wavelength of onset of fluorescence at the short-wavelength side of the emission band, and T_1 energies were calculated using DFT methods. $E^{e}(PC^{\cdot+}/PC)$ values measured by cyclic voltammetry were taken from Refs. [6,7,18]. Locally excited (LE) or charge-transfer (CT) characters of the excited states were deduced from the computed molecular orbitals.

(c) PC-N4 does not fluoresce so E(PC*) could not be determined.

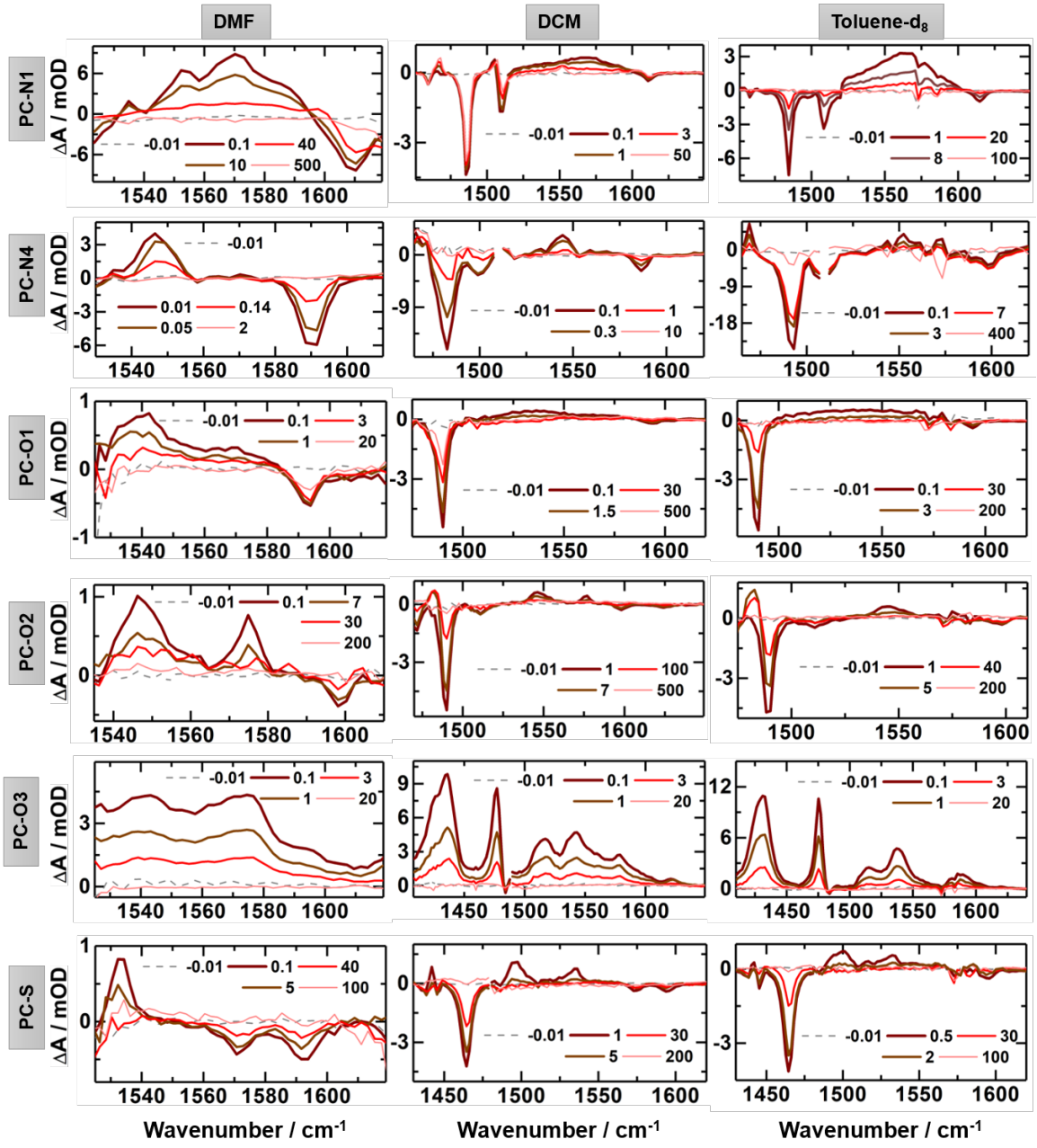

Figure 3.3. *TVAS measurements for six PCs in solution in DMF, DCM, and toluene-d8, shown at the selected time delays in nanoseconds indicated by the inset keys. In each case, measurements were also made at multiple time delays up to 10 µs (not shown). A negative time trace (-0.01 ns) is shown as a dashed grey line in all the panels to provide a reference for the baseline. The concentrations of the solutions were 4.2 mM (PC-N1), 10 mM (PC-N4), 3.2 mM (PC-O1), 2.9 mM (PC-O2), 1 mM (PC-O3), and 7.5 mM (PC-S). Gaps in the data (PC-N4 in DCM and in toluene-d8 at 1510 cm^{-1}; PC-O3 in DCM at 1480 cm^{-1}) resulted from damaged pixels in the MCT array detector. A discontinuity in the spectrum for PC-N1 in toluene-d8 at 1520 cm^{-1} was an artefact of joining two separate MCT detectors. The spectral noise in the TVAS measurements in toluene-d8 at 1575 and 1585 cm^{-1} was caused by low counts on the detector because of solvent infrared absorption features.*

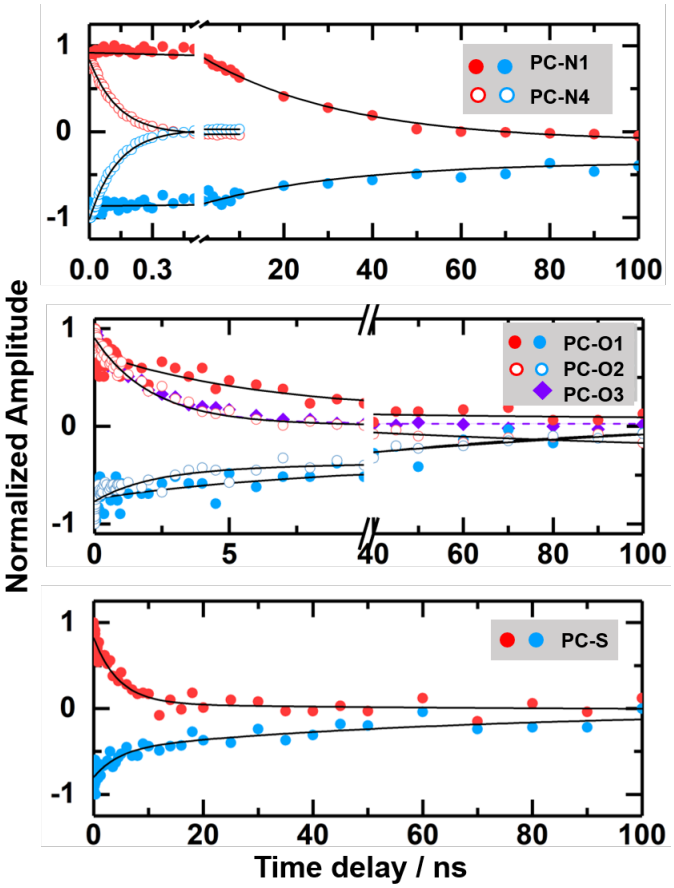

Figure 3.4. *Kinetic traces from TVAS for six UV-photoexcited PCs in DMF obtained by integrating band intensities at different time delays. Positive amplitude traces with red or purple symbols denote excited state absorption (ESA), and negative amplitude traces with blue symbols denote ground state bleaches (GSB). Insets show to which PCs the traces correspond. Note that the magnitudes of all peak amplitudes are normalized to one. For a given PC, the decays of both ESA and GSB intensities were globally fitted (solid black lines) to single or biexponential functions to extract a consistent set of photophysical time constants (see* ***Table 3.3****).*

Table 3.2. *Time Constants (in ns) Obtained from the Fitting of Kinetic Data from TVAS and TCSPC Measurements for UV-Photoexcited Dihydrophenazine PCs in Three Solvents, DMF, DCM and Toluene-d_8 (Toluene for TCSPC).*

		Time constants from TVAS and TCSPC data / ns [(b)]		
Photocatalyst	**Method [(a)]**	**DMF**	**DCM**	**Toluene-d_8**
PC-N1	TVAS	0.15 ± 0.07 [(c)] 38.5 ± 1.3	0.030 ± 0.004 [(c)] 2.2 ± 0.1[(d)]	0.077 ± 0.007 [(c)] 11.7 ± 0.2
	TCSPC	19.55 ± 0.17	0.30 ± 0.17 [(f)] (43%) 2.30 ± 0.17 [(d)] (57%)	10.95 ± 0.17
PC-N2	TVAS	16.8 ± 2.0 287 ± 21 [(e)]	0.013 ± 0.002[(c)] 2.77 ± 0.40 [(d)] [(g)]	25.5 ± 7.6 104 ± 15 [(e)] [(g)]
	TCSPC	12.98 ± 0.17	0.24 ± 0.17 [(f)] (37%) 2.55 ± 0.17 (63%)	8.83 ± 0.17
PC-N3	TVAS	0.635 ± 0.022	2.85 ± 0.1 970 ± 160 [(e)]	3.07 ± 0.24 36.4 ± 5.7 [(e)]
	TCSPC	0.76 ± 0.17 (94%)	2.62 ± 0.17	3.25 ± 0.17
PC-N4	TVAS	0.135 ± 0.003 [(g)]	0.51 ± 0.03 [(g)]	5.7 ± 0.3 398 ± 16 [(e)]
	TCSPC	0.20 ± 0.17 (58%) 2.58 ± 0.17 (42%)[(h)]	0.72 ± 0.17 (93%)	5.31 ± 0.17
PC-N5	TVAS[(i)]	5.2 ± 0.4	0.060 ± 0.008[(c)] 17 ± 1 500 ± 100[(e)]	25 ± 1
	TCSPC	5.33 ± 0.17	10.85 ± 0.17	6.13 ± 0.17

(a) 370 nm excitation was used for all measurements on dihydrophenazines.
(b) Single or double entries denote time-constants derived from mono and bi-exponential fits, and percentages in parentheses show relative amplitudes of the components for TCSPC data. Quoted uncertainties are from the experimentally determined IRF, with fits to data returning smaller errors.
(c) Time constant corresponds to growth of S_1 population, perhaps with a vibrational cooling component.
(d) S_1 lifetime shortened by reaction with solvent (dichloromethane).
(e) Assigned to T_1 lifetimes and likely to be affected by O_2 quenching.
(f) Suspected to be fluorescence from UV-excitation of ground state $PC^{\cdot+}$ generated in the solution by light-induced ET reaction of $PC(S_1)$ with DCM. Once formed, the $PC^{\cdot+}$ is stable in solution and can absorb the 370 nm pump light.
(g) Data obtained using the ULTRA laser system at the RAL Central Laser Facility.
(h) Fluorescence spectrum shows unusual behaviour in DMF, with an unexplained second decay component.
(i) Time constants from TVAS data were previously reported,[26] and are added here for comparison.

Table 3.3. *Time Constants (in ns) Obtained from the Fitting of Kinetic Data from TVAS and TCSPC Measurements for UV-Photoexcited Phenoxazine and Phenothiazine PCs in Three Solvents, DMF, DCM and Toluene-d_8 (protio Toluene for TCSPC).*

		Time constants from TVAS and TCSPC data / ns [(b)]		
Photocatalyst	**Method [(a)]**	**DMF**	**DCM**	**Toluene-d_8**
PC-O1	TVAS[(g)]	2.1 ± 0.1 46 ± 12 [(d)]	0.02 ± 0.01 [(c)] 1.5 ± 0.2 43 ± 9 [(d)]	0.014 ± 0.002 [(c)] 2.4 ± 0.2 27 ± 2 [(d) (e)]
	TCSPC[(g)]	2.61 ± 0.26 (79%) [(f)]	1.20 ± 0.26 (84%) [(f)]	2.77 ± 0.26
PC-O2	TVAS	0.07 ± 0.04 [(c)] 8.6 ± 1.2 75 ± 13 [(d)]	0.040 ± 0.008 [(c)] 6.4 ± 0.3 112 ± 4 [(d)(h)]	0.035 ± 0.008 [(c)] 2.4 ± 0.3 57 ± 4 [(d)]
	TCSPC	11.59 ± 0.26	6.55 ± 0.26	2.57 ± 0.26
PC-O3	TVAS	0.58 ± 0.18 3.3 ± 0.4	0.25 ± 0.02 2.57 ± 0.05	0.50 ± 0.12 2.4 ± 0.3
	TCSPC	2.72 ± 0.17	2.40 ± 0.17	2.01 ± 0.17
PC-S	TVAS	5.9 ± 0.6 78 ± 30 [(d)]	0.014 ± 0.003 [(c)] 3.8 ± 0.2 395 ± 10 [(d)]	0.007 ± 0.001 [(c)] 1.77 ± 0.08 673 ± 18 [(d)]
	TCSPC	6.27 ± 0.26	3.90 ± 0.26	1.85 ± 0.26

(a) Excitation wavelengths were 318 nm for TVAS and 340 nm for TCSPC, with the exception of PC-O3 which was excited at 389 nm for TVAS and 370 nm for TCSPC.
(b) Single or double entries denote time-constants derived from mono and bi-exponential fits, and percentages in parentheses show relative amplitudes of the components for TCSPC data. Quoted uncertainties are from the experimentally determined IRF, with fits to data returning smaller errors.
(c) Time constant corresponds to growth of S1 population, perhaps with a vibrational cooling component.
(d) Assigned to T1 lifetimes and likely to be affected by O2 quenching.
(e) Extends to 840 ± 31 ns with improved N2 purging.
(f) Minor contributions from a second time constant of 6.78 ± 0.26 ns in DMF and 6.10 ± 0.26 ns in DCM are also observed in the TCSPC experiments.
(g) Time constants for PC-O1 were previously reported from the Orr-Ewing laboratory,27 and are added here for comparison.
(h) Extends to 1.63 ± 0.03 μs with improved N2 purging.

Complementary TEAS measurements for DMF, DCM and toluene solutions of the PCs are shown in **Figure 3.6**. The methods for spectral decomposition into S_n, S_1 and T_1 ESA bands, performed using the KOALA program,[29] are reported in the Experimental Section 7.4. Kinetic fitting of the time-dependent intensities of the spectral components gave the exponential time constants summarized in **Table 3.4**. The following discussion considers in turn the photodynamics of the dihydrophenazine, phenoxazine and phenothiazine PCs deduced from all the excited-state population growth and decay time constants summarized in **Tables 3.2 – 3.4**.

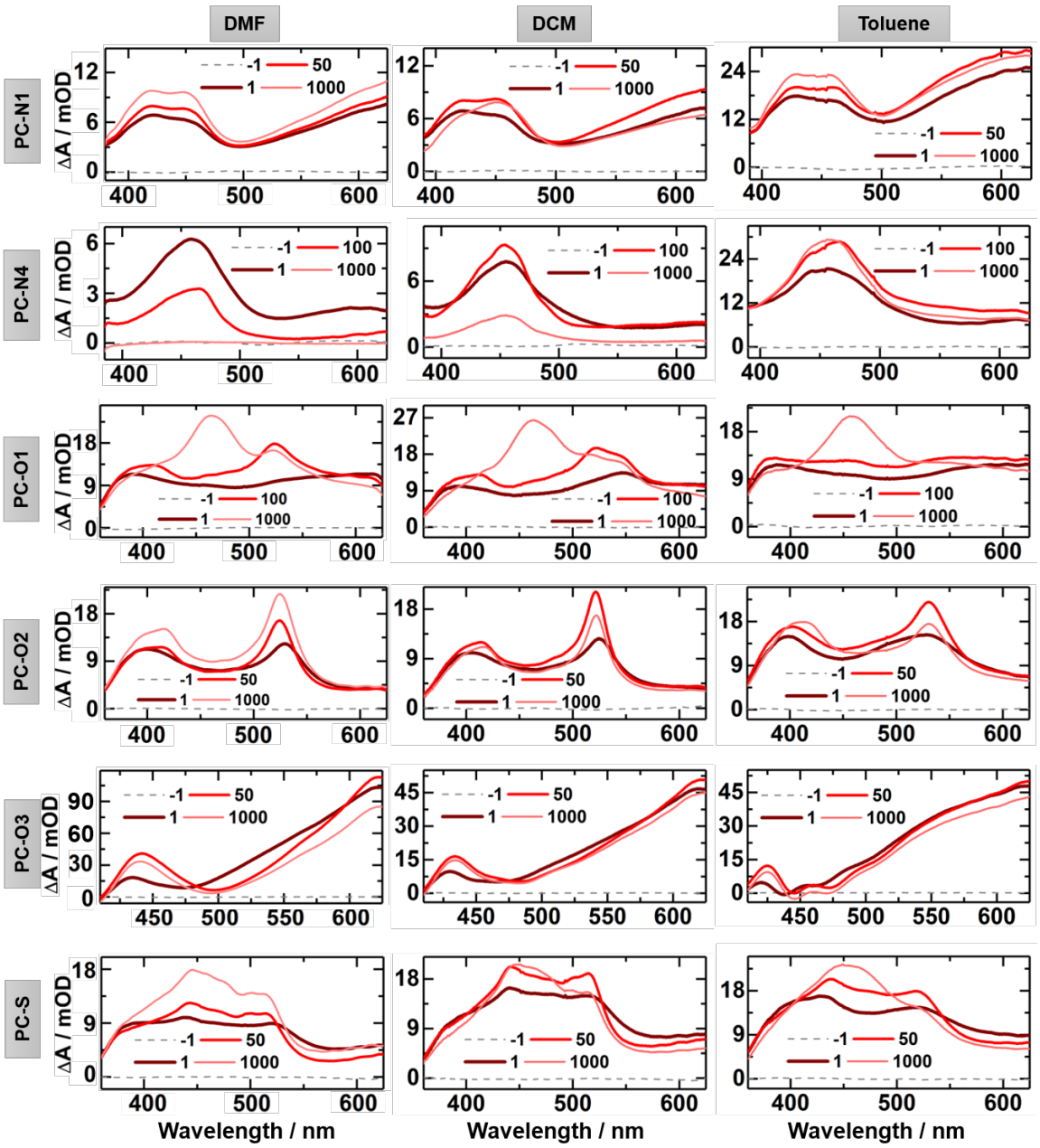

Figure 3.5. *Transient electronic absorption spectra measured for six PCs in DMF, DCM and toluene up to a maximum time interval of 1 ns. The legend indicates representative pump-probe time-delays in picoseconds. The solid grey line (-1 ps, where the probe pulse arrives at the sample before the pump pulse) provides a reference for the baseline.* ***Figure E13*** *of the Experimental section further shows TEAS data measured in DMAc.*

Table 3.4. *Exponential Time-Constants for Growth and Decay of Bands in the TEAS Spectra of the Dihydrophenazine, Phenoxazine and Phenothiazine PCs in DMF, DCM and Toluene Solutions.*

	Time constants / ps [(a) (b) (c)]		
Photocatalyst	**DMF**	**DCM**	**Toluene**
PC-N1	2.8 ± 0.4 (↑ S_1) 134 ± 12 (↑ S_1)	30 ± 4 (↑ S_1) 2200 ± 100 (↓ S_1)	2.7 ± 0.6 (↑ S_1) 54 ± 6 (↑ S_1)
PC-N2	13 ± 2 (↑ S_1) [(d)]	18 ± 3 (↑ S_1) ~2770 (↓ S_1, ↑ T_1)	23 ± 2 (↑ S_1)
PC-N3	613 ± 54	0.400 ± 0.01(↑ S_1) 31.0 ± 5.0 (↑ S_1)	1.7 ± 0.1 (↑ S_1) ~3000 (↓ S_1, ↑ T_1)
PC-N4	2.4 ± 0.2 (↑ S_1) 136 ± 9 (↓ S_1)	1.1 ± 0.1 (↑ S_1) 18.4 ± 1.6 (↑ S_1) ~510(↓S_1)	1.0 ± 0.1 (↑ S_1) 17.7 ± 1.4 (↑ S_1)
PC-N5	10.4 ± 2.6 (↑ S_1) 111 ± 8 (↑ S_1)	3.4 ± 0.7 (↑ S_1) 54.6 ± 3.3 (↑ S_1)	4.7 ± 0.3 (↑ S_1) 91 ± 5 (↑ S_1)
PC-O1	14.8 ± 0.3 (↑ S_1) 2100 ± 100 (↓ S_1, ↑ T_1)	14.8 ± 0.4 (↑ S_1) 1500 ± 200 (↓ S_1, ↑ T_1)	22.8 ± 1.0 (↑ S_1) 2400 ± 200 (↓ S_1, ↑ T_1)
PC-O2	1.9 ± 0.2(↑ S_1) 77 ± 6(↑ S_1) ~8600(↓ S_1, ↑ T_1)	0.60 ± 0.01(↑ S_1) 20 ± 0.5(↑ S_1) ~6400(↓ S_1, ↑ T_1)	2.1 ± 0.1(↑ S_1) 21.0 ± 1.5 (↑ S_1) ~2400(↓ S_1, ↑ T_1)
PC-O3	2.9 ± 0.1 (↑ S_1) ≥ 2500 (↓ S_1)	250 (↑ S_1) 2400 (↓ S_1)	500 (↑ S_1) 2400 (↓ S_1)
PC-S	1.4 ± 0.1 (↑ S_1) 51.0±5.2 (↑ S_1) 4900 (↓ S_1, ↑ T_1)	0.9 ± 0.1 (↑ S_1) 21 ± 2 (↑ S_1) ~3900 (↓ S_1, ↑ T_1)	2.0 ± 0.1(↑ S_1) 19.4 ± 3.2(↑ S_1) ~1770(↓ S_1, ↑ T_1)

(a) The symbols ↑ and ↓ denote growth and decay, respectively, of the intensities of ESA bands assigned to the specified states.
(b) Recovery of S_0 population may be biexponential, but always shows one time constant in agreement with S_1 population decay.
(c) Time constants greater than 1000 ps are poorly determined from fits to the TEAS measurements which extend only to 1.3 ns. Instead, time constants from TVAS (**Tables 3.2** and **3.3**) were shown to be consistent with the TEAS data.
(c) Value obtained in DMAc.

3.2.3 Dihydrophenazine Catalysts

PC-N1 and PC-N4 are examples of dihydrophenazine catalysts with electron-donating (-OMe, PC-N1) and electron withdrawing (-CN, PC-N4) N-phenyl para-substituents, and are chosen as the focus of the discussion because of these contrasting electronic properties. Where appropriate, further comparisons are drawn with the other dihydrophenazine PCs studied. The triplet excited-state reduction potentials, $E^{\circ}(PC^{\cdot+}/^{3}PC^{*})$, of PC-N1 and PC-N4, obtained by combining DFT calculations of excitation energies and ground-state redox potentials (versus saturated calomel electrode) are -2.15 V and -1.89 V, respectively.[6] These values are compared

with the corresponding estimates for the S_1-state reduction potentials in **Table 3.1**. Without any N-phenyl substituents (i.e., PC-N2), the corresponding T_1-state reduction potential is -2.15 V. All these dihydrophenazine derivatives are more reducing from their T_1 states (and by implication, their S_1 states) than commonly used metal-centred PCs such as polypyridyl iridium complexes following photoexcitation.[11]

The electron-withdrawing substituents stabilize excited states of CT character and lower their reduction potentials compared to states with LE character. In these ππ* CT states, the electron density in the lower-lying π-SOMO is mainly on the dihydrophenazine core whereas that in the higher π*-SOMO is mainly on the N-phenyl ring(s). This delocalization is augmented by -CN (in PC-N4) or $-CF_3$ (in PC-N3) groups in the para position. Miyake and co-workers hypothesized that the superior photocatalytic ATRP performances of PC-N4 and PC-N3 in comparison to PC-N1 derives from their excited-state CT character, and used this principle as the basis for further PC design.[6,18] The quantification of the effects of the N-phenyl ring substituents, and hence of the CT or LE character of the T_1 (or S_1) states, on the rate coefficients for intermolecular electron transfer reactions that initiate an ATRP cycle is the subject of Chapter 4.

The TDDFT calculations indicate that photoexcitation is to the S_2 state in PC-N1 and the S_4 state in PC-N4 at the near-UV wavelengths used here. Internal conversion to S_1 proceeds on ultrafast timescales, faster than intermolecular electron-transfer reactions or radiative decay, in accordance with Kasha's rule.[30] This ultrafast relaxation $S_n \rightarrow S_1$ is mostly comparable to, or faster than, the temporal resolution of TVAS experiments performed in this study, but can be observed by this spectroscopic method in the case of PC-N1 as a combination of internal conversion and vibrational cooling kinetics (see **Tables 3.2** and **3.4**).

When photoexcited at 370 nm, PC-N1 shows strong, moderate, and weak GSB features at 1485, 1511, and 1613 cm^{-1}, respectively, in the TVAS spectra of **Figure 3.3**. In contrast to these sharp depletion bands, which have 5 to 10 cm^{-1} full-widths-at-half-maximum (FWHM), the feature due to ESA is unusually broad, spanning from 1530 to 1590 cm^{-1}. This width is likely to derive from overlapping vibrational bands of the S_1 state (as discussed below and in Section 3.2.5, there is no clear evidence for T_1 population in the data for PC-N1). In comparison, PC-N4 shows one strong and two weak GSB features at 1488, 1503, and 1595 cm^{-1}, respectively, when photoexcited at 370 nm. An observed ESA band at 1547 cm^{-1} is much narrower than for PC-N1; for PC-N4, all peaks have a width of 15 to 20 cm^{-1}. The ground-state FTIR spectral

absorptions in this region match the wavenumbers of the GSB features and have a FWHM of 10 cm^{-1}, which is ascribed to inhomogeneous broadening by interaction with the solvent (see Section 7.3 of the Experimental section for steady state FTIR spectra).

N,N-dimethylacetamide (DMAc) is the solvent medium used in several reported O-ATRP photopolymerization studies. Of the three solvents used here, DMF most closely resembles DMAc in terms of polarity, and it is a useful analogue because the IR spectrum of DMAc masks all the transient absorption features of interest. Inspection of **Figures 3.3** and **3.4** shows that all the spectral features described above which fall in the narrow IR-transparent window of DMF decay completely to zero. However, ground-state recovery is much faster for PC-N4 than PC-N1. Reasonable agreement between time constants deduced from the analysis of TVAS and TCSPC data (**Table 3.2**) confirms a faster decay of S_1 population in PC-N4. The recovery of the GSB mirrors the decay of the ESA, which indicates a predominantly direct relaxation pathway from the S_1 to the S_0 state without significant involvement of any intermediate electronic state (e.g., T_1).

Both prior and the current measurements for DMF solutions of PC-N3, which has para, electron-withdrawing $-CF_3$ substituents on the N-phenyl groups, show fast (~700 ps) internal conversion to the ground state, on timescale approaching that for PC-N4 relaxation.[16] Based on this observation, it is posited that the polar solvent apparently stabilizes the CT-character S_1 states of PC-N4 and PC-N3, thereby reducing the S_1-S_0 energy gap and opening up a rapid internal conversion (IC) route to S_0 (most likely through a conical intersection), which outcompetes fluorescence decay or ISC. Such pathways are not accessible for the LE-character S_1 state of PC-N1, nor for PC-N2 studied both here and previously by Koyama *et al.*[16] The S_1 excited-state lifetime for PC-N4 in DMF was independently verified using TEAS to be 136 ± 9 ps (*c.f.* 135 ps by TVAS), following a 2.4 ± 0.2 ps growth by IC from the photoexcited S_4 state. The experimentally determined S_1 lifetime for PC-N4 in DMAc was found to be ~180 ps by TEAS, consistent with expectations based on the similar polarities of the two solvents. Thus, for PC-N4 and PC-N3, both of which have been shown to provide good dispersity control in the polymer products of O-ATRP, the excited state lifetime is found to be shorter than nanosecond timescales for diffusional bimolecular electron transfer reactions at the concentrations used in O-ATRP synthesis.

In DCM, PC-N4 ground state recovery is also complete (**Figure 3.3**), and the timescale matches that of the decay of the S_1 ESA bands observed by TVAS, indicating little or no branching into

the triplet manifold by ISC. Comparison of the time constants in **Tables 3.2** and **3.4** shows that the relaxation dynamics in DCM (510 ± 30 ps) are comparable to those in DMF (135 ± 3 ps). In toluene, however, PC-N4 behaves differently: while the S_1 ESA decays with a time constant of 5.7 ± 0.3 ns, the ground state bleach shows a biexponential recovery with time constants of 5.7 ± 0.3 ns and 398 ± 16 ns. This second time constant is assigned to the quenching of T_1-state population by dissolved oxygen, details of which are discussed in Section 3.2.5. The longer S_1 lifetime in toluene is supported by TCSPC data, and by observation of strong fluorescent emission from PC-N4 in this solvent, but not in DMF or DCM under the same measurement conditions. TEAS measurements show that the main S_1 ESA band of PC-N4 centred at 450 nm grows with 1.0 ± 0.1 ps and 17.7 ± 1.4 ps time constants in toluene (and 1.1 ± 0.1 ps and 18.4 ± 1.6 ps in DCM) which is attributed to IC and vibrational cooling in the S_1 state, respectively. A shift of the band maximum to shorter wavelength at times longer than 5 ps is consistent with this latter interpretation.

For PC-N1 in toluene-d_8, TVAS measurements show that the ground-state recovery is complete within 100 ns. The time constant for the decay (11.7 ± 0.6 ns) matches that obtained from TCSPC (10.95 ± 0.17 ns), and in DMF the ground-state recovery is even slower (time constants of 38.5 ± 1.3 ns from TVAS, 19.55 ± 0.17 ns from TCSPC, with unclear reasons for the discrepancy in the values). However, in DCM the photophysical behaviour is noticeably different, with an ESA decay time constant of 2.2 ± 0.1 ns. Although the ESA bands assigned to photoexcited PC-N1 in DCM decay completely to zero, the GSB recovery remains 70% incomplete at time delays up to 10 μs, indicating a long-lived intermediate state or reactive loss. Four small positive differential absorbance peaks are noted at 1466, 1508, 1552 and 1601 cm^{-1}, and these bands are assigned to the PC-N1$^{\cdot+}$ radical cation, pointing to an electron transfer reaction of the photoexcited PC-N1 with the DCM solvent. This interpretation is consistent with prior reports of halogenated solvents such as DCM participating in electron transfer reactions with photoexcited organic molecules.[28] No such indications of cation formation are seen for photoexcited PC-N4 in DCM, most likely because the sub-ns relaxation to S_0 (**Table 3.3**) outcompetes intermolecular electron transfer to the solvent.

The extended timescale TVAS measurements performed in this work also reveal PC-N2 behaviour that is similar to PC-N1 in the three solvents studied. In DMF and toluene-d_8 solutions, the PC-N2 S_1-state population decays with time constants of 16.8 ± 2.0 ns, and 25.5 ± 7.6 ns respectively, whereas in DCM, PC-N2 has a shorter S_1 lifetime and incomplete ground-

state recovery indicating a reaction with the solvent. Both PC-N1 and PC-N2 have LE character in their S_1 states, and the large S_1-state reduction potentials can drive ET reactions with the chlorinated solvent. However, for PC-N2 solutions in DMF and toluene-d_8, the GSB recovery includes a second, slower component with a time constant of ~100-300 ns which is assigned to quenching of T_1-state population by dissolved oxygen.

The TEAS data for PC-N1 shown in **Figure 3.5** for solutions in DMF confirm the kinetics of excited state relaxation derived from the TVAS measurements. The observed bands are assigned to S_1 ESA, and spectral decomposition and kinetic analysis give time constants for the growth of this ESA as 2.8 ± 0.4 ps and 134 ± 12 ps. The two time constant values most likely represent steps of internal conversion to S_1 from the initially photoexcited S_2 state and subsequent vibrational cooling in S_1, but a component of direct excitation to the S_1 state followed by vibrational relaxation cannot be discounted. Although formally an electronically forbidden transition (**Table 3.1**), the $S_0 \rightarrow S_1$ excitation might become weakly allowed by vibronic coupling. In toluene, the corresponding time constants for growth of the S_1 absorption are 2.7 ± 0.6 ps and 54 ± 6 ps; the latter time constant is also obtained from TVAS band intensity analysis (**Table 3.3**). Again, these processes are interpreted as signatures of IC from the photoexcited S_2 state and vibrational relaxation of internally hot PC-N1(S_1) molecules. In DCM, the PC-N1 S_1 population growth with time constant of 30 ± 4 ps is indicative of $S_2 \rightarrow S_1$ internal conversion and vibrational cooling in S_1. The rate of S_1 population loss is consistent with TVAS measurements, with a time constant of 2.2 ± 0.1 ns. A band consistent with PC-N1$^{\cdot+}$ production grows on this same timescale, providing further evidence for charge transfer from the PC-N1 S_1-state to the solvent DCM competing with relaxation to S_0.

On the 1.3 ns timescales of the TEAS measurements in DMF and toluene, there is no evidence for the growth of additional features that might correspond to ESA from the T_1 states of the dihydrophenazine PCs PC-N1 and PC-N4. Similar conclusions were drawn in prior studies from the Orr-Ewing group of PC-N3 and PC-N5,[16,26] although spectroscopic evidence for some branching into T_1 was reported for PC-N2 in both DMF and DCM solutions,[16] and is discussed further in Section 3.2.5.

An interesting trend emerges when the five dihydrophenazine PCs are compared for solutions in DMF: the PCs with CT excited-state character have shorter S_1-state lifetimes - PC-N3 (136 ps), PC-N4 (500 ps) and PC-N5 (5 ns) - than the PCs with LE character - PC-N1 (11 ns) and

PC-N2 (17 ns). These observations may hold clues to the S_1-state relaxation mechanisms, but further theoretical work is required to identify the details of the decay pathways.

3.2.4 Phenothiazine Catalyst

PC-S is a phenothiazine catalyst that possesses a puckered central ring.[31] There are conflicting views about the excited state(s) responsible for the photoredox reactivity of phenothiazine PCs, with prior studies pointing to either the short-lived singlet state or the much longer-lived triplet state.[12,32] At the chosen excitation wavelength of 318 nm, it is likely the S_2 state of PC-S (**Table 3.1**) is excited with a weaker contribution from the $S_0 \rightarrow S_1$ transition, and perhaps also from the $S_0 \rightarrow S_3$ transition computed to lie at higher energy.

The TVAS spectra of PC-S (**Figure 3.3**), photoexcited at 318 nm in DCM or toluene-d_8, show a strong GSB feature at 1463 cm^{-1} corresponding to depletion of ground-state population, and two weak GSBs at 1573 cm^{-1} and 1591 cm^{-1}. Only the latter two depletions are observed in DMF, with the other masked by strong solvent absorption. ESA bands are evident for PC-S solutions in DCM and toluene-d_8 near 1500 and 1530 cm^{-1} which decay completely to zero within a few tens of nanoseconds. In DMF, only the higher energy ESA feature can be resolved and decays to zero within 40 ns after photoexcitation.

Time constants extracted from kinetic fits to TVAS data (**Table 3.3**) show S_1 relaxation with time constants of 5.9 ± 0.6 ns, 3.8 ± 0.2 ns, and 1.77 ± 0.08 ns in DMF, DCM, and toluene-d_8, respectively. This interpretation is confirmed by TCSPC measurements of fluorescence lifetimes (**Table 3.3**), and by a prior report of a singlet state lifetime for PC-S of 7.6 ns in 3-methylpentane at 298 K.[32] The second, slower time components observed in GSB recovery kinetics in all three solvents indicate quenching of T_1-state population, most likely accelerated by dissolved O_2 in the samples.

The TEAS data for PC-S in DMF (**Figure 3.5**) show three broad and overlapping peaks, with continued growth of some components up to the longest measured delay time of 1.3 ns. In DCM, the spectra are best described by a decaying exponent with time constant 0.9 ± 0.1 ps, an intermediate with two time constants (0.9 ± 0.1 ps and 21 ± 2 ps) for growth, which then decays as a third Gaussian band centred at 460 nm grows in with a ~ 3.9 ns time constant. The kinetics of the intermediate component are in reasonable agreement with the 14 ± 3 ps growth and 3.8 ± 0.2 ns decay time constant for PC-S (S_1) ESA bands observed by TVAS (**Table 3.3**), and this feature is therefore assigned to ESA from the S_1 state. Initial population of S_1 is by

internal conversion from the optically excited S_n states, and the band emerging at later times and centred near 460 nm is likely to correspond to ESA from the T_1 state of PC-S, populated by ISC from S_1. Similar behaviour is observed for PC-S in toluene, with a T_1 absorption band centred at 460 nm (**Figure 3.5**). This band grows as the broad intermediate S_1 ESA band decays, albeit faster than in DCM, with a time constant of 1.77 ns. Further analysis of the kinetics of ISC in PC-S is presented in the following section.

3.2.5 Triplet State Branching

Where spectroscopic evidence for triplet state population in the various PCs studied, either from distinct absorption bands in the TEAS measurements or from biexponential kinetics for GSB recovery, rate-coefficients for ISC and the triplet-state branching from the S_1 state in competition with relaxation to S_0 are deduced. The T_1-state lifetime can be several hundred microseconds.[10] In such a case, the PC ground-state depletion is not expected to recover completely on a ns-to-μs timescale. However, T_1 populations are quenched more rapidly by small amounts of dissolved O_2, which happened to be persistent in the sample flow system even in solutions purged by N_2. Under these conditions, the T_1 lifetimes shortened to tens of nanoseconds or longer. Another contributing factor towards partial or incomplete recovery of the ground state could be reaction from the photoexcited state, for example by electron transfer to a solvent molecule, and evidence for this is seen in some of the experiments conducted in DCM, as discussed earlier. Here, the observed amplitudes of components of biexponential or triexponential ground-state recovery in the TVAS experiments are used to guide determinations of an upper limit for the branching into triplet states. For example, for a biexponential GSB recovery with amplitudes of the faster (S_1 decay) and slower (T_1 decay) components denoted by A_1 and A_2 respectively, the T_1 quantum yield from $\Phi_{ISC} = A_2/(A_1 + A_2)$ can be estimated. Uncertainties in Φ_{ISC} are obtained by appropriate propagation of the fit uncertainties in A_1 and A_2 values. This analysis assumes that any dissolved O_2 does not influence the rates of ISC or S_1 quenching to S_0. **Table 3.5** summarizes the resulting quantum yields (Φ_{ISC}) and rate coefficients (k_{ISC}) for ISC in the PC solutions studied. The latter values are evaluated using $k_{ISC} = \Phi_{ISC}/\tau(S_1)$ where $\tau(S_1)$ is the measured S_1-state lifetime (**Tables 3.2 – 3.3**).

Table 3.5. *Estimated Intersystem Crossing Quantum Yields, Φ_{ISC}, and Rate Coefficients, k_{ISC}, Derived from Ground-State Bleach Recovery Kinetics Measured by TVAS.* [(a), (b)]

Photocatalyst	S_1 and T_1 character		Solvent		
			DMF	DCM	Toluene-d_8
PC-N1	LE	Φ_{ISC}	–	–	–
		k_{ISC} / 10^8 s^{-1}	–	–	–
PC-N2	LE	Φ_{ISC}	0.71 ± 0.03	–	0.82 ± 0.16
		k_{ISC} / 10^8 s^{-1}	0.42 ± 0.06	–	2.7 ± 0.6
PC-N3	CT	Φ_{ISC}	–	0.19 ± 0.01	0.60 ± 0.06
		k_{ISC} / 10^8 s^{-1}	–	0.68 ± 0.04	1.2 ± 0.2
PC-N4	CT	Φ_{ISC}	–	–	0.57 ± 0.06
		k_{ISC} / 10^8 s^{-1}	–	–	1.0 ± 0.1
PC-N5	CT	Φ_{ISC}	–	0.14 ± 0.02	–
		k_{ISC} / 10^8 s^{-1}	–	0.08 ± 0.01	–
PC-O1	LE	Φ_{ISC}	0.84 ± 0.21	0.43 ± 0.05	0.56 ± 0.03
		k_{ISC} / 10^8 s^{-1}	4.0 ± 1.0	2.9 ± 0.5	2.3 ± 0.2
PC-O2	CT	Φ_{ISC}	0.74 ± 0.09	0.56 ± 0.03	0.70 ± 0.03
		k_{ISC} / 10^8 s^{-1}	0.9 ± 0.2	0.9 ± 0.1	2.9 ± 0.4
PC-O3	CT	Φ_{ISC}	–	–	–
		k_{ISC} / 10^8 s^{-1}	–	–	–
PC-S	CT	Φ_{ISC}	0.37 ± 0.07	0.63 ± 0.03	0.57 ± 0.05
		k_{ISC} / 10^8 s^{-1}	0.6 ± 0.1	1.7 ± 0.1	3.2 ± 0.3

(a) An entry of – indicates no evidence of T_1-state population, suggesting $\Phi_{ISC} \approx 0$.
(b) Uncertainties are from the fitted errors in the amplitudes of the components of multi-exponential fits to single kinetic data sets.

Intersystem crossing is a minor pathway in the relaxation of most of the photoexcited dihydrophenazine PCs studied, particularly in DCM and DMF.[16] For PC-N5 solution in DCM, a value of $\Phi_{ISC} = 0.13 \pm 0.02$ was recently reported, consistent with this general conclusion.[26] The exception is toluene, where three out of the five dihydrophenazine PCs (PC-N2, PC-N3, PC-N4) show significant intersystem crossing efficiencies. PC-N4 in toluene is an interesting

case, as in this solvent the greater S_1-state lifetime (5.31 ± 0.17 ns from TCSPC) apparently provides sufficient time for ISC to compete with radiative decay to S_0. In contrast, despite PC-N1 having S_1 lifetimes of several ns in the three solvents (only shortened to ~2 ns in DCM by electron transfer reactions with the solvent), no evidence for ISC is seen, indicating weak spin-orbit coupling and/or no accessible regions of near-degeneracy between the singlet and triplet manifolds. Higher triplet-state quantum yields are observed for the phenoxazine and phenothiazine PCs studied, which may reflect the longer S_1 lifetimes of these compounds, as well as the influence of a larger spin-orbit interaction in the sulfur-containing phenothiazine.

Sartor *et al*. recently reported a time-resolved spectroscopy study of four N-aryl phenothiazines with biphenyl core substituents.[9] They showed the importance of singlet states with CT character involving the nearly orthogonal N-aryl group in promoting ISC to a triplet state characterized by partial charge transfer to one biphenyl group. The large change in orbital angular momentum associated with the change in electron density between these nearly orthogonal molecular orbitals of CT character enhances the spin-orbit interaction.[33,34] ISC quantum yields therefore depended sensitively on the electron-withdrawing character of the N-aryl substituent, and by implication, the choice of solvent because of the influence of solvent polarity on the energies of the CT states. For measurements made in DMAc, their deduced quantum yields Φ_{ISC} were in the range 0.4 – 1.0 for N-phenyl, N-naphthyl and N-fluoro-naphthyl substituents, with the corresponding k_{ISC} values in DMAc ranging from (1.0 – 2.0) × 10^8 s^{-1}. These values are comparable to those reported for PC-S in **Table 3.5**, although the mechanism for ISC explored by Sartor *et al*. requires CT states localized on core substituents such as biphenyl groups and does not apply to PC-S which has no such core substituents. Measurements across dihydrophenazine, phenoxazine and phenothiazine PCs suggest that CT character is not a pre-requisite for ISC in these classes of compounds because triplet-state population growth is seen from S_1 states of both LE and CT character. The ISC rate coefficients are comparable, and both these and Φ_{ISC} values are sensitive to the properties of the solvent, indicating tuning of excited state energies by the environment plays an important role.

3.2.6 Structural and Solvent Effects on Excited State Lifetimes and Electronic Properties

In all the dihydrophenazine PCs studied, the S_1-state lifetimes are highly sensitive to the electron withdrawing or donating nature of the N-aryl substituents, as well as to the properties of the solvent. The excited states of the phenoxazine PCs also show sensitivity to these types

of structural and environmental change. In DCM solutions, the highly reducing excited states of these PCs facilitate electron transfer reactions with the solvent, but no such reactions shorten the S_1-state lifetimes in DMF and toluene. Instead, the different dielectric constants of the two solvents modify to greater or lesser extents the energies of the CT and LE character excited states, as do the N-aryl substituents. In the cases of PC-N3 and PC-N4, which have electron-withdrawing N-aryl substituents and hence CT-character S_1 states, the effect of solvent is most pronounced. In these two PCs, which are known to exert good control over polymer dispersity in O-ATRP,[6] the S_1 lifetimes in DMF (and DMAc) are less than 1 ns. The likelihood is that the tuning in energy of the CT states by these intramolecular and environmental influences makes efficient pathways for non-radiative $S_1 \rightarrow S_0$ decay accessible via conical intersections between the electronic states. Further investigation of this supposition requires electronic structure calculations which map the structure and energy dependences of seams of intersection between the excited and ground state potential energy surfaces. For catalysts which have short excited state lifetimes, but still demonstrate good O-ATRP control, an obvious question arises about how this control realised, as the excited state is unlikely to have a lifetime long enough to diffuse and quench by ET reaction. What may instead be occurring is that a significant proportion of reactive radicals are created by static quenching of the excited state. This mechanism would produce only a small concentration of radicals, thus allowing much greater control over polymer dispersity by reducing radical-radical side reactions and radical chain propagations.

Changes to S_1-state lifetimes have consequences for the quantum yields for ISC, because short-lived S_1 states favour relaxation within the singlet spin manifold over spin-changing dynamics. From a combination of the experimental evidence reported here for dihydrophenazine PC-N1, PC-N3 and PC-N4 photocatalysts, and experimental polymerization studies using these PCs, it is suggested that population via ISC of a long-lived triplet state of the optically excited PC is not an essential prerequisite for effective ATRP control of polymer dispersity. These and the other dihydrophenazine compounds show little or no propensity for ISC (**Table 3.5**), with the exception of PC-N2 which was reported to be an inferior PC for photoredox catalysed control of polymer dispersity in O-ATRP.[6] PC-N3 shows solvent-dependent ISC quantum yields and rate coefficients, but its S_1 lifetime in DMF is short enough to outcompete ISC. Hence, PC-N3(T_1) is unlikely to play a significant role in radical generation for O-ATRP synthesis in solvents such as DMF and DMAc.

Several photocatalysts based on a phenoxazine core are reported to show strong solvent dependence to their fluorescence spectra, indicating CT character of the emissive S_1 state.[7] TVAS and TCSPC data (**Table 3.3**) reveal singlet lifetimes of a few ns in the three solvents studied, but also a slower component to the ground-state recovery in two of the chosen phenoxazine PCs, indicating ISC to the triplet manifold of states. Reduction by electron transfer from either the S_1 or T_1 state may therefore contribute to photoredox catalysed O-ATRP activity in these two cases.

Instead of focusing on ISC propensities, this study proposes that the Gibbs energy change for the electron transfer reaction is an important metric for assessing the efficacy of these PCs in O-ATRP control, as outlined in Marcus theory and suggested in earlier work.[16,31] This argument is developed further in Chapter 4 in which supporting evidence is presented from direct measurements of intermolecular electron transfer for the nine PCs studied here. However, it should be noted that whether electron transfer occurs from the S_1 or T_1 state will influence the Gibbs energy changes and hence ET rate coefficients, and the results presented in this study unravel the PC-structure and solvent-dependent propensities for S_1 population to undergo ISC. The S_1 lifetime also appears to be an important factor for consideration, with consequences both for the propensity for diffusive intermolecular electron transfer and ISC quantum yields. In several of the PCs studied here, and more so for the dihydrophenazine derivatives, S_1-state lifetimes are controlled by non-radiative and radiative relaxation pathways to S_0, not by ISC dynamics to populate T_1.

The sensitivity of the excited-state dynamics of the various PCs to the choice of solvent raises interesting questions about the effects of the environment on PC performance in O-ATRP. Under the types of conditions used for polymer growth, the solvent is typically DMAc or DMF, but the solution also includes a significant fraction of a lower polarity monomer. As the solvent-dependent measurements reported in **Tables 3.2 – 3.5** show, the local solvation environment of a photoexcited PC in these mixed solutions will affect its S_1-state lifetime and ISC yield.

3.3 Conclusion

Study of the femtosecond to nanosecond timescale photophysical dynamics of organic molecular photocatalysts is essential to identify the electronic states that underlie their useful photocatalytic properties. This chapter reports the lifetimes and relaxation pathways of the

excited electronic states of nine representative molecular photocatalysts for O-ATRP. Time-resolved spectroscopic measurements performed with sub-picosecond time resolution in three solvents (DMF, DCM and toluene) directly explore the states involved in the photoredox behaviour of these compounds. In conjunction with quantum-chemical calculations and global kinetic fitting, the observed spectroscopic features reveal the electronic states populated upon photoexcitation and internal conversion, the efficacies for triplet state branching and ground state recovery, and their dependence on solvent. The results are consolidated with the group's previous publications on this topic to outline general photophysical principles.[16,26,27]

For solutions of dihydrophenazine PCs in DMF, catalysts possessing CT excited-state character have relatively short S_1-state lifetimes (e.g., 136 ps for PC-N3 and 500 ps for PC-N4), whereas those with LE character have longer S_1 lifetimes (e.g., 11 ns for PC-N1 and 17 ns for PC-N2). Experimental results point towards polar solvents shortening the excited state lifetimes, most likely by stabilizing the CT state energies relative to the corresponding ground states and opening non-radiative relaxation pathways via conical intersections. Detailed quantum chemical calculations should help ascertain the state-specific relaxation mechanisms in the future.

The S_1-state lifetimes range from sub-ns to a few tens of ns for all the OPCs studied. ISC is found to be a minor relaxation pathway for PCs with short-lived S_1 states. In these cases, bimolecular, excited-state electron transfer reactions must compete with the (ultra)fast intramolecular energy relaxation timescale if the PCs are to play an effective role in O-ATRP. Rapid loss of the excited state population may be partially compensated for by the high reduction potentials of the excited singlet states, which minimize activation barriers for bimolecular electron-transfer reactions. Crucially, the T_1 state need not be the sole electronic state responsible for electron transfer, as is often assumed in O-ATRP studies. Spectroscopic data with sub-picosecond time resolution underline the importance of considering both S_1 and T_1 state reduction potentials in assessing the usefulness of organic photocatalysts for ATRP. These results will further guide the design principles and applications of these general and widespread classes of PC compounds.[35,36,37]

3.4 References

1. Matyjaszewski K, Xia J. Atom Transfer Radical Polymerization. *Chem Rev* 2001, **101**(9)**:** 2921-2990.

2. Romero NA, Nicewicz DA. Organic Photoredox Catalysis. *Chem Rev* 2016, **116:** 10075−10166.

3. Treat NJ, Sprafke H, Kramer JW, Clark PG, Barton BE, de Alaniz JR*, et al.* Metal-Free Atom Transfer Radical Polymerization. *J Am Chem Soc* 2014, **136:** 16096−16101.

4. Chen M, Zhong M, Johnson JA. Light-Controlled Radical Polymerization: Mechanisms, Methods, and Applications. *Chem Rev* 2016, **116:** 10167−10211.

5. Corrigan N, Shanmugam S, Xu J, Boyer C. Photocatalysis in Organic and Polymer Synthesis. *Chem Soc Rev* 2016, **45:** 6165−6212.

6. Theriot JC, Lim C-H, Yang H, Ryan MD, Musgrave CB, Miyake GM. Organocatalyzed Atom Transfer Radical Polymerization Driven by Visible Light. *Science* 2016, **352**(6289)**:** 1082-1086.

7. McCarthy BG, Pearson RM, Lim C-H, Sartor SM, Damrauer NH, Miyake GM. Structure−Property Relationships for Tailoring Phenoxazines as Reducing Photoredox Catalysts. *J Am Chem Soc* 2018, **140:** 5088−5101.

8. Discekici EH, Pester CW, Treat NJ, Lawrence J, Mattson KM, Narupai B*, et al.* Simple Benchtop Approach to Polymer Brush Nanostructures Using Visible-Light-Mediated Metal-Free Atom Transfer Radical Polymerization. *ACS Macro Lett* 2016, **5:** 258−262.

9. Sartor SM, Chrisman CH, Pearson RM, Miyake GM, Damrauer NH. Designing High-Triplet-Yield Phenothiazine Donor−Acceptor Complexes for Photoredox Catalysis. *J Phys Chem A* 2020, **124:** 817−823.

10. Sartor SM, McCarthy BG, Pearson RM, Miyake GM, Damrauer NH. Exploiting Charge-Transfer States for Maximizing Intersystem Crossing Yields in Organic Photoredox Catalysts. *J Am Chem Soc* 2018, **140:** 4778−4781.

11. Prier CK, Rankic DA, MacMillan DWC. Visible Light Photoredox Catalysis with Transition Metal Complexes: Applications in Organic Synthesis. *Chem Rev* 2013, **113:** 5322−5363.

12. Jockusch S, Yagci Y. The Active Role of Excited States of Phenothiazines in Photoinduced Metal Free Atom Transfer Radical Polymerization: Singlet or Triplet Excited States? *Polymer Chem* 2016, **7:** 6039-6043.

13. Bressler C, Milne C, Pham V-T, ElNahhas A, van der Veen RM, Gawelda W*, et al.* Femtosecond XANES Study of the Light-Induced Spin Crossover Dynamics in an Iron(II) Complex. *Science* 2009, **323**(5913)**:** 489-492.

14. Auböck G, Chergui M. Sub-50-fs Photoinduced Spin Crossover in [Fe(bpy)3]2+. *Nat Chem* 2015, **7:** 629-633.

15. Monnia R, Capanoa G, Auböcka G, Gray HB, Vlcek A, Tavernellie I*, et al.* Vibrational Coherence Transfer in the Ultrafast Intersystem Crossing of a Diplatinum Complex in Solution. *Proc Nat Acad Sci* 2018, **115**(28)**:** 6396-6403.

16. Koyama D, Dale HJA, Orr-Ewing AJ. Ultrafast Observation of a Photoredox Reaction Mechanism: Photoinitiation in Organocatalyzed Atom-Transfer Radical Polymerization. *J Am Chem Soc* 2018, **140:** 1285−1293.

17. Ryan MD, Theriot JC, Lim C-H, Yang H, Lockwood AG, Garrison NG*, et al.* Solvent Effects on the Intramolecular Charge Transfer Character of N,N-Diaryl Dihydrophenazine Catalysts for Organocatalyzed Atom Transfer Radical Polymerization *J Polym Sci, Part A: Polym Chem* 2017, **55:** 3017−3027.

18. Lim C-H, Ryan MD, McCarthy BG, Theriot JC, Sartor SM, Damrauer NH*, et al.* Intramolecular Charge Transfer and Ion Pairing in N,N-Diaryl Dihydrophenazine Photoredox Catalysts for Efficient Organocatalyzed Atom Transfer Radical Polymerization. *J Am Chem Soc* 2017, **139:** 348−355.

19. Pearson RM, Lim C-H, McCarthy BG, Musgrave CB, Miyake GM. Organocatalyzed Atom Transfer Radical Polymerization Using N-Aryl Phenoxazines as Photoredox Catalysts. *J Am Chem Soc* 2014, **136:** 16096−16101.

20. Dadashi-Silab S, Pan X, Matyjaszewski K. Phenyl Benzo[b]phenothiazine as a Visible Light Photoredox Catalyst for Metal-Free Atom Transfer Radical Polymerization. *Chem Eur J* 2017, **23:** 5972 – 5977.

21. Miyake GM, Theriot JC. Perylene as an Organic Photocatalyst for the Radical Polymerization of Functionalized Vinyl Monomers through Oxidative Quenching with Alkyl Bromides and Visible Light. *Macromol* 2014, **47**(23)**:** 8255-8261.

22. Sartor SM, Lattke YM, McCarthy BG, Miyake GM, Damrauer NH. Effects of Naphthyl Connectivity on the Photophysics of Compact Organic Charge-Transfer Photoredox Catalysts. *J Phys Chem A* 2019, **123:** 4727−4736.

23. Wang J-S, Matyjaszewski K. Controlled/"Living" Radical Polymerization. Atom Transfer Radical Polymerization in the Presence of Transition-Metal Complexes. *J Am Chem Soc* 1995, **117**(20)**:** 5614-5615.

24. Rolland M, Whitfield R, Messmer D, Parkatzidis K, Truong NP, Anastasaki A. Effect of Polymerization Components on Oxygen-Tolerant Photo-ATRP. *ACS Macro Lett* 2019, **8**(12)**:** 1546-1551.

25. Martinez MR, Sobieski J, Lorandi F, Fantin M, Dadashi-Silab S, Xie G*, et al.* Understanding the Relationship between Catalytic Activity and Termination in PhotoATRP: Synthesis of Linear and Bottlebrush Polyacrylates. *Macromol* 2020, **53**(1)**:** 59-67.

26. Lewis-Borrell L, Sneha M, Bhattacherjee A, Clark IP, Orr-Ewing AJ. Mapping the Multi-Step Mechanism of a Photoredox Catalyzed Atom-Transfer Radical Polymerization Reaction by Direct Observation of the Reactive Intermediates. *Chem Sci* 2020, **11**(17)**:** 4475-4481.

27. Sneha M, Lewis-Borrell LJ, Shchepanovska D, Bhattacherjee A, Tyler JL, Orr-Ewing AJ. Solvent-Dependent Photochemical Dynamics of a Phenoxazine-Based Photoredox Catalyst. *Z Phys Chem* 2020, **234:** 1475 – 1494

28. Chaudhuri S, Rudshteyn B, Prémont-Schwarz M, Pines D, Pines E, Huppert D*, et al.* Ultrafast Photo-Induced Charge Transfer of 1-Naphthol and 2-Naphthol to Halocarbon Solvents. *Chem Phys Lett* 2017, **683:** 49–56.

29. Grubb MP, Orr-Ewing AJ, Ashfold MNR. KOALA: a Program for the Processing and Decomposition of Transient Spectra. *Rev Sci Instrumen* 2014, **85**(6)**:** 064104.

30. Turro NJ, Ramamurthy V, Scaiano JC. Modern Molecular Photochemistry of Organic Molecules. *University Science Books: Mill Valley, CA* 2010.

31. Pan X, Fang C, Fantin M, Malhotra N, So WY, Peteanu LA*, et al.* Mechanism of Photoinduced Metal-Free Atom Transfer Radical Polymerization: Experimental and Computational Studies. *J Am Chem Soc* 2016, **138:** 2411−2425.

32. Theriot JC, McCarthy BG, Lim C-H, Miyake GM. Organocatalyzed Atom Transfer Radical Polymerization: Perspectives on Catalyst Design and Performance. *Macromol Rapid Commun* 2017, **38:** 1700040.

33. Benniston AC, Harriman A, Li P, Rostron JP, van Ramesdonk HJ, Groeneveld MM*, et al.* Charge Shift and Triplet State Formation in the 9-Mesityl-10-methylacridinium Cation. *J Am Chem Soc* 2005, **127**(46)**:** 16054-16064.

34. Dance ZEX, Mickley SM, Wilson TM, Ricks AB, Scott AM, Ratner MA*, et al.* Intersystem Crossing Mediated by Photoinduced Intramolecular Charge Transfer: Julolidine−Anthracene Molecules with Perpendicular π Systems. *J Phys Chem A* 2008, **112**(18)**:** 4194-4201.

35. Enciso AE, Fu L, Russell AJ, Matyjaszewski K. A Breathing Atom-Transfer Radical Polymerization: Fully Oxygen-Tolerant Polymerization Inspired by Aerobic Respiration of Cells. *Angew Chem Int Ed* 2018, **57:** 933-936.

36. Luca Buzzetti L, Crisenza GEM, Melchiorre P. Mechanistic Studies in Photocatalysis. *Angew Chem Int Ed* 2019, **58**(12)**:** 3730-3747.

37. Orr-Ewing AJ. How can Ultrafast Laser Spectroscopy Inform the Design of New Organic Photoredox Catalysts for Chemical and Materials Synthesis? . *Struct Dyn* 2019, **6:** 010901.

4 Structure-Dependent Electron Transfer Rates for Dihydrophenazine, Phenoxazine and Phenothiazine Photoredox Catalysts Employed in Atom Transfer Radical Polymerization‡

4.1 Introduction

Atom transfer radical polymerization (ATRP) is a controlled polymerization method which exploits electron transfer (ET) processes leading to activation and deactivation of growing polymer chains.[1,2,3,4] In ATRP, an organic radical is formed by a dissociative electron transfer reaction involving a catalyst and an initiator, often an organohalide. This radical reacts with alkene monomers to grow polymers. Deactivation involves the regeneration of the catalyst by a reverse electron transfer process which terminates further radical addition steps. These sequential processes are shown schematically in **Figure 4.1**. While ATRP has been a popular method for polymer synthesis since its inception in 1995,[2,3] a surge in applications of photoredox catalysis in synthetic organic chemistry[5,6,7] has steered research developments in ATRP in new directions. The first development exploited the benefit that, in photoredox

‡Previously published in: M. Sneha, A. Bhattacherjee, L. Lewis-Borrell, I. P. Clark, and A. J. Orr-Ewing, *J Phys Chem B* **2021** *DOI:* 10.1021/acs.jpcb.1c05069.

And: L. Lewis-Borrell, M. Sneha, A. Bhattacherjee, I. P. Clark, and A. J. Orr-Ewing, *Chem Sci* **2020**, 11, 4475-4481.

The writer is the co-first author of the referenced manuscripts and: has prepared all the samples in the lab of Prof. Varinder Aggarwal (University of Bristol, School of Chemistry) with additional help from Jasper Tyler; has collected transient absorption spectroscopy data with Dr. Aditi Bhattacherjee, Dr. Mahima Sneha (University of Bristol, School of Chemistry, Prof. Andrew Orr-Ewing group), and Ian P. Clark (Central Laser Facility, Research Complex at Harwell, Science and Technology Facilities Council, Rutherford Appleton Laboratory); has discussed and written the manuscript in cooperation with Dr. Aditi Bhattacherjee, Dr. Mahima Sneha and the principal investigator, Prof. Andrew Orr-Ewing.

catalysis, photoinduced ET provides an activation mechanism. The excited states of traditional transition-metal based catalysts were used to drive ET rather than their ground states, thereby exploiting the greater excited-state oxidizing/reducing potentials. Fors and Hawker first demonstrated this strategy by using *fac*-[Ir(ppy)$_3$] as a photocatalyst (PC) for polymerization of methacrylates.[8]

However, the problems of toxicity and scarcity associated with transition-metal based catalysts have refocussed development towards organic dyes as alternative photocatalysts for organocatalyzed ATRP (O-ATRP). The use of organic dyes as photocatalysts has simultaneously gained popularity in multiple fields of synthetic organic chemistry benefiting from photoredox catalysis strategies.[9] Seminal work by Fukuzumi, Nicewicz and others has shown application of organic PCs in accelerating a range of reactions of synthetic utility.[10,11,12,13,14,15,16,17,18,19] Hawker and Matyjaszewski separately demonstrated the use of N-aryl phenothiazines as PCs for O-ATRP.[20,21,22] In recent years, Miyake and co-workers have extended the list of O-ATRP catalysts by introducing a plethora of new N,N-diaryl dihydrophenazine, N-aryl phenoxazine and N-aryl phenothiazine catalysts, with varying degrees of control over polymer molecular weights and dispersity.[23,24,25,26,27,28,29] Kwon and co-workers have also introduced several new organic photocatalysts for O-ATRP, as well as for other controlled polymerization methods.[30,31]

Continuing progress with the design of organic PCs raises the question of what makes an organic dye molecule a good candidate to be an O-ATRP catalyst. For an oxidative quenching cycle, as is the case for most photoredox based ATRP cycles, key requirements are to have a highly reducing PC* (S_1/T_1) excited state which can reduce an alkyl halide radical initiator, and a high oxidizing potential for the $PC^{\bullet+}$ radical cation, such that the growing polymer is efficiently deactivated. Currently, many of these catalysts are designed using principles deriving from transition-metal based photocatalysts, with metal-to-ligand charge transfer (MLCT) character in the excited state, and ultrafast intersystem crossing (ISC) populating long-lived, reducing or oxidizing T_1 states, leading to efficient ET. The organic PC equivalent of this MLCT character is an excited state involving charge transfer from the chromophore moiety to pendant groups such as aryl rings. Miyake and co-workers have reported that O-ATRP catalysts with excited electronic states of CT-character are generally better at controlling polymer dispersity and molecular weights, compared to the PCs which have locally excited (LE) character in which the electron density remains localized on the chromophore moiety

orbitals. They suggested that the CT character in these catalysts promotes ISC and therefore more efficient bimolecular electron transfer.[23,32]

Subsequent photophysical studies by Damrauer and co-workers using transient absorption spectroscopy measurements showed that indeed many of these catalysts with CT character in their S_1 states undergo efficient ISC.[27,28] They invoked spin-orbit charge-transfer ISC to account for this behaviour: PCs with CT-character S_1 states and orthogonally oriented donor and acceptor moieties can undergo efficient ISC because a significant change in orbital angular momentum promotes a change in spin angular momentum.[26,27,28,33,34] However, previous reports, presented in Chapter 3, question the generality and benefits of these photophysical properties on two fronts. First, at least two of the N,N-diaryl dihydrophenazine catalysts previously reported to have CT character in their S_1 states (PC-N3 and PC-N5, shown in **Figure 4.1**), and which exert good ATRP control, do not undergo significant ISC.[35,36] The inefficient ISC might be because of short-lived excited singlet states, particularly in solvents such as N,N-dimethylformamide (DMF) which is one of the preferred solvents for O-ATRP.[36,37] Second, transient vibrational and electronic absorption spectroscopy (TVAS and TEAS) measurements show that some of the LE-character catalysts can also undergo efficient ISC, although they are reported to be poor at controlling polymerization.[38]

Although they display a range of photophysical attributes, catalysts with excited-state CT-character as a class seem to outperform their LE counterparts in controlling polymer dispersity.[23,39] To resolve why that is the case, both activation and deactivation ET steps must be examined. However, mechanistic investigations of these steps have been fewer in number compared to the photophysical studies. One of the first mechanistic investigations involving organic PCs in ATRP was by Matyjaszewski and co-workers; using a combination of computational studies, laser flash photolysis and cyclic voltammetry measurements, they examined both activation and deactivation mechanisms in some N-aryl phenothiazines and other organic PCs.[20] Koyama *et al.* studied both the photophysics and the ET activation step for 5,10-bis(4-trifluoromethylphenyl)-5,10-dihydrophenazine (PC-N3, previously called PCF, and shown in **Figure 4.1b)** and 5,10-bisphenyl-5,10-dihydrophenazine (PC-N2, previously called PCH) using TVAS and TEAS.[36] These investigations, in combination with a recently published study on another N,N-diaryl dihydrophenazine catalyst (PC-N5, previously called PCBN),[37] showed that for PC-N3 and PC-N5, both of which have CT excited-state character and are reported to be good ATRP photocatalysts, negligible ISC was observed in DMF

solution. These studies therefore suggest that the ET happens from these PCs in their highly reducing S_1 states. Moreover, comparison of the electron transfer steps for the three PCs shows that the rates are not dominated by their CT or LE character. The trends in the rates can instead be accounted for by Marcus-Savéant theory,[40] and depend on the Gibbs energies of the PC*(S_1) and $PC^{\bullet+}$(D_0) species.

Previous mechanistic studies have largely focussed on investigating structural modifications within a single class of catalysts. Here, a systematic study is presented of nine PCs chosen from the various N, N-diaryl dihydrophenazine, N-aryl phenoxazine, and N-aryl phenothiazine PCs, with the structures shown in **Figure 4.1b**. The new measurements of the rates of electron transfer reactions use the complementary techniques of TEAS and TVAS. The chosen compounds have been reported as O-ATRP catalysts exerting varying degrees of control over polymer dispersity and molecular weights. Some show LE characteristics (PC-N1, PC-N2, and PC-O1), while others display CT characteristics in their excited states.[23,24,25,41] Although most of the chemical modifications are to the N-aryl groups, PC-O3 is chosen as an example of a core-modified PC. TEAS and TVAS data for three of these catalysts (PC-N2, PC-N3, and PC-N5) were reported in previous publications,[36,37] but the results are incorporated and extended here to provide a consolidated picture of the structural dependence of PC performance.

Using the LIFEtime laser facility at the Rutherford Appleton Laboratory, TVAS measurements have been obtained over time delays extending from 1 ps to tens of microseconds.[42] This broad range of time delays with ultrafast (1 ps) resolution allowed observation of the complete photochemistry of these molecules in a single continuous measurement, from the initial population of the relatively short-lived S_1 states to ISC into longer-lived triplet states and subsequent steps in the photoredox cycle.[43,44] Findings on the solvent-dependent photodynamics of these PCs in the absence of electron-accepting polymerization initiators are reported in Chapter 3.[45] In this chapter, the focus is directed towards the activation step of the O-ATRP process and the subsequent radical reaction with an alkene (exemplified using PC-N5).[35,46] In the activation step, ET occurs from the excited states (PC*) of these PCs to an alkyl halide radical initiator, methyl 2-bromopropionate (MBP).

$$PC^*(S_1/T_1) + MBP \rightarrow PC^{\bullet+}(D_0) + MP^{\bullet}(D_0) + Br^- \quad (50)$$

The reactivity of these PCs from their S_1 and/or T_1 states is investigated in three solvents, toluene (toluene-d_8 for TVAS), dichloromethane (DCM) and DMF, with values for the second

order rate coefficients derived for bimolecular electron transfer reactions. To explain the difference between their reactivities, the "sticky" model of dissociative electron transfer is employed.[20] The model shows that irrespective of their chemical class, the LE catalysts undergo faster ET than their CT counterparts. For PCs with significant T_1 populations, ET is efficient from both S_1 and T_1 states at synthetically relevant concentrations of the PC and MBP. However, efficient ISC is not required for a PC to be an effective O-ATRP catalyst.

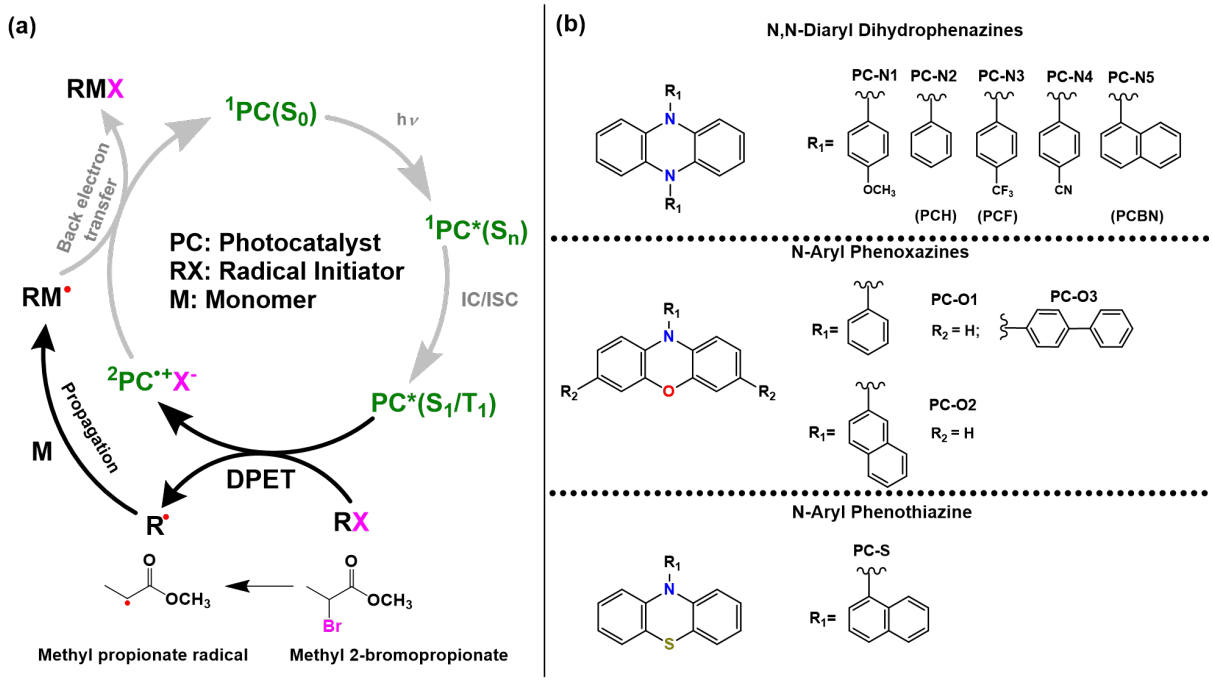

Figure 4.1. A photoredox cycle and the photocatalysts for atom transfer radical polymerization (ATRP) studied in this work. (a) Photoredox cycle operative in the ATRP process. The dissociative photoinduced electron transfer (DPET) activation and propagation steps which are the focus of this chapter are highlighted in black; (b) Structures of the organic PCs studied in this work, and the naming scheme used throughout. Abbreviations in parentheses are the labels used in prior publications.

4.2 Results and Discussion

4.2.1 Steady State Characterization.

The choice of UV or visible photoexcitation wavelength of the PCs requires knowledge of their electronic absorption spectra, and interpretation of TVAS measurements benefits from identification of ground-state IR bands of the PCs. Steady state characterization of solutions of the photocatalysts (by UV-Vis, FTIR and fluorescence spectroscopy) in the three chosen solvents was therefore undertaken and the outcomes are reported in Experimental Section.[45] As the focus of the work reported in this Chapter was on studying the electron transfer reaction between the excited state PCs and MBP, it was important to characterize the resulting intermediates from reaction (1). While the short-lived MP• radicals are hard to characterize by steady state methods, $PC^{\bullet+}$ can be prepared in solution by the oxidation of the PCs in their

ground state using a concentrated $FeCl_3$ solution.[36] The resulting FTIR and UV spectra are shown in the Supporting Information **Figures E3** and **E4**. The UV-Vis spectra of all the oxidized PC solutions show a band shifted to longer wavelengths than the first PC(S_0) absorption band (300-400 nm) and appearing in the region between 400 and 600 nm, which is assigned to the PC radical cation, $^2PC^{\bullet+}(D_0)$.

4.2.2 Tracking Reactive Intermediates.

The electron transfer reactions between excited states of the photocatalysts and the radical initiator MBP were tracked using the complementary methods of transient vibrational and electronic absorption spectroscopies.

4.2.2.1 TVAS Measurements.

The TVAS data shown in this study were collected at the LIFEtime facility at the RAL. This laser system allowed these reactions to be followed over time delays after photoexcitation ranging from 1 ps to beyond 10 μs. In TVAS data, the mid-IR region between 1450 and 1700 cm^{-1} was used as a probe because it covered IR bands associated with both the ring modes of the catalysts and the CO stretching region, allowing PC*, PC, $MP^{\bullet}$ and $PC^{\bullet+}$ vibrational signatures to be tracked simultaneously. Prior to studying the electron transfer step, the TVA spectra of all the PCs shown in **Figure 4.1b** were measured in DCM, DMF and toluene-d_8 to characterize the PC excited state dynamics in the absence of an electron acceptor. A detailed account of this work is reported in Chapter 3,[45] but for illustrative purposes an example set of TVA spectra for PC-S in DCM (with no added MBP) is shown in **Figure 4.2a**. The spectra show a strong ground state bleach (GSB) centred at 1465 cm^{-1} and corresponding to depletion of PC-S (S_0) by photoexcitation, as well as two excited state absorption (ESA) bands of PC-S* (S_1) centred at 1495 cm^{-1} and 1530 cm^{-1} and two weaker GSB features at 1573 and 1591 cm^{-1}. The kinetic traces obtained by fitting Gaussian functions to the GSB and ESA features at 1465 and 1495 cm^{-1} respectively, are shown in **Figure 4.2b**. The kinetics identify a biexponential recovery for the GSB with time constants of 3.9 ± 0.3 ns and 50.4 ± 3.2 ns (with one standard error uncertainties derived from the exponential fits). The first time constant, which can be globally fitted to the ESA decay as well, is assigned to the decay of population of the S_1 state of PC-S, either by relaxation to the ground state through radiative and non-radiative processes, or by populating triplet states through intersystem crossing. The second time constant is assigned to the lifetime of the T_1 state. The triplet lifetimes of these catalysts, which were previously reported to be several μs by Sartor *et al.*,[27,28] are sensitive to the presence of

dissolved oxygen, and 50 ns is a lower limit to the T_1 lifetime of PC-S because of residual oxygen in the samples. The TVA spectra of the other PCs (**Figure 4.1b**) show similar features to PC-S with varying degrees of ISC quantum efficiency, and different excited state lifetimes which also depend to a great extent on the solvent. **Table 4.1** summarizes the PC*(S_1) lifetimes and triplet quantum yields for all the PCs, the derivations of which have been reported in Chapter 3.[45]

To follow the ET reaction, MBP was added in increasing concentrations to a PC solution in DCM. As can be seen in **Figure 4.2c**, with the addition of MBP the TVA spectra change in four distinct ways: (1) a band centred at 1660 cm^{-1} arises which is assigned to $^2MP^{\bullet}(D_0)$ based on previous work;[36] (2) the decay of the PC-S* (S_1) ESA bands becomes faster; (3) A peak corresponding to PC-S radical cation ($PC\text{-}S^{\bullet+}$) appears at 1536 cm^{-1} (See **Figure E3** for support of this assignment from steady state oxidation experiments with $FeCl_3$), shifted to higher wavenumber than the PC*(S_1) ESA feature; (4) all the GSB features (centred at 1465 cm^{-1}, 1573 cm^{-1} and 1591 cm^{-1}) show incomplete recovery on the timescales reported here. In the case of solutions in DMF, the strong solvent absorption allowed only a narrow window of observation in the mid-IR probe region, thus showing only the decay of the PC* ESA and the growth of the $PC^{\bullet+}$ absorption band, as can be seen in **Figure E21** to **E24**.

The changes in intensity of the bands assigned to the $^2MP^{\bullet}(D_0)$ radical, PC-S* (S_1) ESA, $PC\text{-}S^{\bullet+}(D_0)$, and PC-S($S_0$) GSB at 1465 cm^{-1} can be globally fitted to obtain a single exponential time constant as shown in **Figure 4.2d**. For this dataset, the time constant is 1.08 ± 0.04 ns. As this time constant is shorter than the S_1 state lifetime in the absence of MBP, it is evident that at the concentration of MBP used (~100 equivalents of [PC]) most of the electron-transfer reactions between PC* and MBP happen from the PC*(S_1) state for PC-S. Note that the distinctive band for a $PC^{\bullet+}MBP^{\bullet-}$ complex is not observed, in accord with the work of Koyama *et al.*,[36] showing that within the experimental time resolution the C-Br bond promptly dissociates to make the $MP^{\bullet}$ radical, a Br^- ion and the $PC^{\bullet+}$ cation. Indeed, dissociative electron transfer to alkyl halides is a widely observed phenomenon and is well characterized. [47]

The features evident in the spectra in the region 1400-1700 cm^{-1} again do not change markedly between the various N,N-diaryl dihydrophenazine, N-aryl phenoxazine and N-aryl phenothiazine catalysts reported in this study. Full sets of TVA spectra for each of the PCs with MBP in DCM, DMF and toluene-d_8 are shown in the Experimental Section (**Figures E21** to **E29**). An exceptional case arises for PC-N4, where no reaction is observed between

photoexcited PC-N4* and MBP in any of the solvents, even at the higher concentrations of MBP (up to 2 M). Interestingly, PC-N4 which has CT character in both its S_1 and T_1 state, is reported to be a good O-ATRP catalyst for control over polymer dispersity. It is not surprising that no reactivity is observed in the timescales used here (up to 10 μs) from the PC-N4*(S_1) state in DCM and DMF because the S_1 lifetimes are short in these solvents (500 ps in DCM, and 135 ps in DMF) and there is no evidence for ISC to populate the T_1 state.[45] However, in toluene-d_8, the PC behaves very differently, with an S_1 state lifetime of 5.7 ns and significant population of a long lived T_1 state ($\Phi_{ISC} = 0.57$). Hence, reaction between PC-N4* and MBP in toluene-d_8 might be expected. Interestingly, with the addition of MBP at concentrations as low as 0.2 M (and at a 5 mM PC-N4 concentration) precipitate is formed in the solution upon photoexcitation, which may originate from the formation of a PC-N4$^+$Br$^-$ salt.

Experiments conducted with PC-N1 or PC-O1 in DCM without MBP show incomplete recovery of the GSB features as well as the growth of PC$^{\bullet+}$ peaks. These observations are attributed to the reaction between photoexcited PC*(S_1) and DCM, consistent with prior reports of reaction of certain excited organic chromophores with halogenated solvents.[38,48] Nevertheless, in the presence of MBP, electron transfer to this acceptor is faster than to the solvent, even at low MBP concentrations.

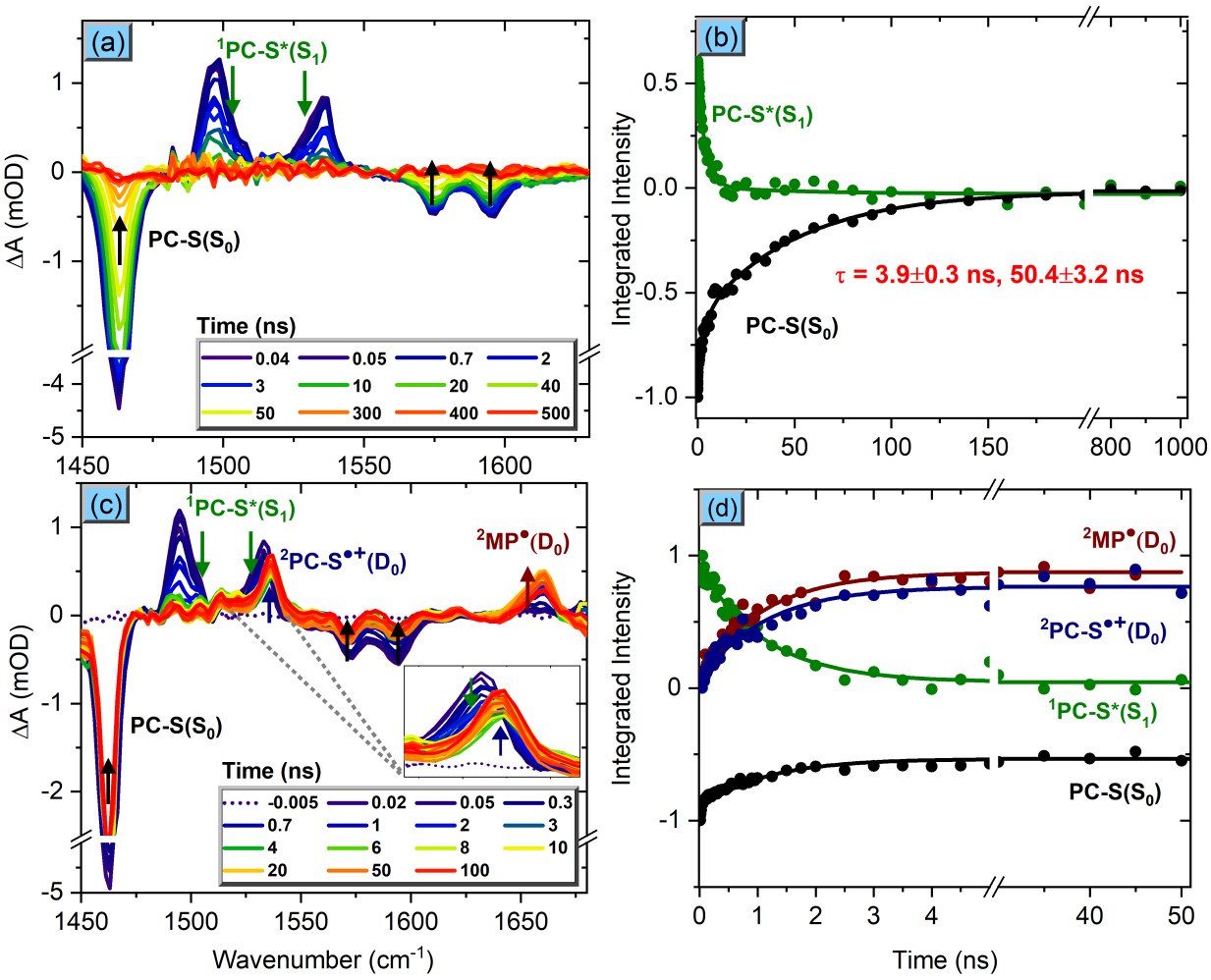

Figure 4.2. *TVAS measurement of PC-S in DCM without and with the electron acceptor MBP. (a) TVA spectra of 7.5 mM PC-S in DCM shown in the wavenumber range of 1450-1680 cm^{-1}; (b) Kinetic traces of PC-S*(S$_1$) and PC-S(S$_0$) band intensities in the absence of MBP (circles) and their single and biexponential fits (solid lines). The first time constant (3.9 ± 0.3 ns) is assigned to the S$_1$ state lifetime, and the second time constant (50.4 ± 3.2 ns) is assigned to quenching of T$_1$ state population by dissolved O$_2$ (with one standard error uncertainties derived from the exponential fits); (c) TVA spectra of PC-S with 0.8 M MBP; (d) Normalized kinetic traces of ^{2}MP$^\bullet$(D$_0$), ^{1}PC-S*(S$_1$), ^{2}PC-S$^{\bullet+}$(D$_0$) and ^{1}PC-S(S$_0$) band intensities, which were obtained by fitting Gaussian functions to the labelled bands in the TVA spectra in panel (c). Solid lines show a global fit of the data to single exponential functions, giving a common time constant of 1.08 ± 0.04 ns. Arrows in panels (a) and (c) are colour coded to their labels and show the directions of change for the associated peaks.*

At the sub-molar concentrations of MBP used in the current study, the ET occurs primarily from the PC*(S$_1$) states, but this behaviour does not rule out the possibility of reaction from the longer-lived PC*(T$_1$) states at lower concentrations of MBP where diffusive encounters are less frequent. However, the absence of observable triplet bands in the probe spectral range for most PCs makes it difficult to observe triplet state reactivity. For example, computational data previously reported for PC-O1 showed that the triplet bands were either weak or shifted from the IR probe window of 1400-1700 cm^{-1}.[38] The decay of intensity of such bands caused by electron transfer to MBP would provide a direct measure of the rate of electron transfer from the T$_1$ state. For PC-O2 a triplet band at 1482 cm^{-1} is observed and analysis of the ET seen using this band is discussed in section 4.2.4.

Table 4.1. *Lifetimes (ns) of the S_1 States of the Studied PCs in DMF, DCM, and Toluene-d_8 Solutions and Intersystem Crossing Quantum Yields (Φ_{ISC}).*[(a),(b)]

Catalyst	***Lifetime (ns) and ISC quantum yield***		
	DMF	**DCM**	**Toluene-d_8**
PC-N1	38.5 ± 1.3	2.2 ± 0.1	11.7 ± 0.2
PC-N2 [(c)]	16.8 ± 2.0 Φ_{ISC} = 0.71	2.8 ± 0.4	25.5 ± 7.6 Φ_{ISC} = 0.82
PC-N3 [(c)]	0.635 ± 0.022	2.9 ± 0.1 Φ_{ISC} = 0.19	3.07 ± 0.24 Φ_{ISC} = 0.60
PC-N4	0.135 ± 0.003	0.51 ± 0.03	5.7 ± 0.3 Φ_{ISC} = 0.57
PC-N5 [(c)]	5.2 ± 0.4	17 ± 1 Φ_{ISC} = 0.14	25 ± 1
PC-O1 [(c)]	2.1 ± 0.1 Φ_{ISC} = 0.84	1.5 ± 0.2 Φ_{ISC} = 0.43	2.4 ± 0.2 Φ_{ISC} = 0.56
PC-O2	8.6 ± 1.2 Φ_{ISC}= 0.74	6.4 ± 0.3 Φ_{ISC} = 0.56	2.4 ± 0.3 Φ_{ISC} = 0.70
PC-O3	3.3 ± 0.4	2.57 ± 0.05	2.4 ± 0.3
PC-S	5.9 ± 0.6 Φ_{ISC} = 0.37	3.8 ± 0.2 Φ_{ISC} = 0.63	1.77 ± 0.08 Φ_{ISC} = 0.57

(a) The ISC quantum yield is given for PCs with non-zero ISC efficiencies.
(b) More detailed descriptions of the photodynamics of these PCs are reported in Chapter 3 and ref [45].
(c) S_1 lifetime values previously reported by Koyama *et al.* [36], Sneha *et al.*[38] and Lewis-Borrell *et al.*[37]

4.2.2.2 TEAS Measurements.

As with the TVAS measurements, TEAS spectra were first collected for the PC in solution without an added electron acceptor. These spectra and their analysis are reported in Chapter 3 and the Experimental Section, and **Table 4.1** summarizes the relevant excited state lifetime data.[45] The reactions between MBP and the photoexcited PC* were then followed by observing the changes in the transient spectra upon addition of MBP. **Figure 4.3** shows examples of such

TEA spectra for PC-N1 with 2.0 M MBP in DCM and DMF solutions. As is evident from the figure, in both solvents the broad double-peaked spectra seen at early times decay, giving rise to a narrower, slightly structured absorption feature centred at 470 nm. The early time spectra are assigned to a combination of PC*(S_n) and PC*(S_1) ESAs, and the late time spectra to the PC-N1$^{\bullet+}$(D_0) cation on the basis of the steady-state UV-Vis spectra obtained by oxidation of the PCs using $FeCl_3$ (see Experimental Section **Figure E3**). The PC-N1$^{\bullet+}$ band changes only slightly between DCM and DMF solutions. However, while the structure of the PC-N1$^{\bullet+}$ absorption band measured by TEAS in DMF closely resembles the steady state absorption spectrum of PC-N1$^{\bullet+}$ (**Figure E3**), the band structures in DCM differ. One explanation could be that in DCM, some of the PC-N1$^{\bullet+}$ forms a complex with Br^-, giving a slightly shifted absorption to that of the free form. Panels 3(b) and (d) show the kinetic traces obtained by decomposing the TEAS data into contributions from an early time basis function (taken from TEA spectrum of PC-N1 in DCM without MBP at 50 ps and attributed to PC*(S_1) ESA) and a PC$^{\bullet+}$ spectral basis function corresponding to the late time spectrum recorded at 1200 ps for each solvent.

The time evolutions of the fits of TEA spectra to these basis functions are shown in **Figures E31-E32** of the Experimental Section. The kinetic traces for decay of PC*(S_1) ESA and growth of PC$^{\bullet+}$ absorption can be globally fitted to biexponential functions. As no triplet state population was observed for PC-N1 in DCM or DMF, and the internal conversion from PC*(S_n) to PC*(S_1) takes only ~4 ps, the electron transfer to MBP is inferred to occur from the PC-N1*(S_1) state. Moreover, in DMF the PC-N1*(S_1) state has a lifetime of ~40 ns, whereas the ET happens with a time constant of ~112 ps for a 2.0 M MBP concentration, showing that ET outcompetes relaxation back to the ground state. This fast electron transfer is investigated further in section 4.2.3.1.

The TEAS measurements for the other studied PCs with MBP are shown in the Experimental Section (**Figures E21-E30**). In contrast to the TVAS data, the TEA spectra do show significant changes in observed bands for different PCs; however, for most cases and at the concentrations of MBP used as discussed in section 4.2.3.1, reactivity is only seen from the PC*(S_1) state. This apparent specificity could be for two reasons: (1) with the exception of PC-O1, no clear signatures are seen for ESA from a PC*(T_1) state in collected TEAS data. Even for PC-O1, the formation of PC$^{\bullet+}$ is seen almost concurrently with the rise of the PC*(T_1) absorption band, which indicates that PC-O1$^{\bullet+}$ originates from reaction in the S_1 state. (2) The TEAS

measurements are limited to reaction times up to ~1.3 ns, which makes it difficult to observe reactivity from the T_1 state.

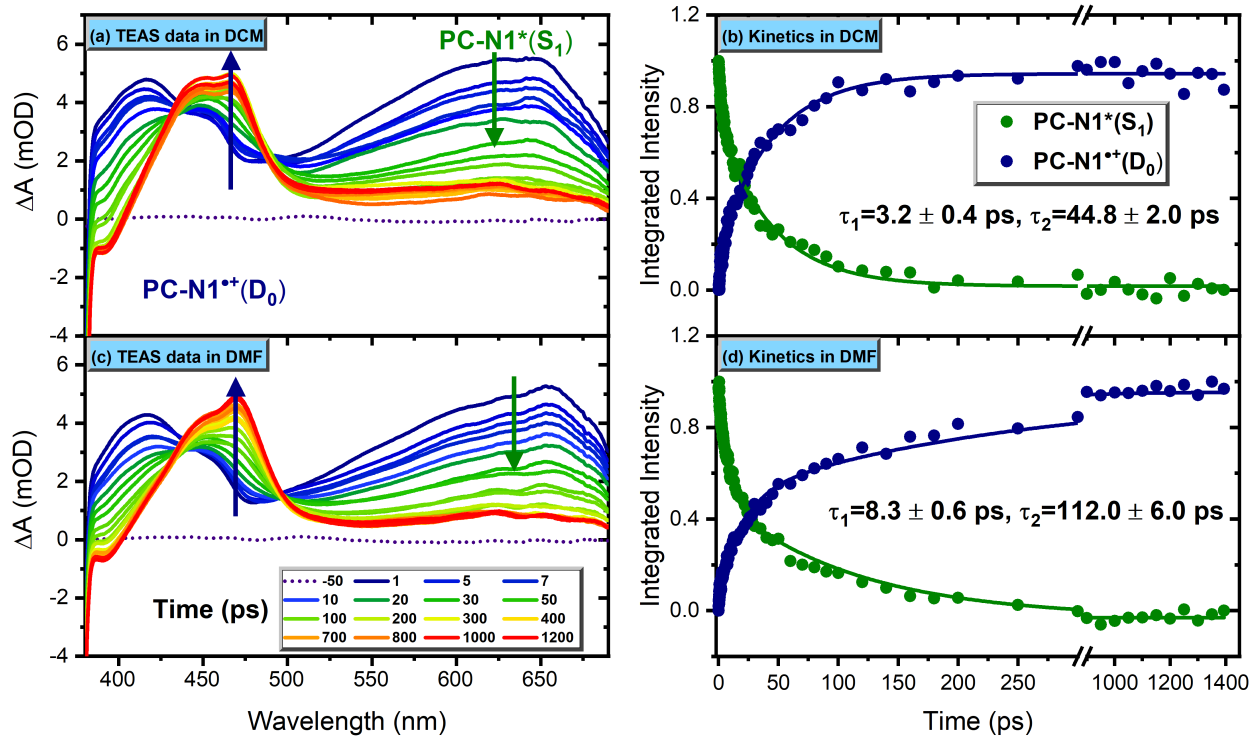

Figure 4.3. *TEAS measurement of reaction of 2.5 mM PC-N1 with 2.0 M MBP. The excitation wavelength was 370 nm and the WLC probe spanned a wavelength range from 340-700 nm. (a) TEA spectra in DCM; (b) kinetic traces for PC-N1* (S_1) and PC-N1$^{\bullet+}$ in DCM obtained using spectral decomposition methods described in the main text; (c) TEA spectra in DMF; (d) kinetic traces of PC-N1*(S_1) and PC-N1$^{\bullet+}$ in DMF. Arrows in (a) and (c) show the directions of change of the electronic bands. For each solvent, the kinetic traces were globally fitted to biexponential functions (solid lines) to account for both static and dynamic reactive quenching of the PC-N1*(S_1) state at this concentration of MBP (see text).*

4.2.3 Rates of Electron Transfer.

The rates of electron transfer between the various PC*(S_1/T_1) and MBP can be determined either by following the growth of the product MP$^{\bullet}$ radical and PC$^{\bullet+}$ absorption bands, or the PC* ESA-band decays in both TEAS and TVAS data (note that the MP$^{\bullet}$ radical is not observed in TEAS). The latter method is equivalent to a Stern-Volmer analysis. Each of these approaches is discussed below, as is the determination of bimolecular rate coefficients for ET by either a pseudo-first order kinetic model or fitting to a diffusional kinetic model based on Smoluchowski theory.

4.2.3.1 Dynamic vs Static Quenching

At low concentrations of MBP (≤0.4 M), the intermolecular electron transfer reactions between an electron donor (PC*) and electron acceptor (MBP) can be treated as requiring diffusional encounters, with single-exponential kinetics in the pseudo-first order regime of [MBP]>>[PC*]. However, at higher sub-molar concentrations of the MBP radical initiator, a

significant fraction of the PC may exist in close proximity to an MBP co-solute, trapped within a solvent cage. This fraction can potentially undergo prompt electron transfer upon photoexcitation without the need for diffusive encounters, which is referred to as static quenching.[49] Under these conditions, electron transfer processes will deviate from single exponential kinetics, and to a first approximation can be treated as biexponential with the larger rate coefficient assigned to the static quenching and the smaller rate coefficient associated with diffusional quenching. The TEAS measurements shown in **Figure 4.3** illustrate these biexponential ET kinetics of PC-N1*(S_1) with MBP; fitting gives two time constants for the ET reaction, 8.3 ± 0.6 ps for static quenching and 112 ± 6 ps for the diffusional quenching component in DMF. When the data show significant deviations from mono-exponential behaviour, they are fitted to biexponential kinetics and the second time constant is used to extract the dynamic/diffusional rate coefficients for electron transfer, as reported in **Table 4.2**. In the following sections, a pseudo first order kinetic model is developed for the diffusive electron transfer process through analysis of PC*(S_1) decay or $MP^{\bullet}$ growth.

Vauthey and co-workers instead described application of a Smoluchowski model of diffusive reactions which takes into consideration the time-dependent rate coefficient as the rate switches from the static limit to the dynamic limit.[49] Kinetic modelling of the data using Smoluchowski theory is discussed in Chapter 2 and results are reported in **Table 4.3**, where rate coefficients obtained with those from single or biexponential kinetic fitting are compared. The two analysis methods are found to be in satisfactory agreement, with the exception of PC-N1 solutions in DCM and toluene, for which Smoluchowski model rate coefficients are reported in **Table 4.3**.

Figures E48 to **E64** show kinetic fits for PCs PC-N1, PC-O1, PC-O2, PC-O3 and PC-S using either the single or bi-exponential fitting procedure or the above-mentioned Smoluchowski model where appropriate. The inset in each figure shows the linear dependence of extracted *k'* values on c_0 = [MBP]. **Table 4.2** compares the use of the two models for deriving electron transfer rate coefficients for reactions between PC*(S_1) and MBP in DCM. The good match between the bimolecular rate coefficients obtained by biexponential and Smoluchowski fits indicates that rate coefficients obtained via single/biexponential fits satisfactorily determine the diffusive electron transfer rate coefficients. An exception however exists for PC-N1, where the biexponential method gives a rate coefficient much larger than the diffusion-limited rate coefficient in DCM ($1.5 \times 10^{10}\ M^{-1}s^{-1}$ at 20 °C),[50] with $k_{ET} = 5.6 \times 10^{10}\ M^{-1}s^{-1}$,

whereas the Smoluchowski model fits the data better and gives a more reasonable value of $2.4 \times 10^{10}\ M^{-1}s^{-1}$.

Table 4.2. *Comparison of bimolecular electron transfer rate coefficients for the reaction between PC*(S_1) and MBP in DCM analysed via exponential kinetic modelling and the Smoluchowski model.*

Catalyst	Exponential k_{ET} / (10^9 M^{-1} s^{-1})	Smoluchowski k_{ET} / (10^9 M^{-1} s^{-1})
PC-N1	56 ± 6	24 ± 2
PC-N2 [a]	20 ± 2	-
PC-N3 [a]	4.4 ± 0.3	2.5 ± 0.1
PC-N5 [b]	2.6 ± 0.3	2.3 ± 0.1
PC-O1	21 ± 3	12 ± 1
PC-O2	1.0 ± 0.1	1.1 ± 0.1
PC-O3	4.1 ± 0.2	2.2 ± 0.1
PC-S	1.4 ± 0.1	0.9 ± 0.2

a. Exponential rate coefficients reported by Koyama *et al.*[36]
b. Value reported previously by Lewis-Borrell *et al.*[37]

4.2.3.2 PC* Quenching

Following photoexcitation from the PC(S_0) state to a higher lying singlet state, the PC*(S_n) state rapidly internally converts and relaxes to the PC*(S_1) state. The population in the PC*(S_1) state can undergo unimolecular decay either by radiative and non-radiative relaxation to the ground state or through ISC to the triplet manifold of states, with decay rate coefficients k_R and k_{ISC} respectively, as shown in equations 1 and 2. Rapid internal conversion is assumed to occur within the triplet manifold to populate T_1. However, upon adding MBP, dissociative electron transfer to MBP, generating an $MP^{\bullet}$ radical, serves as an additional bimolecular decay pathway for PC*(S_1), with a rate coefficient denoted here as k_{ET}, as shown in equation 3. Additionally, MBP can react with PC*(T_1) to generate $PC^{+\bullet}$ + $MP^{\bullet}$ as shown in equation 4. The rate of decay of PC*(S_1) is expressed by equation 5, which includes the above-mentioned pathways. This analysis relates the observed rate coefficient, k_{obs} for the decay of the PC*(S_1) band intensities in either TEA or TVA spectra to the rate coefficient for electron transfer and the lifetime (= $1/k_D$) of PC*(S_1), as shown in equation 6. The corresponding analysis for reactivity from the PC*(T_1) state is reported in Chapter 2.

$$PC^*(S_1) \xrightarrow{k_R} PC(S_0) \quad (1)$$

$$PC^*(S_1) \xrightarrow{k_{ISC}} PC^*(T_n) \rightarrow PC^*(T_1) \quad (2)$$

$$PC^*(S_1) + MBP \xrightarrow{k_{ET}} MP^\bullet + PC^{\bullet+} + Br^- \quad (3)$$

$$PC^*(T_1) + MBP \xrightarrow{k_{ET}^T} MP^\bullet + PC^{\bullet+} + Br^- \quad (4)$$

$$\frac{d[PC^*(S_1)]}{dt} = -k_D[PC^*(S_1)] - k_{ET}[PC^*(S_1)][MBP] \quad (5)$$

where $k_D = k_R + k_{ISC}$, and is the reciprocal of the lifetime of the PC*(S_1) state in the absence of MBP.

$$k_{obs} = k_D + k_{ET}[MBP] \quad (6)$$

Figure 4.4a shows the dependence of the rate coefficient k_{obs} for decay of the PC-N1*(S_1) ESA band intensity on changing [MBP] concentration in DMF solution, measured using TVAS. The gradient of the inset plot of k_{obs} vs [MBP] gives a value of $k_{ET} = (1.0 \pm 0.1) \times 10^{10}\ M^{-1}s^{-1}$ for reaction of PC-N1*(S_1) with MBP in DMF. As is shown in **Table 4.1**, PC-N1 is a photocatalyst with a negligible triplet quantum yield in DMF solution. The data shown in **Figure 4.4a** were obtained for a 4.2 mM PC-N1 solution, with MBP concentrations in the range 0.045 - 0.36 M. The lowest concentration of 0.045 M MBP corresponds to 10 equivalents of the PC, in line with typical polymerization conditions. For experiments where higher MBP concentrations were used, the linearities of this and other pseudo-first-order kinetic plots indicate no adverse effects on the ET kinetics, and that derived rate coefficients for electron transfer can be applied under the synthetic conditions used for polymer growth.

Complementary information can be obtained from analysis of TEAS data, and the global fitting of the kinetics of decay of the PC-N1 ESA band and growth of the PC-N1$^{\bullet+}$ band derived from TEAS measurements for different [MBP] concentrations gives a rate coefficient for ET of $k_{ET} = (1.3 \pm 0.1) \times 10^{10}\ M^{-1}s^{-1}$. This value matches the rate coefficient value derived from the independent TVAS data within two standard errors. This Stern-Volmer type quenching analysis is particularly useful for analysis of decaying ESA bands in TEAS data, or

of TVA spectra in DMF solutions for which the MP$^{\bullet}$ product band is masked by strong solvent absorptions.

4.2.3.3 Growth of MP$^{\bullet}$ Band

In toluene-d_8 and DCM solutions, analysing the growth of the MP$^{\bullet}$ radical absorption band observed at 1660 cm^{-1} in the TVAS data provides an alternative way to obtain k_{ET} values. A kinetic analysis based on this spectroscopic feature must also take account of decay pathways for the MP$^{\bullet}$ radical, as shown in equations 7 and 8. Under the experimental conditions, MP$^{\bullet}$ can primarily decay via two pathways: either by radical-radical self-quenching or by reaction with residual dissolved oxygen. A third pathway of back electron transfer to PC$^{\bullet+}$ is discounted on the timescales of these measurements (up to 10 μs) because decay of the PC$^{\bullet+}$ absorption bands is not observed.

$$MP^{\bullet} + MP^{\bullet} \xrightarrow{k_{t1}} (MP)_2 \quad (7)$$

$$MP^{\bullet} + O_2 \xrightarrow{k_{t2}} MPOO^{\bullet} \quad (8)$$

As can be seen in **Figure E65**, the time constant for decay of the MP$^{\bullet}$ band can vary from 300 ns to ~5 μs (depending on the extent to which dissolved oxygen has been purged out of the flow system), which is 10^2-10^3 times slower than its rise (less than 2 ns at concentrations used here) by an electron transfer reaction. Additionally, at the concentrations of MBP used for most of these studies, the rate of electron transfer is much faster than the rate of ISC, even for the catalysts with otherwise high Φ_{ISC} values reported in **Table 4.1**. The fact that kinetic traces of PC*(S_1), MP$^{\bullet}$, and PC(S_0) can be fit with a global time constant as seen in **Figure 4.2d** further argues that ISC is not significant in these measurements. Hence, under these conditions, a pseudo first order kinetic equation is obtained for the growth of MP$^{\bullet}$ radical concentration within the first ~10-20 ns as shown by equation 9.

$$\frac{d[MP^{\bullet}]}{dt} = k'_{ET}[PC^*(S_1)] \quad (9)$$

where $k'_{ET} = k_{ET}[MBP]$. Substituting the value for [PC* (S_1)] from integration of equation 5, gives the overall rate coefficient for the growth of MP$^{\bullet}$ which is related to the rate coefficient for ET as:

$$k_{MP} = k_D + k_{ET}[MBP] \quad (10)$$

Figure 4.4b shows the kinetic traces obtained for the growth of the MP$^{\bullet}$ band intensity with increasing concentrations of MBP (from 0.18 to 1.4 M) for a 7.5 mM solution of PC-S in DCM. The inset shows a plot of k_{MP} vs [MBP]; the gradient of the linear fit gives the rate coefficient for electron transfer from PC*(S_1) to MBP, $k_{ET} = (1.4 \pm 0.1) \times 10^9\ M^{-1}s^{-1}$. This rate of electron transfer is slower by an order of magnitude than the expected diffusion-controlled rate coefficient in DCM ($1.5 \times 10^{10}\ M^{-1}s^{-1}$) at 20 °C.[50] The rate coefficient for ET in toluene-d_8 obtained from such an analysis also gives $k_{ET} = (1.4 \pm 0.1) \times 10^9\ M^{-1}s^{-1}$.

While the kinetic analysis of the MP$^{\bullet}$ band intensities from TVAS measurements does provide an additional measure for determining the ET rate coefficient, it is not always possible to perform. Firstly, the MP$^{\bullet}$ band is completely masked by strong solvent absorption in DMF solutions. Secondly, for some photocatalysts, the MP$^{\bullet}$ band intensities observed in toluene are much weaker than in DCM. What causes this discrepancy is unclear. The above kinetic analysis is also valid for growth of the intensity of the PC$^{\bullet+}$ product band, as revealed both in TVAS and TEAS data.

Depending on the solvent, and the intensity of the MP$^{\bullet}$ absorption band, both PC*(S_1) quenching and MP$^{\bullet}$ band growth kinetics can be used to determine the rate coefficients for electron transfer between PC*(S_1) and MBP for all the organic PCs studied here (**Figure 4.1b**). Concentration plots akin to **Figure 4.4** are shown in Experimental Section for all the PCs, and the values of k_{ET} obtained are summarized in **Table 4.2**. Note that most of the k_{ET} values reported in **Table 4.2** are derived from the analysis of TVAS data. PC* band decays in the TEAS data were instead used to extract the rate coefficients for those PCs for which the signal-to-noise ratios in TVAS data were poor and resulted in noisy kinetics. Where possible, ET rate coefficients obtained from these two different spectroscopic techniques are reported for better comparison. For example, for PC-O2 in DCM, the rate coefficient for ET from the PC*(S_1) state obtained from TVAS data is $(8.5 \pm 1.5) \times 10^8\ M^{-1}s^{-1}$ which is in reasonable agreement with the k_{ET} value of $(1.0 \pm 0.1) \times 10^9\ M^{-1}s^{-1}$ obtained using TEAS data analysis. The kinetic fits for PC-O2 are shown in the Experimental Section.

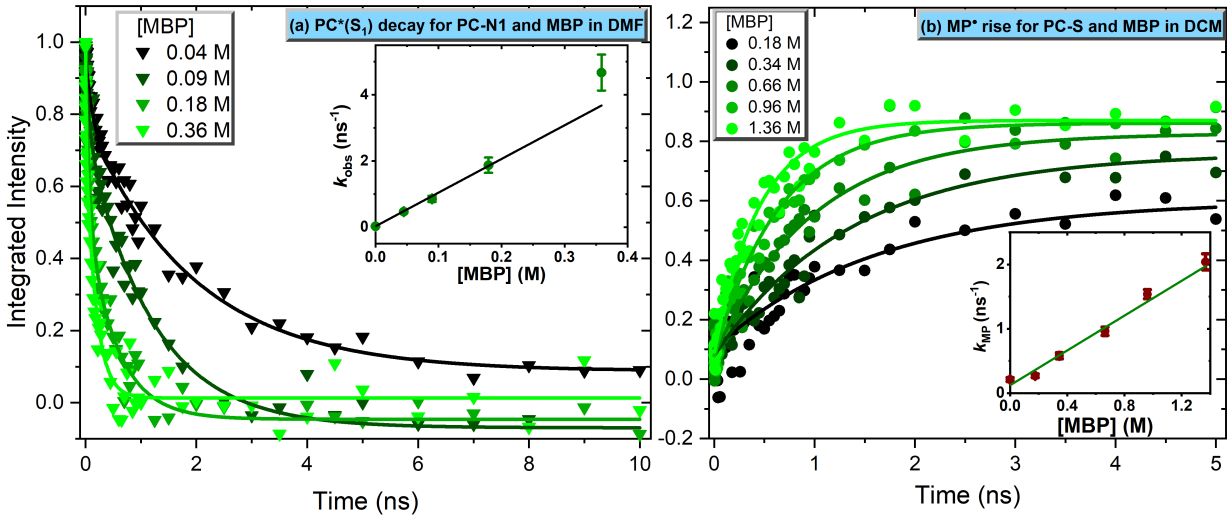

Figure 4.4. *Kinetics of electron transfer reactions of PC-N1*(S_1) and PC-S*(S_1) with MBP from TVAS measurements. Rates of (a) decay of PC-N1*(S_1) in DMF and (b) production of ^{2}MP• (D_0) radical in DCM by electron transfer from PC-S*(S_1) to MBP. Insets show pseudo-first order kinetic plots. The rate coefficient for electron transfer from PC-N1*(S_1) to MBP is obtained from the linear fit as* $k_{ET} = (1.0 \pm 0.1) \times 10^{10}\ M^{-1}s^{-1}$ *in DMF and from PC-S*(S_1) to MBP is* $k_{ET} = (1.4 \pm 0.1) \times 10^{9}\ M^{-1}s^{-1}$ *in DCM.*

For each of the studied PCs, the magnitudes of their ET rate coefficients show some variation, but not marked change, between toluene(-d_8), DCM and DMF solutions. This observation is particularly relevant for the N,N-diaryl dihydrophenazines as most of these PCs show highly solvent dependent photodynamics (as explained in Chapter 3).[45] However, comparing the k_{ET} values between different PCs reveals one important distinction: PC-N1, PC-N2 and PC-O1, all of which have LE character for their S_1 states, have nearly diffusion-controlled rate coefficients for excited-state ET to MBP. In contrast, PC-N3, PC-N5, PC-O3 and PC-S, with S_1 CT-character, undergo slower ET with rate coefficients 5-10 times lower than the predicted diffusion-limited rate coefficients in the respective solvents. These diffusional rate coefficients are estimated to be 1.5×10^{10} M^{-1} s^{-1} in DCM, 1.1×10^{10} M^{-1} s^{-1} in Toluene, and 7.6×10^{9} M^{-1} s^{-1} in DMF at 20 °C.[50] The causes of these differences are discussed in section 4.2.6.

In synthetic O-ATRP experiments, monomers are used in high concentrations to increase polymerization yields. Because these monomers are typically low-polarity molecules, the polarity of the reaction mixture will be lower than that of the solvent. To investigate this effect, the rate constant for ET was measured for a solution of 3.2 mM PC-O2 with 0.3 M MBP in 20 mL dichloromethane, to which the monomer isoprene was added in increasing aliquots up to a final concentration of 2 M. At the higher isoprene concentrations, the measured k_{ET} value is larger than for PC-O2 and MBP in DCM alone. Instead, at a 2-M concentration of isoprene,

$k_{ET} = 2.6 \times 10^9\ M^{-1}\ s^{-1}$ is closer to the value obtained in toluene-d_8 (see **Table 4.3**), most likely because the dielectric constant for isoprene is similar to that of toluene. As most of the monomers used in ATRP studies are low-polarity molecules, measured k_{ET} values in dichloromethane and toluene should serve as good approximations for the solvent mixtures used in O-ATRP.

Table 4.3. *Rate Coefficients for Bimolecular ET between PC*(S_1) and MBP in Toluene-d_8, DCM, and DMF.*[a]

Catalyst	$k_{ET}(S_1)/(10^9\ M^{-1}s^{-1})$		
	Toluene	**DCM**	**DMF**
PC-N1	38 ± 6[†]	24 ± 2[†]	10 ± 1 (13 ± 1[#])
PC-N2[b]	13 ± 0.2	20 ± 2	22 ± 1
PC-N3 [b]	2.90 ± 0.04[#]	4.4 ± 0.3	2.8 ± 0.4
PC-N4 [c]	-	-	-
PC-N5 [d]	3.1 ± 0.1	2.6 ± 0.3	1.8 ± 0.1
PC-O1	17 ± 1[#] (33 ± 2)	21 ± 3[#]	10 ± 1
PC-O2	2.3 ± 0.1	1.0 ± 0.1[#] (0.9 ± 0.2)	2.0 ± 0.3
PC-O3	3.4 ± 0.1	4.1 ± 0.2	3.6 ± 0.2
PC-S	1.4 ± 0.1	1.4 ± 0.1	1.9 ± 0.1

[a] Most of the k_{ET} values reported are from the analysis of TVAS data; TEAS values are instead reported where TVAS data have poorer signal to noise ratios. k_{ET} values obtained from both methods are shown for PCs where possible, with values with the larger standard fitting errors shown in parentheses. [b] The rate coefficient in DCM was reported previously by Koyama *et al.*[36] [c] No electron transfer was observed for PC-N4. [d] Values reported previously by Lewis-Borrell *et al.*[37] [#] value obtained from TEAS data. [†]Rate coefficient obtained by Smoluchowski kinetic analysis.

4.2.4 Reaction from ^{3}PC*(T_1) States

Electron transfer from ^{3}PC*(T_1) is deemed to be desirable in photoredox catalysed synthetic procedures because of the relatively longer lifetimes of triplet states and the lower likelihood of reaction quenching by back electron transfer.[9] Therefore, a preference for PCs with high ISC yields and long-lived triplet states has motivated the design of new PCs for O-ATRP applications. Thus far, this study has only looked at the electron transfer dynamics from the S_1 states of PCs. In part, this is because at the concentrations of MBP used in these studies, the electron transfer is dominated by the S_1 state in all cases. Evidence for a negligible role of the triplet states in most of the studied PCs (**Figure 4.1b**) comes from the ^{1}PC*(S_1), ^{2}PC$^{\bullet+}$(D_0) and MP$^\bullet$ radical kinetic traces all being fitted to the same time constants. Moreover, for several of the PCs, ISC efficiencies are low (**Table 1**),[45] hence ET is favoured from singlet excited states. However, this is not the case for PC-N2, PC-O1, PC-O2 and PC-S, which show high ISC yields irrespective of the solvent used. While the absence of triplet state signatures in the TVAS data for PC-N2, PC-O1 and PC-S makes it difficult to investigate the reactivity of the triplet state

exclusively, TVAS data for PC-O2 in toluene-d_8 show a triplet band at 1482 cm^{-1} (also seen in DCM), as shown in **Figure 4.5**. With increasing MBP concentrations from 0.02 - 0.15 M (6 to 50 equivalents) in a 3.2 mM PC-O2 solution in toluene-d_8, this band is observed decaying faster, as can be seen from the kinetic traces in **Figure 4.5b**. Moreover, by observing the recovery of the GSB band at 1489 cm^{-1} (**Figure 4.5c**), as well as the decay of the PC*(S_1) band and growth of the ^{3}PC*(T_1) band, the reaction is shown to be competitive between S_1 and T_1 states, because with increasing MBP concentrations, the S_1 state population also decays faster. **Figure 4.5d** shows the pseudo first-order rate coefficients for ET from the S_1 and T_1 states (fitted using equation (5) for the S_1 state, and methods discussed in Chapter 2 for the T_1 state). Linear fits gives bimolecular rate coefficients of $k_{ET}(S_1) = (2.6 \pm 0.4) \times 10^9\ M^{-1}s^{-1}$ for reaction from the S_1 state and $k_{ET}(T_1) = (2.1\ \pm\ 0.5) \times 10^7\ M^{-1}s^{-1}$ for reaction from the T_1 state (which could include a component of T_1 quenching to S_0 by the MBP). At MBP concentrations of 0.4 M or higher, the T_1 band is not observed for PC-O2, which shows that at these concentrations, most of the PC*(S_1) state reacts with MBP before ISC can occur. However, it is important to note that under synthetic conditions, the PC:MBP concentrations used are in a 1:10 ratio, similar to that for data plotted in **Figure 4.5**, which shows that for PCs with high ISC yields, ET can happen from both S_1 and T_1 states under synthetically relevant concentrations.

The comparative magnitudes of the ET rate coefficients for the PC*(T_1) and PC*(S_1) states will depend markedly on the energetics of the excited states, as well as their reduction potentials for reaction with the radical initiator. Jockusch and Yagci [51] reported studies on singlet and triplet reactivities of N-phenyl phenothiazine using fluorescence lifetime measurements (for ET from S_1) and laser flash photolysis (for ET from T_1). They found that when using methyl α-bromoisobutyrate (MBI) as a radical initiator in N,N-dimethylacetamide, the rate coefficients for singlet and triplet state reactivity differed by two orders of magnitude ($10^9\ vs\ 10^7\ M^{-1}s^{-1}$ respectively). In contrast, using ethyl α-bromophenylacetate (EBPA) as an electron acceptor / initiator, the rate coefficients of ET from PC*(S_1) and PC*(T_1) were comparable (~10^9 M^{-1} s^{-1}). They reasoned that the difference in reactivity arises from the less favourable reduction potential for MBI (-0.52 V vs. SCE) compared to EBPA (−0.22 V vs. SCE) as well as the lower reduction potential of the PC*(T_1) than the PC*(S_1) state for N-phenyl phenothiazine. Given that MBP is reported to have a reduction potential (-0.56 V vs SCE) with a value similar to MBI, and that the reduction potential for the PC-O2*(S_1) state (-

2.06 V) is higher than that of T_1 (-1.90 V), the observation of 100-fold faster ET from the S_1 than the T_1 state of PC-O2 is in accord with those of Jockusch and Yagci.

4.2.5 Photochemical Quenching Quantum Yields from PC*(S_1/T_1) States.

The quantum yield (QY) for quenching of PC* (S_1/T_1) excited states by an alkyl halide is an important metric in synthetic polymer chemistry. To determine QY values, it is needed to know the PC* singlet and triplet lifetimes, the quantum yields for population of the T_1 states, and the rate constants for ISC and electron transfer from the S_1 and T_1 states. PC* lifetimes and quantum yields are reported in **Table 1**, with detailed descriptions of the measurements of these values provided in Chapter 3.[45] The k_{ET} values for ET from PC*(S_1) are summarized in **Table 2**. In the absence of loss processes for S_1 population other than relaxation (radiative and non-radiative) to S_0, ISC, and bimolecular ET to MBP, the QY for quenching of S_1 by MBP (at any given concentration of the MBP), $\Phi_Q(S_1)$, can be deduced from this information using:

$$\Phi_Q(S_1) = \frac{k_{ET}(S_1)[MBP]}{k_{ET}(S_1)[MBP]+k_D(S_1)} \quad (11)$$

Here, $k_D(S_1) = 1/\tau(S_1)$ is the combined rate constant for decay of S_1 by ISC, IC to S_0, and fluorescence. Example values of $\Phi_Q(S_1)$ are given in **Table 4**.

Similarly, the QY for the T_1 state quenching can be calculated using:

$$\Phi_Q(T_1) = \Phi'(T_1)\ \frac{k_{ET}(T_1)[MBP]}{k_{ET}(T_1)[MBP]+k_D(T_1)} \quad (12)$$

Here, $\Phi'(T_1)$ is the T_1-state quantum yield in the presence of MBP, $\Phi'(T_1) = k_{ISC}/\{k_{ET}(S_1)[MBP] + k_D(S_1)\}$, and $k_D(T_1) = 1/\tau(T_1)$ is the rate constant for decay of T_1 by phosphorescence or other relaxation pathways to S_0. In these experiments, it is difficult to determine a value for $\tau(T_1)$ because of quenching by dissolved oxygen. As polymerization experiments are typically performed in a glove box, $\tau(T_1)$ may be significantly longer than the lifetime for quenching by ET. Under such conditions, the approximation can be made that $k_{ET}(T_1)[MBP] \gg k_D(T_1)$, and hence $\Phi_Q(T_1) \approx \Phi'(T_1)$. However, at the low concentrations of [MBP] used in O-ATRP, this condition may not be fully met, and $\Phi_Q(T_1)$ will be less than $\Phi'(T_1)$. Nevertheless, $\Phi'(T_1)$ will always be the upper limit to the quenching QY from the T_1 state. At low [MBP], $\Phi'(T_1) \rightarrow \Phi(T_1)$, the quantum yield for T_1 population in the absence of MBP (as listed in **Table 1**).

Table 4.4. *Quantum yields $\Phi_Q(S_1)$ for photochemical quenching of the PC*(S_1) state by MBP in DMF solution..*

Catalyst	$k_D(S_1)$ [a] / (10^8 s^{-1})	k_{ET} / (10^9 M^{-1} s^{-1})	$\Phi_Q(S_1)$ [b]	
			[MBP] = 0.4 M	[MBP] = 0.01 M
PC-N1	0.26 ± 0.01	10 ± 1	0.99 ± 0.10	0.80 ± 0.08
PC-N2	0.60 ± 0.07	22 ± 1	0.99 ± 0.08	0.79 ± 0.06
PC-N3	15.75 ± 0.55	2.8 ± 0.4	0.42 ± 0.07	0.018 ± 0.002
PC-N5	1.92 ± 0.15	1.8 ± 0.1	0.79 ± 0.06	0.09 ± 0.01
PC-O1	4.76 ± 0.22	10 ± 1	0.89 ± 0.16	0.17 ± 0.02
PC-O2	1.16 ± 0.16	2.0 ± 0.3	0.87 ± 0.16	0.15 ± 0.03
PC-O3	3.03 ± 0.37	3.6 ± 0.2	0.83 ± 0.07	0.11 ± 0.01
PC-S	1.70 ± 0.17	1.9 ± 0.1	0.82 ± 0.08	0.10 ± 0.01

a. Determined using the $1/\tau(S_1)$ values reported in **Table 4.1** and ref. [45]
b. 0.4 M MBP represents a sample concentration of MBP used in this study, and 0.01 M is typical of concentrations used in O-ATRP. [51]

Quenching of triplet state PCs by dissolved oxygen in these solutions prevents determination of the unquenched triplet state lifetimes; nevertheless, a reasonable estimate can be made of T_1-state quenching yields if these lifetimes are much longer than the lifetimes in the presence of the MBP quencher. At the concentrations of MBP used in this study, for the nine PCs examined, the S_1 state is in large part quenched by MBP. For example, at a concentration of 0.4 M, the greatest extent of S_1 quenching is observed for PC-N1 (99%), and lowest extent is observed for PC-N3 (42%). Consequently, even for PCs with high ISC efficiencies, at these MBP concentrations most of the PC(S_1) will undergo bimolecular ET in preference to crossing to the triplet state manifold. The lower quenching quantum yield for PC-N3 derives from its short S_1 lifetime and relatively smaller rate constant for ET to MBP, not from ISC.

Of particular interest are ET yields at the experimental concentrations of MBP (10 - 50 mM MBP) typically used in polymerization experiments. For LE catalysts with relatively long lived S_1 states (see **Table 4.1**) such as PC-N1 and PC-N2, even at concentrations as low as 10 mM, the quantum yield for S_1-state quenching by MBP is calculated to be 0.80. The corresponding quantum yields are significantly smaller for CT catalysts (e.g., 0.09 for PC-N5 and 0.02 for PC-N3), but this does not imply that quenching occurs by ET from the triplet state because the quantum yields for this process are also very small. Instead, the S_1 state is mostly relaxing by radiative and internal conversion pathways.

The above analysis identifies an important distinction between the CT and LE catalysts studied here: for LE catalysts with long S_1 lifetimes, even at low concentrations of MBP most of the

ET reactivity will come from the S_1 state irrespective of their ISC efficiencies. In contrast, for CT catalysts with high ISC efficiencies, ET from triplet states will become important at the concentrations of MBP used in O-ATRP. For example, for PC-O2 at 10 mM MBP concentration in toluene, only 5% of the S_1 state is quenched by ET, whereas up to 70% of the ET happens from the T_1 state. While quenching by O_2 makes it difficult to determine the exact lifetime of the T_1 state, and hence its quenching quantum yield, an upper limit of this T_1-state reactivity will be given by the T_1 quantum yield. Interestingly, even at such low reactivity from their S_1 states, both PC-N3 and PC-N5, which show no ISC, are reported to exert good control over polymerization, giving low polymer dispersity and high monomer conversion.[23] These combined observations suggest that for O-ATRP, only very low concentrations of the radical are necessary to obtain good polymerization control.

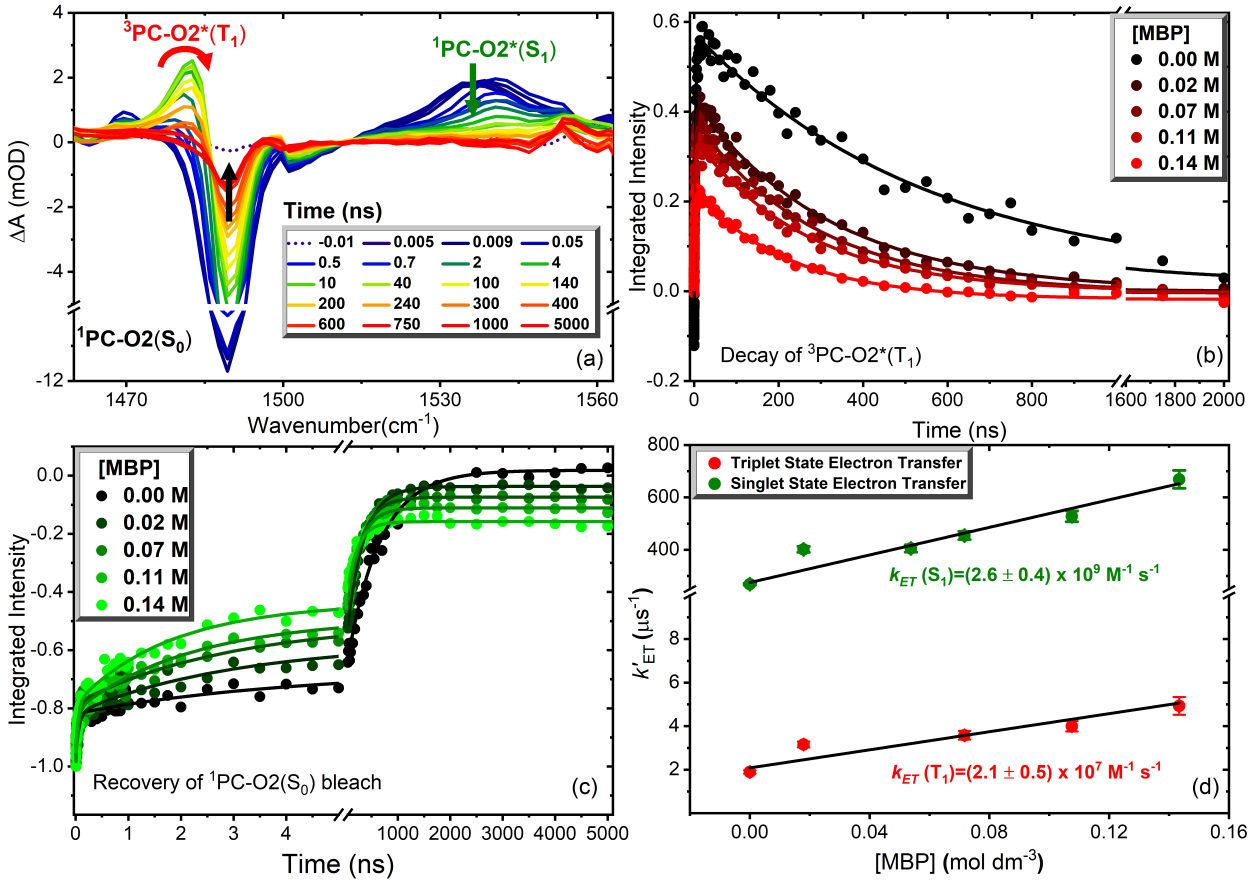

Figure 4.5. *TVAS measurement of electron transfer kinetics of PC-O2 with MBP in toluene-d_8. (a) TVAS of 3.2 mM PC-O2 with 0.14 M MBP in toluene-d_8 shown for time delays from 1 ps – 1 μs. All bands are labelled, and arrows show directions of change. A ^{3}PC-O2*(T_1) band at 1482 cm^{-1} partially overlaps the ground state bleach centred at 1489 cm^{-1}. (b) Kinetic traces showing the growth of the ^{3}PC-O2*(T_1) band (commensurate with the decay of the PC*(S_1) band via ISC) and its decay with increasing MBP concentrations from 0.02 to 0.14 M. Solid lines are biexponential fits to the data (see main text). (c) Kinetic traces for the recovery of the PC-O2 ground state bleach at 1489 cm^{-1}. The GSB recovers faster with increasing MBP concentration at early time scales because of competitive S_1-state reaction with MBP. (d) Pseudo-first order kinetic plots for ET reactions from the PC-O2 S_1 and T_1 states; k'_{ET} is the observed pseudo-first order rate coefficient. The gradients of the linear fits give $k_{ET} = (2.6 \pm 0.4) \times 10^9\ M^{-1}s^{-1}$ for reaction from the S_1 state and $k_{ET} = (2.1 \pm 0.5) \times 10^7\ M^{-1}s^{-1}$ from the T_1 state.*

4.2.6 Modified Marcus Theory for Kinetic Evaluation of the ET Mechanism.

As discussed in section 4.2.3, there is a clear trend of larger rate-coefficients for ET to MBP from the PC*(S_1) states with LE character compared to PC*(S_1) states with CT character. To understand this trend, the "sticky" model of dissociative electron transfer is invoked which is a modification to Marcus-Savéant theory.[40] Electron transfers to alkyl halides are known to be concerted dissociative processes in which C–X bonds dissociate promptly upon RX accepting an electron from the photoexcited PC*. The Gibbs energy of activation for this dissociative ET is determined by the Marcus-Savéant model to be:

$$\Delta G^{\ddagger} = \frac{E_{BD}+\lambda_0}{4}\left(1+\frac{\Delta G_{ET}}{E_{BD}+\lambda_0}\right)^2 \qquad (13)$$

where E_{BD} is the dissociation energy of the C–X bond, λ_0 is the solvent reorganization energy, and ΔG_{ET} is the Gibbs energy for electron transfer, given by equation (14).

$$\Delta G_{ET} = F\{E^o(PC^{\bullet+}/PC) - E^0(RX/R^{\bullet}X^-)\} - E\left(PC^*(S_1)\right) - \frac{N_A e^2}{4\pi\epsilon_0\epsilon r} \qquad (14)$$

In this equation, E^0 are reduction potentials and $E(PC^*(S_1))$ is the energy of the S_1 state of the PC in a given solvent, which is estimated here using the wavelength of the onset of emission of the PC in that solvent.[20] The last term in equation (14) corresponds to the Coulombic interaction between the ionic products of the ET reaction. This analysis is restricted to DMF, as the oxidation and reduction potentials of PC and RX used to determine ΔG_{ET} were measured in either acetonitrile or DMF. As acetonitrile and DMF have similar dielectric constants, the approximation is made that the acetonitrile values of redox potentials can be used for studies in DMF (see Chapter 2 section 2.2.2.4 for details).

Isse *et al*. showed that the kinetics of activation of copper-catalysed ATRP were better described by modifying the Marcus-Savéant model to account for the X^- ion from dissociative electron attachment interacting with the $R^{\bullet}$ radical, forming an ion-radical pair. This modification involved adding a further interaction energy D_p to equation (15).[47] The resulting model is known as the "sticky" model of dissociative electron transfer and was later shown by Matyjaszewski and co-workers to apply to electron transfer from organic phenothiazine based catalysts to RX.[20] According to this model, the Gibbs energy of activation becomes:

$$\Delta G^{\ddagger} = \frac{\lambda_0 + \left(\sqrt{E_{BD}} - \sqrt{D_p}\right)^2}{4}\left(1 + \frac{\Delta G_{ET} - D_p}{\lambda_0 + \left(\sqrt{E_{BD}} - \sqrt{D_p}\right)^2}\right)^2 \quad (15)$$

This activation energy can then be used to calculate the rate coefficient for the ET process using

$$k_{ET} = Ze^{-\frac{\Delta G^{\ddagger}}{RT}} \quad (16)$$

where Z is the collision frequency and R is the gas constant. Details of the calculation of Z, and other parameters in equations (14-16) can be found in Chapter 2.

Table 4.3 shows the important parameters for each PC in DMF, and it compares the calculated and experimentally measured values of the rate coefficients for ET. The comparisons made in **Table 4.3** show that for most PCs in DMF, the calculated and measured k_{ET} values are in reasonable agreement, suggesting that the sticky model of dissociative ET is applicable to the PC* + MBP systems studied in this work. Not including the sticky correction to the Marcus-Savéant model yields k_{ET} values that do not agree as well with the experimental results. The predicted values are reasonable for the PCs with CT S_1 character, while the model overestimates the k_{ET} values for locally excited PCs because these ET reactions are diffusion-limited, and thus experimentally k_{ET} is not determined by the electron transfer step. In addition, the activation energy $\Delta G^{\ddagger}$ values in **Table 4.3** account for trends in PC* electron transfer rates observed experimentally in DMF. As discussed earlier, for PC-N1, PC-N2, and PC-O1, which have LE character in their S_1 state, near diffusion-controlled k_{ET} values are seen, whereas for the other PCs with CT character, ET from the S_1 state is slower. PC-N1, PC-N2, and PC-O1 have lower activation energies for electron transfer compared to the other PCs, which is why these PCs have faster ET rates.

Using the data shown in **Table 4.5** and Chapter 2 **Table 2.2**, the experimental k_{ET} can be plotted against ΔG_{ET} for DMF, commonly referred to as a Rehm-Weller plot, and the data are shown in **Figure 4.6**. The upward trend in the value of k_{ET} with increasingly negative ΔG_{ET} values can be seen for the PCs. The calculated values of k_{ET} for each PC are plotted for comparison, with any values predicted to be above the diffusion limit capped at the estimated diffusion-limited rate coefficient in DMF at 20°C for better comparison.

Comparing the values of k_{ET} in **Table 4.5**, and also in **Figure 4.6**, shows that in DMF solutions, the values of ΔG_{ET} are more negative for the PCs with LE electronic states compared to the CT

character PCs. It is the more exothermic ΔG_{ET} values that result in small (1-2 kJ/mol) activation energies for ET from the LE catalysts, which in turn lead to the values of k_{ET} being close to the estimated diffusional rate coefficients for DMF at 20 °C. Therefore, ΔG_{ET} can be classified as one of the most important factors in the design of such PCs for ATRP, an argument which was also developed in prior publications from the Bristol group.[36,37,45] A recent study by Damrauer and co-workers of four phenoxazine based PCs adopts a similar argument.[52]

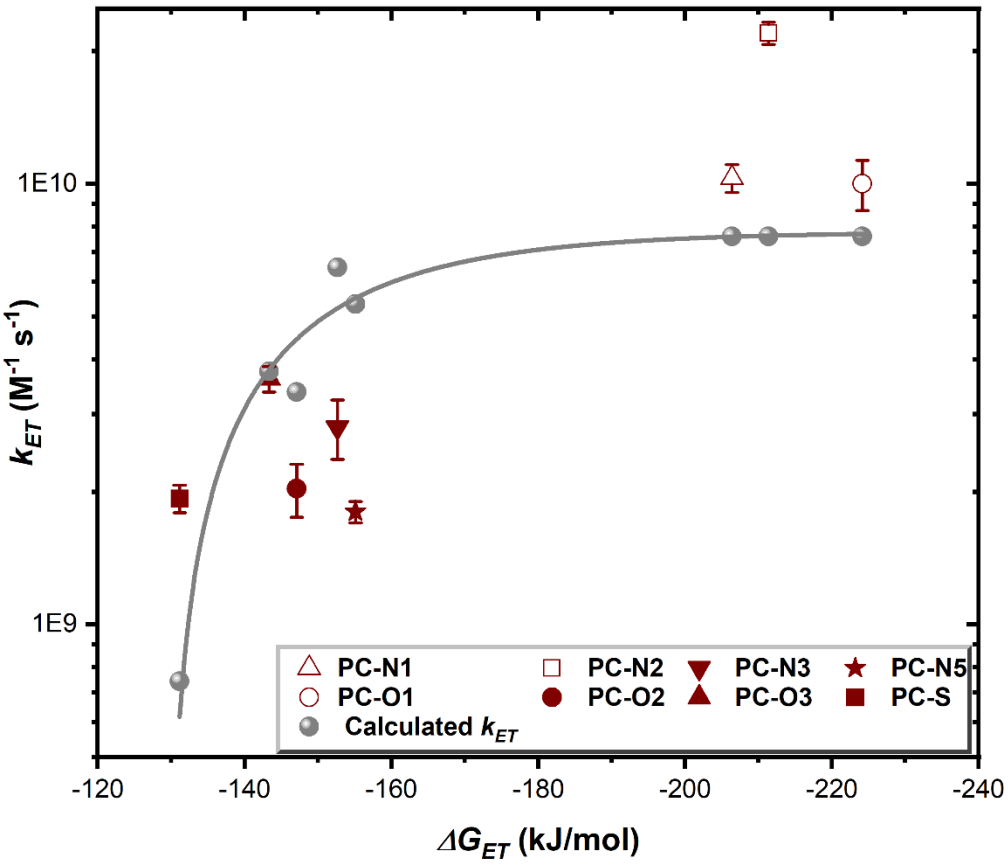

Figure 4.6. *A Rehm-Weller plot for the rate coefficients for electron transfer from the photoexcited PCs shown in* ***Figure 4.1(b)*** *to MBP in DMF. The symbols representing each PC are specified in the inset legend. PCs with locally excited S_1/T_1 character are represented by hollow symbols and PCs with charge transfer S_1/T_1 character are shown as filled symbols. Calculated k_{ET} values are shown for comparison as grey circles and the curved line is added to guide the eye. Calculated values for k_{ET} that exceed the diffusion limit are capped at the predicted diffusion-limited rate coefficient in DMF at 20 °C for better comparison with experiment.*

Table 4.5. *Calculated Values of Activation Energies, Rate Coefficients and Relevant Thermodynamic Parameters Required for the Sticky Model of Dissociative Electron Transfer.*[(a)]

Catalyst	*Excited state character (S_1 and T_1)*	*Measured* k_{ET} $/(10^9\ M^{-1}s^{-1})$	ΔG_{ET} $/(kJ\ mol^{-1})$	$\Delta G^{\ddagger}$ $/(kJ\ mol^{-1})$	Z $/(10^{11}\ s^{-1})$	Calculated k_{ET} $/(10^9\ M^{-1}s^{-1})$
PC-N1	LE	10 ± 1	-206.4	1.93	2.96	134[e]
PC-N2	LE	22 ± 1	-211.5	1.56	2.52	133[e]
PC-N3	CT	2.8 ± 0.4	-152.7	9.53	2.67	5.3[d]
PC-N4	CT	-[(b)]	-	-	2.81	-
PC-N5	CT	1.8 ± 0.1 [(c)]	-155.1	9.07	2.67	6.5[d]
PC-O1	LE	10 ± 1	-224.2	0.75	2.58	190[e]
PC-O2	CT	2.0 ± 0.3	-147.1	10.7	2.72	3.4
PC-O3	CT	3.6 ± 0.2	-156.0	11.4	4.08	3.8
PC-S	CT	1.9 ± 0.1	-131.2	14.3	2.47	0.7

[(a)] For all the PCs studied, parameters correspond to electron transfer to MBP in DMF solution at a temperature of 293 K. [(b)] No ET observed. [(c)] Value reported previously.[37] [(d)] The higher calculated k_{ET}value could result from errors in ΔG_{ET} because of the difficulty in determining the onset emission wavelengths for these PCs in DMF, and/or because the $E^0(\frac{PC^+}{PC})$ values used were measured in acetonitrile for the PC-N species. [(e)] Values will be limited by diffusion.

4.2.7 Propagation Reactions

The data presented up to this point in Chapters 3 and 4 have resolved the picosecond timescale excited state photochemistry of various PCs and the nanosecond timescale competition between ground-state recovery and bimolecular electron transfer reactions with the electron acceptor MBP. The subsequent reaction of the resulting $^2MP^{\bullet}(D_0)$ radicals with an added monomer, corresponding to the first propagation step of the catalytic cycle (see **Figure 4.1**), is now addressed. These longer-time measurements are made by following the decay of the absorption of the MP$^{\bullet}$ radical (generated by SET from PC-N5*(S_1)) over timescales extending beyond 1 μs, as shown in **Figure 4.7a**. The reaction of MP$^{\bullet}$ radicals with dissolved molecular oxygen competes with addition to an unsaturated monomer and therefore necessitates careful purging of the O_2 from the sample.[53] Measurements made with unpurged and N_2-purged samples are compared in **Figure E66** and are consistent with the report by Miyake and co-

workers that oxygen inhibited their polymerization reactions.[54] In a purged and closed-cycle system, the shortening of the MP• lifetime was observed with addition of monomer, chosen to be isoprene because it has no overlapping IR absorption bands in the probe region and has been used previously in ATRP polymerizations.[55] Example data are shown in **Figure 4.7b**. Linear fitting of the pseudo first-order rate constants (see Chapter 2 for a discussion of the kinetic analysis) obtained with different amounts of excess isoprene (at PC : monomer ratios consistent with conditions used for polymerization reactions) gives a rate coefficient for the first step of the propagation of $k_{prop} = (3.1 \pm 0.8) \times 10^5\ M^{-1}s^{-1}$ in DCM. Multiple bimolecular propagation steps extend the subsequent reaction kinetics beyond the experimental time window. Theriot *et al.*[23] have suggested that with PC-N5 as the chosen photocatalyst and methyl methacrylate as a monomer, six propagation steps occur before back-ET to the catalyst and control over polymerization is realised. Completion of the photocatalytic cycle and recovery of the PC(S_0) are not evident in the current TVAS measurements because of flow of the sample out of the probe laser volume on these extended time scales and reaction of radical species with residual dissolved O_2.

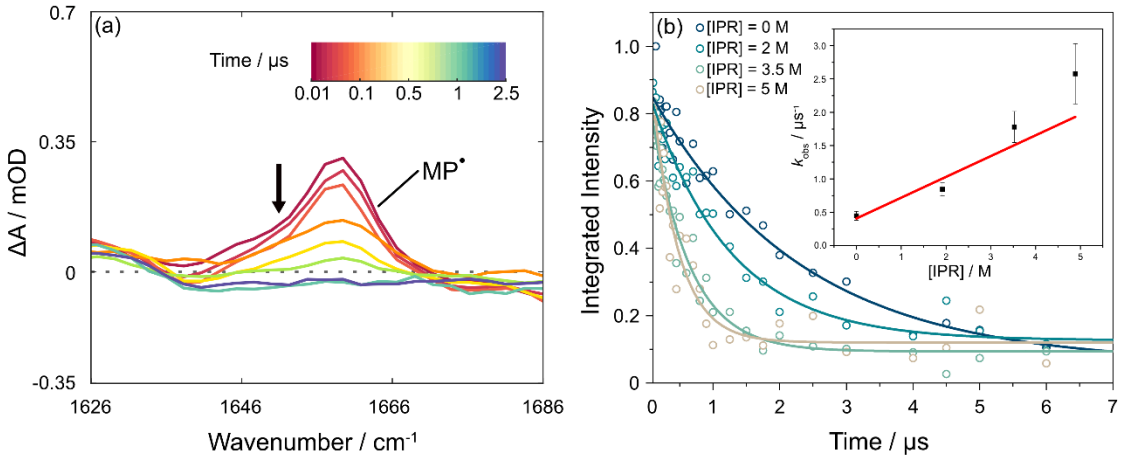

Figure 4.7. *Reaction of the MP radical with isoprene (IPR) in DCM. (a) Transient vibrational absorption spectra showing the extended timescale for decay of the ^{2}MP•(D_0) radical absorption band centred at 1660 cm^{-1} following pulsed excitation of PCBN at 370 nm. The black arrow adjacent to the MP• radical feature indicates the direction of change. (b) Kinetics of decay of ^{2}MP•(D_0) radicals in the presence of IPR on timescales up to 7 μs. Each curve corresponds to a different concentration of isoprene (see legend). The inset is a pseudo-first-order kinetic plot using the model discussed in Chapter 2, with a linear fit weighted to account for the uncertainty at each data point.*

4.3 Conclusions

The kinetics of the O-ATRP activation step involving electron transfer from the excited state of a photocatalyst to a radical initiator have been studied using the complementary techniques of transient vibrational and electronic absorption spectroscopies. Rate coefficients are reported

for ET reactions of nine different organic PCs, selected from the classes of N,N-diaryl dihydrophenazines, N-aryl phenoxazines and N-aryl phenothiazines, with the electron acceptor methyl 2-bromopropionate. These rate coefficients were determined by concentration dependent studies using TEAS and TVAS to measure the loss of photoexcited PC* (S_1/T_1), and TVAS to monitor the growth of the radical product of a dissociative electron transfer to MBP. These PCs all possess highly reducing S_1 and T_1 states, so are attractive candidates for photoredox catalysis, but are known to have varying degrees of control over polymerization from prior synthetic studies. Irrespective of whether they have a long-lived T_1 state, the catalysts with S_1 states of locally excited character were previously shown to be inferior to their counterparts with charge-transfer excited-state character in their control over polymer dispersity.

This behaviour can in part be explained by the current studies. The rate coefficients for ET from the PC(S_1) state to MBP reveal an important distinction: ET-reactions of the LE catalysts have nearly diffusion-controlled rate coefficients, whereas those for CT catalysts are 5-10 times smaller. The origins of this difference are explained by a modified Marcus-Savéant model, the "sticky" model of dissociative electron transfer. Use of this model predicts that the LE-character catalysts have small Gibbs energies of activation ($\Delta G^{\ddagger}$ = 1-2 kJ/mol) for electron transfer to MBP compared to the CT-character catalysts ($\Delta G^{\ddagger}$ = 9-14 kJ/mol) in DMF. These differences arise from the Gibbs energy changes for the electron transfer. The faster rates of ET from the LE-character catalysts may be detrimental for their performance as O-ATRP catalysts because they lead to poorer control of $MP^{\bullet}$ radical concentrations, resulting in polymers with higher dispersity. While it could be argued that a low (e.g., ppm) loading of the PC and/or the MBP initiator might therefore improve the control of the polymerizations, the photoredox cycle deactivation step may also play a major role in determining what makes a PC a good candidate for controlled ATRP.

The concentrations of MBP used in most of these studies are between 50 and 1000 equivalents of the PC concentration. At these high concentrations, ET is predominantly from the PC*(S_1) state, even for PCs with high triplet quantum yields. At these high MBP concentrations, ET serves as the primary channel for PC*(S_1) quenching, and it outcompetes the radiative or non-radiative decay back to the ground state and ISC to the triplet manifold. Analysis of the MBP-dependent decay of the T_1-state population seen in TVAS data for PC-O2 shows that at synthetically relevant concentrations of radical initiator (10 equivalents of [PC]), the ET

reaction can happen from both S_1 and T_1 states for PCs which have sufficiently high ISC quantum yields. The absence of triplet state signatures in the TVA spectra for other PCs prevented further such studies.

The solvent and photocatalyst dependent kinetic parameters of excited state lifetimes, ISC timescales, and electron transfer rate coefficients derived from these measurements can be used to make quantitative estimations of the quantum yields for excited-state quenching by the electron acceptor MBP, and their variation with MBP concentration. Interesting insights emerge from this analysis about the balance between the efficiencies of electron-transfer from the S_1 and T_1 states. When compared with synthetic data, this analysis shows that for O-ATRP, a high ISC efficiency is not necessarily required for a PC to be effective at controlling polymerization. For example, PC-N3 and PC-N5 have short S_1 lifetimes and low triplet quantum yields, with the consequence that at MBP concentrations relevant to polymer synthesis, less than 5% of the PC* S_1 states are quenched by MBP. Yet these PCs have been shown to exert good control over polymerization, with high monomer conversions and low polymer dispersity. In contrast, LE catalysts such as PC-N1 and PC-N2, show much higher quenching quantum yields from their S_1 states, but are poorer at polymerization control. For PCs with high ISC efficiencies, reaction from the triplet state will be the major contributor at synthetic MBP concentrations, but the polymer growth will depend on the k_{ET} and hence the PC*(T_1) reduction potential. While an outcome that may not hold true for all PCs and radical initiators, for PC-O2 the rate coefficient for electron transfer to MBP from the T_1 state, with a reported reduction potential of -1.90 V, is two orders of magnitude smaller than that for the S_1 state, which has a reduction potential of -2.06 V in toluene-d_8.

The work presented in this chapter has also sought to look beyond this first ET step and understand other important elements of the O-ATRP mechanism. The rate coefficient for the first propagation step has been measured in experiments that also highlight the challenges of observing later-time species in O-ATRP reactions using TVAS techniques. Chapter 5 will look to quantify further the reactivity in chemical cycles beyond the first bimolecular steps, and it shows how applying the TVAS measurements over picosecond to sub-millisecond timescales can unravel important mechanistic details.

The extensive study of the nine catalysts based on three different core structural motifs reported here brings important insights to PC design for O-ATRP. While long-lived triplet states for PCs may be a desirable property in many photoredox catalysed synthetic chemistry processes,

for ATRP this is not a defining factor in designing a good photocatalyst for polymer dispersity control. Instead, the design of these catalysts can be based on quantifiable thermodynamic parameters such as Gibbs energies of electron transfer which control the activation and deactivation steps.

4.4 References

1. Matyjaszewski K, Xia J. Atom Transfer Radical Polymerization. *Chem Rev* 2001, **101**(9)**:** 2921-2990.

2. Wang J-S, Matyjaszewski K. Controlled/"living" Radical Polymerization. Atom Transfer Radical Polymerization in the Presence of Transition-Metal Complexes. *J Am Chem Soc* 1995, **117**(20)**:** 5614-5615.

3. Kato M, Kamigaito M, Sawamoto M, Higashimura T. Polymerization of Methyl Methacrylate with the Carbon Tetrachloride/Dichlorotris-(triphenylphosphine)ruthenium(II)/Methylaluminum Bis(2,6-di-tert-butylphenoxide) Initiating System: Possibility of Living Radical Polymerization. *Macromolecules* 1995, **28**(5)**:** 1721-1723.

4. Kamigaito M, Ando T, Sawamoto M. Metal-Catalyzed Living Radical Polymerization. *Chem Rev* 2001, **101**(12)**:** 3689-3746.

5. Nicewicz DA, MacMillan DWC. Merging Photoredox Catalysis with Organocatalysis: The Direct Asymmetric Alkylation of Aldehydes. *Science* 2008, **322**(5898)**:** 77-80.

6. Ischay MA, Anzovino ME, Du J, Yoon TP. Efficient Visible Light Photocatalysis of [2+2] Enone Cycloadditions. *J Am Chem Soc* 2008, **130**(39)**:** 12886-12887.

7. Narayanam JMR, Tucker JW, Stephenson CRJ. Electron-Transfer Photoredox Catalysis: Development of a Tin-Free Reductive Dehalogenation Reaction. *J Am Chem Soc* 2009, **131**(25)**:** 8756-8757.

8. Fors BP, Hawker CJ. Control of a Living Radical Polymerization of Methacrylates by Light. *Angew Chem Int Ed* 2012, **51**(35)**:** 8850-8853.

9. Romero NA, Nicewicz DA. Organic Photoredox Catalysis. *Chem Rev* 2016, **116**(17)**:** 10075-10166.

10. Ohkubo K, Mizushima K, Fukuzumi S. Oxygenation and Chlorination of Aromatic Hydrocarbons with Hydrochloric Acid Photosensitized by 9-mesityl-10-Methylacridinium under Visible Light Irradiation. *Res Chem Intermed* 2013, **39**(1)**:** 205-220.

11. Ohkubo K, Mizushima K, Iwata R, Fukuzumi S. Selective Photocatalytic Aerobic Bromination with Hydrogen Bromide via an Electron-Transfer Atate of 9-mesityl-10-methylacridinium Ion. *Chem Sci* 2011, **2**(4)**:** 715-722.

12. Ohkubo K, Kobayashi T, Fukuzumi S. Direct Oxygenation of Benzene to Phenol Using Quinolinium Ions as Homogeneous Photocatalysts. *Angew Chem Int Ed* 2011, **50**(37)**:** 8652-8655.

13. Hamilton DS, Nicewicz DA. Direct Catalytic Anti-Markovnikov Hydroetherification of Alkenols. *J Am Chem Soc* 2012, **134**(45)**:** 18577-18580.

14. Nguyen TM, Nicewicz DA. Anti-Markovnikov Hydroamination of Alkenes Catalyzed by an Organic Photoredox System. *J Am Chem Soc* 2013, **135**(26)**:** 9588-9591.

15. Perkowski AJ, Nicewicz DA. Direct Catalytic Anti-Markovnikov Addition of Carboxylic Acids to Alkenes. *J Am Chem Soc* 2013, **135**(28)**:** 10334-10337.

16. Romero NA, Margrey KA, Tay NE, Nicewicz DA. Site-Selective Arene C-H Amination via Photoredox Catalysis. *Science* 2015, **349**(6254)**:** 1326.

17. McManus JB, Nicewicz DA. Direct C–H Cyanation of Arenes via Organic Photoredox Catalysis. *J Am Chem Soc* 2017, **139**(8)**:** 2880-2883.

18. Yoshimi Y, Itou T, Hatanaka M. Decarboxylative Reduction of Free Aliphatic Carboxylic Acids by Photogenerated Cation Radical. *Chem Comm* 2007(48)**:** 5244-5246.

19. Ryder ASH, Cunningham WB, Ballantyne G, Mules T, Kinsella AG, Turner-Dore J*, et al.* Photocatalytic α-Tertiary Amine Synthesis via C−H Alkylation of Unmasked Primary Amines. *Angew Chem Int Ed* 2019, **59**(35)**:** 14986-14991.

20. Pan X, Fang C, Fantin M, Malhotra N, So WY, Peteanu LA*, et al.* Mechanism of Photoinduced Metal-Free Atom Transfer Radical Polymerization: Experimental and Computational Studies. *J Am Chem Soc* 2016, **138**(7)**:** 2411-2425.

21. Pan X, Lamson M, Yan J, Matyjaszewski K. Photoinduced Metal-Free Atom Transfer Radical Polymerization of Acrylonitrile. *ACS Macro Lett* 2015, **4**(2)**:** 192-196.

22. Treat NJ, Sprafke H, Kramer JW, Clark PG, Barton BE, Read de Alaniz J*, et al.* Metal-Free Atom Transfer Radical Polymerization. *J Am Chem Soc* 2014, **136**(45)**:** 16096-16101.

23. Theriot JC, Lim C-H, Yang H, Ryan MD, Musgrave CB, Miyake GM. Organocatalyzed atom transfer radical polymerization driven by visible light. *Science* 2016, **352**(6289)**:** 1082-1086.

24. McCarthy BG, Pearson RM, Lim C-H, Sartor SM, Damrauer NH, Miyake GM. Structure-Property Relationships for Tailoring Phenoxazines as Reducing Photoredox Catalysts. *J Am Chem Soc* 2018, **140**(15)**:** 5088-5101.

25. Pearson RM, Lim C-H, McCarthy BG, Musgrave CB, Miyake GM. Organocatalyzed Atom Transfer Radical Polymerization Using N-Aryl Phenoxazines as Photoredox Catalysts. *J Am Chem Soc* 2016, **138**(35)**:** 11399-11407.

26. Sartor SM, Chrisman CH, Pearson RM, Miyake GM, Damrauer NH. Designing High-Triplet-Yield Phenothiazine Donor-Acceptor Complexes for Photoredox Catalysis. *J Phys Chem A* 2020, **124**(5)**:** 817-823.

27. Sartor SM, Lattke YM, McCarthy BG, Miyake GM, Damrauer NH. Effects of Naphthyl Connectivity on the Photophysics of Compact Organic Charge-Transfer Photoredox Catalysts. *J Phys Chem A* 2019, **123**(22)**:** 4727-4736.

28. Sartor SM, McCarthy BG, Pearson RM, Miyake GM, Damrauer NH. Exploiting Charge-Transfer States for Maximizing Intersystem Crossing Yields in Organic Photoredox Catalysts. *J Am Chem Soc* 2018, **140**(14)**:** 4778-4781.

29. Theriot JC, Miyake GM, Boyer CA. N,N-Diaryl Dihydrophenazines as Photoredox Catalysts for PET-RAFT and Sequential PET-RAFT/O-ATRP. *ACS Macro Lett* 2018, **7**(6)**:** 662-666.

30. Singh VK, Yu C, Badgujar S, Kim Y, Kwon Y, Kim D*, et al.* Highly Efficient Organic Photocatalysts Discovered via a Computer-Aided-Design Strategy for Visible-Light-Driven Atom Transfer Radical Polymerization. *Nat Cat* 2018, **1**(10)**:** 794-804.

31. Song Y, Kim Y, Noh Y, Singh VK, Behera SK, Abudulimu A*, et al.* Organic Photocatalyst for ppm-Level Visible-Light-Driven Reversible Addition–Fragmentation Chain-Transfer (RAFT) Polymerization with Excellent Oxygen Tolerance. *Macromolecules* 2019, **52**(15)**:** 5538-5545.

32. Theriot JC, McCarthy BG, Lim C-H, Miyake GM. Organocatalyzed Atom Transfer Radical Polymerization: Perspectives on Catalyst Design and Performance. *Macromol Rapid Commun* 2017, **38**(13)**:** 1700040.

33. Benniston AC, Harriman A, Li P, Rostron JP, van Ramesdonk HJ, Groeneveld MM*, et al.* Charge Shift and Triplet State Formation in the 9-Mesityl-10-methylacridinium Cation. *J Am Chem Soc* 2005, **127**(46)**:** 16054-16064.

34. Dance ZEX, Mickley SM, Wilson TM, Ricks AB, Scott AM, Ratner MA*, et al.* Intersystem Crossing Mediated by Photoinduced Intramolecular Charge Transfer: Julolidine−Anthracene Molecules with Perpendicular π Systems. *J Phys Chem A* 2008, **112**(18)**:** 4194-4201.

35. Lewis-Borrell L, Sneha M, Bhattacherjee A, Clark IP, Orr-Ewing AJ. Mapping the multi-step mechanism of a photoredox catalyzed atom-transfer radical polymerization reaction by direct observation of the reactive intermediates. *Chem Sci* 2020, **11**(17)**:** 4475-4481.

36. Koyama D, Dale HJA, Orr-Ewing AJ. Ultrafast Observation of a Photoredox Reaction Mechanism: Photoinitiation in Organocatalyzed Atom-Transfer Radical Polymerization. *J Am Chem Soc* 2018, **140**(4)**:** 1285-1293.

37. Lewis-Borrell L, Sneha M, Bhattacherjee A, Clark IP, Orr-Ewing AJ. Mapping the Multi-Step Mechanism of a Photoredox Catalyzed Atom-Transfer Radical Polymerization Reaction by Direct Observation of the Reactive Intermediates. *Chem Sci* 2020, **11**(17)**:** 4475-4481.

38. Sneha M, Lewis-Borrell L, Shchepanovska D, Bhattacherjee A, Tyler J, Orr-Ewing AJ. Solvent-Dependent Photochemical Dynamics of a Phenoxazine-based Photoredox Catalyst. *Z Phys Chem* 2020, **234:** 1475-1494.

39. Lim C-H, Ryan MD, McCarthy BG, Theriot JC, Sartor SM, Damrauer NH*, et al.* Intramolecular Charge Transfer and Ion Pairing in N,N-Diaryl Dihydrophenazine Photoredox Catalysts for Efficient Organocatalyzed Atom Transfer Radical Polymerization. *J Am Chem Soc* 2017, **139**(1)**:** 348-355.

40. Saveant JM. A Simple Model for the Kinetics of Dissociative Electron Transfer in Polar Solvents. Application to the Homogeneous and Heterogeneous Reduction of Alkyl Jalides. *J Am Chem Soc* 1987, **109**(22)**:** 6788-6795.

41. McCarthy B, Miyake GM. Organocatalyzed Atom Transfer Radical Polymerization Catalyzed by Core Modified N-Aryl Phenoxazines Performed under Air. *ACS Macro Lett* 2018, **7**(8)**:** 1016-1021.

42. Donaldson PM, Greetham GM, Shaw DJ, Parker AW, Towrie M. A 100 kHz Pulse Shaping 2D-IR Spectrometer Based on Dual Yb:KGW Amplifiers. *J Phys Chem A* 2018, **122**(3)**:** 780-787.

43. Bhattacherjee A, Sneha M, Lewis-Borrell L, Tau O, Clark IP, Orr-Ewing AJ. Picosecond to Millisecond Tracking of a Photocatalytic Decarboxylation Reaction Provides Direct Mechanistic Insights. *Nat Comm* 2019, **10**(1)**:** 1-7.

44. Orr-Ewing AJ. Perspective: How can Ultrafast Laser Spectroscopy Inform the Design of New Organic Photoredox Catalysts for Chemical and Materials Synthesis? *Struct Dyn* 2019, **6**(1)**:** 010901/010901-010901/010906.

45. Bhattacherjee A, Sneha M, Lewis-Borrell L, Amoruso G, Oliver TAA, Tyler J*, et al.* Singlet and Triplet Contributions to the Excited-State Activities of Dihydrophenazine, Phenoxazine, and Phenothiazine Organocatalysts Used in Atom Transfer Radical Polymerization. *J Am Chem Soc* 2021, **143**(9)**:** 3613–3627.

46. Sneha M, Bhattacherjee A, Lewis-Borrell L, Clark IP, Orr-Ewing AJ. Structure-Dependent Electron Transfer Rates for Dihydrophenazine, Phenoxazine, and Phenothiazine Photoredox Catalysts Employed in Atom Transfer Radical Polymerization. *J Phys Chem B* 2021.

47. Isse AA, Bortolamei N, De Paoli P, Gennaro A. On the Mechanism of Activation of Copper-Catalyzed Atom Transfer Radical Polymerization. *Electrochimica Acta* 2013, **110:** 655-662.

48. Chaudhuri S, Acharya A, Nibbering E, Batista V. Regioselective Ultrafast Photoinduced Electron Transfer from Naphthols to Halocarbon Solvents. *J Phys Chem Lett* 2019, **10**(11)**:** 2657-2662.

49. Rosspeintner A, Angulo G, Vauthey E. Bimolecular Photoinduced Electron Transfer Beyond the Diffusion Limit: The Rehm–Weller Experiment Revisited with Femtosecond Time Resolution. *J Am Chem Soc* 2014, **136**(5)**:** 2026-2032.

50. Montalti M, Credi A, Prodi L, Gandolfi MT, Editors. *Handbook of Photochemistry - Third Edition*. CRC Press LLC, 2006.

51. Jockusch S, Yagci Y. The active role of excited states of phenothiazines in photoinduced metal free atom transfer radical polymerization: singlet or triplet excited states? *Poly Chem* 2016, **7**(39)**:** 6039-6043.

52. Lattke YM, Corbin DA, Sartor SM, McCarthy BG, Miyake GM, Damrauer NH. Interrogation of O-ATRP Activation Conducted by Singlet and Triplet Excited States of Phenoxazine Photocatalysts. *J Phys Chem A* 2021, **125**(15)**:** 3109-3121.

53. Koyama D, Donaldson PM, Orr-Ewing AJ. Femtosecond to microsecond observation of the photochemical reaction of 1,2-di(quinolin-2-yl)disulfide with methyl methacrylate. *PCCP* 2017, **19**(20)**:** 12981-12991.

54. McCarthy B, Miyake GM. Organocatalyzed Atom Transfer Radical Polymerization Catalyzed by Core Modified N-Aryl Phenoxazines Performed under Air. *ACS Macro Lett* 2018, **7**(8)**:** 1016-1021.

55. Wootthikanokkhan J, Peesan M, Phinyocheep P. Atom transfer radical polymerizations of (meth)acrylic monomers and isoprene. *Eur Polym J* 2001, **37**(10)**:** 2063-2071.

5 Looking Beyond: Direct Observation of Reactive Intermediates by Transient Spectroscopy Unravels the Mechanism of a Radical-Induced 1,2-Metallate Rearrangement[§]

5.1 Introduction

The pinacol boronic ester (Bpin) is a versatile moiety in organic chemistry since it can be readily employed in a myriad of C–C and C–heteroatom bond forming reactions, allowing direct access to a variety of organic molecules.[1] The versatility of organoboron reagents cannot be overstated, as many modern pharmaceuticals utilise boron in their synthesis,[2] and contemporary boron chemistries can produce complex three-dimensional structures that are desirable in drug discovery.[3,4] The reactivity of alkyl pinacol boronic esters usually proceeds via the formation of the corresponding boronate complex by reaction with a nucleophile (e.g., alkoxides or organometallics), from which intermolecular (e.g. transmetallation) or intramolecular (1,2-metallate rearrangement) transfer of the alkyl substituent is observed. The latter pathway is a particularly powerful tool because stereoelectronic requirements ensure the 1,2-metallate rearrangements proceed in a stereospecific manner, therefore the stereochemical integrity of the migrating alkyl substituent is maintained throughout the reaction. Indeed, the last decades have witnessed significant advances in the chemistry of boronate complexes.

[§]Manuscript Submitted: L. Lewis-Borrell, M. Sneha, I. P. Clark, V. Fasano, Adam Noble, Varinder K. Aggarwal, and A. J. Orr-Ewing, *J. Am. Chem. Soc.* **2021,** Accepted

The writer is the first author of the referenced manuscript and: prepared all the samples in the lab of Prof. Varinder Aggarwal (University of Bristol, School of Chemistry); collected transient absorption data with Dr. Mahima Sneha (University of Bristol, School of Chemistry, Prof. Andrew Orr-Ewing group), and Dr. Ian P. Clark (Central Laser Facility, Research Complex at Harwell, Science and Technology Facilities Council, Rutherford Appleton Laboratory); performed quantum mechanical calculations on infrared frequencies while transition state calculations were performed by Dr. Valerio Fasano (University of Bristol, School of Chemistry, Prof Varinder Aggarwal group); analysed the data and interpreted the data; wrote the manuscript in cooperation with Dr. Mahima Sneha, Dr. Adam Noble, Dr. Valerio Fasano and the principal investigators, Prof. Varinder Aggarwal, and Prof. Andrew Orr-Ewing.

These range from classic examples like the Suzuki-Miyaura cross-coupling,[5] Zweifel olefination,[6] and the Matteson homologation,[7] to more contemporary processes where the 1,2-metallate rearrangement is induced by initial reaction of a boronate complex with an alkyl radical.[8] This radical-induced 1,2-metallate rearrangement chemistry was first discovered independently by the groups of Aggarwal and Studer.[9,10,11] They showed that vinyl boronate complexes react with alkyl radicals to furnish an intermediate boronate radical which was proposed to undergo electron transfer with another molecule of alkyl iodide, triggering a 1,2-metallate rearrangement. Since these initial reports, there have been many other examples that utilise this general idea because these methods are particularly useful for forming C–C bonds between two sp^3 centres.[8,12,13]

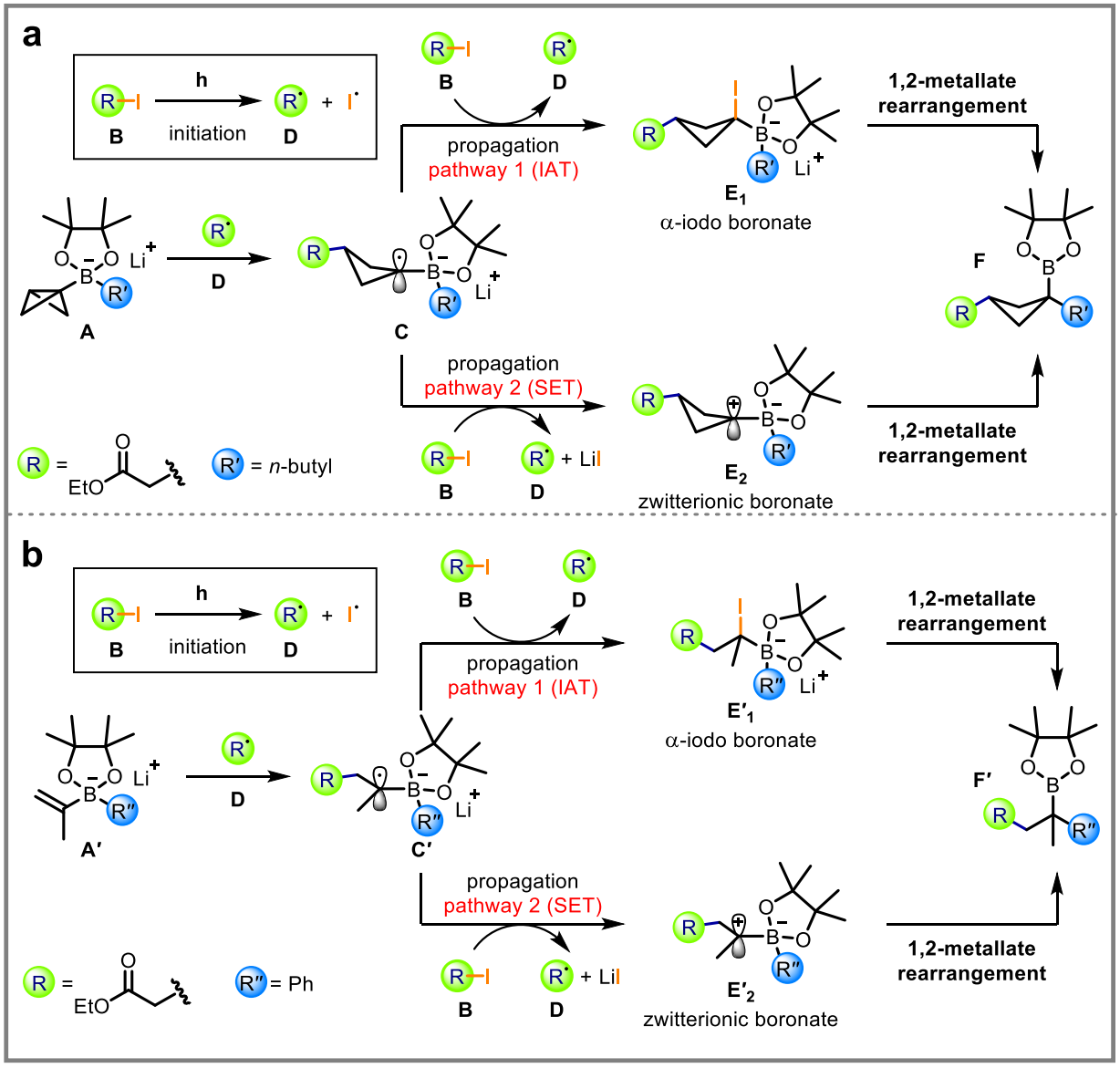

Figure 5.1. *Proposed mechanisms for the radical-induced 1,2-metallate rearrangement of* ***a.*** *BCB boronates with electron-deficient alkyl iodides.* ***b.*** *Vinyl boronates with electron-deficient alkyl iodides.*

The Aggarwal group recently reported a radical-induced 1,2-metallate rearrangement of bicyclo[1.1.0]butyl (BCB) boronate complexes.[12] The mechanism of this process is shown in **Figure 5.1a**, with the reaction of *n*-butyl BCB boronate complex **A** with ethyl iodoacetate (**B**) used as a representative example. Photolysis of the C–I bond of **B** generates an electrophilic radical **D** that adds to the strained central C–C σ-bond of the BCB group in **A** to form α-boryl radical **C**. From **C**, the reaction may proceed via two separate pathways: (1) Iodine atom transfer (IAT) to generate α-iodo boronate complex $\mathbf{E_1}$; or (2) single electron transfer (SET) to form zwitterionic boronate complex $\mathbf{E_2}$. Both pathways regenerate radical **D** to propagate the radical chain cycle, and both $\mathbf{E_1}$ and $\mathbf{E_2}$ undergo facile 1,2-metallate rearrangement to furnish product **F**. This sequence of α-boryl radical formation followed by IAT or SET occurs in all radical-induced 1,2-metallate rearrangements. While both pathways are often considered possible, all previous reports have favoured the SET pathway, but lack direct experimental evidence.[8,9,10,12,14]

5.1.1 Previous Mechanistic Studies of Radical Induced 1,2-Metallate Rearrangements

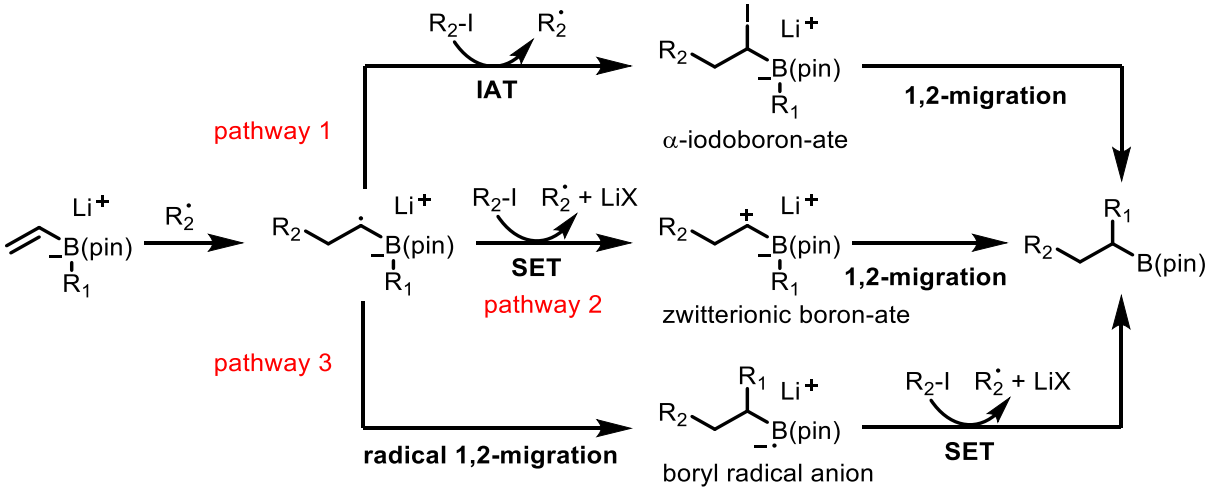

Figure 5.2. *Proposed propagation pathways for the radical-induced 1,2-metallate rearrangement using vinyl boronates.*

This section will describe in more detail how the proposed SET mechanism was rationalised and the evidence behind it. One key question about the mechanism is what pathway the chain propagation operates through (**Figure 5.2**): iodine atom transfer (IAT, pathway 1), single electron transfer (SET, pathway 2) or radical 1,2-migration (pathway 3). Reports by Aggarwal[9] and Studer[10] both highlighted that the chain propagating step could operate under either SET or IAT mechanisms, while the radical migration was not discussed. However, Studer and coworkers argued that the reaction operates through a SET mechanism based upon the following indirect observations. Use of Togni's reagent as a radical precursor, which cannot

react via IAT but will provide a CF_3 radical upon SET, in combination with vinyl phenyl pinacolboron ate in acetonitrile at room temperature and in the presence of tetrabutylammonium iodide as an initiator gave the alcohol (after NaOOH oxidation) in 41 % yield. Consequently, this process was argued to occur through an SET mechanism. It was also argued that successful transformations were accomplished in electron deficient alkyl iodides which would be easily reduced by SET. Likewise, cyclohexyl iodide and 1-iodoademantane, which are usually reactive in IAT mechanisms, did not produce products. However, the authors did concede that reactivity of the sec- and tert- alkyl radical species would be lowered toward boron ate, presumably due to steric demands. Finally, Studer and coworkers pointed to DFT studies which show electron removal from the α-boryl radical intermediate is a highly exothermic process. However, from these same studies, they also showed that IAT was kinetically feasible and were unable to calculate the transition state for the SET process. Their calculations of the orbitals involved in the electron transfer revealed that the orbital energy gap ($\Delta\varepsilon$= 3.5 eV) is low, and the orbitals are in close proximity. These computational outcomes suggest that the coupling between the ground state and the electron transfer state promotes ET, but they noted that, based on the same argument, IAT would also be possible.

A complementary study by Renaud and coworkers, proposed an operationally simpler form of Studer's work.[14] This study investigated the reaction mechanism, and the authors proposed that on top of the already mentioned SET and IAT pathways, a third pathway may also be possible in which a radical 1,2-migration takes place followed by SET from the boryl radical anion (**Figure 5.2**, pathway 3). Renaud et al. performed four key mechanistic experiments (**Scheme 5.1**) to try to discern between the three pathways in **Figure 5.2**. Firstly, a radical clock experiment (**Scheme 5.1a**) with 3,3-(dimethylprop-2-en-1yl)malonate **3** and vinyl boron ate produced **2** in 63% yield. They claimed that no cyclisation product formation, which for a 5-exo-trig is expected to be very fast, supports a SET mechanism. The second experiment (**Scheme 5.1b**) involved coupling the vinyl boron ate with either bromide **5a** or the selenide **5b,** in which only the bromide produced products while the selenide did not, and the starting selenide was not fully consumed. These observations argued against the atom transfer pathway and added credence to the SET pathway. Their third experiment (**Scheme 5.1c**) explored the possibility of pathway 3; here, boron ate complex is reacted with Bu_3SnH and AIBN. Only products **7** and **8** were isolated stemming from a 5-exo-trig cyclisation, HAT, and subsequent oxidative work-up. The authors argued that this outcome proves that the radical 1,2-migration is not in operation.

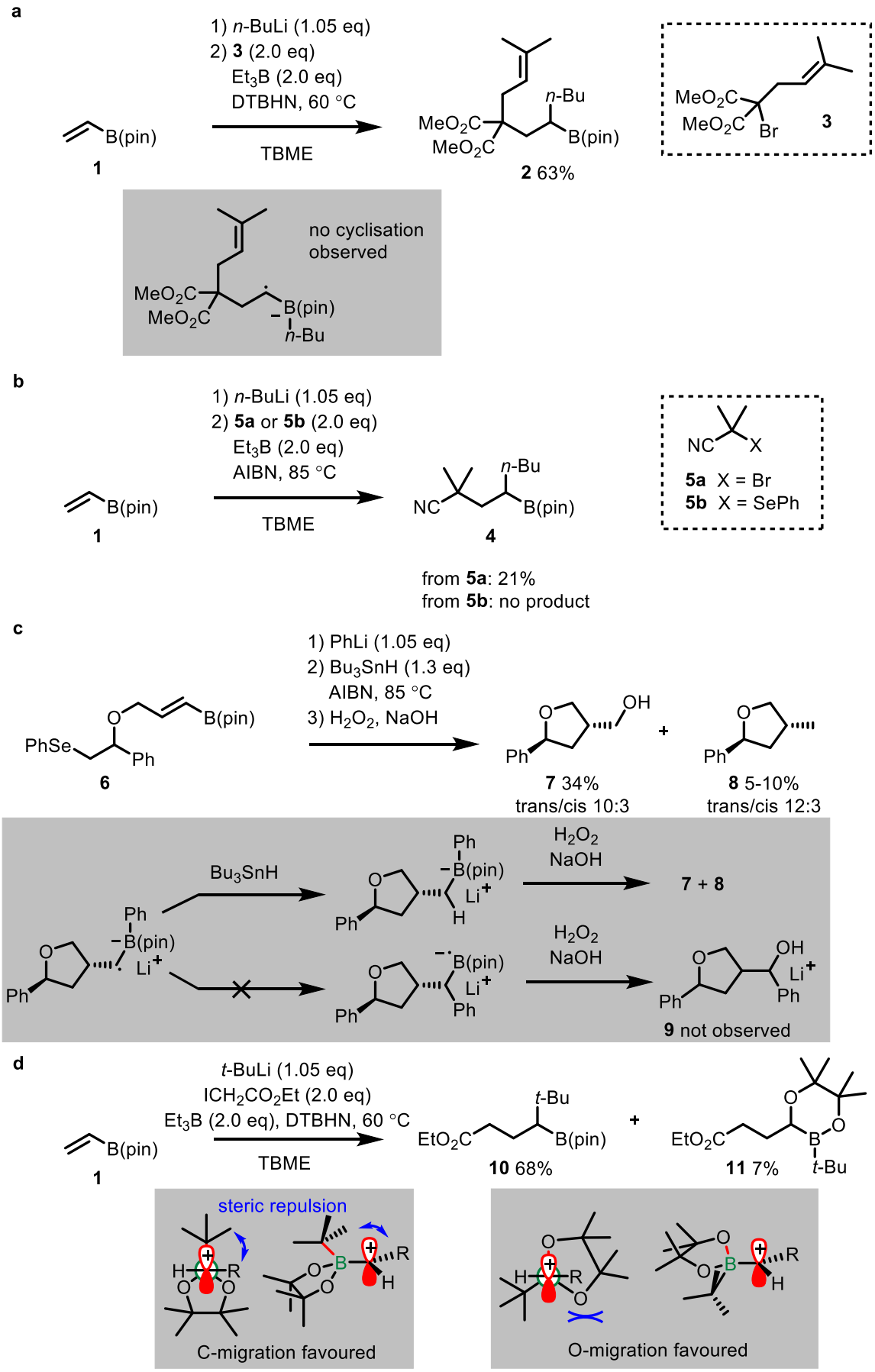

Scheme 5.1. *Renaud's mechanistic investigations, adapted from ref:* [14].

Finally, the fourth experiment (**Scheme 5.x1d**) showed that when ethyl iodoacetate is coupled with vinyl boron ate there is a 68 % yield for the desired C-migration product while a 7 % yield is observed for the unproductive O-migration. From this, Renaud and coworkers contended that the experiment supports formation of the zwitterionic intermediate through a SET pathway as high selectivity (C-migration vs O-migration) suggests a fast 1,2 migration.

5.1.2 Outlook

This chapter presents new evidence from direct spectroscopic observations of intermediate species that, in contrast to previous reports,[9,10,14] supports an IAT pathway. This evidence derives from two experimental systems: the first uses BCB boronate, and the second vinyl boronate (for which the mechanism is shown in **Figure 5.1b**). Consistent mechanistic conclusions drawn from the two studies provide a basis for a revised interpretation of previously reported radical-induced 1,2-metallate rearrangements and firm principles for rational design of new 1,2-metallate reactions. Furthermore, the mechanistic distinction between IAT and SET becomes important for stereoselective 1,2-metallate rearrangements, where the stereochemical outcome of the reaction is determined by the approach of the alkyl iodide to the sterically less hindered face of the α-boryl radical (e.g., **C**).[12] This steric influence is expected to be greater for the inner-sphere IAT mechanism than the outer-sphere SET mechanism, because the two species must approach more closely to reach the transition state.[15] An understanding of the mechanism for this step will guide future research in stereoselective radical-induced 1,2-metallate rearrangements, including extending this concept to enantioselective catalysis.[16]

The balance of competition between pathways can be unravelled by monitoring the spectroscopic signatures of the reactive intermediates directly and tracking their reaction kinetics by time-resolved measurements. One technique capable of this is transient absorption spectroscopy (TAS), because it can access the timescales over which photochemical and bimolecular reactions occur.[17,18,19] As synthetic photochemistry has seen a surge in popularity over the last decade, so too has the use of TAS to tackle mechanistic questions about newly developed photochemical and photoredox catalysed reactions.[20,21,22,23] Quantitative mechanistic studies such as these are necessary to progress beyond the qualitative models commonly used to develop new catalysts and chemical schemes.

The experimental method used in the present study combines the strengths of both femtosecond and nanosecond TAS methods in a single experiment, allowing photochemical reactions to be

observed over a wide range of timescales from sub-picosecond to milliseconds.[17,19,24,25,26,27] Important here is the use of an infrared probe which allows the various functional groups within different intermediates to be identified because they are more spectrally distinct than for UV-visible probes. In this thesis, the experiment is referred to as transient vibrational absorption spectroscopy (TVAS). The Orr-Ewing laboratory has previously applied this approach to study various reaction pathways,[17,19,28] including a photoredox decarboxylation reaction catalysed by phenanthrene and dicyanobenzene.[18] The current study demonstrates application of this TVAS method over a wide range of timescales to understand the mechanism of the radical-induced 1,2-metallate rearrangement. In so doing, it illustrates why access to these different dynamic timescales proves useful for unravelling the pathways of photochemical reactions.

By moving from a qualitative understanding of the radical-induced 1,2-metallate rearrangement to a quantitative description, it is hoped further innovation within this chemical space will be encouraged − either through new applications or new variants of the chemistry.[17,20,21,23,29,30] The results herein lead to a more holistic understanding of the reaction mechanism and support a different mechanistic hypothesis to the one proposed previously.[9,10,12,14]

5.2 Results and Discussion

5.2.1 BCB Boronate

5.2.1.1 Spectral Decomposition

Before performing the TVAS studies of the radical-induced 1,2-metallate rearrangement shown in **Figure 5.1**, the steady state behaviour of ethyl iodoacetate is first examined in the UV-visible and infrared regions, which dictated the choices for pump and probe wavelengths. **Figure E5** shows the UV-vis spectrum of ethyl iodoacetate, which is comprised of two bands, typically referred to as the A (210-310 nm) and B (190-200 nm) bands.[31] To achieve optimal absorption by ethyl iodoacetate, the UV pump laser was set to 280 nm to excite the A band and induce C–I bond photolysis to produce an iodine atom and ethyl acetate radical **D**. **Figure E6** shows the infrared absorption spectra of tetrahydrofuran (THF) and ethyl iodoacetate in THF between 500 and 2500 cm^{-1}. THF is almost transparent in a window around 1450 – 1950 cm^{-1}, and the carbonyl stretch for ethyl iodoacetate lies within this range. Hence, a broadband IR probe spanning this wavenumber interval was used to observe transient spectra.

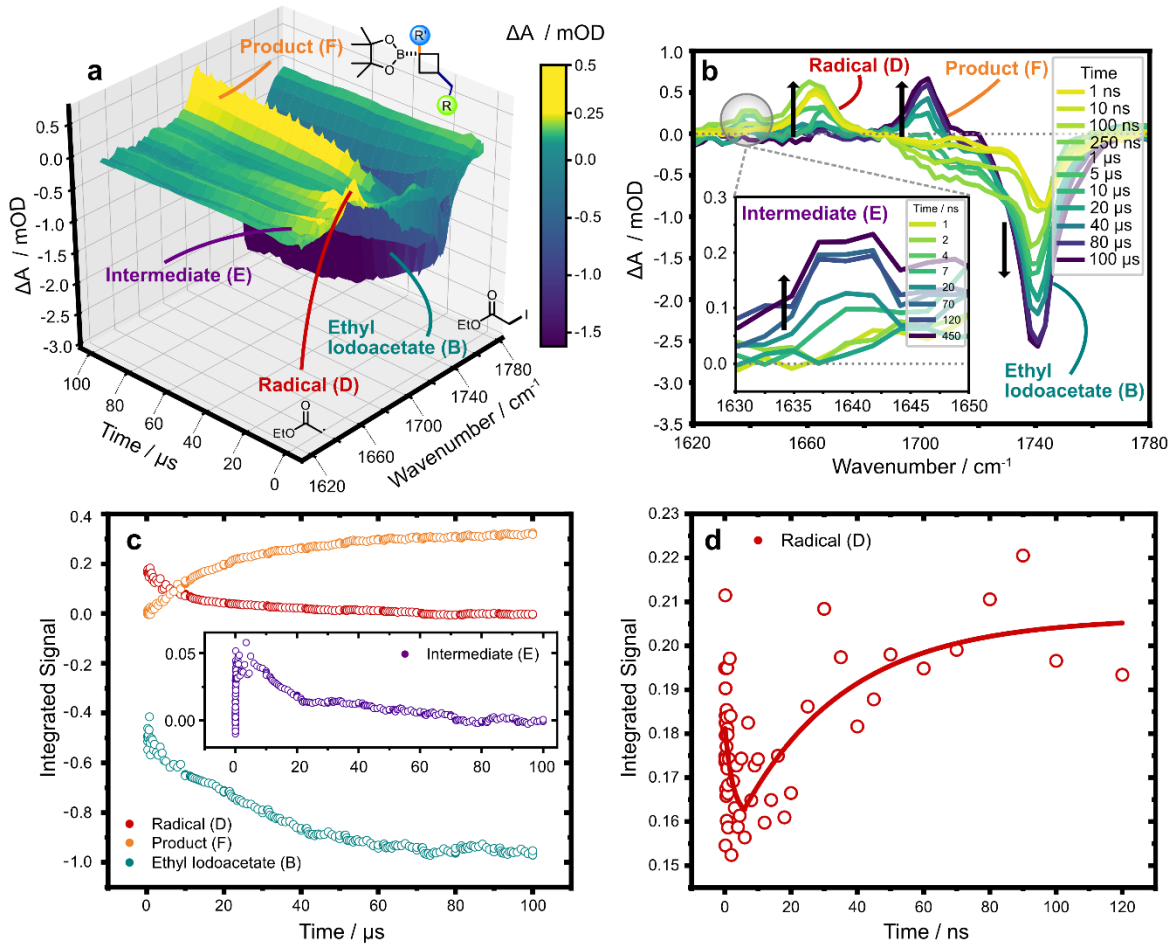

Figure 5.3. TVAS measurements for the radical chain reaction of ethyl iodoacetate (40 mM) and BCB boronate (30 mM) in THF following pulsed excitation of ethyl iodoacetate at 280 nm. ***a:*** *TVA spectra presented as a surface plot.* ***b:*** *Example TVA spectra at selected time delays shown by the inset key. Black arrows adjacent to features indicate directions of change;* ***c:*** *Corresponding kinetic traces for times from 100 ns - 100 μs for radical D (red), ethyl iodoacetate (turquoise), intermediate E (purple, inset), and product F (orange) obtained by decomposition of the time-dependent spectra in (a). Data have been passed through a Savitzky-Golay filter to remove electronic noise from the transient spectra. Integrated intensities are scaled to maximum magnitude of 1 at late time for the ethyl iodoacetate depletion.* ***d:*** *Corresponding kinetic trace for the pre-steady state behaviour (10 ps – 120 ns) for radical D (red). Solid lines are independent exponential fits to the decay and rise of this feature giving time constants* $\tau_1 = 110 \pm 60$ *ps,* $\tau_2 = 38.9 \pm 8.1$ *ns. The uncertainties reported are standard errors from the least squares fit of the exponential model to the data.*

Figures 3a and **3b** show two representations of the TVA spectra for a solution containing both ethyl iodoacetate and BCB boronate **A** following excitation of ethyl iodoacetate by a pump laser at 280 nm. **Figure 5.3a** is a surface plot with colour representing a pump induced change in absorbance, and **Figure 5.3b** is a line plot in which each coloured line represents a separate time delay. Four absorption features are present in the spectra: (i) At 1736 cm^{-1} there is a ground-state bleach (GSB) corresponding to depletion of the ethyl iodoacetate starting material, which grows deeper in time because the radical chain cycle removes further ethyl iodoacetate; (ii) At 1700 cm^{-1} a feature appears which is assigned to product **F**; (iii) An absorption band at 1660 cm^{-1} corresponds to the ethyl acetate radical **D**; (iv) A weak feature at

1640 cm^{-1} grows in over hundreds of nanoseconds and then decays away in microseconds, which is assigned to an intermediate **E** in the radical chain cycle whose importance will become clearer below.

Kinetics for the BCB boronate spectra are split into two separate time windows: **Figure 5.3c** shows the kinetics of the reaction in the period when radical **D** is reacting but being regenerated by radical chain propagation (see **Figure 5.1**), from 100 ns to 100 μs; and **Figure 5.3d** highlights the kinetics of the initial depletion of radical **D** and recovery by the early stages of chain propagation, from 10 ps to 120 ns. The kinetics in **Figure 5.3d** show a distinct decay and rise which are attributed to the following two processes: (i) boronate **A** reacting with radical **D** (decay, 110 ± 60 ps); and (ii) intermediate **C** reacting with ethyl iodoacetate to reform radical **D** (rise, 38.9 ± 8.1 ns). This is a rare example where in real time the initial depletion of the radical species compensated by its reformation in a chain propagation cycle can be seen. The initial decay is too fast to happen by diffusive reactions alone, and therefore static (non-diffusive) reactions must also be occurring. The kinetics in **Figure 5.3c** show the radical decaying to baseline while the product grows, with the ethyl iodoacetate depletion increasing until all radical chains terminate and the reaction finishes on a timescale spanning tens of microseconds. If the proposed SET mechanism were to be in operation (see pathway 2 in **Figure 5.1**), the kinetics of growth of the product should approximately match those of recovery of the radical after its initial depletion. This is because the zwitterionic intermediate species (**E_2**) formed by SET is expected to undergo rapid 1,2-rearrangement to form the product, with previous density functional theory (DFT) studies reporting a barrierless transition for a related system.[10] However, these kinetics are not observed in the data; instead, recovery of the radical and formation of products show exponential time constants that differ by a factor of 500. In addition, an intermediate spectral feature **E** is observed which is not accounted for by the SET model, but instead suggests the formation of α-iodo boronate **E_1** via the IAT model.

5.2.1.2 Kinetic Modelling

In this section, it is shown how the kinetic model was iteratively developed through consideration of the parameters needed to describe the observed kinetic data. Five models are described for the BCB boronate system, each of which improves on the previous one. With each step, the considerations made to improve the overall fit to the experimental data are laid out. This approach shows how the final model was reached, and demonstrates that the simpler models are not adequate to describe the recorded observations. Lessons learnt from the BCB

boronate data are then applied to a different system which employs a vinyl boronate, Section 5.2.2. Here, the original model is again shown not to map well onto the measured data and a new model is derived which adequately explains all the experimental observations. Finally, the fitting of each model to the experimental data is described, as well as the constraints that were applied in determining the optimum least squares fit.

5.2.1.2.1 Model 1: Simple radical chain

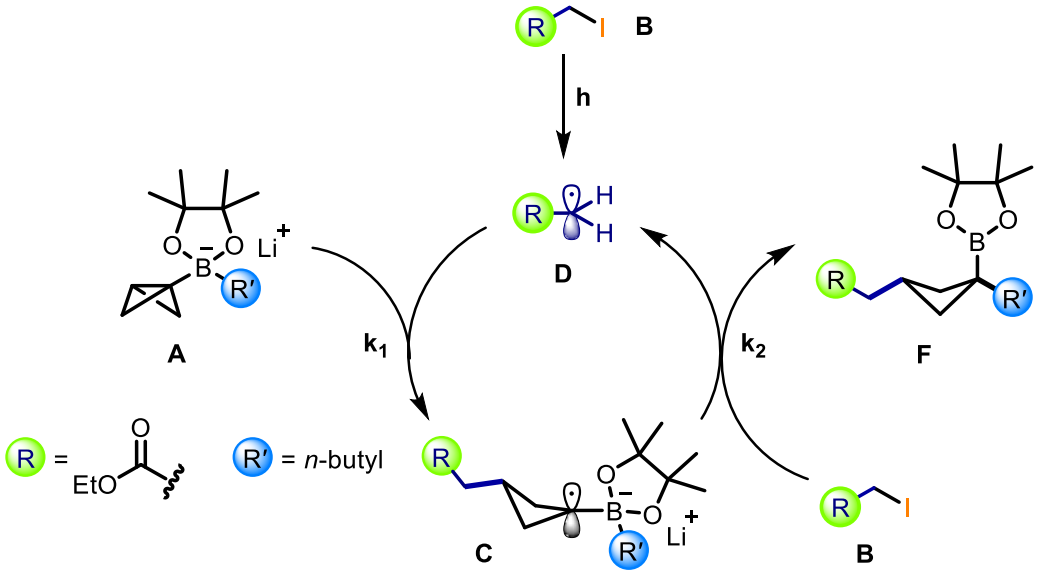

Figure 5.4. *A chemical scheme for the reactions assumed to occur in model 1.*

The differential equations which describe model 1 are:

$$\frac{d[A]}{dt} = -k_1[D][A]$$

$$\frac{d[B]}{dt} = -k_2[C][B]$$

$$\frac{d[C]}{dt} = k_1[A][D] - k_2[C][B]$$

$$\frac{d[D]}{dt} = -k_1[D][A] + k_2[C][B]$$

$$\frac{d[F]}{dt} = k_2[C][B]$$

Initial approximations of these rate coefficients come from preliminary exponential fits to the experimental data for the decay and rise of radical **D**. i.e.

$$k_1 = \frac{\frac{1}{110\ ps}}{30\ mM} = 3.03\ \times 10^{11}\ M^{-1}s^{-1} \cong 1.3 \times 10^{10}\ M^{-1}s^{-1}$$

$$k_2 = \frac{\frac{1}{38.9\ ns}}{40\ mM} = 6.4\ \times 10^{8} M^{-1}s^{-1}$$

Because the current model does not account for any static reactions (reactions happening without diffusion because of pre-associated reactants in the equilibrated solution) an upper limit for k_1 is the diffusion limiting value of $1.3\ \times 10^{10}\ M^{-1}s^{-1}$.[32] The fit outcomes are plotted as simulated time-dependent concentrations of various species, calculated from the kinetic model using best fit values of the kinetic parameters, for direct comparison with experimental data.

Solving these equations numerically produces the plots in **Figure 5.5**. From these plots, areas where model 1 performs well and where it does not can be seen, as summarised in **Table 5.1**.

Table 5.1. *Summary of positive and negative features of the predictions from kinetic model 1 shown in Figure 5.4.*

Model captures	**Model does not capture**
The qualitative decay and rise of the radical **D** concentration.	Initial rise of radical **D**, which is 3 orders of magnitude slower than experimental data.
	Depth of decay and rise of the radical **D** is deeper than experimentally observed.
	Formation of product is about 50 times too fast.
	Radical **D** does not decay at longer times.
	Initial concentration of radical **D** (currently set at 1mM) is too high.

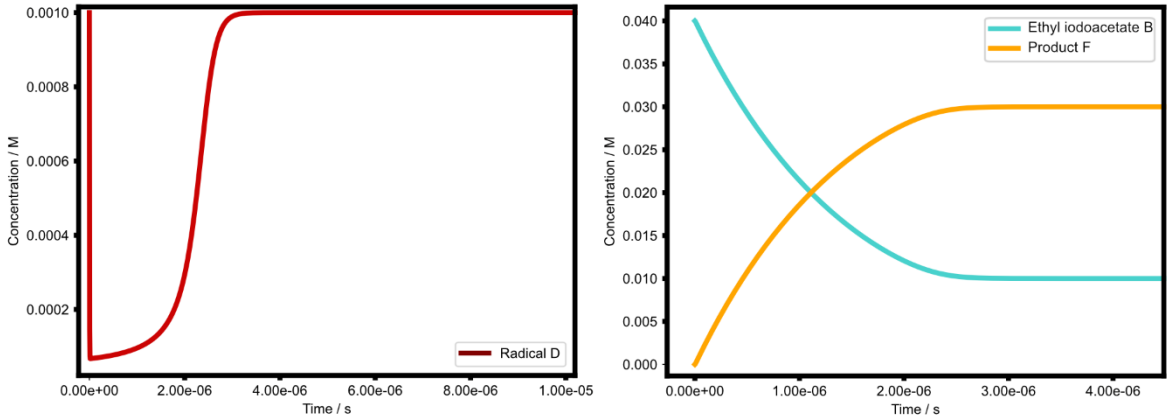

Figure 5.5. *The integrated kinetic model 1 for radical* ***D****, ethyl iodoacetate and product* ***F****. The plotted curves are produced by numerically integrating the differential equations derived from the model shown in Figure 5.4.*

5.2.1.2.2 Model 2: Adding radical termination

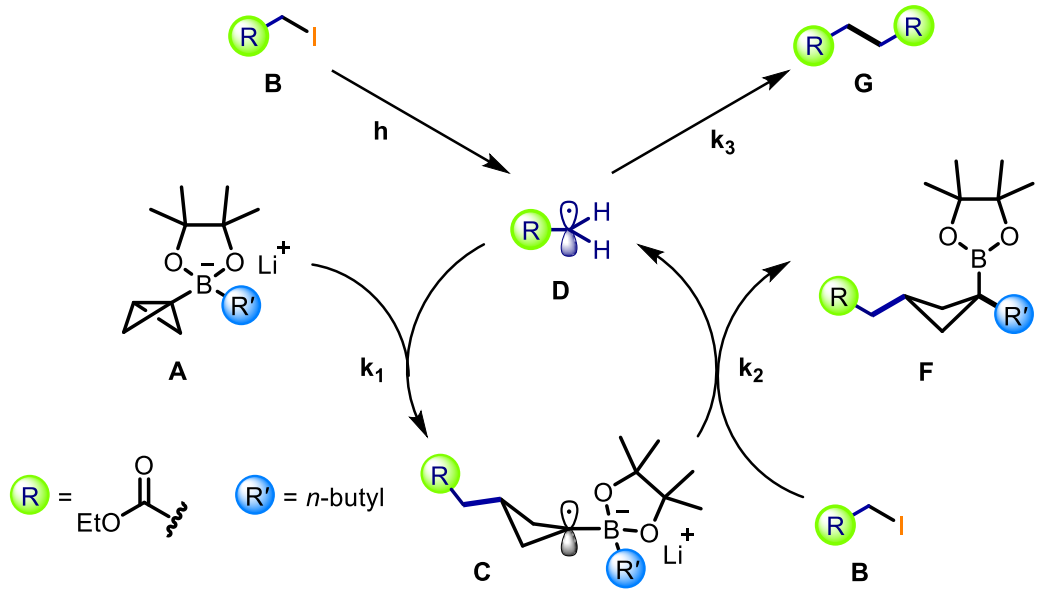

Figure 5.6. *A chemical scheme for the reactions assumed to occur in model 2.*

The differential equations which describe model 2 are shown below. The additional parameters needed to account for the decay of radical **D** by radical-radical termination are highlighted in bold.

$$\frac{d[A]}{dt} = -k_1[D][A]$$

$$\frac{d[B]}{dt} = -k_2[C][B]$$

$$\frac{d[C]}{dt} = k_1[D][A] - k_2[C][B]$$

$$\frac{d[D]}{dt} = -k_1[D][A] + k_2[C][B] - \mathbf{2}\boldsymbol{k_3}[\boldsymbol{D}][\boldsymbol{D}]$$

$$\frac{d[F]}{dt} = k_2[C][B]$$

$$\frac{\boldsymbol{d[G]}}{\boldsymbol{dt}} = \boldsymbol{k_3}[\boldsymbol{D}][\boldsymbol{D}]$$

Where $k_1 = 1.3 \times 10^{10} M^{-1}s^{-1}$, $k_2 = 6.4 \times 10^{8} M^{-1}s^{-1}$, and $k_3 = 0.8 \times 10^{9} M^{-1}s^{-1}$

k_3 has been approximated from an exponential fit to the long-time decay of radical **D** in the same manner as k_1 and k_2 in model 1. Solving these equations numerically produces the plots in **Figure 5.7**. From these plots, areas where the model performs well and where it does not are summarised in **Table 5.2**.

Table 5.2. *Summary of positive and negative features of the predictions from the kinetic model 2 shown in Figure 5.6.*

Model captures	**Model does not capture**
Initial decay and rise of the radical **D** concentration	Initial rise of radical **D**, which is 3 orders of magnitude too slow.
Radical **D** decays at longer times.	Depth of decay and rise of the radical **D** is too deep.
	Formation of product is about 50 times too fast.
	Initial concentration of radical **D** (currently set at 1mM) is too high.

The additions to the model have solved one of the issues set out in **Table 5.1**. This is apparent in **Figure 5.7**, where the radical concentration is now predicted to decay at longer times due to the radical-radical termination reaction included in the model.

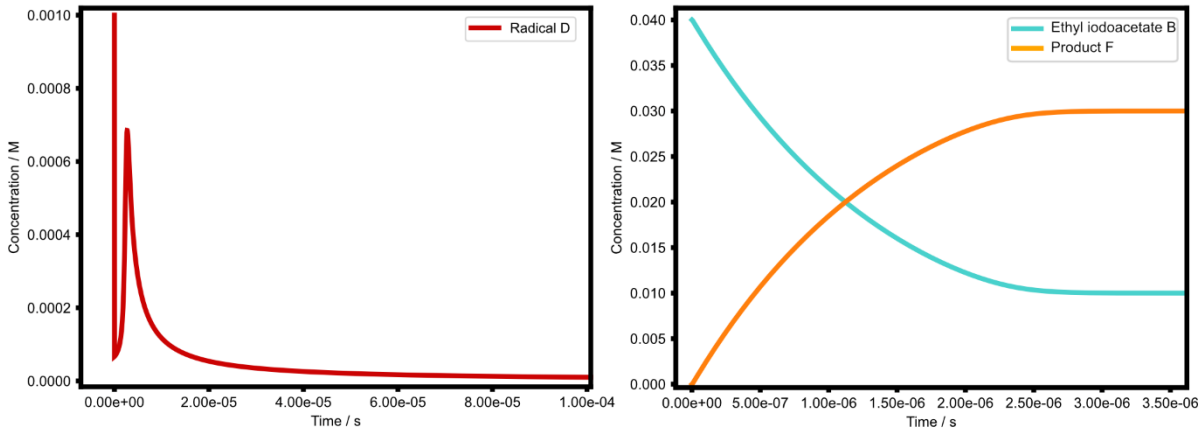

Figure 5.7. *The integrated kinetic model 2 for radical* ***D****, ethyl iodoacetate and product* ***F****. The plotted curves are produced by numerically integrating the differential equations derived from the model shown in Figure 5.6.*

5.2.1.2.3 Model 3: Adding intermediate E

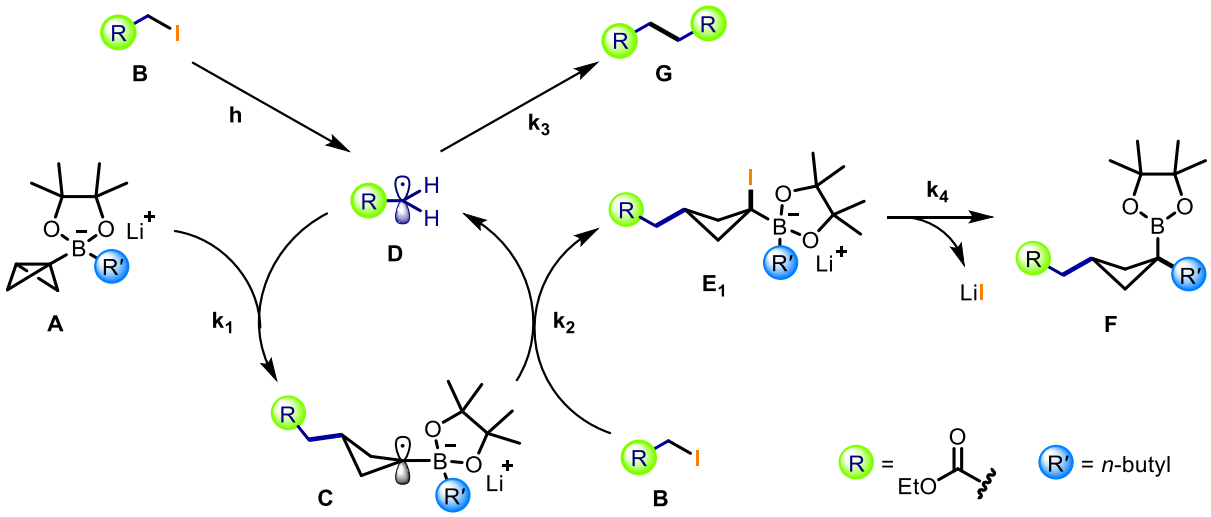

Figure 5.8. *A chemical scheme for the reactions assumed to occur in model 3.*

To correct for the too-rapid growth of product F in model 2, an intermediate species E is invoked in the third iteration of the model, as shown in **Figure 5.8**. The differential equations which describe model 3 are shown below. The additional parameters needed to account for the inclusion of intermediate **E** are highlighted in bold font.

$$\frac{d[A]}{dt} = -k_1[D][A]$$

$$\frac{d[B]}{dt} = -k_2[C][B]$$

$$\frac{d[C]}{dt} = k_1[D][A] - k_2[C][B]$$

$$\frac{d[D]}{dt} = -k_1[D][A] + k_2[C][B] - 2k_3[D][D]$$

$$\boldsymbol{\frac{d[E]}{dt} = k_2[C][B] - k_4[E]}$$

$$\boldsymbol{\frac{d[F]}{dt} = k_4[E]}$$

Where $k_1 = 1.3 \times 10^{10}\ M^{-1}s^{-1}$, $k_2 = 6.4 \times 10^{8}\ M^{-1}s^{-1}$, $k_3 = 0.8 \times 10^{9}\ M^{-1}s^{-1}$, and $k_4 = 4.2 \times 10^{4}\ s^{-1}$

Solving these equations numerically produces the plots in **Figure 5.9**. From these plots, areas where the model performs well and where it does not are summarised in **Table 5.3** .

Table 5.3. *Summary of positive and negative features of the predictions from the kinetic model 3 shown in Figure 5.8.*

Model captures	**Model does not capture**
Initial decay and rise of the radical **D** concentrations	Rate of initial rise of radical **D**, which is 3 orders of magnitude too slow.
Radical **D** decays at longer times.	Depth of decay and rise of the radical **D** is too deep.
Product **F** forms at rates similar to experimental kinetics.	Initial concentration of radical **D** (currently set at 1mM) is too high.

The addition of intermediate **E** has solved one of the issues set out in **Table 5.2**. As is now evident in **Figure 5.9**, the rate of product formation is controlled by the rates of growth and decay of intermediate **E**.

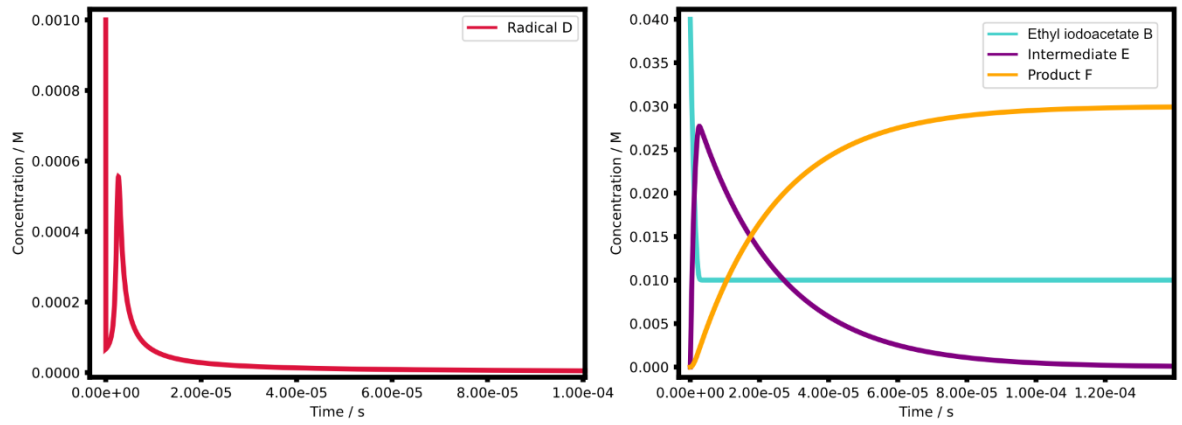

Figure 5.9. *The integrated kinetic model 3 for radical* ***D****, ethyl iodoacetate, intermediate* ***E*** *and product* ***F****. The plotted curves are produced by numerically integrating the differential equations derived from the model shown in Figure 5.8.*

5.2.1.2.4 Model 4: Adding static quenching

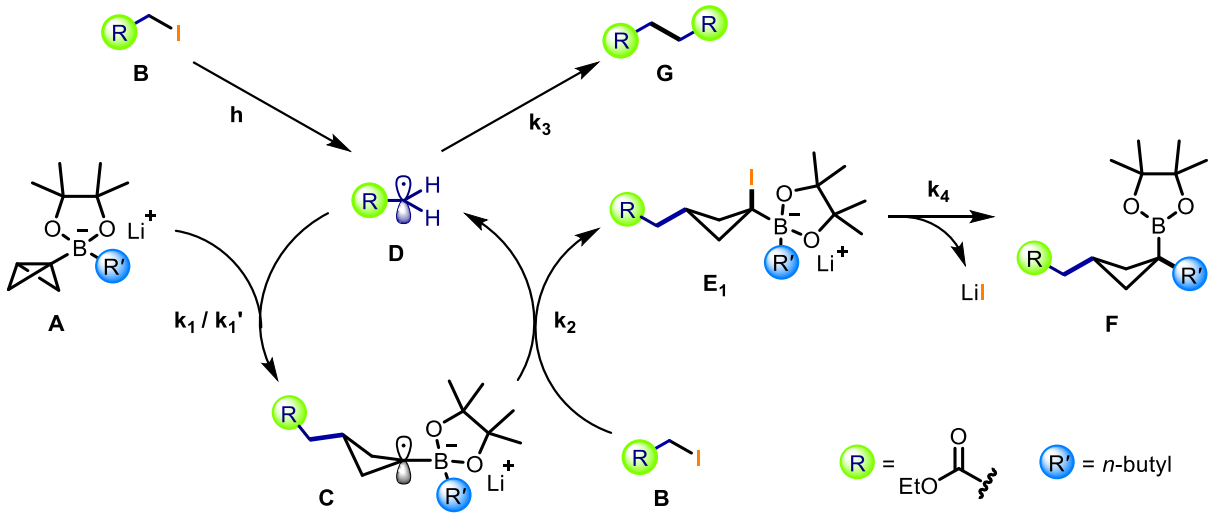

Figure 5.10. *A chemical scheme for the reactions assumed to occur in model 4.*

The next adjustment to the model, denoted as model 4 and shown in **Figure 5.10**, addresses the rate of growth of radical D, which is three orders of magnitude too slow in model 3. The key addition is a static reaction pathway for A with photochemically produced radical D (from photolysis of B), with a rate coefficient k_1'. The differential equations which describe model 4 are shown below. The additional terms needed to account for the static quenching of radical **D** (denoted in the equations as a separate species **H** when initially in close proximity to **A**) are highlighted in bold font. To correct the pre-steady state kinetics of the radical, a new rate coefficient k_1' has been introduced which signifies a static reaction between the boronate **A** and 'static radical' **H**. This reaction is included to account for observed reactions that are *faster* than the rate of diffusion.

$$\frac{d[A]}{dt} = -k_1[D][A] - \boldsymbol{k_1'[A][H]}$$

$$\frac{d[B]}{dt} = -k_2[C][B]$$

$$\frac{d[C]}{dt} = k_1[D][A] + \boldsymbol{k_1'[A][H]} - k_2[C][B]$$

$$\frac{d[D]}{dt} = -k_1[D][A] + k_2[C][B] - 2k_3[D][D]$$

$$\frac{d[E]}{dt} = k_2[C][B] - k_4[E]$$

$$\frac{d[F]}{dt} = k_4[E]$$

$$\frac{d[G]}{dt} = k_3[D][D]$$

$$\boldsymbol{\frac{d[H]}{dt} = -k_1'[A][H]}$$

Where $k_1 = 1 \times 10^8\, M^{-1}s^{-1}$, $k_1' = 3.03 \times 10^{11} M^{-1}s^{-1}$, $k_2 = 6.4 \times 10^8\, M^{-1}s^{-1}$, $k_3 = 0.8 \times 10^9\, M^{-1}\, s^{-1}$, $k_4 = 4.2 \times 10^4\, s^{-1}$

The initial concentrations of **H** (static radical) and **D** (corresponding to a radical that reacts after diffusion, henceforth described as a diffusive radical) sum to a total initial concentration of 0.1 mM ($[H]_0 + [D]_0$ = 0.05 mM + 0.05 mM = 0.1 mM), which is slightly lower than the previous approximation but still an order of magnitude away from the value calculated from knowledge of the experimental parameters (see later). As can be seen from the plots in **Figure 5.11**, the initial fall and recovery of the radical concentrations now happen at faster rates, in better agreement with experimental data. **Table 5.4** highlights the few remaining problems in the model.

Table 5.4. *Summary of positive and negative features of the predictions from the kinetic model 4 shown in Figure 5.10.*

Model captures	**Model does not capture**
Initial decay and rise of the radical **D** kinetics are observed in the model.	Initial concentration of radical **D** (currently set at 0.1 mM) is too high.
Radical **D** decays at longer times.	
Product **F** forms at rates similar to the experimental kinetics.	
Correct **rates** of initial decay and rise of radical **D** are observed due to the inclusion of static reactions.	
Depth of decay and rise of the radical **D**.	

Splitting the initial quenching reaction of radical with boronate into static and diffusive components has solved the issues with the pre-steady state kinetics of the radical. The final issue to resolve arises because the initial total concentration of the radical (**D** + **H**) has been set to 0.1 mM, which is higher than expectations based on experimental parameters, so the model needs to be refined further.

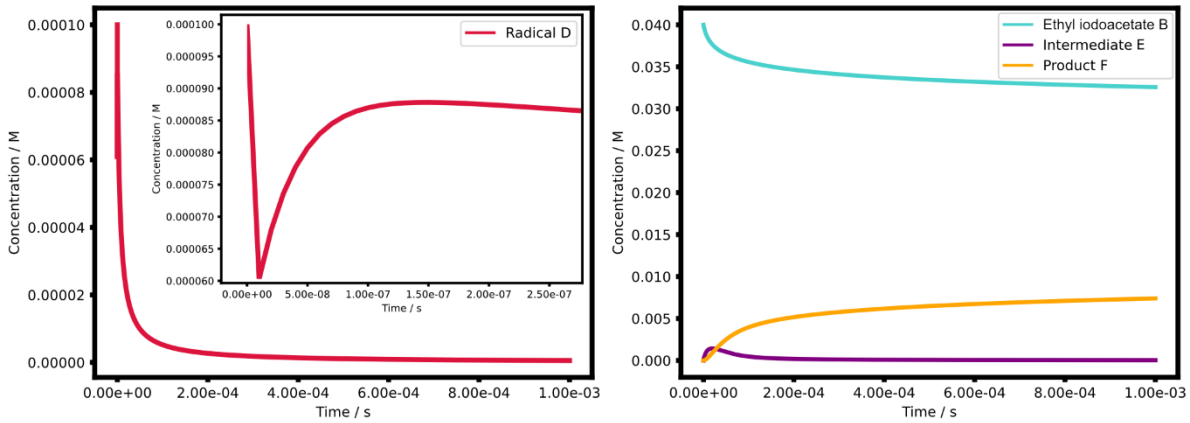

Figure 5.11. *The integrated kinetic model 4 for radical **D**, ethyl iodoacetate, intermediate **E** and product **F**. The plotted curves are produced by numerically integrating the differential equations derived from the model shown in Figure 5.10.*

5.2.1.2.5 Model 5: Adding correct radical concentration and additional termination pathway

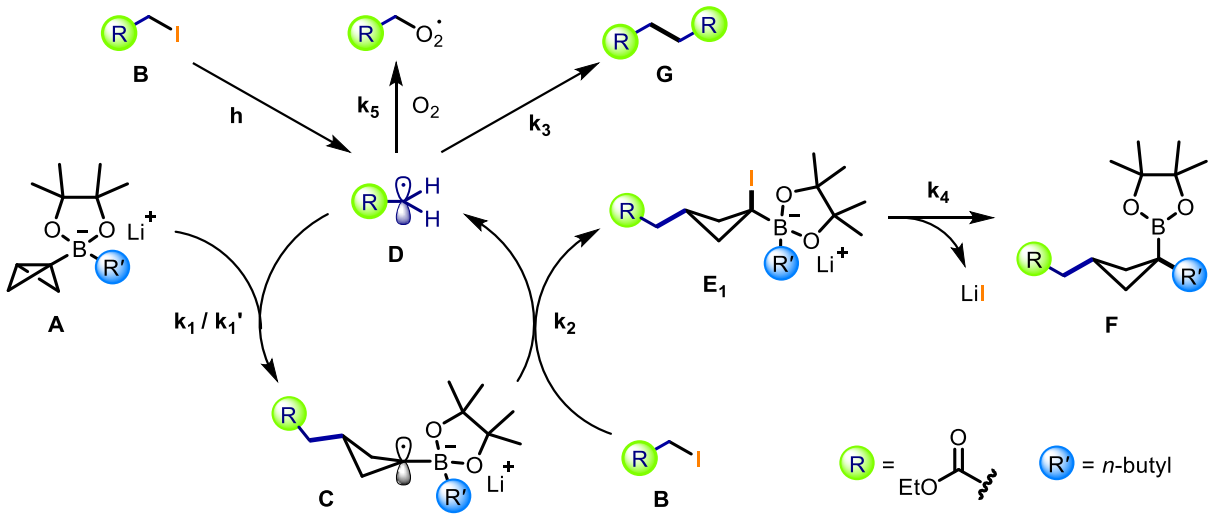

Figure 5.12. *A proposed model for the radical-induced 1,2-metallate rearrangement of BCB boronates which accounts for the current experimental observations. Derived values of the rate coefficients are given in the main text.*

The final iteration to the model addresses the disagreement between the value of the initial radical concentration that works best in the numerical fits and the expected concentration based on the experimental conditions. To bring these values into better agreement, an additional radical termination pathway with dissolved O_2 is required in version 5 of the model. The differential equations which describe model 5 are shown below. The additional parameters needed to account for the termination reaction with O_2 are highlighted in bold font.

$$\frac{d[A]}{dt} = -k_1[D][A] - k_1'[A][H]$$

$$\frac{d[B]}{dt} = -k_2[C][B]$$

$$\frac{d[C]}{dt} = k_1[D][A] + k_1'[A][H] - k_2[C][B]$$

$$\frac{d[D]}{dt} = -k_1[D][A] + k_2[C][B] - 2k_3[D][D] - \boldsymbol{k_5[O_2][D]}$$

$$\frac{d[E]}{dt} = k_2[C][B] - k_4[E]$$

$$\frac{d[F]}{dt} = k_4[E]$$

$$\frac{d[G]}{dt} = 2k_3[D][D]$$

$$\frac{d[H]}{dt} = -k_1'[A][H]$$

$$\boldsymbol{\frac{d[O_2]}{dt} = k_5[O_2][D]}$$

Where $k_1 = 1 \times 10^9\ M^{-1}s^{-1}$, $k_1' = 3.03 \times 10^{11}\ M^{-1}s^{-1}$, $k_2 = 6.4 \times 10^9\ M^{-1}s^{-1}$, $k_3 = 0.8 \times 10^9\ M^{-1}s^{-1}$, $k_4 = 4.2 \times 10^5\ s^{-1}$, and $k_5 = 3.1 \times 10^5 M^{-1}s^{-1}$ are input as fixed values.

The additional termination pathway accounts for the remaining dissolved O_2 known to be in the system when running experiments.[17] The initial concentration of radical **D** has now been lowered from 0.1 mM to 48 μM which is in close agreement witha calculated value of 39 μM. This initial concentration was estimated using the Beer-Lambert law, the UV excitation laser beam volume (calculated from the UV beam radius (75 μm) at the laser focus and the UV beam pathlength (300 μm)) and the photolysis quantum yield.

$$UV\ photons\ per\ pulse = \frac{E\lambda}{hc} = \frac{0.22 \times 10^{-6} \cdot 280 \times 10^{-9}}{hc} = 3.1 \times 10^{11}$$

$$Photons\ absorbed\ per\ pulse\ = 10^{-A} \cdot UV\ photons\ per\ pulse = 10^{-0.4} \cdot 3.1 \times 10^{11}$$

$$= 1.23 \times 10^{11}$$

$$\phi = 1.00$$

Volume of the UV laser beam $V = \pi r^2 l = 5.3 \times 10^{-9}\ dm^3$

$$[Radical\ D] = \left(\frac{Photons\ asborbed\ per\ pulse\ \times\ \phi}{V}\right) / N_A$$

$$= 39\ \mu M$$

To compensate for the lower radical concentrations, the values of the rate coefficients k_1, k_2 and k_4 derived from the fit all increase in magnitude, as can be seen in **Figure 5.13**. **Table 5.5** summarises where the model is now.

Table 5.5. *Summary of positive and negative features of the predictions from the kinetic model 5 shown in Figure 5.12.*

Model captures	**Model does not capture**
Decay and rise of the radical **D** kinetics	
Radical **D** does not decay away.	
Product **F** is formed at rates similar to experimental kinetics.	
Initial rise of radical **D**	
Depth and rates of decay and rise of the radical **D**	
Initial concentration of radical **D** set at a value close to the estimated true value.	

As **Table 5.5** shows, a point has been reached where the problems set out with the initial model have all been resolved. Hence the kinetic model satisfactorily accounts for the observations from time-resolved spectroscopy and can now be applied in a global fit to the experimental data.

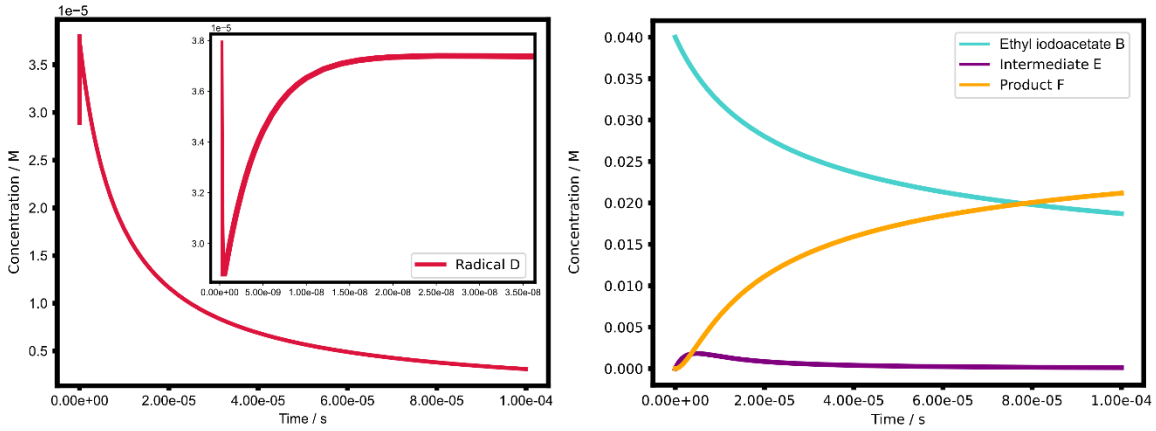

Figure 5.13. *The integrated kinetic model 5 for radical **D**, ethyl iodoacetate, intermediate **E** and product. Solid lines were produced by numerically integrating the differential equations derived from the model shown in Figure 5.12.*

Figure 5.12 shows the final version of the proposed model to account for the experimental data. In addition to a diffusive reaction of boronate **A** with radical **D** (with rate coefficient k_1), a static reaction between **A** and **D** is included (k_1') to account for the observed fast initial depletion of radical **D** after geminate recombination has finished. Radical termination by either self-reaction (k_3) or reaction with dissolved molecular oxygen (k_5) models the decay of the concentration of **D** observed over microseconds. Intermediate $\mathbf{E_1}$ is included to account for the

separate kinetic timescales for the radical chain propagation and the polar 1,2-rearrangement forming product **F**, as well as the observed absorption band at 1640 cm^{-1}. The slow conversion of intermediate $\mathbf{E_1}$ to product **F** is quantified by a unimolecular rate coefficient (k_4), and is the rate determining step in the reaction.

5.2.1.2.6 Chain Length

Chain length is an important metric for determining the efficiency of a propagating chain reaction. Here, two methods are detailed to calculate this. One uses a method previously reported by Yoon and co-workers[33] and another uses the knowledge gained about time scales from transient absorption measurements reported in this chapter.

Method 1

$$Number\ of\ cycles = \frac{[F]_{t\ =\ all\ chains\ terminated}}{[D]_0}$$

$$= \frac{30\ mM}{48\ \mu M} = 625\ cycles$$

Method 2

$$Number\ of\ cycles = \frac{t_{all\ chains\ terminated}}{t_{one\ chain\ cycle}}$$

$$= \frac{100\ \mu s}{100\ ns} = 1000\ cycles$$

5.2.1.2.7 Fitting

Having developed a plausible model for the chemistry, the experimental data were fitted to the model kinetic scheme, using measurements for three separate concentrations of boronate (30 mM, 50 mM, and 70 mM). Global least squares fitting of the full data set was done with a custom Python script using the lmfit, numpy and matplotlib packages.[34,35,36] To obtain a satisfactory fit with minimal correlation between the fitted variables (correlation < 0.5) the following additional parameterizations and constraints were put in place:

- The model represents data as concentration vs. time, whereas the experimental measurements were obtained as integrated absorbance vs. time. Therefore, a conversion had to be performed from concentration to integrated absorbance, and since

the conversion factors were not known, they were included as parameters in the least squares fitting.

- The ratio of diffusive radical to static radical concentrations was fixed to 3.8:1, so [Diffusive Radical]$_0$ = 38 μM and [Static Radical]$_0$ = 10 μM. A slightly higher concentration than what was calculated in section 5.2.1.2.5 was needed to achieve the best fit.
- The value of the rate coefficient k_1' was fixed in the fit to prevent any correlations between it and the k_1 value. The fixed value of k_1' was determined by exponential fitting of the early time decay of radical intensity on timescales where contributions from diffusive reaction are negligible.
- The rate coefficient k_2 was fixed to the calculated rate coefficient for diffusion in THF to avoid correlations with k_1.[32] This choice was guided by preliminary fits in which k_2 was allowed to vary and consistently returned values at, or close to, the diffusion limit.
- The rate coefficient k_5 was fixed in the fit to prevent any correlations with the value of k_3. The value is already known from previous data recorded on a similar system,[17] so a fitted value is not necessary in this case.
- The initial concentration of O_2 was taken to be 1×10^{-4} mol dm^{-3}, chosen by varying this parameter in the final fit to minimize the cross correlations between parameters. Although this value is an approximation of the true concentration (which is unknown in these measurements), it does lie below the maximum concentration for dissolved O_2 in THF of 10×10^{-3} mol dm^{-3} and so is a reasonable approximation of the true value for the N_2-sparged solutions used in this study.[32]

With the model now accounting for the key characteristics of the data, a global fit to all the experimental data was performed to derive values for the rate coefficients. The global fits to data for three concentrations of boronate **A** are shown in **Figure 5.14**, with data for 30 mM in **5.14a**, 50 mM in **5.14b**, and 70 mM in **5.14c**. For the 30 and 50 mM data sets, fits are to the time-dependent band intensities for radical **D**, intermediate $\mathbf{E_1}$ and product **F**, but only **D** and **F** band intensities are fitted for the 70 mM data because the weak absorption of intermediate $\mathbf{E_1}$ is masked at high concentrations of the boronate (**Figure E43**). The rate coefficients obtained from this global fit are $k_1 = 1.48 \times 10^9$ M^{-1} s^{-1}, $k_1' = (3.0 \pm 1.7) \times 10^{11}$ M^{-1} s^{-1}, $k_2 = 1.3 \times 10^{10}$ M^{-1} s^{-1}, $k_3 = 1.85 \times 10^9$ M^{-1} s^{-1}, and $k_4 = 3.5 \times 10^5$ s^{-1} (this value represents a lower bound of the true value, as shown by the sensitivity analysis presented in the Experimental Section, **Table E1**), and $k_5 = 3.1 \times 10^5$ M^{-1} s^{-1}. Use of a global fit gives negligible statistical errors for

the floated parameters k_1, k_3, and k_4 (< 0.1 %), but does not account for any systematic errors that may occur during data collection, or from the choice of kinetic model. The error shown for k_1', which was fixed in the fitting process, has been propagated from the measured time constant, τ_2.

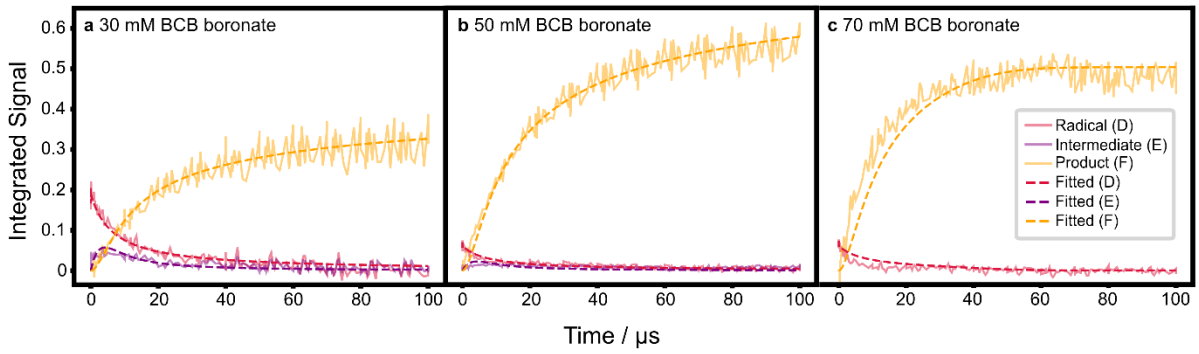

Figure 5.14. *Global least squares fit of model 5 in Figure 5.12 to data obtained for solutions with three different concentrations of the boronate **A**. The following fit parameters are used: rate coefficients for the reaction model in Figure 5.12; initial concentrations of radical **D** (for both static and diffusive reactions), BCB boronate and ethyl iodoacetate; and conversion factors to account for the change in scale from concentration in mM to Integrated Signal in arbitrary units. **a:** 30 mM boronate. **b:** 50 mM boronate. **c:** 70 mM boronate. Note that periodically repeating scatter in the data points at longer times is a consequence of the instrumental methods used to generate extended time delays for the measurements (see Methods).*

To assess which step is rate determining, the 2nd order rate coefficients must first be converted into pseudo 1st order rate coefficients by multiplying by the concentration of one reactant. Here, reaction steps 1 and 4 are compared. Multiplying k_1 by the initial concentration of boronate gives:

$$k_1(1^{st}\ order) \cong k_1 \times [A]_0 = (1.48 \times 10^9\ M^{-1}s^{-1}) \times (0.03\ M) = 4.44 \times 10^7 s^{-1}$$

The initial rate of this reaction is therefore about 100× faster than for step 4, which shows that *step 4* is indeed the rate determining step.

The observation of a rate-determining 1,2-metallate rearrangement (k_4) from an intermediate species to product **F** favours the model shown in **Figure 5.3**, where the intermediate is ascribed to α-iodo boronate $\mathbf{E_1}$. The data support a mechanism involving IAT from ethyl iodoacetate to intermediate **C**, which contrasts with previous reports by Studer,[10] Aggarwal[9,12] and Renaud,[14] who previously argued in favour of a SET pathway followed by 1,2-metallate rearrangement (see pathway 2 in **Figure 5.1a** and **b**).

5.2.1.2.8 Computational Studies

The predicted IR band wavenumber for the IAT intermediate $\mathbf{E_1}$ is consistent with the observed band position (**Figure E11**). However, distinguishing $\mathbf{E_1}$ from the SET pathway intermediate

$\mathbf{E_2}$ solely based on this IR band position is not possible because of the similarity between the predicted wavenumbers of their carbonyl bands. To support the intermediacy of $\mathbf{E_1}$ in the catalytic cycle, DFT calculations (M062X/6-311G(d,p)+LANL2DZ, with a polarizable continuum model [in THF])[37] were performed on a model substrate (**Figure 5.5**). While a barrier-less 1,2-metallate rearrangement was found for $\mathbf{E_{2\text{-}calc}}$ (generated upon SET), a significant kinetic barrier ($\Delta G^{\ddagger}$ = 35.7 kJ mol^{-1}) was calculated for $\mathbf{E_{1\text{-}calc}}$ (the product of IAT). Using the Eyring equation, the rate coefficient for this process is calculated to be 3.6 × 10^6 s^{-1} (at 298 K), which is in reasonable agreement with the measured value (≥ 3.5 × 10^5 s^{-1}). The combination of kinetic, spectroscopic, and computational theory therefore supports an IAT mechanism for this reaction. From these results it can be inferred that for the IAT mechanism to dominate the SET pathway, the formation of $\mathbf{E_2}$ must be slower than for $\mathbf{E_1}$.

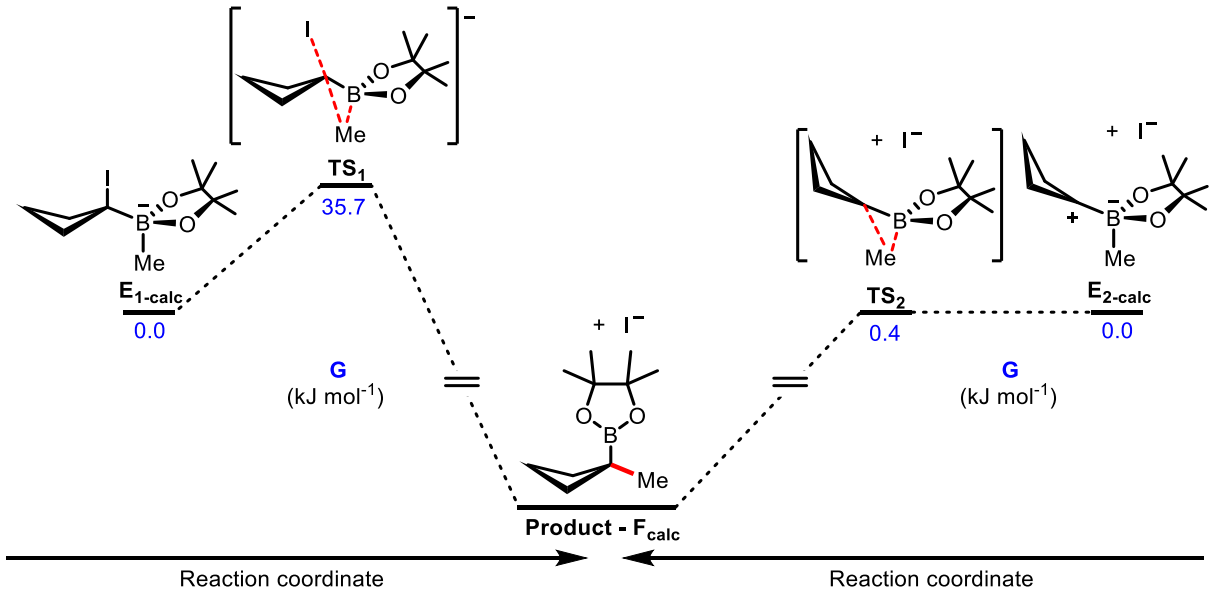

Figure 5.15. *Computed energy profiles for the 1,2-metallate rearrangement with and without the iodide as a leaving group.* $\boldsymbol{E_{1\text{-}calc}}$ *forms via the IAT pathway while* $\boldsymbol{E_{2\text{-}calc}}$ *forms via the SET pathway. The energies of* $\boldsymbol{E_{1\text{-}calc}}$ *and* $\boldsymbol{E_{2\text{-}calc}}$ *will differ, but both are arbitrarily set to 0.0 kJ mol*$^{-1}$ *to compare the energies of the transition states relative to the* $\boldsymbol{E}$ *intermediates for the two proposed reaction pathways.*

5.2.1.2.9 Literature Precedent

Although this assignment of IAT contrasts with the prior reports discussed in section 5.1.1, it should be noted that the assignment to SET itself was at odds with both prior and current work.[38,39,40,41,42,43,44,45] Atom transfer radical addition (ATRA) reactions have been well studied, particularly by Curran and coworkers who argued that IAT reactions typically take place with near-diffusion limited kinetics. **Table 5.6** summarizes deductions from studies of these kinetics.[38]

Table 5.6. *Typical rate coefficients for atom transfer reactions with differing C-X bonds. Recreated from ref: [38].*

X	Estimated k_X / M^{-1} s^{-1}	Propagation Efficiency
I	~10^9	excellent
Br	~10^6	very good
H	<10^3	poor

Work by Hiatt provides a more quantitative explanation of the observed rates, emphasizing that in systems containing radicals and iodides the IAT reaction will be orders of magnitude faster than any other competitive radical process.[43] Modern studies of ATRA reactions, in which the radicals are generated through photoredox cycles, show that atom transfer type products are dominant in radical chain systems similar to the one presented here.[41] Furthermore, in recent ATRA studies which use pinacol and benzyl N-methyliminodiacetyl (MIDA) boronic esters as radical acceptors, halogen atom transfer products also dominate.[44,45] Indeed, it appears appropriate to classify the radical-induced 1,2-metallate rearrangement under the umbrella of ATRA reactions.

5.2.2 Vinyl Boronate

Spurred on by both the literature precedent and results indicating the BCB boronate system proceeds through an IAT mechanism, the generality of this mechanistic pathway in other radical-induced 1,2-metallate rearrangements was examined. Therefore, the well-studied vinyl boronate complexes were also investigated. Their reactions are proposed to follow a similar mechanism to the BCB boronate system, as shown in **Figure 5.1b**.[9,10,14] For discussion of the analysis of the transient absorption spectra, please refer to the Experimental Section.

5.2.2.1 Kinetic Modelling

In this section, the reasoning developed for the successive kinetic model describing the BCB boronate system is applied to a new set of reactions using a vinyl boronate as the radical trap. The two possible pathways available in the vinyl boronate system are shown in **Figure 5.1b**. Note the different R' group used here, corresponding to a phenyl group rather than the *n*-butyl group used for the BCB boronate studies. This substitution might have consequences for the association of ions, as is discussed later.

5.2.2.1.1 Model 1: Simple chain with termination

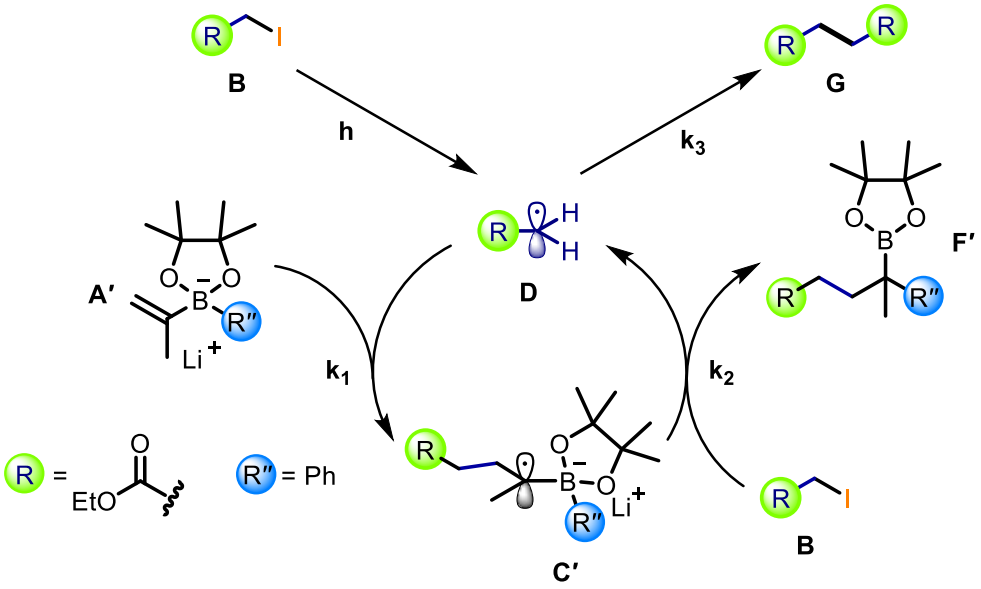

Figure 5.16. *A chemical scheme for the reactions assumed to occur in model 1.*

The simplest model developed to account for the observed kinetics of the vinyl boronate system is shown in **Figure 5.16** and labelled as model 1. This model used a simple chain mechanism previously proposed by Aggarwal and coworkers, and Studer and coworkers, with inclusion of a termination reaction to account for radical decay (**Figure 5.16**).[9,10] The differential equations which describe model 1 are:

$$\frac{d[A']}{dt} = -k_1[D][A']$$

$$\frac{d[B]}{dt} = -k_2[C'][B]$$

$$\frac{d[D]}{dt} = -k_1[D][A'] + k_2[C'][B] - 2k_3[D][D]$$

$$\frac{d[F']}{dt} = k_2[C'][B]$$

Where $k_1 = 1.3 \times 10^{10} M^{-1}s^{-1}$, $k_2 = 1.3 \times 10^{10} M^{-1}s^{-1}$ and $k_3 = 1 \times 10^{9} M^{-1}s^{-1}$

TVAS data for the photoinitiated reaction of ethyl iodoacetate and vinyl boronate indicate the reaction is approximately 25 times faster than for the BCB boronate under comparable conditions of starting material concentrations. The greater rate of reaction is proposed to be a consequence of a greater contribution from reactions of pre-associated reagents (i.e., a greater proportion of static instead of diffusional reactions) during the early stages of the reaction, and evidence for this proposition is presented here. The greater propensity for reagent pre-association may result from the additional π-bonds present in the chosen boronate (which contains vinyl and phenyl groups) and consequent halogen bonding between the ethyl iodoacetate and the vinyl boronate.

Model 1 shown in **Figure 5.16** does not correctly account for the experimental data. In particular, the predicted recovery of the pre-steady state radical **D** concentration after initial depletion occurs too slowly in the model simulations. Because, in this model, the rise of the product is controlled by the rate of this radical recovery, the product formation is predicted to be too fast. The experimentally observed rate of product formation is faster than observed for the BCB boronate reaction, but even if rate coefficients for the vinyl boronate system are set to the diffusion limit the model underpredicts the rate of radical **D** growth. A refined model is therefore required in which a larger contribution from static (non-diffusive) reactions is invoked. Such reactions were already shown to play a part in the chemistry of the BCB boronate, but now their importance is elevated. The suggested total contribution from static reactions may not be the entire truth and it is likely that diffusional reactions will take place at later times once all precoordinated radicals have reacted. However, to model this behaviour fully, k_1 would have to be allowed to switch from a static to a diffusional reaction value over time, which is not possible with the choice of modelling method.

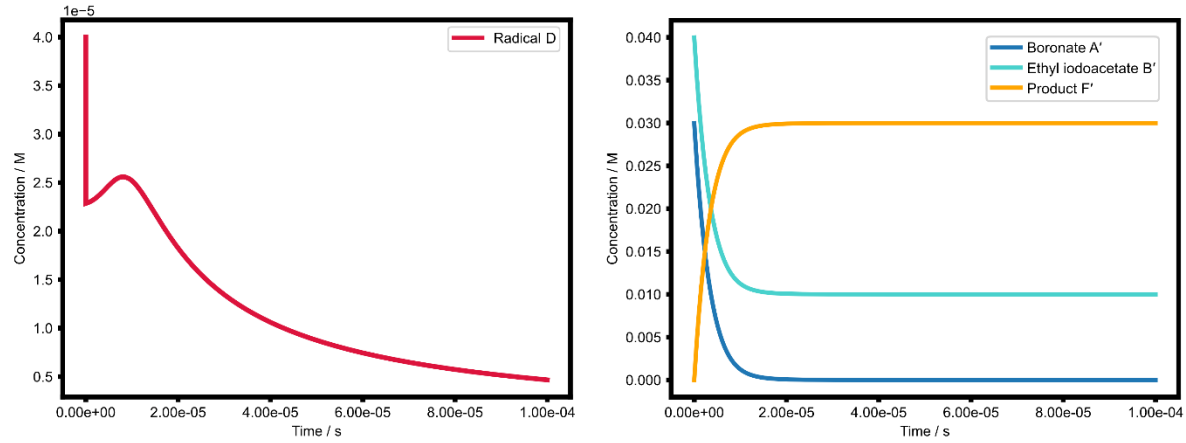

Figure 5.17. *The integrated kinetic model 1 for radical* ***D****, vinyl boronate, ethyl iodoacetate and product* ***F′****. The plotted curves were produced by numerically integrating the differential equations derived from the model shown in Figure 5.16.*

5.2.2.1.2 Model 2: Static chain reaction with termination

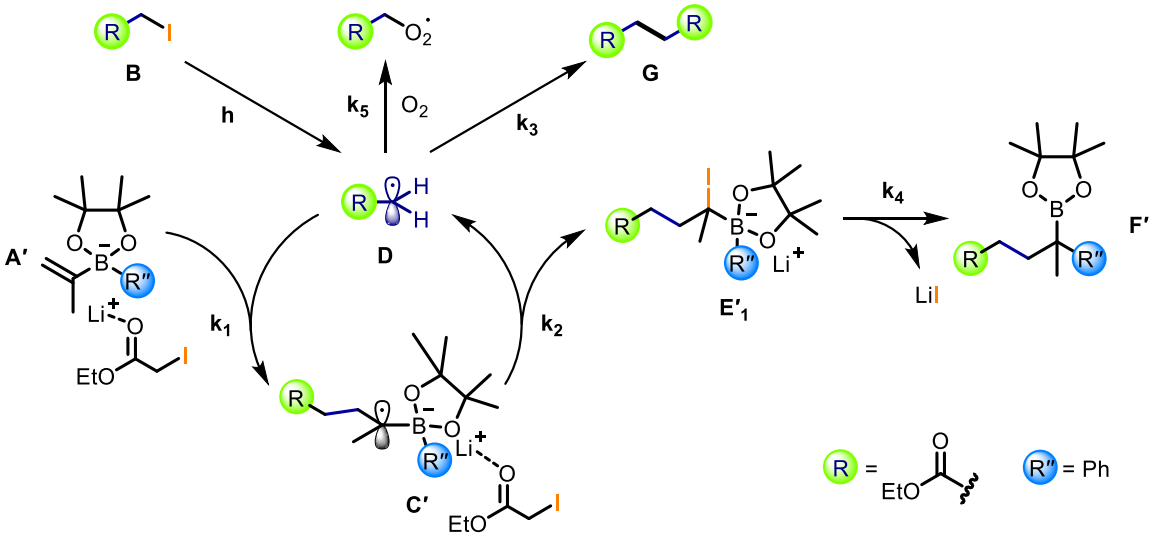

Figure 5.18. *A proposed model 2 for the radical-induced 1,2-metallate rearrangement of the chosen vinyl boronate system which accounts for the current experimental observations.*

To account for the fast rise of the radical and the slower rise of the product, a variant of intermediate **E₁′** invoked for the BCB boronate reaction is added to the next iteration of the model, denoted here as model 2 and shown in **Figure 5.18**. The differential equations which describe model 2 are shown below. Rate coefficients k_1 and k_2 now represent static reactions and terms corresponding to a vinyl derived version of intermediate **E₁′** have also been added. These changes are highlighted in bold.

$$\frac{d[A']}{dt} = -k_1[A'][D]$$

$$\frac{d[C']}{dt} = k_1[A][D] - \boldsymbol{k_2}[\boldsymbol{C'}]$$

$$\frac{d[D]}{dt} = -k_1[A'][D] + \boldsymbol{k_2}[\boldsymbol{C'}] - 2k_3[D][D] - k_5[D][O]$$

$$\frac{\boldsymbol{d[E']}}{\boldsymbol{dt}} = \boldsymbol{k_2}[\boldsymbol{C'}] - \boldsymbol{k_4}[\boldsymbol{E'}]$$

$$\frac{\boldsymbol{d[F']}}{\boldsymbol{dt}} = \boldsymbol{k_4}[\boldsymbol{E'}]$$

Where $k_1 = 8 \times 10^{11} M^{-1}s^{-1}$, $k_2 = 5 \times 10^{10}\, s^{-1}$, $k_3 = 3 \times 10^{10}\, M^{-1}s^{-1}$, $k_4 = 1 \times 10^{6}\, s^{-1}$, and $k_5 = 3.1 \times 10^{5}\, M^{-1}s^{-1}$

In a similar manner to the BCB system, intermediate $\mathbf{E_1'}$ stems from the iodine atom transfer reaction between intermediate $\mathbf{E_1'}$ and ethyl iodoacetate. This addition to the mechanism allows the quick recovery of the radical and a slower rise of products by separating the kinetics. There is some evidence for an intermediate $\mathbf{E_1'}$ type species in the recorded spectra based on the kinetics derived from the overlapping bands, as can be seen in Experimental Section 1.4.3.3.1. Using model 2 presented in **Figure 5.18** and **Figure 5.19**, the experimental data can be fitted. The fit procedure is discussed in the Section 5.2.2.1.3.

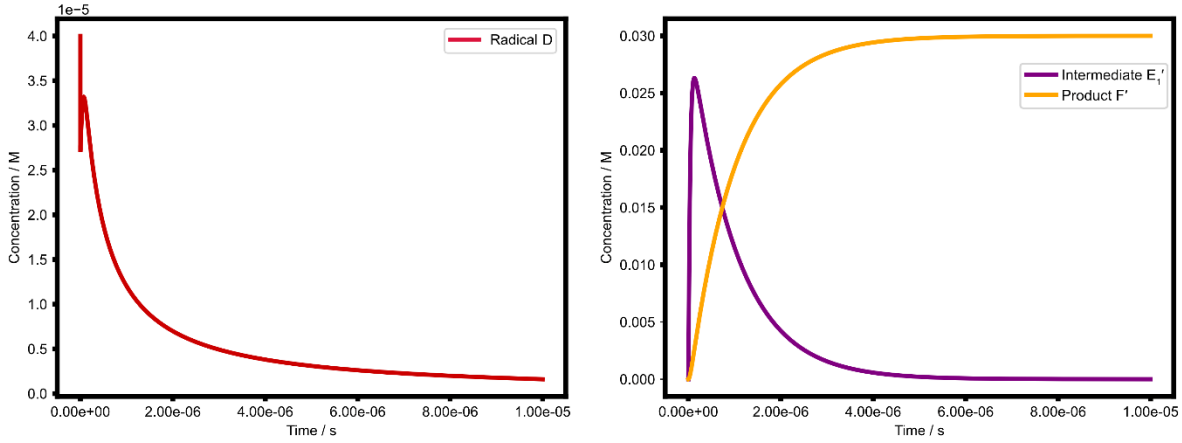

Figure 5.19. *The integrated kinetic model 2 plotted against time.*

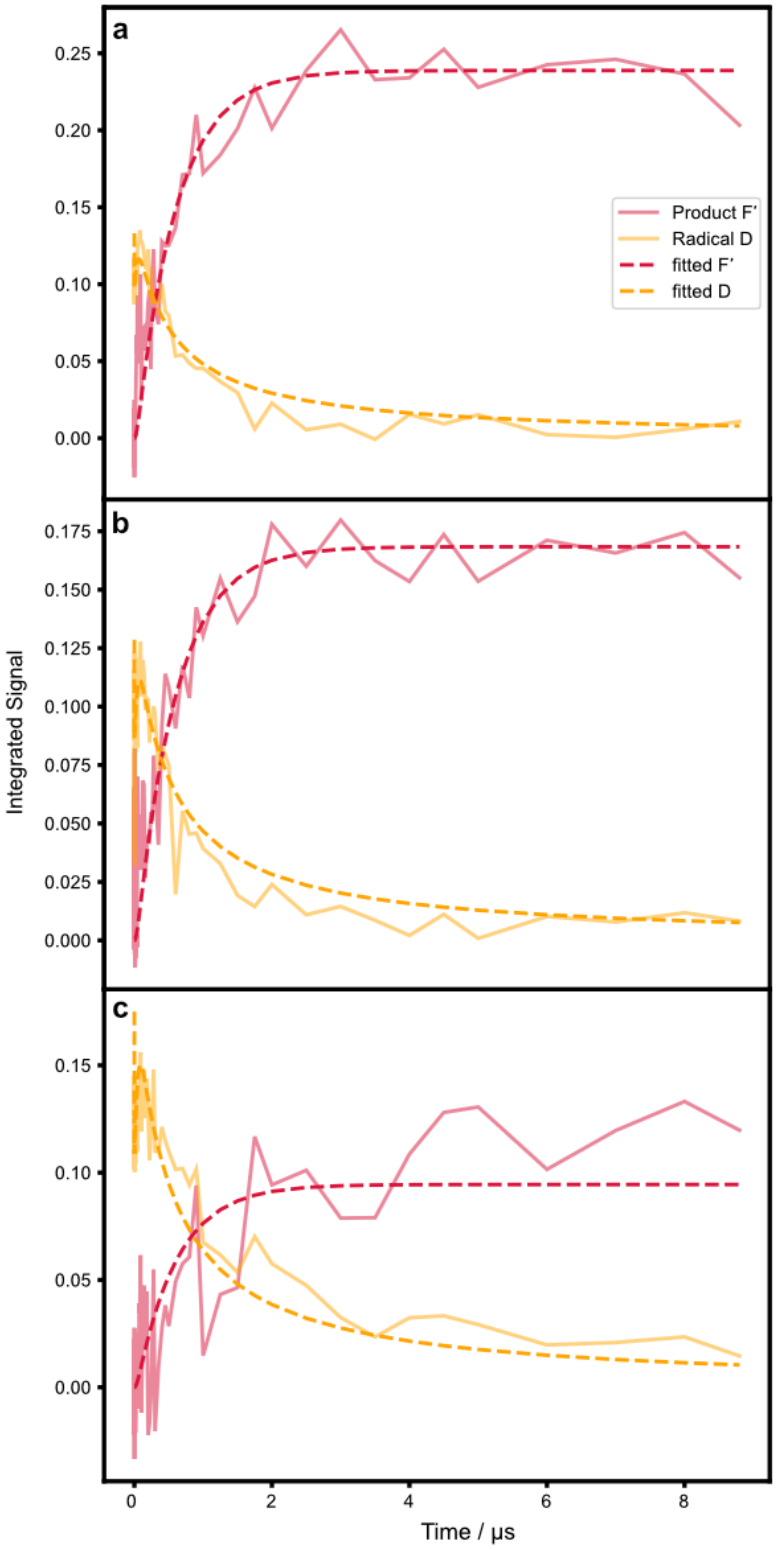

Figure 5.20. *Global least squares fit of model 2 in Figure 5.18 to integrated absorbance data from TVAS measurements using three different concentrations of the vinyl boronate. The following input parameters are used: rate coefficients; initial concentrations of the radical, vinyl boronate, and ethyl iodoacetate; and conversion factors to account for the change in y axis from concentration in mM to Integrated Signal in arbitrary units.* ***a:*** *30 mM vinyl boronate* ***b:*** *40 mM vinyl boronate.* ***c:*** *50 mM vinyl boronate.*

5.2.2.1.3 Fitting

The fits of experimental data for the vinyl boronate system to model 2 followed the procedure used to fit the BCB data described in Section 5.2.1.2. To obtain a satisfactory fit with minimal correlation between the fitted variables (correlation < 0.5) the following constraints were applied:

- The initial radical **D** concentration was fixed to a value of 60 μM corresponding to estimates based on the experimental conditions.
- The rate coefficient for the termination reaction of radical **D** was fixed at $k_3 = 1.5 \times 10^{10}\, M^{-1}s^{-1}$.

Using this method, the global fit for time-evolving absorption data obtained at three initial concentrations of the vinyl boronate is shown in **Figure 5.20**. The fit returned the following estimates for the rate coefficients in the model:

$$k_1 = 5.1 \times 10^{11}\, M^{-1}s^{-1}$$

$$k_2 = 4.31 \times 10^{10}\, s^{-1}$$

$$k_3 = 1.5 \times 10^{10}\, M^{-1}s^{-1}$$

$$k_4 = 2 \times 10^{6}\, s^{-1}$$

$$k_5 = 3.1 \times 10^{5}\, M^{-1}s^{-1}$$

TAS measurements and associated kinetic modelling indicate that IAT also operates for the vinyl boronate system. **Figure 5.18** shows the mechanism proposed to account for these measurements, the rate coefficients for which are highlighted above. Use of a global fit gives negligible statistical errors for the floated parameters k_1, k_2, and k_4 (< 0.1 %), while the values of k_3 and k_5 were fixed to values recorded previously. The derived magnitudes of the bimolecular rate coefficients suggest that during the early stages of the chain, reactions take place within pre-associated complexes, and hence without the need for diffusion.

5.2.2.1.4 Computational Studies

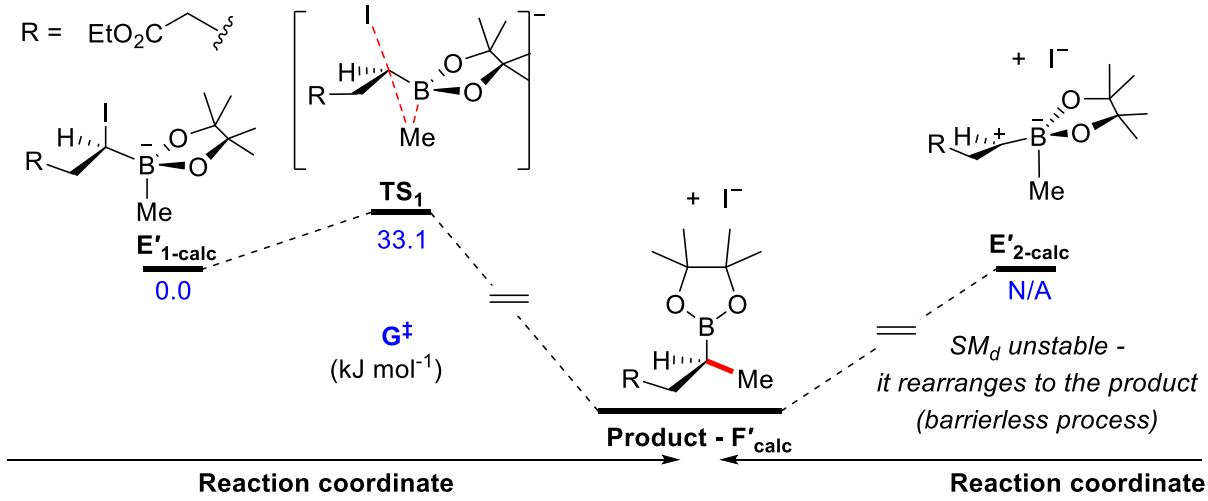

Figure 5.21. *Computed energy profiles for the 1,2-migration with and without the iodide as a leaving group.* ***E'***$_{1\text{-}calc}$ *starts the IAT pathway while* ***E'***$_{2\text{-}calc}$ *starts the SET pathway. Note that* ***E'***$_{2\text{-}calc}$ *was not stable and immediately collapsed to the product and so a transition state could not be isolated. The same result was obtained by Studer and coworkers when they attempted a similar calculation.*[10]

Using the Eyring equation, the rate constant for 1,2-migration can be calculated to be 1×10^7 s^{-1}, which is in reasonable agreement with the experimental value $k_4 = 2 \times 10^6$ s^{-1}. It is interesting to compare the k_4 values for the BCB boronate 1,2-migration rate ($k_{4(observed)} = 3.5 \times 10^5$ s^{-1}, $k_{4(calculated)} = 3.6 \times 10^6$ s^{-1}) and vinyl boronate 1,2-migration rate ($k_{4(observed)} = 2 \times 10^6$ s^{-1}, $k_{4(calculated)} = 1.0 \times 10^7$ s^{-1}). The slower rate of BCB 1,2-migration can be explained by the increase in ring strain during the 1,2-metallate rearrangement, which is absent in the acyclic vinyl boronate system, resulting in a slightly higher activation barrier.

5.3 Conclusion

This chapter has presented the use of cutting-edge mid-IR TAS methods to identify spectral features for transient participants in the radical-induced 1,2-metallate rearrangement of a BCB boronate complex, and to track their evolution over 8 orders of magnitude of time, from 1 ps to 100 μs. With this unprecedented set of measurements for such a reaction, the radical is observed entering the chain cycle, followed by decay of the radical concentration through termination, formation of a key reactive intermediate, and complete formation of products over the full length of the radical chain. Using the approach of Yoon and coworkers,[33] kinetic analysis indicates this chain propagates over more than 500 cycles. Based on the mid-IR spectral signatures, kinetic modelling, and computational theory, intermediate $\mathbf{E_1}$ is invoked which is proposed to stem from an IAT reaction. This mechanistic interpretation contrasts with propositions by others in the field that rely on less direct methods of observation.[9,10,12,14] Data

from this chapter also show that the 1,2-metallate rearrangement from intermediate $\mathbf{E_1}$ is rate determining in this reaction, an observation which may be counter-intuitive to practitioners in the field. When TVAS is applied to a system in which the vinyl boronate is the radical acceptor, the main reactive pathway is also via IAT. The outcomes of this study should encourage others to question the common inference of a SET mechanism in other examples of radical-induced 1,2-metallate chemistry using alkyl iodides.[8,10,13,14,46,47,48]

5.4 References

1. Sandford C, Aggarwal VK. Stereospecific functionalizations and transformations of secondary and tertiary boronic esters. *Chem Commun* 2017, **53**(40)**:** 5481-5494.

2. Leśnikowski ZJ. Recent developments with boron as a platform for novel drug design. *Expert Opin Drug Discov* 2016, **11**(6)**:** 569-578.

3. Lovering F. Escape from Flatland 2: complexity and promiscuity. *MedChemComm* 2013, **4**(3)**:** 515-519.

4. Lovering F, Bikker J, Humblet C. Escape from Flatland: Increasing Saturation as an Approach to Improving Clinical Success. *J Med Chem* 2009, **52**(21)**:** 6752-6756.

5. Miyaura N, Suzuki A. Palladium-Catalyzed Cross-Coupling Reactions of Organoboron Compounds. *Chem Rev* 1995, **95**(7)**:** 2457-2483.

6. Zweifel G, Arzoumanian H, Whitney CC. A convenient stereoselective synthesis of substituted alkenes via hydroboration-iodination of alkynes. *J Am Chem Soc* 1967, **89**(14)**:** 3652-3653.

7. Matteson DS, Mah RWH. Neighboring Boron in Nucleophilic Displacement. *J Am Chem Soc* 1963, **85**(17)**:** 2599-2603.

8. Kischkewitz M, Friese FW, Studer A. Radical-Induced 1,2-Migrations of Boron Ate Complexes. *Adv Synth Catal* 2020, **362**(11)**:** 2077-2087.

9. Silvi M, Sandford C, Aggarwal VK. Merging Photoredox with 1,2-Metallate Rearrangements: The Photochemical Alkylation of Vinyl Boronate Complexes. *J Am Chem Soc* 2017, **139**(16)**:** 5736-5739.

10. Kischkewitz M, Okamoto K, Mück-Lichtenfeld C, Studer A. Radical-polar crossover reactions of vinylboron ate complexes. *Science* 2017, **355**(6328)**:** 936-938.

11. Wang Y, Noble A, Sandford C, Aggarwal VK. Enantiospecific Trifluoromethyl-Radical-Induced Three-Component Coupling of Boronic Esters with Furans. *Angew Chem Int Ed* 2017, **56**(7)**:** 1810-1814.

12. Silvi M, Aggarwal VK. Radical Addition to Strained σ-Bonds Enables the Stereocontrolled Synthesis of Cyclobutyl Boronic Esters. *J Am Chem Soc* 2019, **141**(24)**:** 9511-9515.

13. Wang D, Mück-Lichtenfeld C, Studer A. Hydrogen Atom Transfer Induced Boron Retaining Coupling of Organoboronic Esters and Organolithium Reagents. *J Am Chem Soc* 2019, **141**(36)**:** 14126-14130.

14. Tappin NDC, Gnägi-Lux M, Renaud P. Radical-Triggered Three-Component Coupling Reaction of Alkenylboronates, α-Halocarbonyl Compounds, and Organolithium Reagents: The Inverse Ylid Mechanism. *Chem Eur J* 2018, **24**(44)**:** 11498-11502.

15. Zhang N, Samanta SR, Rosen BM, Percec V. Single Electron Transfer in Radical Ion and Radical-Mediated Organic, Materials and Polymer Synthesis. *Chem Rev* 2014, **114**(11)**:** 5848-5958.

16. Lovinger GJ, Morken JP. Recent Advances in Radical Addition to Alkenylboron Compounds. *Eur J Org Chem* 2020, **2020**(16)**:** 2362-2368.

17. Lewis-Borrell L, Sneha M, Bhattacherjee A, Clark IP, Orr-Ewing AJ. Mapping the multi-step mechanism of a photoredox catalyzed atom-transfer radical polymerization reaction by direct observation of the reactive intermediates. *Chem Sci* 2020, **11**(17)**:** 4475-4481.

18. Bhattacherjee A, Sneha M, Lewis-Borrell L, Tau O, Clark IP, Orr-Ewing AJ. Picosecond to millisecond tracking of a photocatalytic decarboxylation reaction provides direct mechanistic insights. *Nat Commun* 2019, **10**(1)**:** 5152.

19. Koyama D, Donaldson PM, Orr-Ewing AJ. Femtosecond to microsecond observation of the photochemical reaction of 1,2-di(quinolin-2-yl)disulfide with methyl methacrylate. *PCCP* 2017, **19**(20)**:** 12981-12991.

20. Shields BJ, Kudisch B, Scholes GD, Doyle AG. Long-Lived Charge-Transfer States of Nickel(II) Aryl Halide Complexes Facilitate Bimolecular Photoinduced Electron Transfer. *J Am Chem Soc* 2018, **140**(8)**:** 3035-3039.

21. Ting SI, Garakyaraghi S, Taliaferro CM, Shields BJ, Scholes GD, Castellano FN*, et al.* 3d-d Excited States of Ni(II) Complexes Relevant to Photoredox Catalysis: Spectroscopic Identification and Mechanistic Implications. *J Am Chem Soc* 2020, **142**(12)**:** 5800-5810.

22. Coles MS, Quach G, Beves JE, Moore EG. A Photophysical Study of Sensitization-Initiated Electron Transfer: Insights into the Mechanism of Photoredox Activity. *Angew Chem Int Ed* 2020, **59:** 2-7.

23. Till NA, Tian L, Dong Z, Scholes GD, MacMillan DWC. Mechanistic Analysis of Metallaphotoredox C–N Coupling: Photocatalysis Initiates and Perpetuates Ni(I)/Ni(III) Coupling Activity. *J Am Chem Soc* 2020.

24. Hammarback LA, Clark IP, Sazanovich IV, Towrie M, Robinson A, Clarke F*, et al.* Mapping out the key carbon–carbon bond-forming steps in Mn-catalysed C–H functionalization. *Nat Catal* 2018, **1**(11)**:** 830-840.

25. Greetham GM, Donaldson PM, Nation C, Sazanovich IV, Clark IP, Shaw DJ*, et al.* A 100 kHz Time-Resolved Multiple-Probe Femtosecond to Second Infrared Absorption Spectrometer. *Appl Spectrosc* 2016, **70**(4)**:** 645-653.

26. Greetham GM, Sole D, Clark IP, Parker AW, Pollard MR, Towrie M. Time-resolved multiple probe spectroscopy. *Rev Sci Instrum* 2012, **83**(10)**:** 103107.

27. Bhattacherjee A, Sneha M, Lewis-Borrell L, Amoruso G, Oliver TAA, Tyler J*, et al.* Singlet and Triplet Contributions to the Excited-State Activities of Dihydrophenazine, Phenoxazine, and Phenothiazine Organocatalysts Used in Atom Transfer Radical Polymerization. *J Am Chem Soc* 2021, **143**(9)**:** 3613-3627.

28. Orr-Ewing AJ. Perspective: How can ultrafast laser spectroscopy inform the design of new organic photoredox catalysts for chemical and materials synthesis? *Struct Dyn* 2019, **6**(1)**:** 010901.

29. Koyama D, Dale HJA, Orr-Ewing AJ. Ultrafast Observation of a Photoredox Reaction Mechanism: Photoinitiation in Organocatalyzed Atom-Transfer Radical Polymerization. *J Am Chem Soc* 2018, **140**(4)**:** 1285-1293.

30. Romero NA, Nicewicz DA. Mechanistic Insight into the Photoredox Catalysis of Anti-Markovnikov Alkene Hydrofunctionalization Reactions. *J Am Chem Soc* 2014, **136**(49)**:** 17024-17035.

31. Ross PL, Johnston MV. Excited State Photochemistry of Iodoalkanes. *J Phys Chem* 1995, **99**(12)**:** 4078-4085.

32. Marco Montalti AC, Luca Prodi, M. Teresa Gandolfi. *Handbook of Photochemistry*, Third edn. Taylor & Francis Group: Boca Raton, FL, 2006.

33. Cismesia MA, Yoon TP. Characterizing chain processes in visible light photoredox catalysis. *Chem Sci* 2015, **6**(10)**:** 5426-5434.

34. Harris CR, Millman KJ, van der Walt SJ, Gommers R, Virtanen P, Cournapeau D*, et al.* Array programming with NumPy. *Nature* 2020, **585**(7825)**:** 357-362.

35. Newville MS, Till; Allen, Daniel B; Ingargiola, Antonino. LMFIT: Non-Linear Least-Square Minimization and Curve-Fitting for Python *Zenodo* 2014.

36. Hunter JD. Matplotlib: A 2D Graphics Environment. *Comput Sci Eng* 2007, **9**(3)**:** 90-95.

37. Essafi S, Tomasi S, Aggarwal VK, Harvey JN. Homologation of Boronic Esters with Organolithium Compounds: A Computational Assessment of Mechanism. *J Org Chem* 2014, **79**(24)**:** 12148-12158.

38. Studer A, Curran DP. Catalysis of Radical Reactions: A Radical Chemistry Perspective. *Angew Chem Int Ed* 2016, **55**(1)**:** 58-102.

39. Curran DP, Chen MH, Kim D. Atom-transfer cyclization. A novel isomerization of hex-5-ynyl iodides to iodomethylene cyclopentanes. *J Am Chem Soc* 1986, **108**(9)**:** 2489-2490.

40. Curran DP, Bosch E, Kaplan J, Newcomb M. Rate constants for halogen atom transfer from representative .alpha.-halo carbonyl compounds to primary alkyl radicals. *J Org Chem* 1989, **54**(8)**:** 1826-1831.

41. Bag D, Kour H, Sawant SD. Photo-induced 1,2-carbohalofunctionalization of C–C multiple bonds via ATRA pathway. *Org Biomol Chem* 2020, **18**(41)**:** 8278-8293.

42. Hiatt R, Benson SW. Rate constants for radical recombination. III. The trifluoromethyl radical. *Int J Chem Kinet* 1972, **4**(5)**:** 479-486.

43. Hiatt R, Benson SW. New method for measuring the ratios of rate constants for radical recombination. *J Am Chem Soc* 1972, **94**(1)**:** 25-29.

44. Yang L, Tan D-H, Fan W-X, Liu X-G, Wu J-Q, Huang Z-S*, et al.* Photochemical Radical C–H Halogenation of Benzyl N-Methyliminodiacetyl (MIDA) Boronates: Synthesis of α-Functionalized Alkyl Boronates. *Angew Chem Int Ed* 2021, **60**(7)**:** 3454-3458.

45. Fang T, Qiu J, Yang K, Song Q. Photo-induced weak base-catalyzed synthesis of α-haloboronates from vinylboronates and polyfluoroalkyl halides. *Org Chem Front* 2021, **8**(9)**:** 1991-1996.

46. Silvi M, Schrof R, Noble A, Aggarwal VK. Enantiospecific Three-Component Alkylation of Furan and Indole. *Chem Eur J* 2018, **24**(17)**:** 4279-4282.

47. Davenport R, Silvi M, Noble A, Hosni Z, Fey N, Aggarwal VK. Visible-Light-Driven Strain-Increase Ring Contraction Allows the Synthesis of Cyclobutyl Boronic Esters. *Angew Chem Int Ed* 2020, **59**(16)**:** 6525-6528.

48. Wang D, Mück-Lichtenfeld C, Studer A. 1,n-Bisborylalkanes via Radical Boron Migration. *J Am Chem Soc* 2020, **142**(20)**:** 9119-9123.

6 Conclusion

The renaissance of synthetic photochemistry brought about by photoredox catalysis has seen an explosion of new ideas around how visible light can drive chemical reactivity, impacting almost every area of synthetic chemistry. As is often the case when new fields emerge, the question of "How?" rather than "Why?" is asked more frequently. However, as the field has matured over the last decade researchers have become increasingly interested in why these new methods exhibit such useful reactivity, and by doing so have driven further innovation. This thesis has looked to answer the "why?" question in two separate and important areas of chemistry: O-ATRP and organic synthesis.

From the outset of O-ATRP as a methodology, qualitative descriptions were used to describe the reactivity of organic photocatalysts, with the prevailing wisdom being that catalysts with charge transfer excited states and high triplet quantum yields were best for controlling polymerisation.[1] However, the work presented in Chapters 3 and 4 of this thesis has sought to understand why these descriptors are useful, and contextualize this new field within the existing body of photochemical and ATRP knowledge.[2,3,4] Indeed, Chapter 3 dispelled the myth that only triplet states can induce desired reactivity in O-ATRP; instead, due to the mixed ISC efficiencies of these catalysts, there can be multiple excited states responsible for the observed catalysis. Further to this, Chapter 4 examined the polymerisation activation step. As is well documented in the ATRP literature, control of polymer quality comes from the equilibrium between activation and deactivation of the polymer chain. By controlling this, one controls the concentration of active radicals in the system. There should be no reason why this same argument should not apply for O-ATRP. As is shown in Chapter 4, this line of thinking is indeed true: rather than the qualitative charge transfer vs. locally excited descriptors advocated to date, the fundamental property that determines the rate of activation is the Gibbs energy barrier for electron transfer, and it can be quantitatively interpreted using the Marcus-Savéant "sticky" model. Hidden behind these descriptors is the fundamental physical truth that when excited states undergo intramolecular charge-transfer they are stabilised by the polar solvent environments used in O-ATRP. This stabilization in turn leads to an increase in the activation barrier and decreased rate of electron transfer. Overall, assuming a constant rate of deactivation, the equilibrium constant will be reduced, thus controlling the concentration of active radicals in the system, in line with the current understanding of ATRP in the literature.

It is reassuring to now see that O-ATRP practitioners are taking on board these arguments and looking to characterize and design other catalysts using these quantitative descriptors.[5]

The final study presented in this thesis sought to look beyond the first bimolecular steps to understand *all* the steps in a reaction cycle. An apparently simple radical induced 1,2-mettalate reaction was chosen because it is chemistry developed in the Aggarwal group, and experimental studies were designed the expectation of spectral separation between the reactive intermediates. Indeed, the spectra collected gave excellent separation of key species and provided kinetic information for multiple components of the reaction. Most important was the recorded feature of intermediate E which allowed the reassignment of the mechanism to iodine atom transfer (IAT) rather single electron transfer, based on the observed kinetics which could only be explained by a slow 1,2-mettalate rearrangement. Important here were the dynamic time ranges that could be accessed by a wide timescale TVAS experiment. These measurements over picoseconds to microseconds revealed the time evolution the early-time radical concentration while also allowing long enough time scales to observe the formation of products over the full length of the radical chain. The lasting impact of this study will be to encourage other synthetic chemists to question the validity of the single electron transfer mechanism, not only in radical-induced 1,2-mettalate rearrangements but also for any organic reaction employing alkyl iodide initiators. It is this author's opinion that in the absence of any competing evidence, many of these reactions should be assumed to pass through iodine atom transfer. Indeed, there are still new reactions published that do not take IAT into account in the proposed mechanisms.[6]

Overall, the three studies presented in this thesis have shown how powerful transient absorption spectroscopy, and in particular wide timescale TVAS, can be for mechanistic study of visible-light-induced synthetic chemistry. The field is certainly growing, and it is exciting to see so many more spectroscopists asking interesting questions about the fundamental pathways which facilitate this chemistry. The more times the question "Why?" is asked, the more we will all understand.

References

1. Theriot JC, Lim C-H, Yang H, Ryan MD, Musgrave CB, Miyake GM. Organocatalyzed atom transfer radical polymerization driven by visible light. *Science* 2016, **352**(6289)**:** 1082-1086.

2. Pan X, Fang C, Fantin M, Malhotra N, So WY, Peteanu LA*, et al.* Mechanism of Photoinduced Metal-Free Atom Transfer Radical Polymerization: Experimental and Computational Studies. *J Am Chem Soc* 2016, **138**(7)**:** 2411-2425.

3. Matyjaszewski K, Xia J. Atom Transfer Radical Polymerization. *Chem Rev* 2001, **101**(9)**:** 2921-2990.

4. Romero NA, Nicewicz DA. Organic Photoredox Catalysis. *Chem Rev* 2016, **116**(17)**:** 10075-10166.

5. Lattke YM, Corbin DA, Sartor SM, McCarthy BG, Miyake GM, Damrauer NH. Interrogation of O-ATRP Activation Conducted by Singlet and Triplet Excited States of Phenoxazine Photocatalysts. *J Phys Chem A* 2021, **125**(15)**:** 3109-3121.

6. Pickford HD, Nugent J, Owen B, Mousseau JJ, Smith RC, Anderson EA. Twofold Radical-Based Synthesis of N,C-Difunctionalized Bicyclo[1.1.1]pentanes. *J Am Chem Soc* 2021, **143**(26)**:** 9729-9736.

7 Experimental

7.1 General Information

For the synthesis of the photocatalysts used in Chapters 3 and 4, anhydrous solvents were commercially supplied or provided by the stills in the School of Chemistry, University of Bristol, and were dried using a purification column composed of activated alumina and stored over thoroughly dried 3-Å molecular sieves. All other solvents were bought through Sigma-Aldrich. 2- Dicyclohexylphosphino-2,6-diisopropoxybiphenyl (RuPhos) and Chloro-(2-Dicyclohexylphosphino-2,6-diisopropoxy-1,1-biphenyl) [2-(2-aminoethyl)phenyl] palladium(II) - methyl-t-butyl ether adduct (RuPhos precatalyst) were bought from Sigma-Aldrich and stored under a nitrogen atmosphere. All other reagents were used as received.

For the syntheses of compounds used in Chapter 5, 2-((1r,3r)-bicyclo[1.1.0]butan-1-yl)-4,4,5,5-tetramethyl-1,3,2-dioxaborolane, lithium 4,4,5,5-tetramethyl-2-phenyl-2-(prop-1-en-2-yl)-1,3,2-dioxaborolan-2-uide, and ethyl 4-phenyl-4-(4,4,5,5-tetramethyl-1,3,2-dioxaborolan-2-yl)pentanoate, anhydrous solvents were commercially supplied or provided by the communal stills of the School of Chemistry, University of Bristol, and were dried using a purification column composed of activated alumina and stored over thoroughly dried 3 Å molecular sieves. All other solvents were bought through Sigma-Aldrich. *tert*-Butyllithium (1.7 M in pentane), methyllithium (1.6 M in diethyl ether), *n*-butyllithium (1.6 M in hexanes) and phenyllithium (1.9 M in dibutyl ether) used were all purchased from Sigma-Aldrich and their concentrations were determined prior to use by titration using *N*-benzyl benzamide as an indicator. All other reagents were used as received.

^{1}H NMR spectra were recorded using Jeol ECS 400 MHz and Varian VNMR 400 MHz spectrometers. Chemical shifts (δ) are given in parts per million (ppm). The ^{1}H NMR spectra are reported as follows: ppm (multiplicity, integration).

For all transient spectroscopy experiments, the solvents N,N-dimethylformamide, dichloromethane, toluene (all anhydrous, ≥99.8%), toluene-d_8 (99 atom% D), and anhydrous tetrahydrofuran (THF) were used (>99.9% Anhydrous, inhibitor free). All solvents were purchased from Sigma Aldrich and used without further purification. All chemicals and solvents were degassed with nitrogen for 30-40 minutes prior to use in experiments.

The transient spectroscopy measurements employed solutions of the PCs in Chapter 3 and 4 in various concentrations, adjusted for the sample pathlength (see below), that were chosen not to exceed an absorbance of 0.5 at the excitation wavelength. Typical concentrations, unless otherwise indicated, were 4.2 mM (PC-N1), 5 mM (PC-N4), 3.2 mM (PC-O1), 2.9 mM (PC-O2), 1 mM (PC-O3), and 7.6 mM (PC-S). To ensure a fresh part of the sample was excited and probed with every laser measurement, the solutions were circulated from a 10-ml sample vial using a peristaltic pump, and sample cells were spatially rastered. For most measurements, samples were not purged by nitrogen because the excited-state dynamics of interest were too rapid to be affected by dissolved oxygen. However, to assist the assignment of triplet-state contributions to the photochemistry of the PCs, the effects of quenching by oxygen over longer (ns to μs) timescales were tested by comparing with measurements made on samples purged with nitrogen. Even with the use of a sealed flow system reported previously,[1] interference by dissolved oxygen could not be completely suppressed.

Solutions used in the study presented in Chapter 5 were prepared to desired concentrations of various reagents in a Duran bottle which was attached to a sealed flow system. To avoid oxygen contamination, the solutions were prepared using degassed solvents and were thoroughly sparged with nitrogen. The headspace and PTFE tubing of the bottle were filled with nitrogen prior to sealing. Unfortunately, with the sample flow system it was difficult to exclude oxygen leaks completely over the ~10 minute course of the experiments. The bottle was connected via PTFE tubing to a Harrick cell comprising two CaF_2 windows (1.5 mm thick) separated by a PTFE spacer of thickness 100-200 μm (which set the pathlength) and sealed by Kalrez O-rings. The solutions were continuously flowed through the cell, with circulation driven by a peristaltic pump. The continuous flow ensured that consecutive pump and probe pulses sampled fresh volumes of solution. The cell was also rastered in the xy-plane perpendicular to the direction of beam propagation to avoid burn spots and accumulation of photoproducts on the windows. For experiments involving BCB boronate **A**, the boronate solution was prepared immediately prior to the experiment due to the difficulty of isolating a stable boronate species. This was done by the following method:

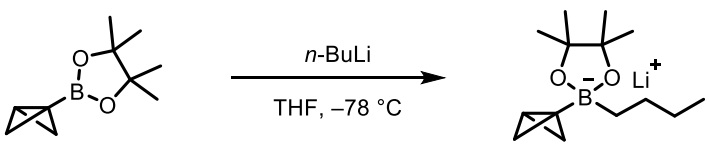

BCB-Bpin **A**

A flame dried Schlenk flask was charged with dry THF (4 mL) and BCB-Bpin (144 mg, 0.800 mmol, 1.0 eq). The reaction mixture was cooled to –78 °C and *n*-BuLi[a] (1.6 M in hexanes, 0.50 mL, 0.80 mmol, 1.0 eq) was added dropwise. The reaction mixture was stirred at –78 °C for 5 min and then warmed to room temperature. The solution was diluted with dry THF to the desired concentration needed for transient absorption spectroscopy experiments and then transferred to the Duran bottle under N_2. Before the experiment was started, degassed ethyl iodoacetate was added to the Duran bottle containing the boronate solution under N_2 to reach a concentration of 40 mM.

7.2 Synthesis

7.2.1 Chapter 3 and 4

7.2.1.1 Synthesis of dihydrophenazine derivatives

7.2.1.1.1 5, 10-dihydrophenazine

A conical flask was charged with phenazine **1** (2.0 g, 11 mmol) in ethanol (50 mL) and heated to reflux. A solution of $Na_2S_2O_4$ (23.3 g, 134 mmol) in water (200 mL) was then added over a period of 5 minutes with the solution being continuously stirred, leading to the formation of a pale green precipitate after 10 min. The crude solid was isolated via vacuum filtration, washed thoroughly with water, and dried in vacuo to afford 5,10-dihydrophenazine **2** (1.73 g, 10.4 mmol, 94 %) as a pale green powder. No further purification was performed on **2** and dihydrophenazines **PC-N1** and **PC-N4** were synthesised immediately after exposing **2** to the atmosphere.

7.2.1.1.2 5,10-bis(4-methoxyphenyl)-5,10-dihydrophenazine (PC-N1)

The photocatalyst **PC-N1** was synthesised via a Buchwald-Hartwig coupling reaction. An oven-dried Schlenk tube was charged with a magnetic stirrer bar, **2** (1.00 g, 5.5 mmol), NaO^{t}Bu (2.11 g, 22.0 mmol), RuPhos (103 mg, 0.22 mmol), RuPhos precatalyst (180 mg, 0.22 mmol), 4-bromoanisole (4.05 g, 22 mmol) and 1,4-dioxane (8 ml) and heated to 110 °C under an atmosphere of nitrogen. After 16 hours, the solution had turned green and a yellow precipitate had formed. The reaction was then cooled to room temperature. The reaction mixture was diluted in DCM (200 ml) and washed with water (3× 200 ml); the organic layer was subsequently dried over $MgSO_4$, and vacuum filtered. Finally, the DCM was removed under vacuum to obtain a yellow solid. The solid was recrystallized by dissolving in minimal DCM and then pipetting hexane into the solution until precipitation was observed. The product was

obtained as fluffy yellow crystals (1.6 g, 4.1 mmol, 73 %). Characterization was confirmed by comparison with previously reported values.[2]

^{1}H NMR (d_8-toluene, 400 MHz) δ 7.07 – 7.04 (m, 4H), 6.78 – 6.75 (m, 4H), 6.33 - 6.30 (m, 4H), 5.85 - 5.82 (m, 4H).

7.2.1.1.3 4,4'-(phenazine-5,10-diyl)dibenzonitrile (PC-N4)

The photocatalyst **PC-N4** was synthesised via a Buchwald-Hartwig coupling reaction. An oven-dried Schlenk tube was charged with a magnetic stirrer bar, **2** (1.00 g, 5.5 mmol), NaO^{t}Bu (2.11 g, 22.0 mmol), RuPhos (103 mg, 0.22 mmol), RuPhos precatalyst (180 mg, 0.22 mmol), 1-4-bromobenzonitrile (4.00 g, 22 mmol) and 1,4-dioxane (10 ml), and heated to 110 °C under an atmosphere of nitrogen. After 1 hr, a golden-yellow precipitate was formed, and the reaction was cooled to room temperature. The precipitate was collected and dissolved in DCM (250 mL), and any undissolved material was removed by filtration. The solvent was removed under vacuum to give a yellow solid. The solid was recrystallized by dissolving in minimal DCM and then gradually pipetting out hexane until precipitation was observed. The product was obtained as a fluffy golden yellow solid (1.00 g, 2.6 mmol, 47 %). Characterization was confirmed by comparison with previously reported values.[2]

^{1}H NMR (d_8-toluene, 400 MHz) δ 6.99 – 6.98 (m, 4H), 6.75 – 6.72 (m, 4H), 6.39 - 6.34 (m, 4H), 5.68 - 5.64 (m, 4H).

7.2.1.1.4 5,10-di(naphthalen-1-yl)-5,10-dihydrophenazine (PC-N5)

The photocatalyst **PC-N5** was synthesised via a Buchwald-Hartwig coupling reaction. An oven-dried round-bottom flask was charged with a magnetic stirrer bar, **2** (0.50 g, 2.7 mmol), NaO^{t}Bu (2.11 g, 22.0 mmol), RuPhos (103 mg, 0.22 mmol), RuPhos precatalyst (180 mg, 0.22 mmol), 1-bromonapthalene (4.55 g, 22 mmol) and 1,4-dioxane (10 ml) and heated to 110 °C under an atmosphere of nitrogen. After 16 hr the solution had turned green and a yellow precipitate had been formed. The reaction mixture was diluted in DCM (200 ml) and water (200 ml), causing further precipitation so the solid was isolated and washed with hexane and kept to the side. The remaining DCM solution was washed with water again (2 x 200 ml), the organic layer was dried over $MgSO_4$, and vacuum filtered. Finally, the DCM was removed under vacuum until precipitation could be seen, hexane was then added dropwise to induce further precipitation. The precipitate was collected as a bright yellow solid and combined with the previously isolated precipitate as both were determined to be product (1.05 g, 2.41 mmol, 43 %). Characterization was confirmed by comparison with previously reported values.[2]

^{1}H NMR (d_8-toluene, 400 MHz) δ 8.64 – 8.54 (m, 2H), 7.73 – 7.63 (m, 4H), 7.47 (m, 2H), 7.33 – 7.22 (m, 6H), 6.12 – 6.03 (dd, 4H), 5.70 – 5.63 (dd, 4H).

PC-N2, PC-N3 were synthesised previously in Bristol by Koyama et al. and identical procedures were followed.[3]

7.2.1.2 Synthesis of phenoxazine derivatives

7.2.1.2.1 phenyl-10-phenoxazine (PC-O1)

The photocatalyst **PC-O1** was synthesised via a Buchwald-Hartwig coupling reaction. To a dry Schlenk tube was added phenoxazine (733 mg, 4.0 mmol, 1.00 eq.), NaO^{t}Bu (769 mg, 8.0 mmol, 2.00 eq.), RuPhos (48.4 mg, 0.12 mmol, 0.03 eq.) and RuPhos Precat. (21mg, 0.12 mmol, 0.03 eq.). The Schlenk tube was degassed before addition of bromobenzene (0.42 mL, 4.0 mmol 1.00 eq.) and dry dioxane (1 mL). The suspension was stirred at 100 °C under an atmosphere of N_2 for 4 hours. The reaction mixture was allowed to cool to room temperature, diluted water and extracted with CH_2Cl_2. The organic phase was dried over anhydrous $MgSO_4$, filtered and the solvent was removed under vacuum. The residue was purified by flash column chromatography on silica gel eluting with pentane and EtOAc to afford **PC-O1** as a white solid (836 mg, 3.22 mmol, 81%)).

^{1}H NMR (400 MHz, $CDCl_3$) δ 7.58 (t, *J* = 7.7 Hz, 2H), 7.50 – 7.42 (m, 1H), 7.33 (d, *J* = 8.2 Hz, 2H), 6.71 – 6.53 (m, 6H), 5.90 (d, *J* = 7.7 Hz, 2H). Characterisation was confirmed by comparison with reported values.[4]

7.2.1.2.2 10-(naphthalen-2-yl)-10H-phenoxazine (PC-O2)

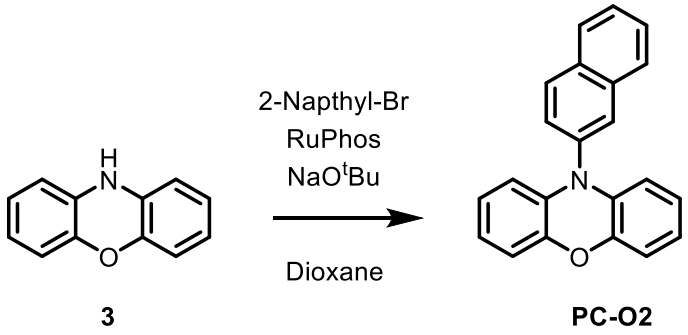

3 **PC-O2**

The photocatalyst **PC-O2** was synthesised via a Buchwald-Hartwig coupling reaction. An oven-dried Schlenk tube was charged with a magnetic stirrer bar, phenoxazine **3** (1.00 g, 5.46 mmol), NaO^{t}Bu (1.05 g, 10.9 mmol), RuPhos (66 mg, 0.16 mmol), RuPhos precatalyst (115 mg, 0.16 mmol), 2-bromonapthalene (2.26 g, 10.9 mmol) and 1,4-dioxane (6 ml), and heated

to 100 °C under an atmosphere of nitrogen. A colour change upon heating was observed from brown/black to sandy-yellow. The reaction was heated for 18 hrs and then allowed to cool. The reaction mixture was dissolved in DCM (200 mL) and washed with water (3 × 200 mL) and then brine (200 mL). The organic layer was collected and dried over $MgSO_4$, and the solvent was removed under vacuum forming a white solid. The product was purified by flash column chromatography on silica gel (pentane / 1% EtOAc). The product was recrystallised in minimal EtOAc and obtained as pale-yellow crystals (1.15 g, 3.71 mmol, 68 %). Characterization was confirmed by comparison with previously reported spectroscopic values.[5]

^{1}H NMR ($CDCl_3$, 400 MHz) δ 8.08 (d, J = 8.6 Hz, 1H), 7.94 (d, *J* = 7.1 Hz, 1H), 7.88 (m, 2H), 7.65 (pd, *J* = 7.0, 1.5 Hz, 2H), 7.46 (dd, *J* = 8.6, 2.0 Hz, 1H), 6.72 (dd, *J* = 7.8, 1.6 Hz, 2H), 6.65 (t, J = 7.52 ,2H), 6.66 (td, *J* = 7.7, 1.7 Hz, 2H), 5.95 (dd, *J* = 8.0, 1.5 Hz, 2H).

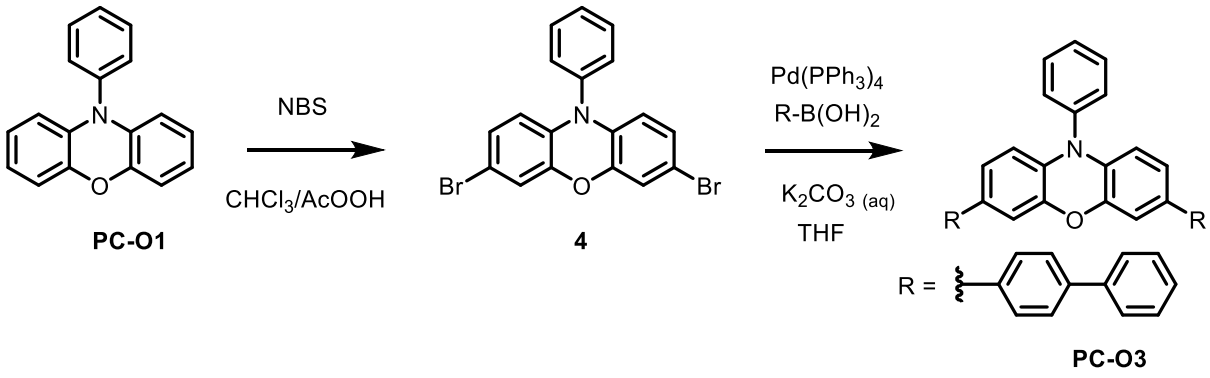

PC-O1 **4** **PC-O3**

7.2.1.2.3 3,7-Dibromo Phenyl-10-Phenoxazine

To a stirred solution of **PC-O1** (500 mg, 1.93 mmol) dissolved in chloroform and glacial acetic acid (50 mL/50 mL), NBS was added (686 mg, 3.86 mmol) slowly over 15 minutes. The resulting mixture was stirred in the dark at room temperature for 2 hours. The solution was quenched with saturated $NaHCO_3$, extracted with CH_2Cl_2, and washed with water. The organic phase was dried over anhydrous $MgSO_4$, filtered, and the solvent was removed under vacuum. The residue was purified by flash column chromatography on silica gel (pentane / 1% EtOAc) to afford **4** as a white solid (651 mg, 1.56 mmol, 81%)). Characterization was confirmed by comparison with previously reported values.[5]

^{1}H NMR (400 MHz, $CDCl_3$) δ 7.63 – 7.57 (m, 2H), 7.52 – 7.46 (m, 1H), 7.31 – 7.27 (m, 2H), 6.81 (d, J = 2.2 Hz, 2H), 6.69 (dd, J = 8.6, 2.2 Hz, 2H), 5.75 (d, J = 8.6 Hz, 2H).

7.2.1.2.4 3,7-Di(4-biphenyl) Phenyl-10-Phenoxazine (PC-O3)

The photocatalyst **PC-O3** was synthesised with a Suzuki-Miyaura coupling reaction. To an oven-dried Schlenk tube was added **4** (150 mg, 0.360 mmol), $Pd(Ph_3)_4$ (41.6 mg, 0.036 mmol) and biphenyl boronic acid (249 mg, 1.26 mmol). The reagents in the Schlenk tube were then cycled three times under vacuum and nitrogen before being dissolved in dry THF (8.00 mL). Sparged aqueous 2.00 M K_2CO_3 solution (4 mL) was added to the flask and the reaction mixture was refluxed at 100 °C for 4 h. The solution was concentrated under reduced pressure, diluted with DCM / hexane and passed through a short plug of silica gel. The resulting mixture was then washed with de-ionized water, dried over magnesium sulfate, and the solvent removed under vacuum. The residue was recrystallized in EtOAc to yield **PC-O3** as bright yellow/green crystals (271 mg, 0.481 mmol, 67 %). Characterization was confirmed by comparison with previously reported values.[5]

^{1}H NMR (400 MHz, $CDCl_3$) δ 7.68 – 7.56 (m, 14H), 7.52 (t, J = 7.5 Hz, 1H), 7.47-7.40 (m, 6H), 7.38-7.33 (m, 2H), 7.06 (d, J = 2.1 Hz, 2H), 6.92 (dd, J = 8.4, 2.1 Hz, 2H), 6.03 (d, J = 8.3 Hz, 2H).

7.2.1.3 Synthesis of phenothiazine derivative

7.2.1.3.1 10-(naphthalen-1-yl)-10H-phenothiazine (PC-S)

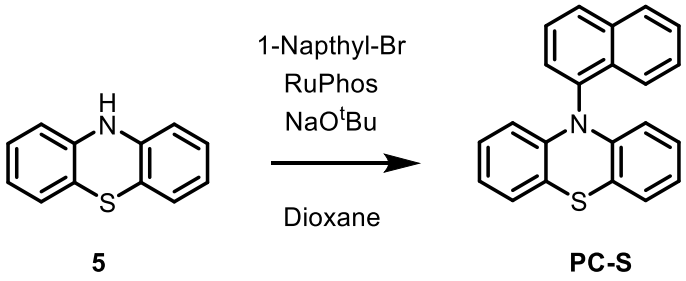

5 **PC-S**

The photocatalyst **PC-S** was synthesised via a Buchwald-Hartwig coupling reaction. An oven-dried Schlenk tube was charged with a magnetic stirrer bar, phenothiazine (1.00 g, 5.02 mmol), NaO^{t}Bu (1.05 g, 10.9 mmol), RuPhos (66 mg, 0.16 mmol), RuPhos precatalyst (115 mg, 0.16 mmol), 1-bromonapthalene (2.07 g, 10.0 mmol) and 1,4-dioxane (6 ml), and heated to 100 °C under an atmosphere of nitrogen. A colour change upon heating was observed from brown/black to sandy yellow. The reaction was heated for 24 hrs and then allowed to cool to room temperature. The reaction mixture was dissolved in DCM (50 mL) and washed with water (3 × 50 mL). The organic layer was collected and dried over $MgSO_4$, and the solvent

was removed under vacuum, forming a dark brown oil. The product was purified by flash column chromatography on silica gel (pentane / 10 % EtOAc) and then recrystallised in minimal EtOAc to give pale-yellow crystals (1.03 g, 3.17 mmol, 63%). Characterization was confirmed by comparison with previously reported values.[6]

^{1}H NMR ($CDCl_3$, 400 MHz) δ 8.10 (d, J = 9.1 Hz, 1H), 7.99 (t, J = 8.6 Hz, 2H), 7.69 –7.62 (m, 2H), 7.54 (ddd, *J* = 8.2, 6.8, 1.3 Hz, 1H), 7.46 (ddd, *J* = 8.2, 6.8, 1.3 Hz, 1H), 7.02 (dd, *J* = 7.4, 1.8 Hz, 2H), 6.79 –6.68 (m, 4H), 6.02 (dd, *J* = 8.2, 1.4 Hz, 2H)

7.2.2 Chapter 5

7.2.2.1 2-((1r,3r)-Bicyclo[1.1.0]butan-1-yl)-4,4,5,5-tetramethyl-1,3,2-dioxaborolane (BCB Bpin)

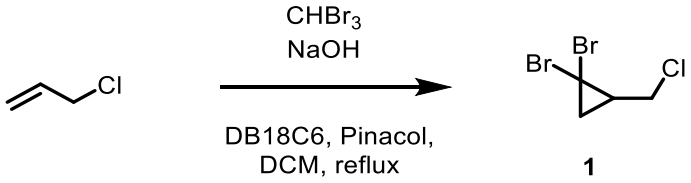

The following procedure was adapted from Silvi et al.[7] A 250 ml two-necked flask was charged with dibenzo-18-crown-6 (DB18C6, 2.14 g, 5.93 mmol, 0.05 eq) and pinacol (0.608 g, 5.14 mmol, 0.04 eq). Solids were dissolved in dichloromethane (75 mL) under N_2. Allyl chloride (15.8 mL, 193 mmol, 1.5 eq) was added followed by bromoform (11.3 mL, 129 mmol, 1 eq). To the solution, NaOH (48.9 g, 1.22 mol, 9.5 eq) dissolved in H_2O (49 mL) was added all at once. The flask was equipped with a reflux condenser and an N_2 balloon, the reaction mixture was heated at 40 °C for 20 h. After 20 h GC-MS of the crude reaction mixture revealed that only part of the bromoform had been converted to product. To push the reaction to completion more allyl chloride was added to the reaction mixture (15.8 mL, 193 mmol, 1.5 eq) along with DB18C6 (2.14 g, 5.93 mmol, 0.05 eq) and pinacol (0.608 g, 5.14 mmol, 0.04 eq). GC-MS taken the following day showed full conversion to product. The reaction mixture was allowed to cool down to r.t. and poured into a 500 mL beaker containing 250 mL of pentane. The mixture was gently stirred with a glass stick and sonicated for five minutes. The mixture was left to sediment for 20 minutes and the supernatant pentane was passed through a celite/silica plug, collecting the solution. Extra attention should be paid to avoid pouring the black precipitate or the water phase over the filter. The black precipitate was washed two more times with 250 mL of pentane repeating the stirring-sonication-plug procedure. The solvent was removed under vacuum and the resulting residue was redissolved in pentane (300 mL) and passed through silica. Solvent

was again removed to give a light-yellow liquid. The product was redissolved in pentane (10 mL) and passed through a Pasteur pipette filled with a small amount of oven dried $MgSO_4$. Solvent was evaporated and the product afforded as a light-yellow liquid (19.8 g, 80 mmol, 62% yield).

^{1}H NMR ($CDCl_3$, 400 MHz) δ (ppm): 3.63 (d, *J* = 7.5, 1.5 Hz, 2H), 2.03 (m, 1H), 1.91 (dd, J = 10.3, 7.6 Hz, 1H), 1.47 (t, *J* = 7.5 Hz, 1H); **^{13}C NMR** ($CDCl_3$, 101 MHz) δ (ppm): 46.3, 32.3, 29.1, 25.8. The spectral data were in accordance with the data reported in literature.[7,8]

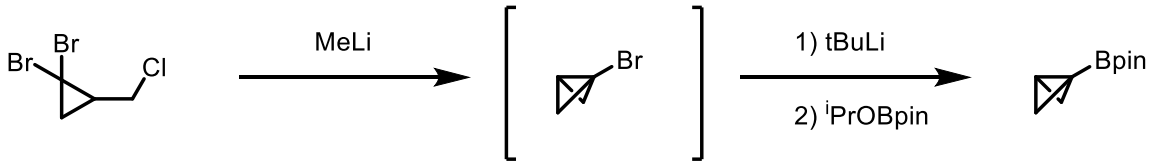

1

BCB-Bpin was made following literature porcedure.[9] A 250 mL three-necked flask was charged with 1,1-dibromo-2-(chloromethyl)cyclopropane **1** (3.85 g, 15.5 mmol, 1.0 eq) and Et_2O (80 mL). **1** The solution was cooled to –78 °C (dry ice/acetone) then methyllithium (1.6 M in Et_2O, 9.69 mL, 15.5 mmol, 1.0 eq) was added at a rate of 0.6 mL/min (syringe pump). The reaction was stirred for 30 min at –78 °C followed by 1 h at –50 °C. The solution was then cooled back to –78 °C (dry ice/acetone) and a high vacuum was applied for 2 min to remove the volatile MeBr. *t*BuLi (1.7 M in pentane, 10.1 mL, 17.1 mmol, 1.1 eq) was then added at a rate of 0.6 mL/min (syringe pump) and stirred for 1 h at –78 °C. After that, a solution of pre-distilled *i*PrOBpin (4.11 mL, 20.2 mmol, 1.3 eq) in Et_2O (20 mL) was added at a rate of 0.6 mL/min (syringe pump). The reaction mixture was stirred at –78 °C for 1 h and then at r.t. overnight. NH_4Cl (saturated aqueous solution, 100 mL) was added and the organic layer was collected. The aqueous phase was washed with Et_2O (3 × 100 mL) and then the combined organic phases were dried ($MgSO_4$), filtered, and concentrated under reduced pressure. After the removal of solvent, pure BCB-Bpin was obtained by distillation from the crude mixture (BCB-Bpin can be distilled at between 130-140 °C at 8 mbar pressure). The product was obtained as clear liquid (1.59 g, 8.83 mmol, 57% yield).

^{1}H NMR (400 MHz, $CDCl_3$) δ (ppm): 1.78 –1.75 (m, 1H), 1.65 (d, J = 2.7 Hz, 2H), 1.24 (s, 12H), 0.58 –0.56 (m, 2H); **^{13}C NMR** (101MHz, $CDCl_3$) δ (ppm): 83.2, 33.2, 24.6, 8.4 *Carbon attached to boron not observed*; The spectral data were in accordance with the data reported in literature.[9]

7.2.2.2 Lithium 4,4,5,5-tetramethyl-2-phenyl-2-(prop-1-en-2-yl)-1,3,2-dioxaborolan-2-uide (Vinyl boronate)

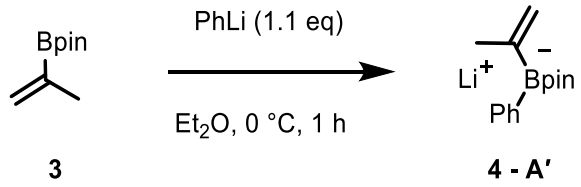

The following procedure was adapted from Silvi et al.[10] To a stirred solution of isopropenylboronic acid pinacol ester **3** (270 µL, 1.41 mmol, 1.0 eq) in Et_2O (5 mL) under N_2 at –78 °C was added dropwise phenyllithium (1.9 M in Bu_2O, 0.74 mL, 1.41 mmol, 1.0 eq). The mixture was stirred for 1 h at –78 °C, followed by further two hours at 0 °C. The suspension was allowed to settle and the supernatant removed with a syringe, dry Et_2O (5 mL) was added, stirred for 2 mins, allowed to settle and the supernatant was again removed and discarded. This process was repeated three more times. Solvent was removed under reduced pressure and dried overnight under vacuum (0.5 mbar) to remove any traces of solvents and residual water. The title boronate complex **4** was obtained as a hygroscopic colourless solid, stable for several weeks if stored under N_2 (0.204 g, 0.832 mmol, 59% yield).

^{1}H NMR (DMSO-d_6, 400 MHz) δ (ppm): 7.35 (d, *J* = 7.0 Hz, 2H), 6.88 (t, *J* = 7.0 Hz, 2H), 6.74 (m, 1H), 4.79 (d, *J* = 6.5 Hz, 1H), 4.46 (d, *J* = 6.5 Hz, 1H), 1.39 (s, 3H), 0.94 (s, 6H), 0.79 (s, 6H); **^{13}C NMR** (DMSO-d_6, 101 MHz) δ (ppm): 131.7, 124.9, 121.9, 108.1, 76.8, 26.7, 26.5, 24.7, *carbons attached to boron not observed due to quadrupolar relaxation*; **^{11}B NMR** (DMSO-d_6, 128 MHz) δ (ppm): 4.8. The spectral data were in accordance with the data reported in literature.[10]

7.2.2.3 Ethyl 4-phenyl-4-(4,4,5,5-tetramethyl-1,3,2-dioxaborolan-2-yl)pentanoate (Vinyl boronate photoproduct)

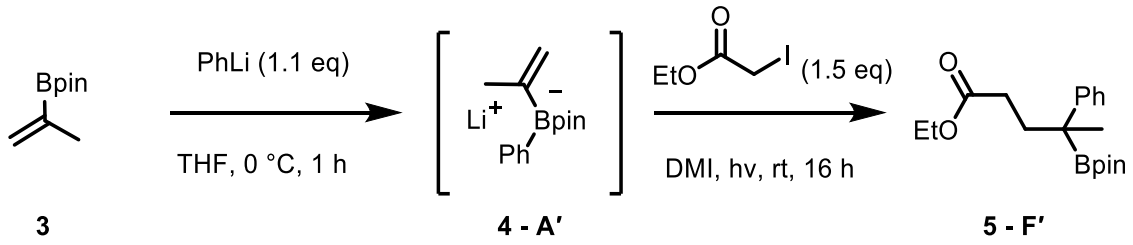

The following procedure was adapted from Silvi et al.[10] To a stirred solution of pre-distilled isopropenylboronic acid pinacol ester **3** (0.24 mL, 215 mg, 1.27 mmol, 1.0 eq) in THF (2.4

mL) under N_2 at 0 °C was added phenyllithium (1.8 M in Bu_2O, 0.78 mL, 1.4 mmol, 1.1 eq) dropwise. The solution was then stirred for 1 h at 0 °C, warmed to r.t. and stirred for a further 5 min. The reaction was placed into a crystallizing basin equipped with a 1 m length blue LED strip. To the suspension, a degassed solution (30 minutes of N_2 sparging in the dark) of ethyl iodoacetate (0.23 mL, 1.9 mmol, 1.5 equiv.) in 1,3-dimethyl-2-imidazolidinone (DMI, 3.0 mL) was added under irradiation, and the mixture was stirred vigorously overnight under constant irradiation (16 h). The reaction mixture was diluted with EtOAc (150 mL) and the solution washed with water (4 × 50 mL + 2 mL brine), 10% solution of sodium thiosulfate (25 ml) and with brine (50 mL). The resulting organic phase was dried ($MgSO_4$), filtered and concentrated under reduced pressure. Crude product **5** was retrieved as a yellow oil and purified by flash column chromatography (SiO_2, pentane:EtOAc 100:0 to 95:5) to obtain the product as a clear oil (140 mg, 0.42 mmol, 33% yield).

^{1}H NMR (400 MHz, $CDCl_3$) δ (ppm): 7.32-7.25 (m, 4H), 7.15 (m, 1H), 4.07 (q, *J* = 7.1 Hz, 2H), 2.29 – 2.01 (m, 4H), 1.35 (s, 3H), 1.23 (t, *J* = 7.1 Hz, 3H), 1.22 – 1.16 (m, 12H); **^{13}C NMR** (101 MHz, $CDCl_3$) δ (ppm): 174.38, 145.99, 128.34, 127.06, 125.49, 83.61, 60.30, 34.33, 30.66, 24.72, 24.69, 21.22, 14.36 *Carbon attached to boron not observed*; **FTIR** (Solution in DCM, 360 mM, 300 μm path length) ν_{max}/cm^{-1}: 1605, 1620, 1726, 1772, 2883, 2936, 2975, 2994, 3064, 3406, 3593.

7.3 Steady State Spectra

7.3.1 Chapter 3

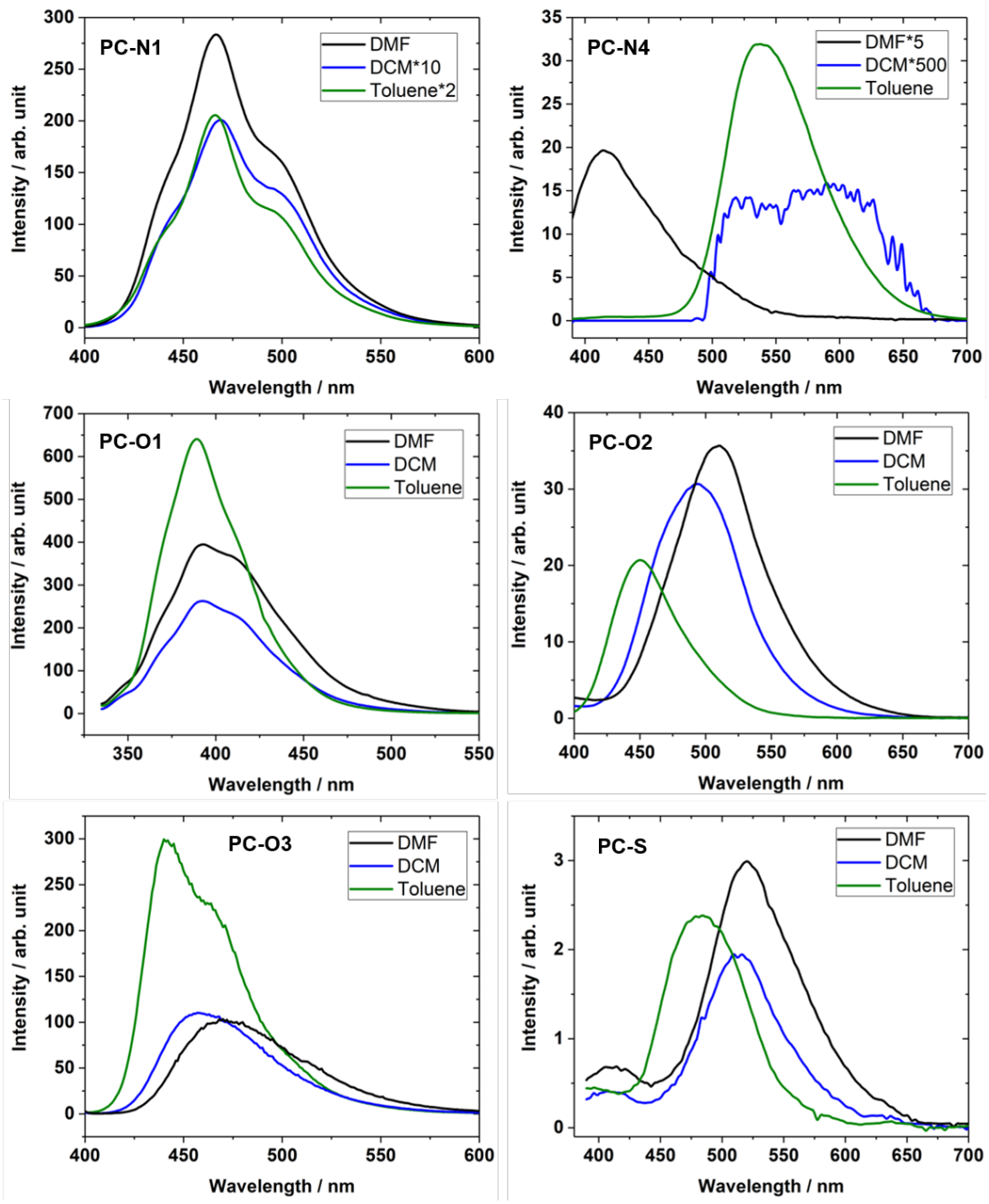

Figure E1. *Fluorescence emission spectra of six organic photocatalysts measured in the solvents DMF (black), DCM (blue), and toluene (green). Photoexcitation wavelengths are 370 nm (PC-N1 and PC-N4), 318 nm (PC-O1, PC-O2, PC-S), and 389 nm (PC-O3). The emission spectra for PC-N1 in DCM, PC-N1 in toluene, PC-N4 in DMF and PC-N4 in DCM are scaled in intensity by factors of 10, 2, 5, and 500, respectively. The data indicate solvatochromic shifts in emission for PC-O2, PC-O3 and PC-S, consistent with emissive (S1) states with charge-transfer character.*

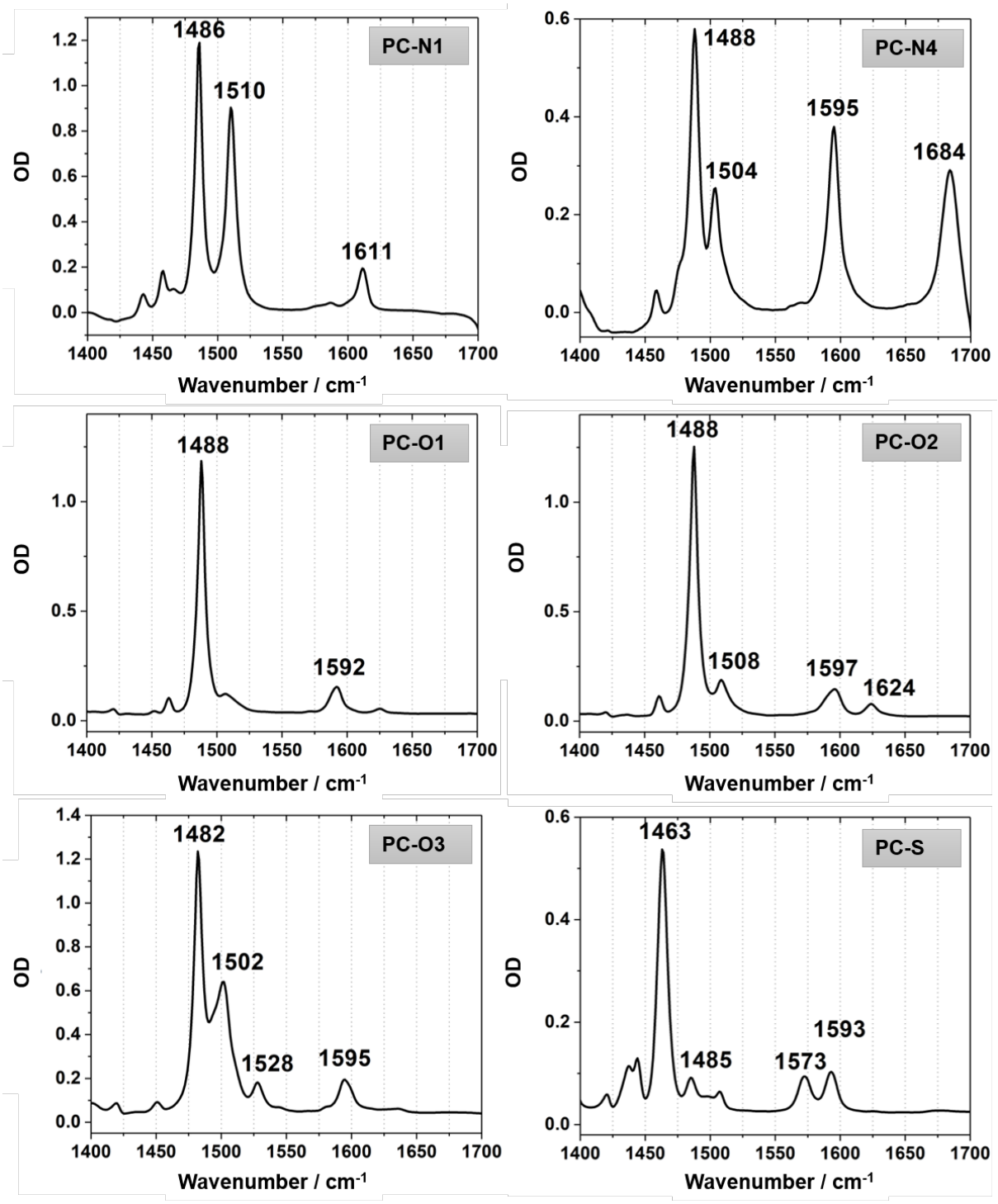

Figure E2. *Steady state FTIR spectra of six organic photocatalysts measured in DCM. The prominent peaks are annotated. These features can be identified in the time-resolved vibrational absorption spectra reported in Figure 3 as ground state bleaches.*

7.3.2 Chapter 4

7.3.2.1 FTIR Spectra of PC and $PC^{\bullet+}$ in DCM

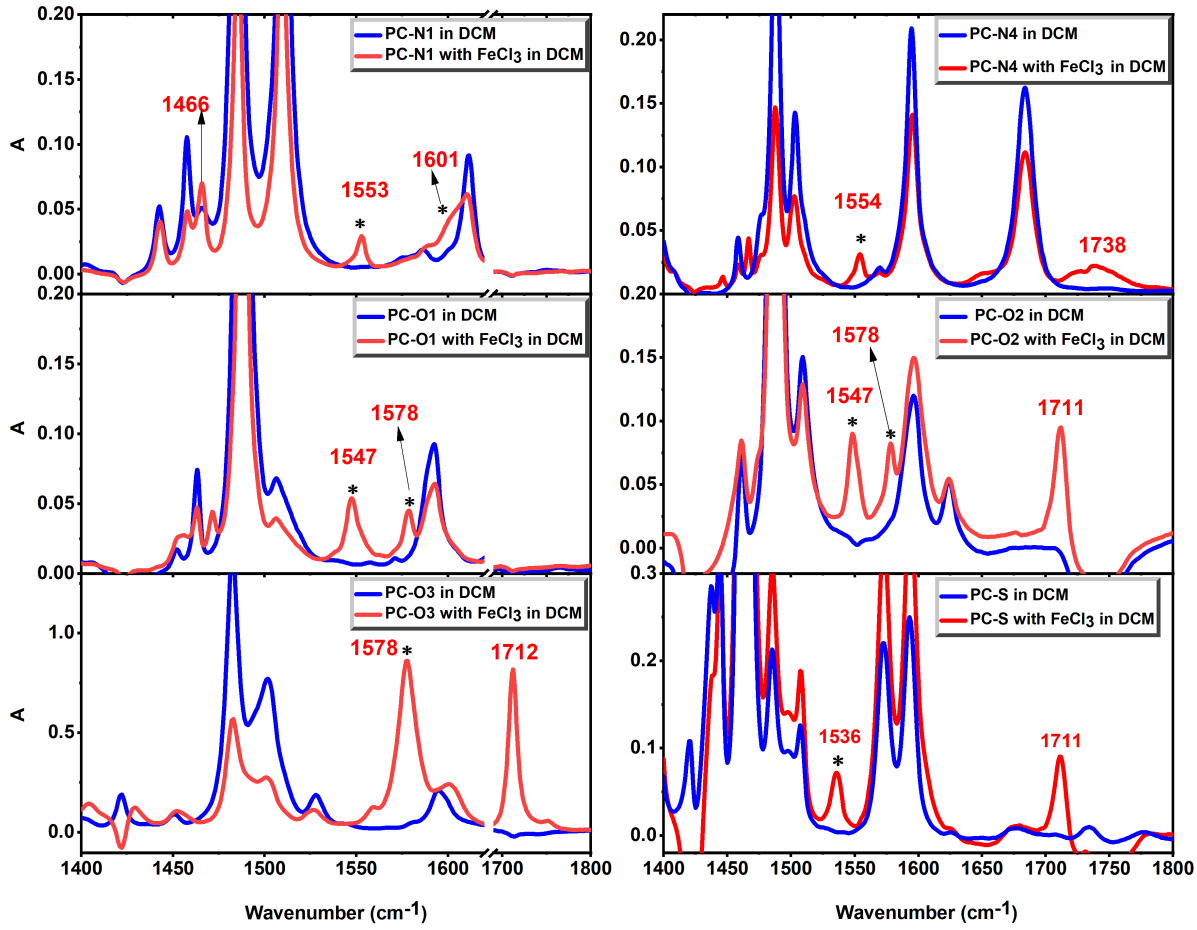

Figure E3. *FTIR spectra of PCs in dichloromethane (in blue) and PCs with 3 equivalents of $FeCl_3$ (in red) in DCM. Concentrations of PCs used were 21 mM for PC-N1, PC-O1, PC-O2, PC-O3; 50mM for PC-N4, and 80 mM for PC-S. Spectra were taken using a Harrick cell with path length of 200 µm and a Perkin Elmer Spectrum-Two FTIR spectrometer. $FeCl_3$ was used to oxidize PC to generate $PC^{\bullet+}$. The $PC^{\bullet+}$ cation peaks observed in the TVAS experiments are marked by * symbols. FTIR spectra for PC-N2, PC-N3, and PC-N5 with $FeCl_3$ are reported elsewhere.*[1,3]

7.3.2.2 UV-Vis Spectra of PC and $PC^{\bullet+}$ in DCM

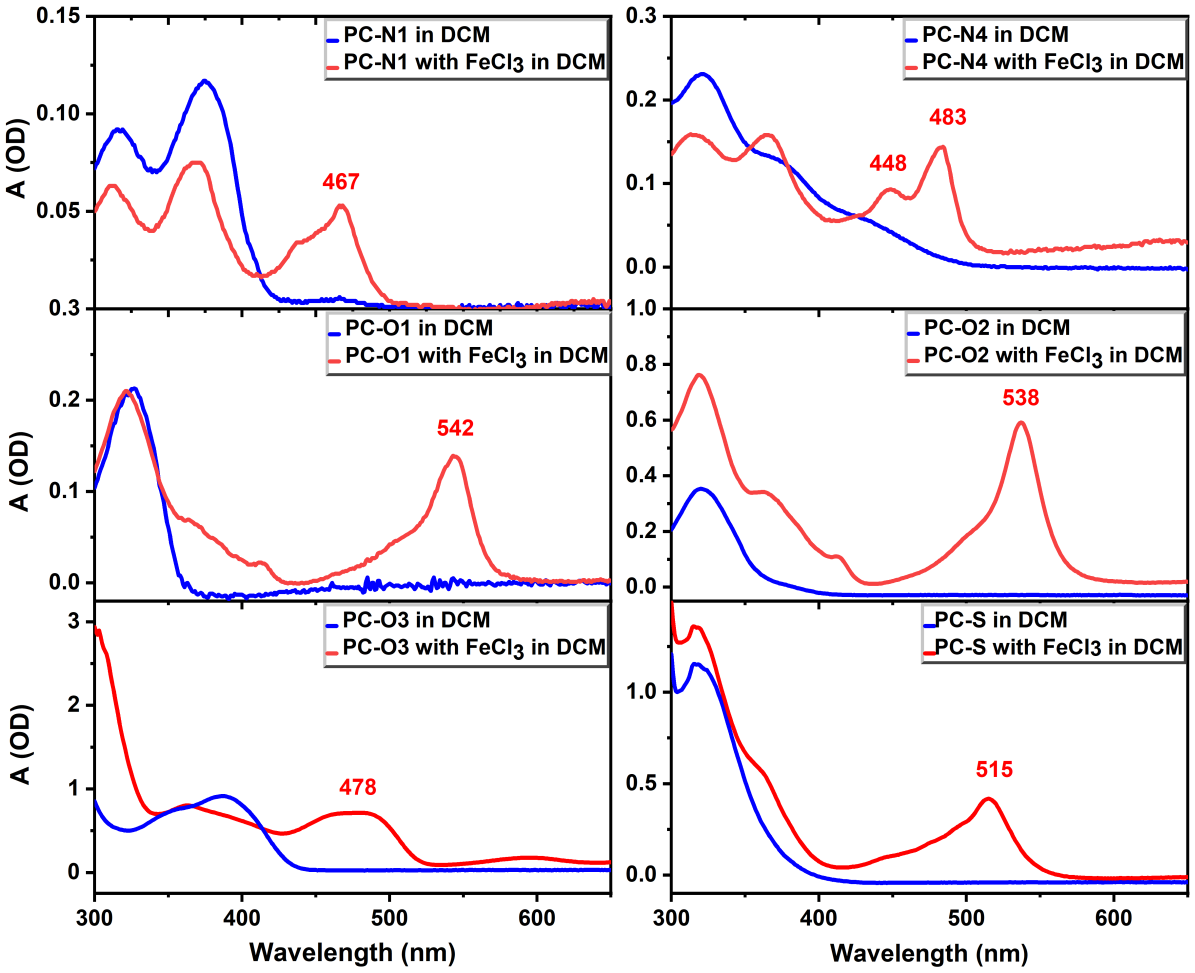

Figure E4. *UV-Vis spectra of PCs in dichloromethane (in blue) and with 3 equivalents of $FeCl_3$ (in red). Concentrations of PCs used were 2.1 mM for PC-N1, PC-O1, PC-O2, PC-O3; 5 mM for PC-N4, and 8 mM for PC-S. Spectra were taken using a Harrick cell with pathlength of 200 µm and a Thermo Scientific Genesys 10S spectrophotometer. $FeCl_3$ was used to oxidize the PCs to generate $PC^{\bullet+}$. UV-Vis Spectra for PC-N2, PC-N3, and PC-N5 with $FeCl_3$ are reported elsewhere.*[1,3]

7.3.3 Chapter 5

7.3.3.1 UV-Vis Spectra

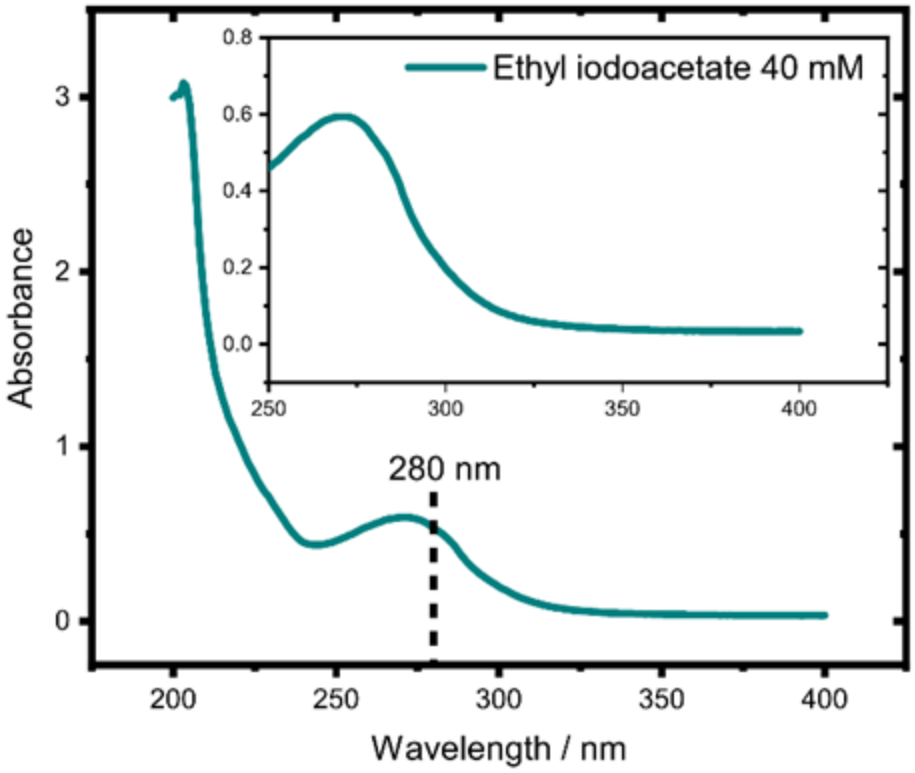

Figure E5. *Steady state UV-Vis absorption spectrum of 40 mM ethyl iodoacetate in tetrahydrofuran (pathlength = 300 μm). The A band (210 – 310 nm) is highlighted along with the chosen UV pump wavelength used for the TRIR experiments. Inset is an expanded view of the A band.*

7.3.3.2 FTIR Spectra

7.3.3.2.1 Ethyl iodoacetate (ethyl iodoacetate)

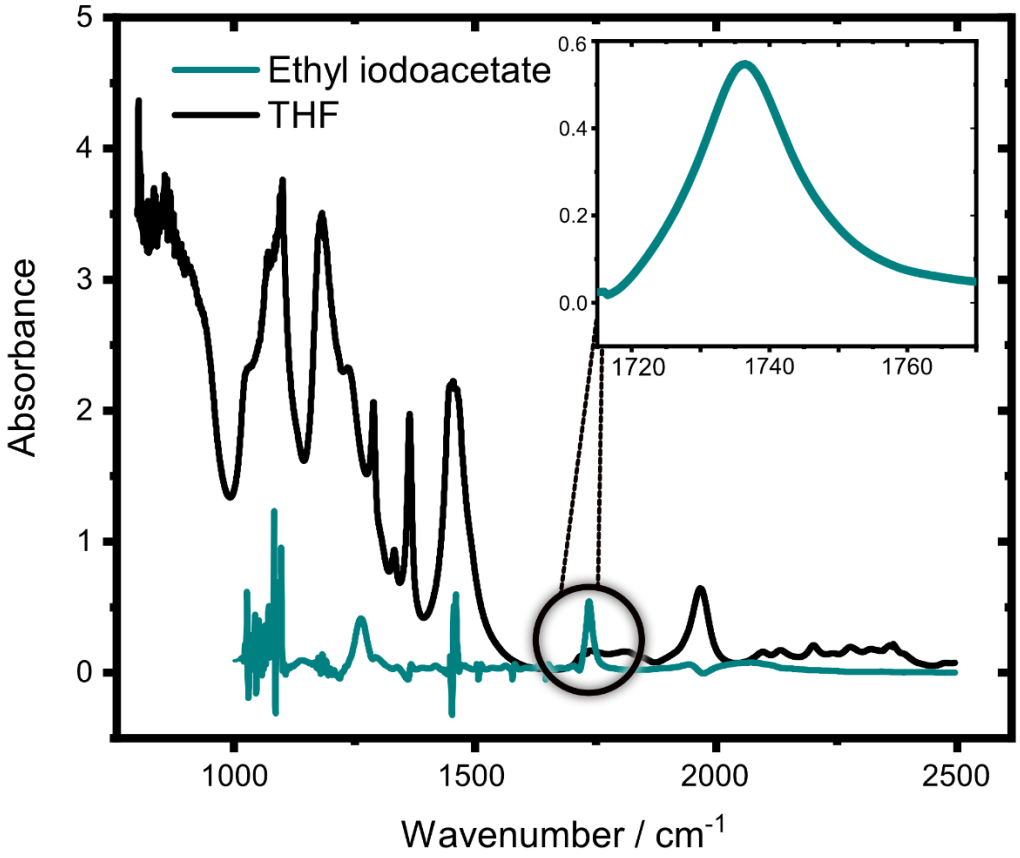

Figure E6. *FTIR absorption spectrum of 40 mM ethyl iodoacetate in THF (solvent features have been subtracted) overlaid with the solvent spectrum of THF. Inset shows an expanded view of the carbonyl stretch at 1736 cm^{-1} which sits between the THF absorption bands at 1450 cm^{-1} and 1950 cm^{-1}.*

7.3.3.2.2 *Ethyl-2-(3-cyclohexyl-3-(4,4,5,5-tetramethyl-1,3,2-dioxaborolan-2-yl)cyclobutyl)acetate (BCB boronate photoproduct **F**)*

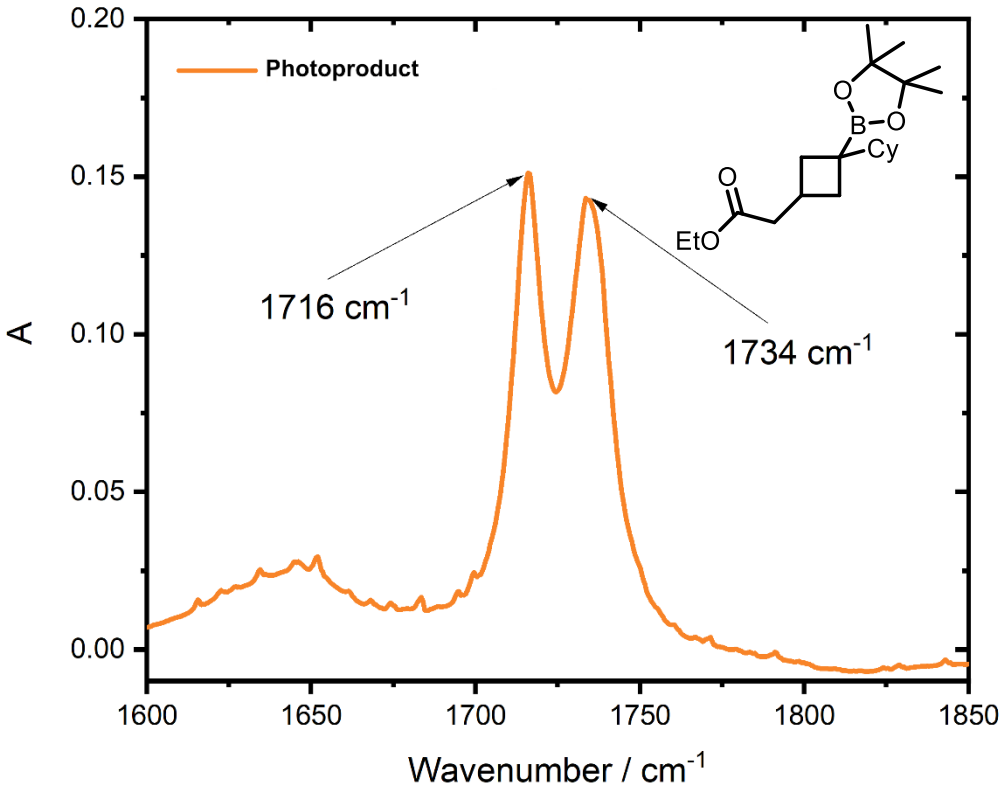

Figure E *FTIR absorption spectrum for ethyl 2-(3-cyclohexyl-3-(4,4,5,5-tetramethyl-1,3,2-dioxaborolan-2-yl)cyclobutyl)acetate (BCB boronate photoproduct **F**, 100 mM, 380 µm path length) taken in THF. Solvent absorption bands have been subtracted from the spectrum. The important peaks are labelled. Note that the compound used in this FTIR study is slightly different to the one produced in TRIR experiments for reasons of availability; here, a cyclohexane group is exchanged for the n-butyl group. This change is unlikely to have a significant effect on the FTIR shifts. The sample was synthesised previously by Silvi et al.*[7]

*7.3.3.2.3 Lithium 4,4,5,5-tetramethyl-2-phenyl-2-(prop-1-en-2-yl)-1,3,2-dioxaborolan-2-uide (Vinyl boronate **A'**)*

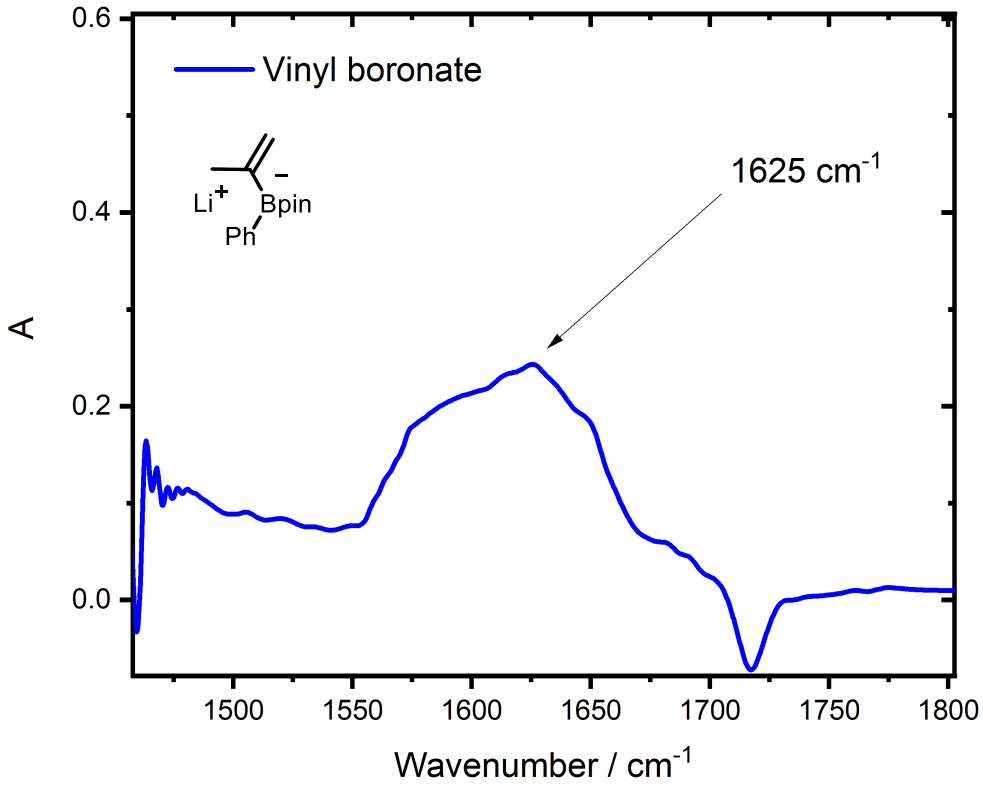

Figure E7. *FTIR absorption spectrum for lithium 4,4,5,5-tetramethyl-2-phenyl-2-(prop-1-en-2-yl)-1,3,2-dioxaborolan-2-uide (Vinyl boronate **A'**, 40 mM, 380 μm path length) taken in THF. Solvent absorption bands have been subtracted from the spectrum. The important peak is labelled.*

*7.3.3.2.4 Ethyl 4-phenyl-4-(4,4,5,5-tetramethyl-1,3,2-dioxaborolan-2-yl)pentanoate (Vinyl boronate photoproduct **F'**)*

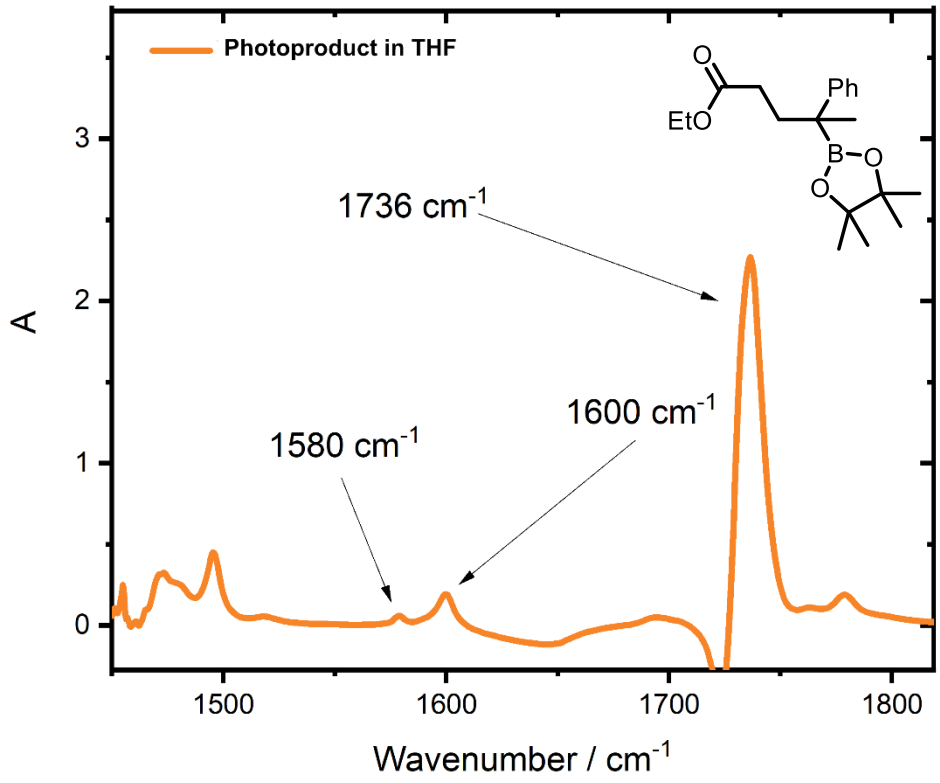

Figure E8. *FTIR absorption spectrum for ethyl 4-phenyl-4-(4,4,5,5-tetramethyl-1,3,2-dioxaborolan-2-yl)pentanoate (Vinyl boronate photoproduct **F'**, 100 mM, 300 µm path length) taken in THF. Solvent absorption bands have been subtracted from the spectrum. All the important peaks are labelled.*

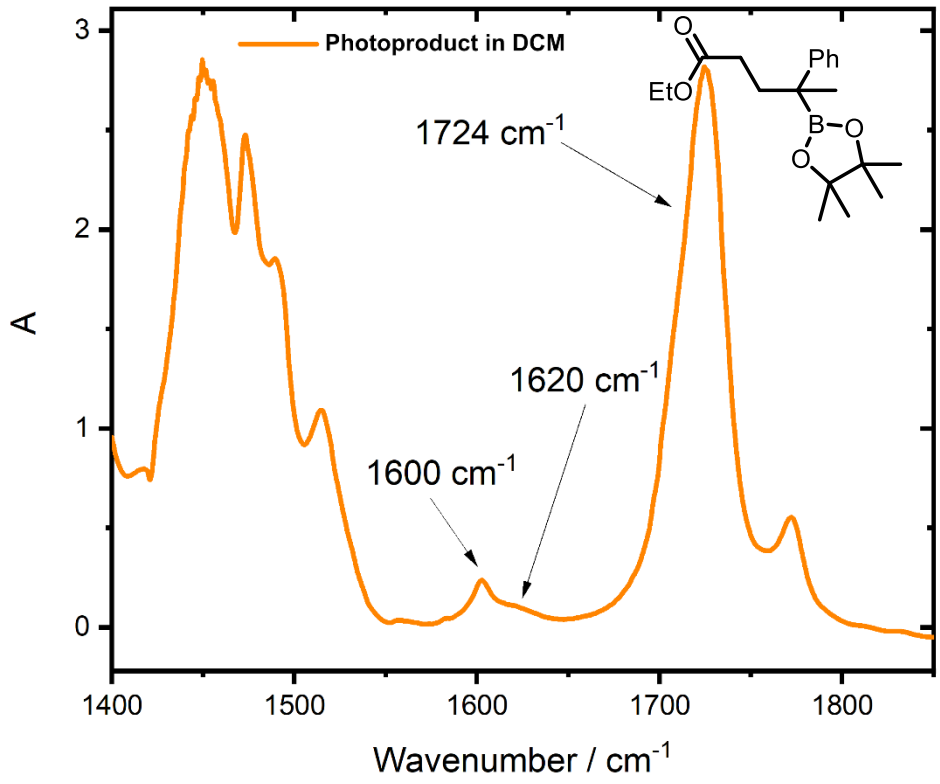

Figure E9. *FTIR absorption spectrum for ethyl 4-phenyl-4-(4,4,5,5-tetramethyl-1,3,2-dioxaborolan-2-yl)pentanoate (Vinyl boronate photoproduct* ***F'****, 360 mM, 300 μm path length) taken in dichloromethane (DCM) to obtain peak information in regions where THF absorbs all the IR light. Solvent absorption bands have been subtracted from the spectrum. All the important peaks are labelled.*

7.3.3.3 Calculated FTIR spectra

*7.3.3.3.1 BCB boronate photoproduct **F**, IAT intermediate **E**$_1$, and SET intermediate **E**$_2$*

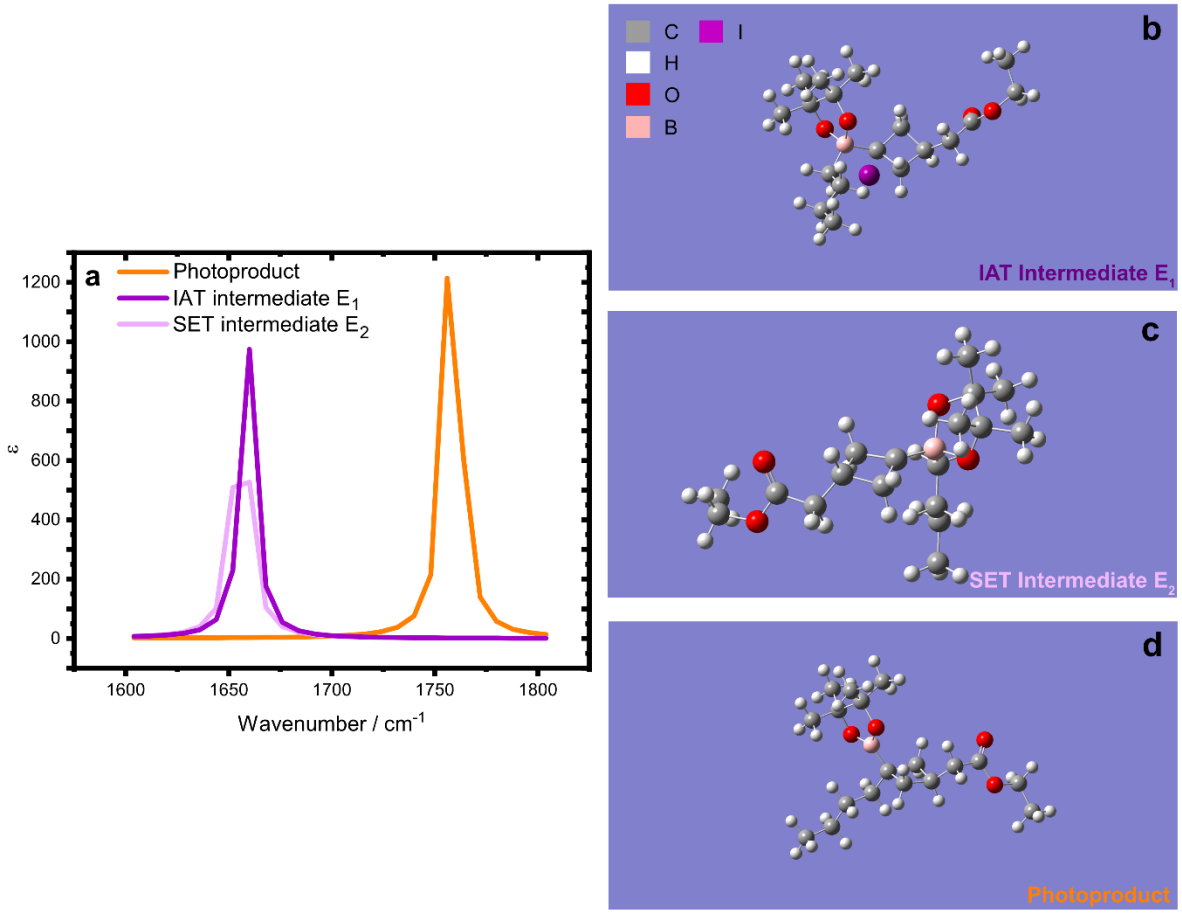

Figure E10. *Calculated structures and spectra of the BCB boronate photoproduct **F**, IAT Intermediate **E**$_1$, and SET Intermediate **E**$_2$ obtained using a LANL2DZ basis set and functional B3LYP (a) Vibrational modes observed in the 1600 cm^{-1} to 1800 cm^{-}1 range. (b) Optimised ground state structure of the IAT intermediate **E**$_1$. (c) Optimised ground state structure of the SET intermediate **E**$_2$. Please note that to avoid rearrangement to product during optimisation the coordinates between boron and carbon on the n-butyl group were input as redundant coordinates. (d) Optimised ground state structure of the BCB boronate photoproduct **F**.*

*7.3.3.3.2 Vinyl boronate photoproduct **F'** and Vinyl Intermediate **E'**$_1$ overlap*

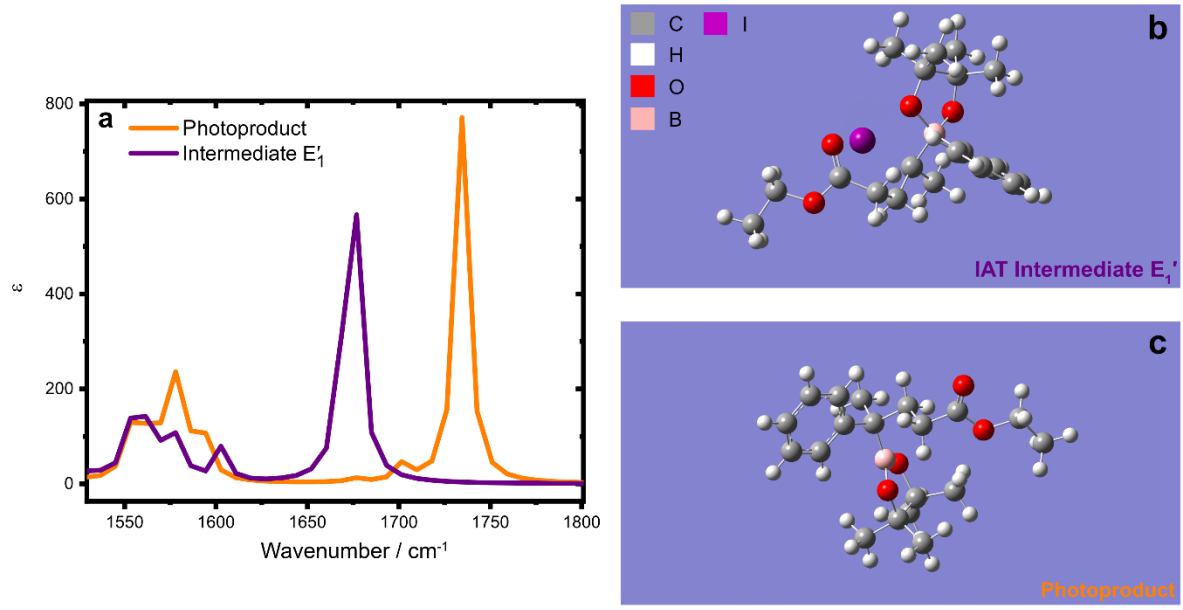

Figure E11 *Calculated structures and spectra of the Vinyl boronate photoproduct **F'** and Vinyl IAT Intermediate **E** obtained using a LANL2DZ basis set and functional B3LYP. (a) Vibrational modes observed in the 1545 cm^{-1} to 1800 cm^{-1} range. Each wavenumber has been scaled by a factor of 1.01. Note the overlapping C-H bending absorptions from 1550 cm^{-1} to 1625 cm^{-1} for the Vinyl boronate photoproduct and Vinyl intermediate **E**. (b) Optimised ground state structure of the vinyl intermediate **E**. (c) Optimised ground state structure of the reaction product.*

7.4 Transient Spectra

7.4.1 Chapter 3

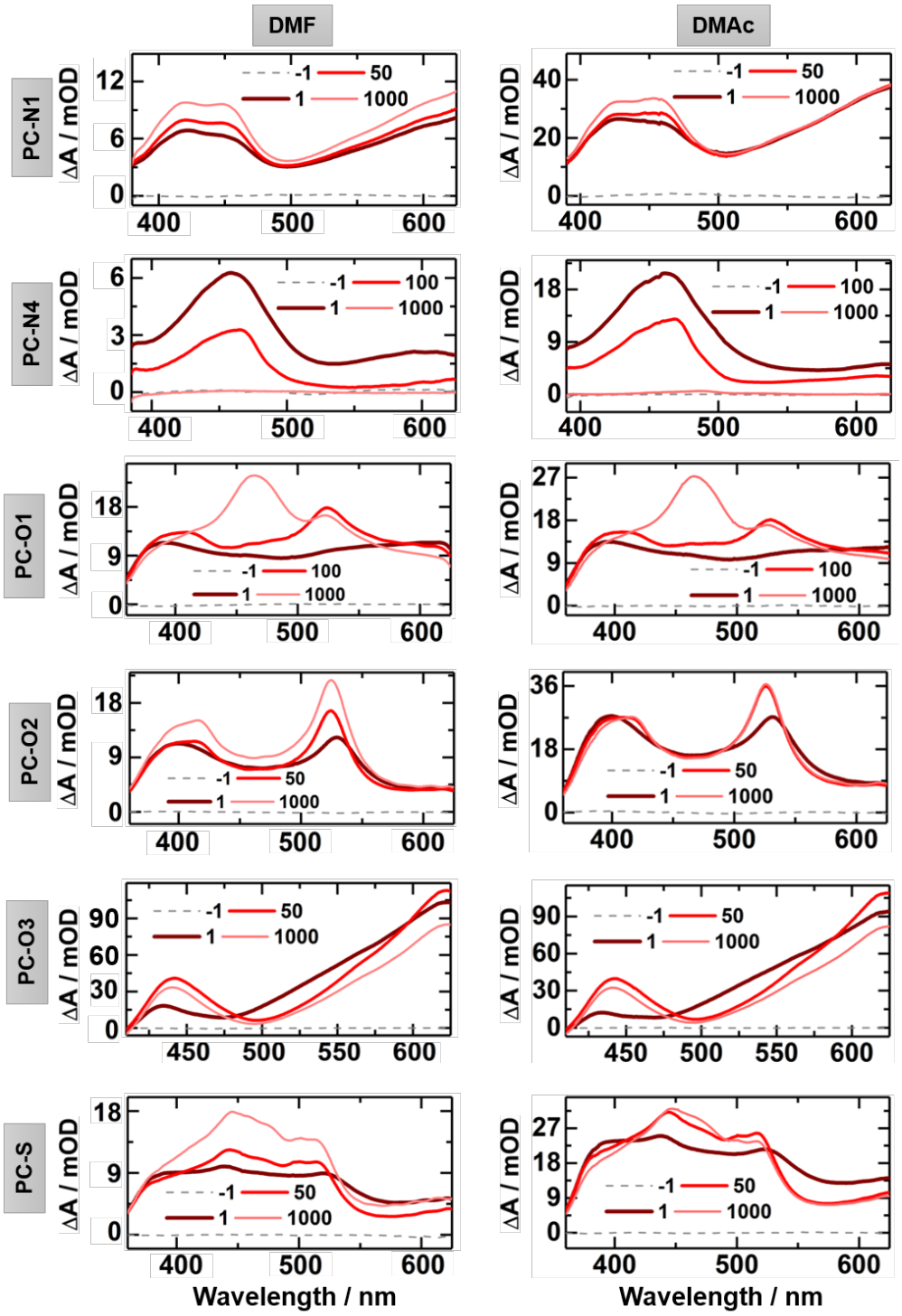

Figure E12. *Comparison of time-resolved electronic absorption spectroscopic data measured for six PCs in N,N-dimethylformamide (DMF) and N,N-dimethylacetamide (DMAc). In each panel, the inset key shows the pump-probe time delay in picoseconds. The data shown in column 1 are also included in Figure 5 of the main paper.*

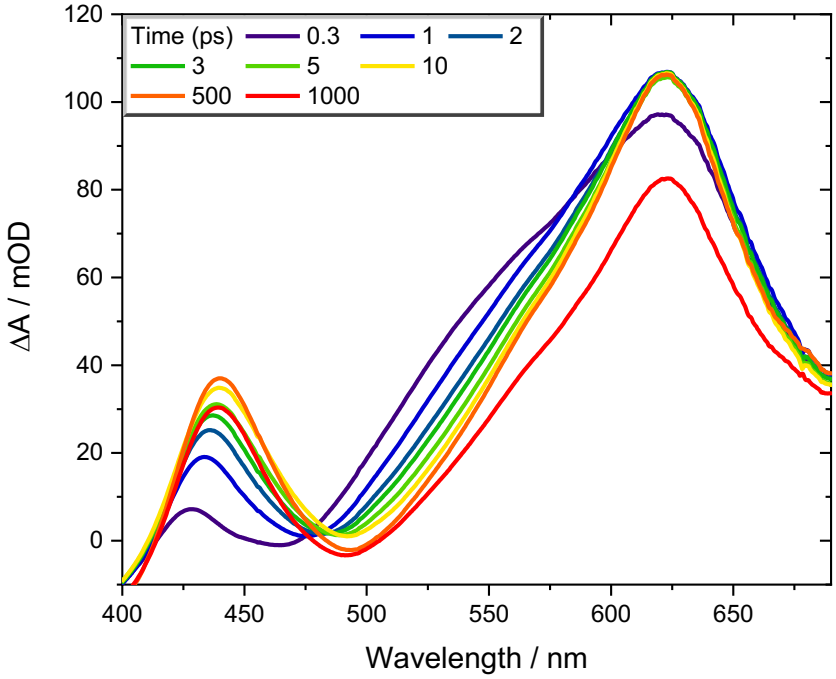

Figure E13. *Transient electronic absorption spectroscopy data measured for PC-O3 in N,N-dimethylformamide. The data shown here are an extension of Figure 5 of the main paper. They display the absorption spectra in the wavelength range from 400-690 nm to highlight the changes to the S_1 ESA band centred at ~625 nm and the decay of a shoulder located around 540 nm. The inset key shows the pump-probe time delay in picoseconds.*

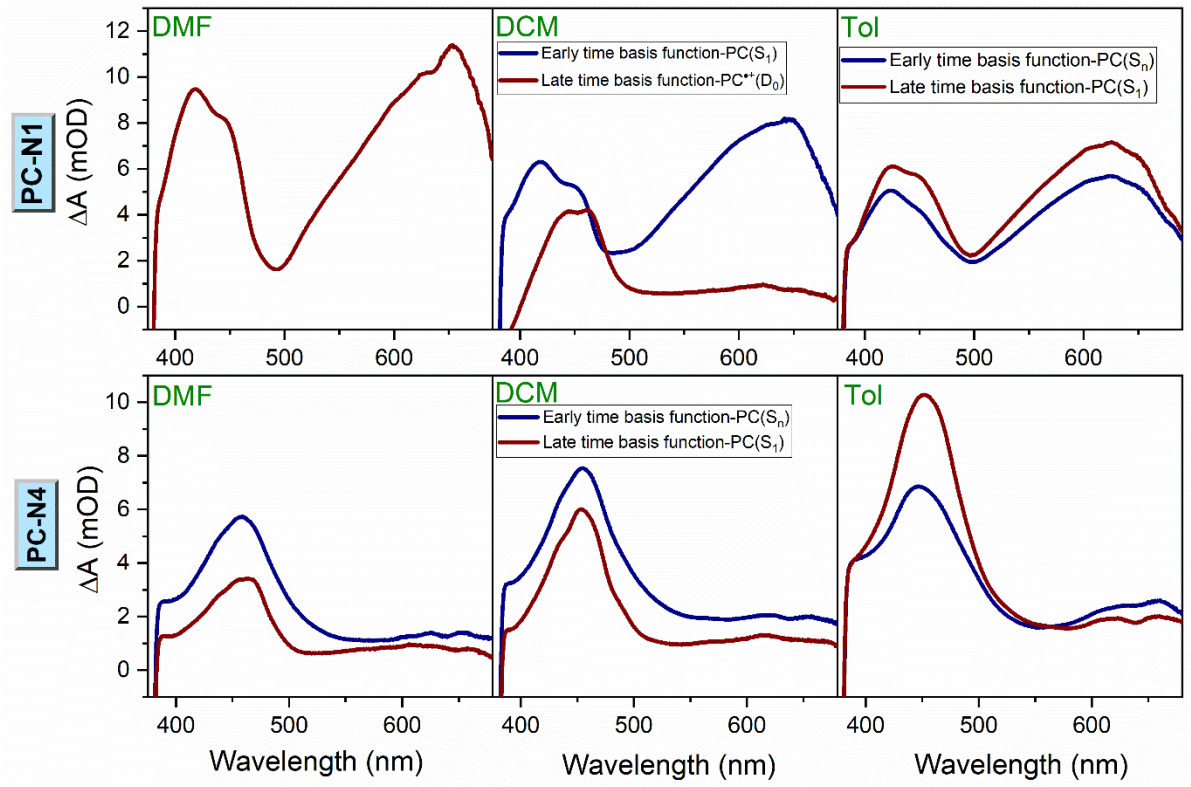

Figure E14. *Basis functions used to fit the TEAS data for PC-N1 and PC-N4 in N,N-dimethylformamide, dichloromethane, and toluene. For both PC-N1, and PC-N4, the experimental spectra can be satisfactorily decomposed using only two basis functions. For PC-N1 in DMF and toluene, and PC-N4 in all solvents, the basis function characterizing PC*(Sn) absorption spectra (blue trace) is chosen to be the early time spectrum at a time delay of 1 ps in the experimentally measured TEAS data. The second basis function is chosen from a later delay time measurement (~500-600 ps) and represents the PC(S1) absorption spectrum, with the exception of PC-N1 in DMF where only one basis function proved sufficient. For PC-N1 in DCM, reaction with the solvent causes the late time basis function to resemble the PC-N1•+ absorption spectrum and is obtained using a TEAS spectrum at a time delay of 1200 ps for a solution of PC-N1 with 2 M methyl 2-bromopropionate in DCM.*

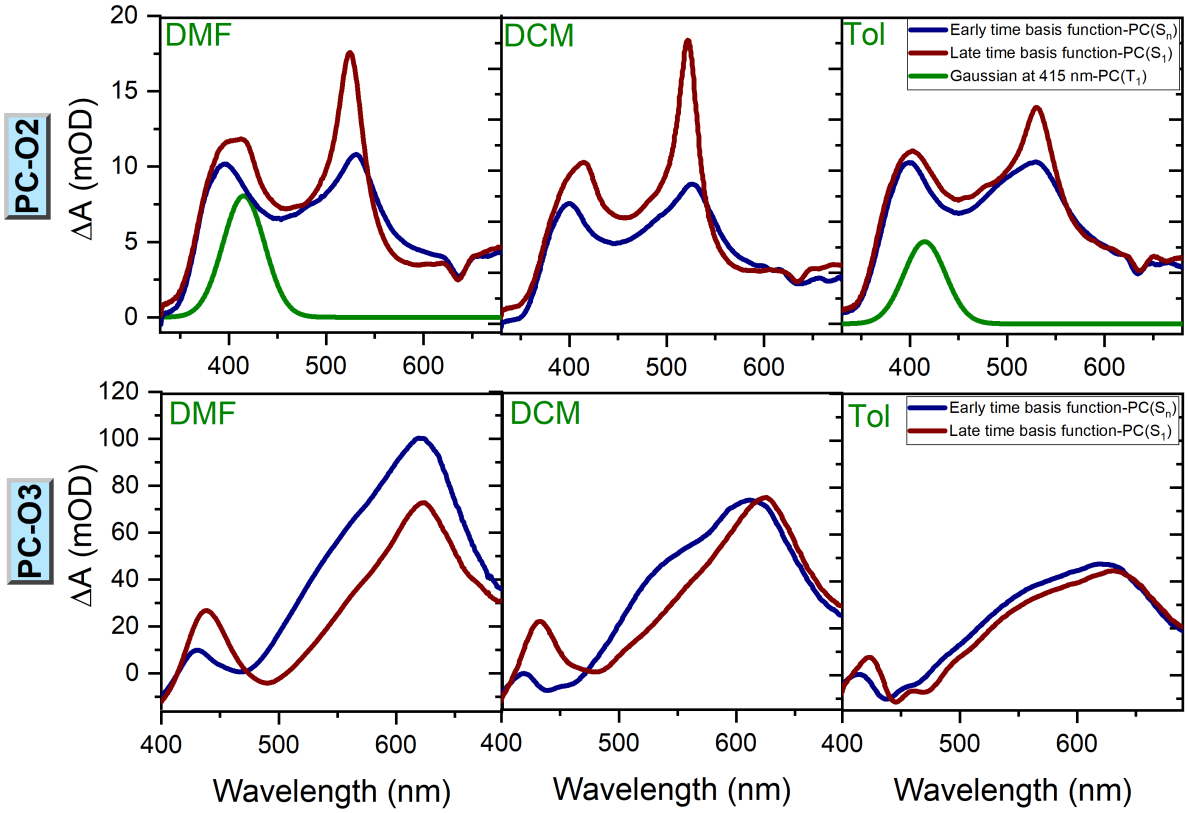

Figure E15. *Basis functions used to fit the TEAS data for PC-O2 and PC-O3 in N,N- dimethylformamide, dichloromethane, and toluene. For PC-O2 in DMF and toluene, the experimental spectra can be satisfactorily decomposed using three basis functions. The basis function characterizing PC-O2*(S_n) absorption (blue) is chosen to be the early time spectrum at a time delay of 1 ps in the experimentally measured TEAS data. The late time basis function (maroon) is selected as the 50 ps measurement in the TEAS data and represents the PC-O2 (S_1) absorption spectrum. A Gaussian function centred at 415 nm (green) is used as a basis function to represent PC-O2 (T_1) state absorption. In DCM, this Gaussian basis function is not required because the triplet state population does not grow on the time scale of the reported TEAS data. For PC-O3, only two basis functions are required: an early time function characterizing vibrationally hot PC-O3 (S_1) state in the Franck Condon region, and a late time basis function representing the absorption spectrum of the vibrationally relaxed PC-O3 (S_1) state. In the top-row spectra, the dips centred at 636 nm are caused by scattered light from the excitation wavelength detected in second order.*

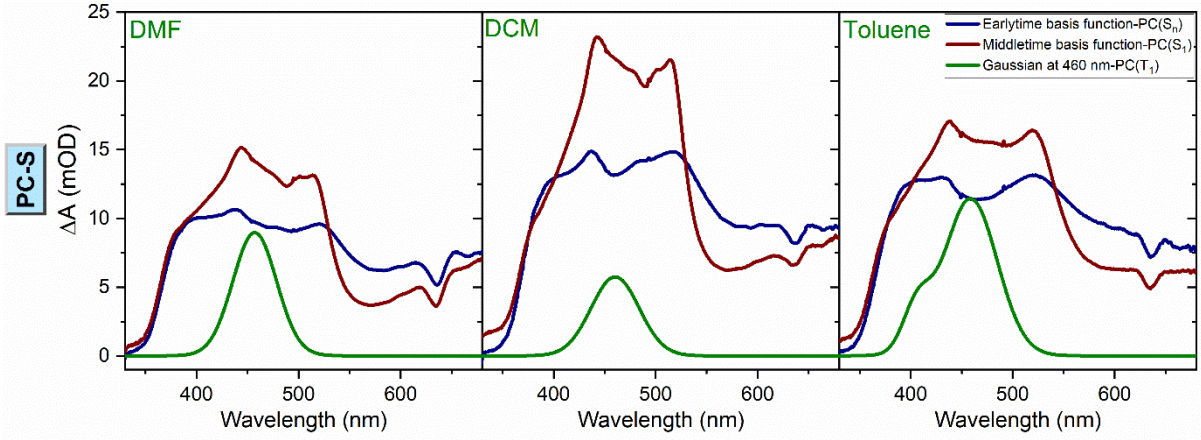

Figure E16. *Basis functions used to fit the TEAS data for PC-S in N,N-dimethylformamide, dichloromethane, and toluene. In all solvents, the experimental spectra can be satisfactorily decomposed using three basis functions. In each panel, the basis function characterizing the PC*(Sn) absorption (blue) is chosen to be the early time spectrum at a time delay of 1 ps in the experimentally measured TEAS data. The middle-time basis function (shown in maroon) represents the PC (S1) absorption and is taken from the TEAS data at a time delay of 50 ps. A Gaussian function centred at 460 nm (shown in green) represents the PC-S (T1) spectrum in DMF and DCM. For toluene, a function constructed from two Gaussians best fits the late time spectrum. The dips in the spectra at 636 nm are attributed to scattered light from the excitation laser pulse observed in second order in the spectrometer.*

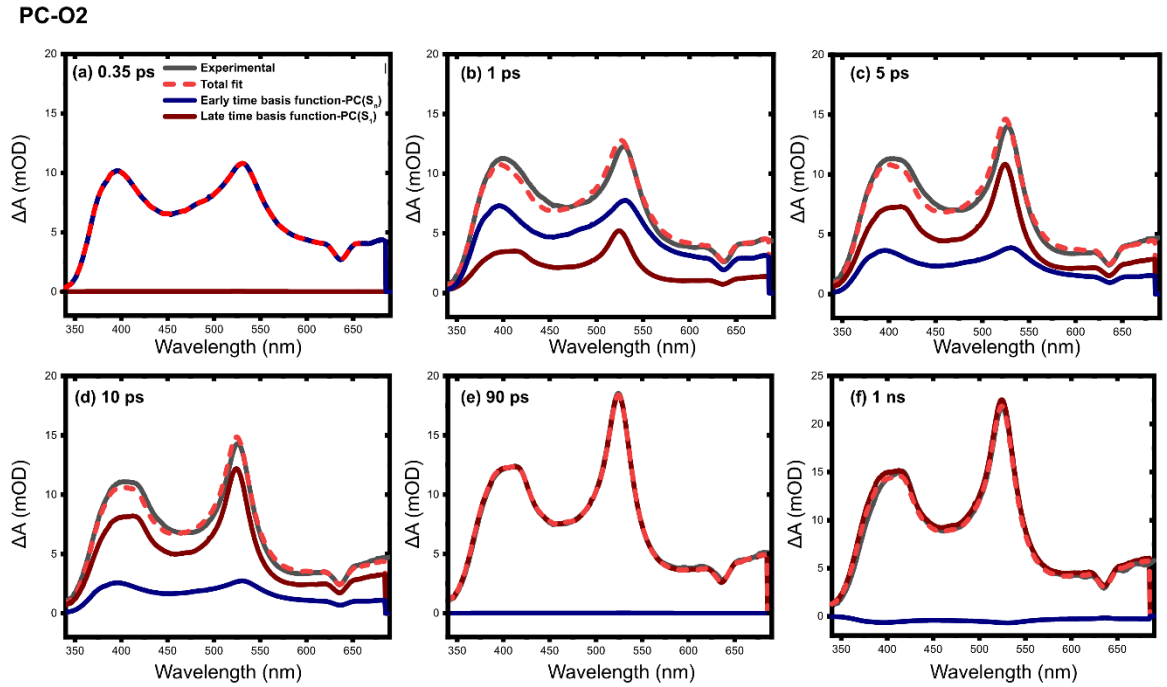

Figure E17. *Progression of the spectral decomposition of TEAS data illustrated for PC-O2 in DMF, using the basis functions plotted in figure S6. Panels show the evolution of the spectral fits from early (a, b and c) to intermediate (d and e) and later times (f) as indicated by inset time delays. Early and late time basis functions are represented by blue and burgundy lines, respectively. The total fit is shown by the dashed red line, and the recorded spectra are plotted as solid grey lines. The dips in the spectra at 636 nm are attributed to scattered light from the excitation laser pulse observed in second order in the spectrometer.*

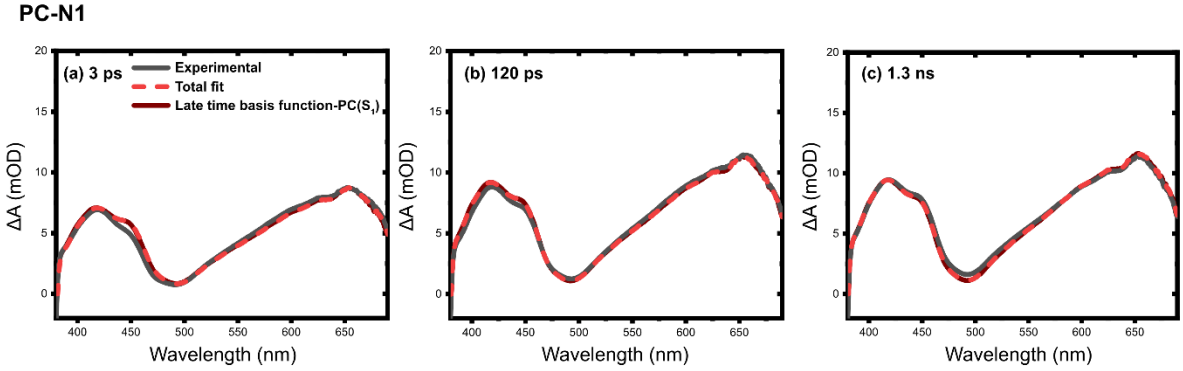

Figure E18. *Progression of the spectral decomposition of TEAS data illustrated for PC-N1 in DMF, using the basis functions plotted in* ***Figure E14****. Panels show the evolution of the spectral fits from early (a) to intermediate (d) and later times (c) as indicated by inset time delays. The single late time basis function used in the analysis is shown by the burgundy line. The total spectral fit is shown by the dashed red line, and the recorded spectra are plotted as solid grey lines.*

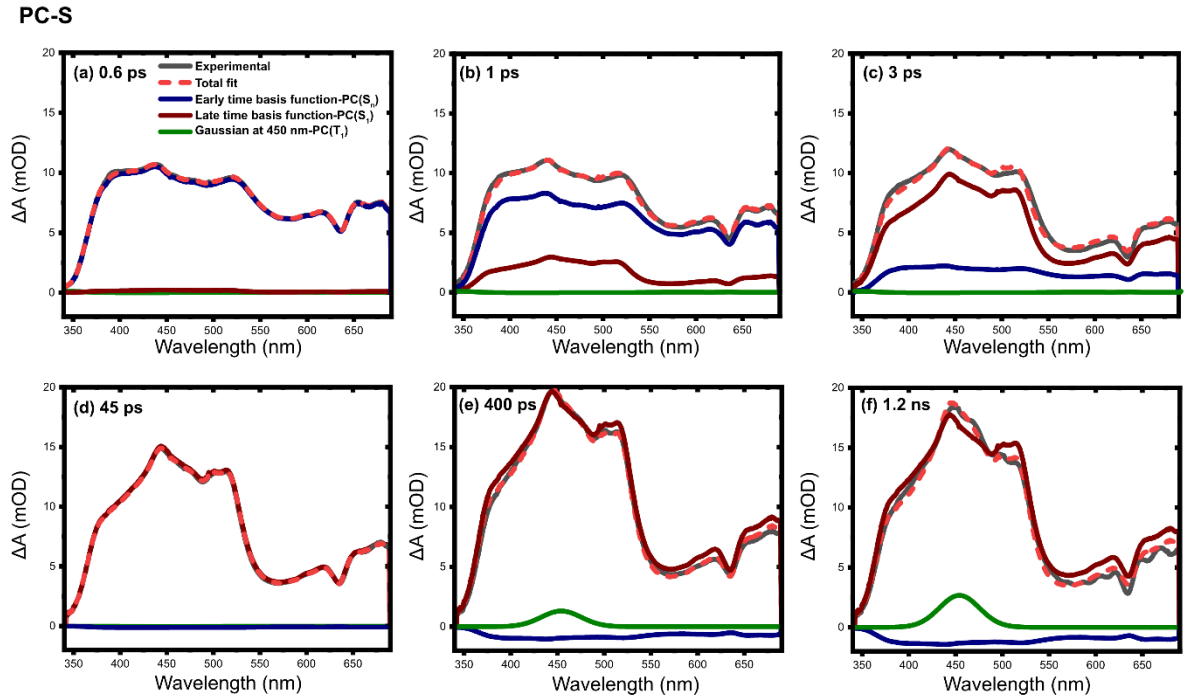

Figure E19. *Progression of the spectral decomposition of TEAS data illustrated for PC-S in DMF, using the basis functions plotted in* ***Figure E16****. Panels show the evolution of the spectral fits from early (a, b and c) to intermediate (d and e) and later (f) times as indicated by inset time delays. Early and late time basis functions are represented by blue and burgundy lines, respectively. The Gaussian fit function is shown in green, the total fit is shown by the dashed red line, and the recorded spectra are plotted as solid grey lines.*

7.4.2 Chapter 4

7.4.2.1 TVAS of PC-N1 with MBP

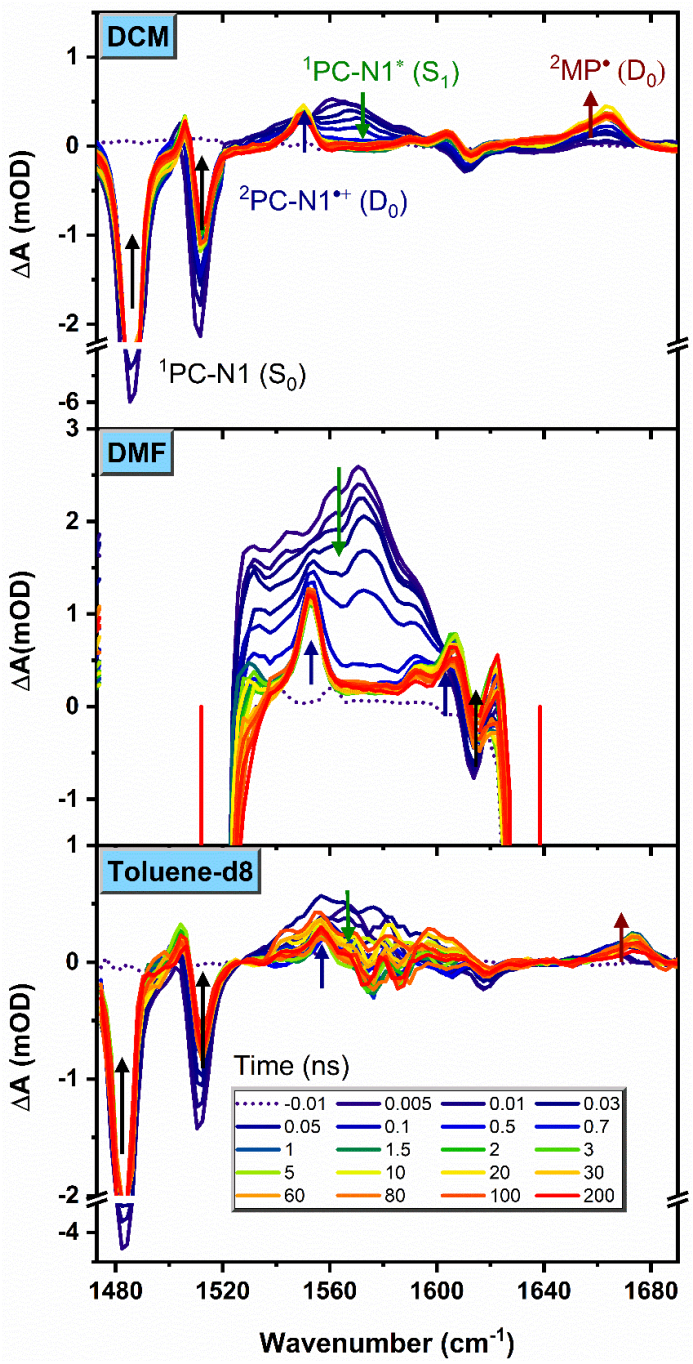

Figure E20. *TVAS measurement for 4.2 mM PC-N1 (pathlength 100 µm) with 0.8 M MBP in DCM, DMF and toluene-d_8. Arrows show the directions of change of the IR bands and are colour coded to the labels of the corresponding IR bands.*

7.4.2.2 TVAS of PC-O1 with MBP

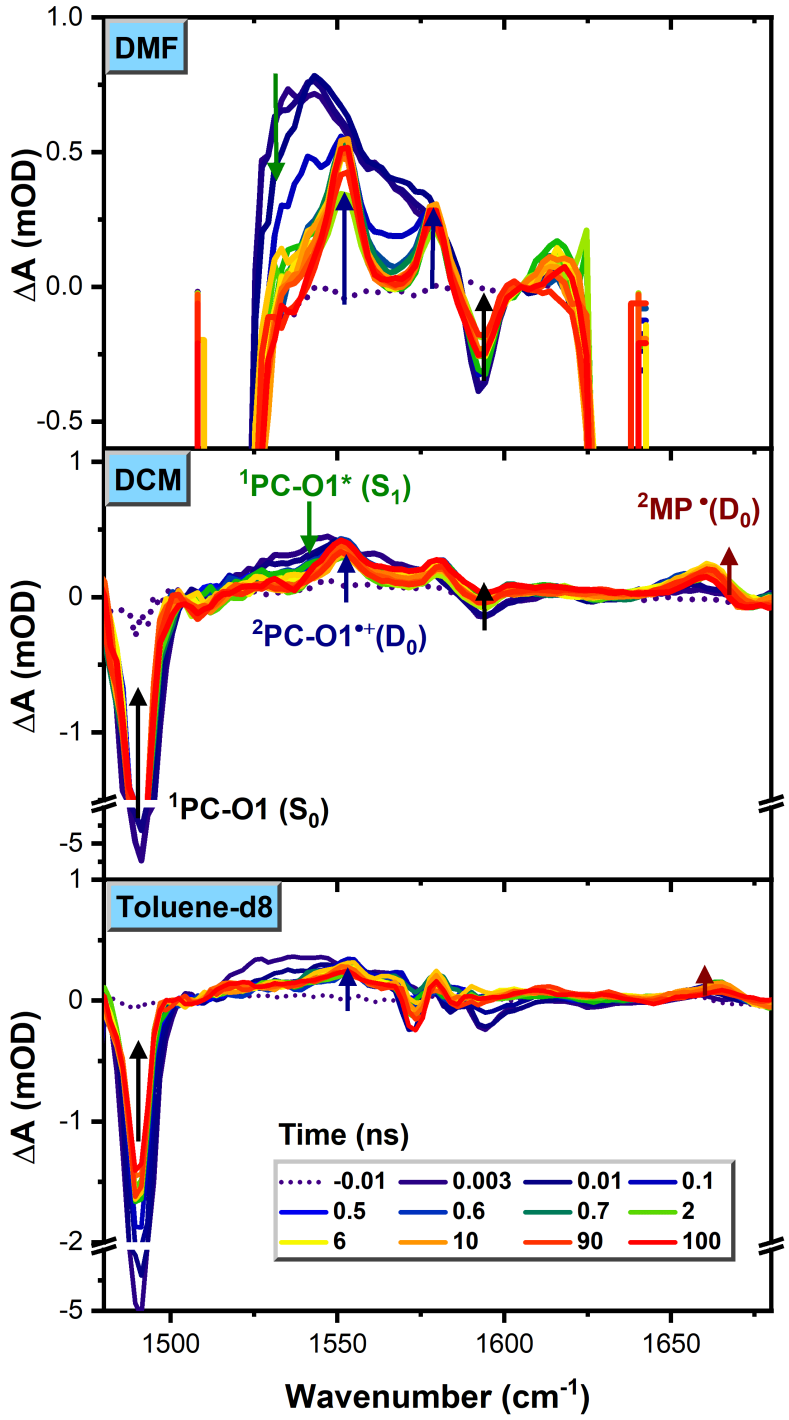

Figure E21. *TVAS measurement for 3.2 mM PC-O1 (pathlength 100 μm) with 0.8 M MBP in DMF, DCM and toluene-d_8. Arrows show the directions of change of the IR bands and are colour coded to labels of the corresponding IR bands.*

7.4.2.3 TEAS Measurement of PC-O1 with MBP

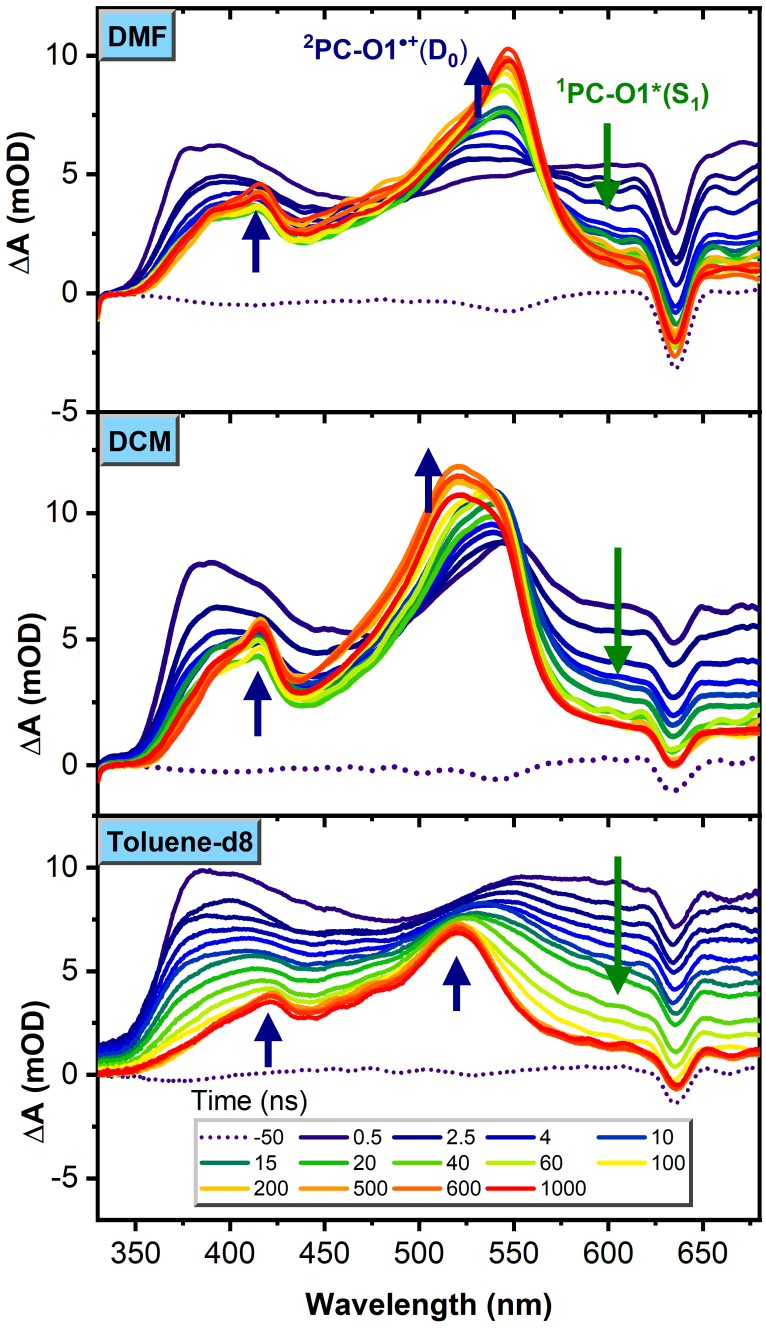

Figure E22. *TEAS measurement for 3.2 mM PC-O1 (pathlength 380 μm) with 1.5 M MBP in DMF, DCM and toluene. The dips centred at 636 nm result from pump-laser scatter detected in second order by the spectrometer (λ_{exc}=318 nm). Arrows show the directions of change of the IR bands and are colour coded to the labels of the corresponding IR bands.*

7.4.2.4 TVAS Measurement of PC-O2 with MBP

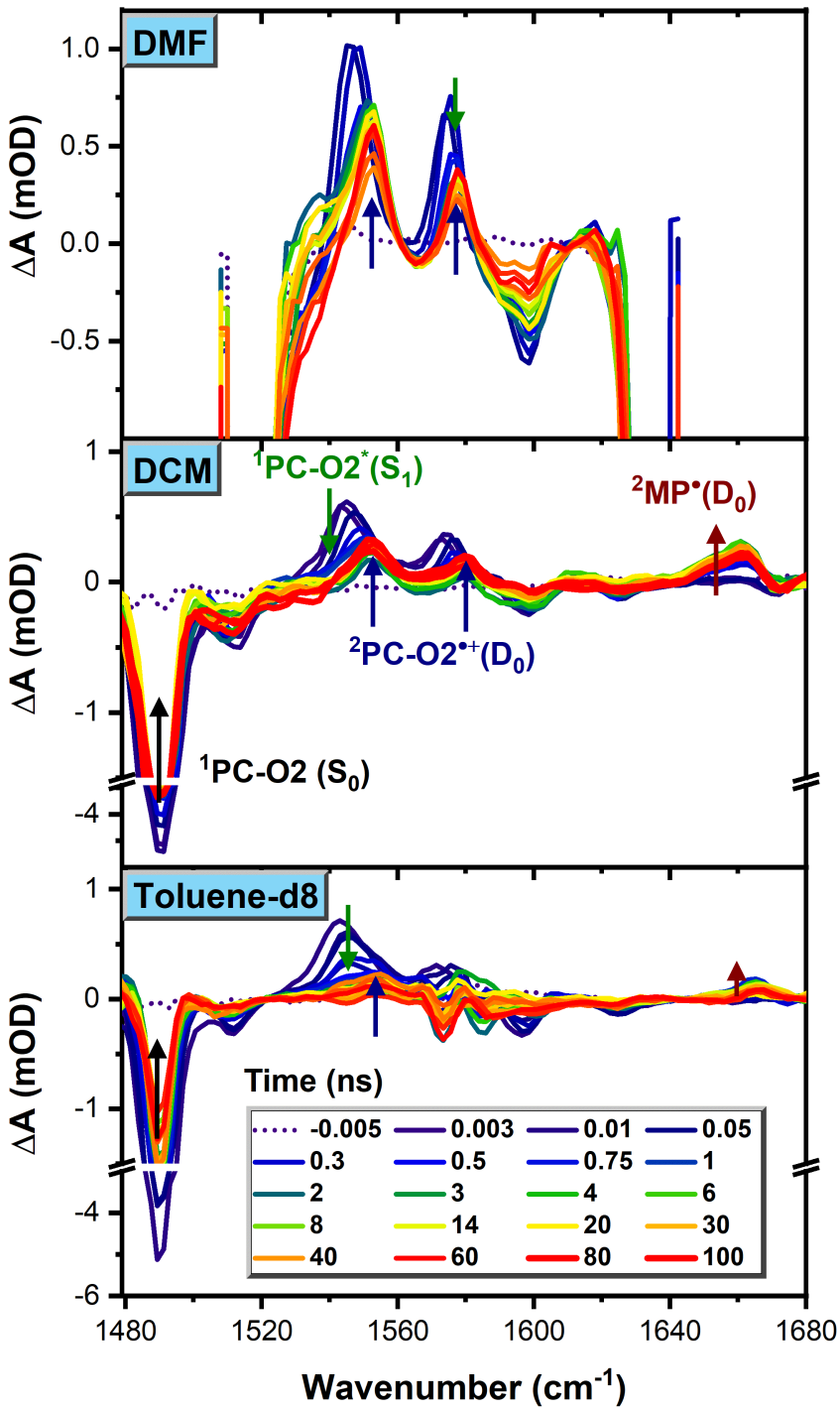

Figure E23. *TVAS measurements for PC-O2 (2.9 mM) with 0.8 M MBP in DMF, DCM and toluene-d_8 with a pathlength of 100 µm. Arrows show the directions of change of the IR bands and are colour coded to the labels of the corresponding IR bands.*

7.4.2.5 TEAS Measurement of PC-O2 with MBP

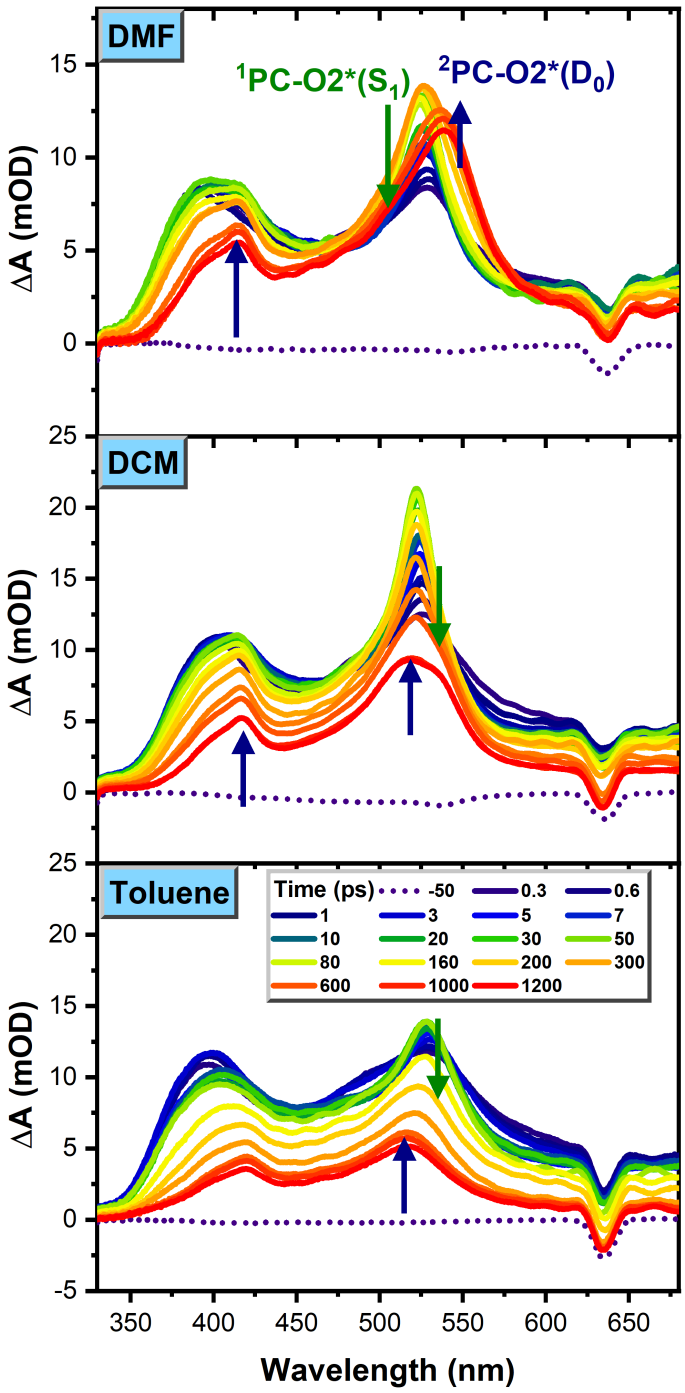

Figure E24. *TEAS measurements for PC-O2 (2.9 mM) with 2.0 M MBP in DMF, DCM and toluene with a pathlength of 380 µm. The dips centred at 636 nm result from pump-laser scatter detected in second order by the spectrometer (λ_{exc}=318 nm). Arrows show the directions of change of the electronic absorption bands and are colour coded to the labels of the corresponding bands.*

7.4.2.6 TVAS Measurement of PC-O3 with MBP

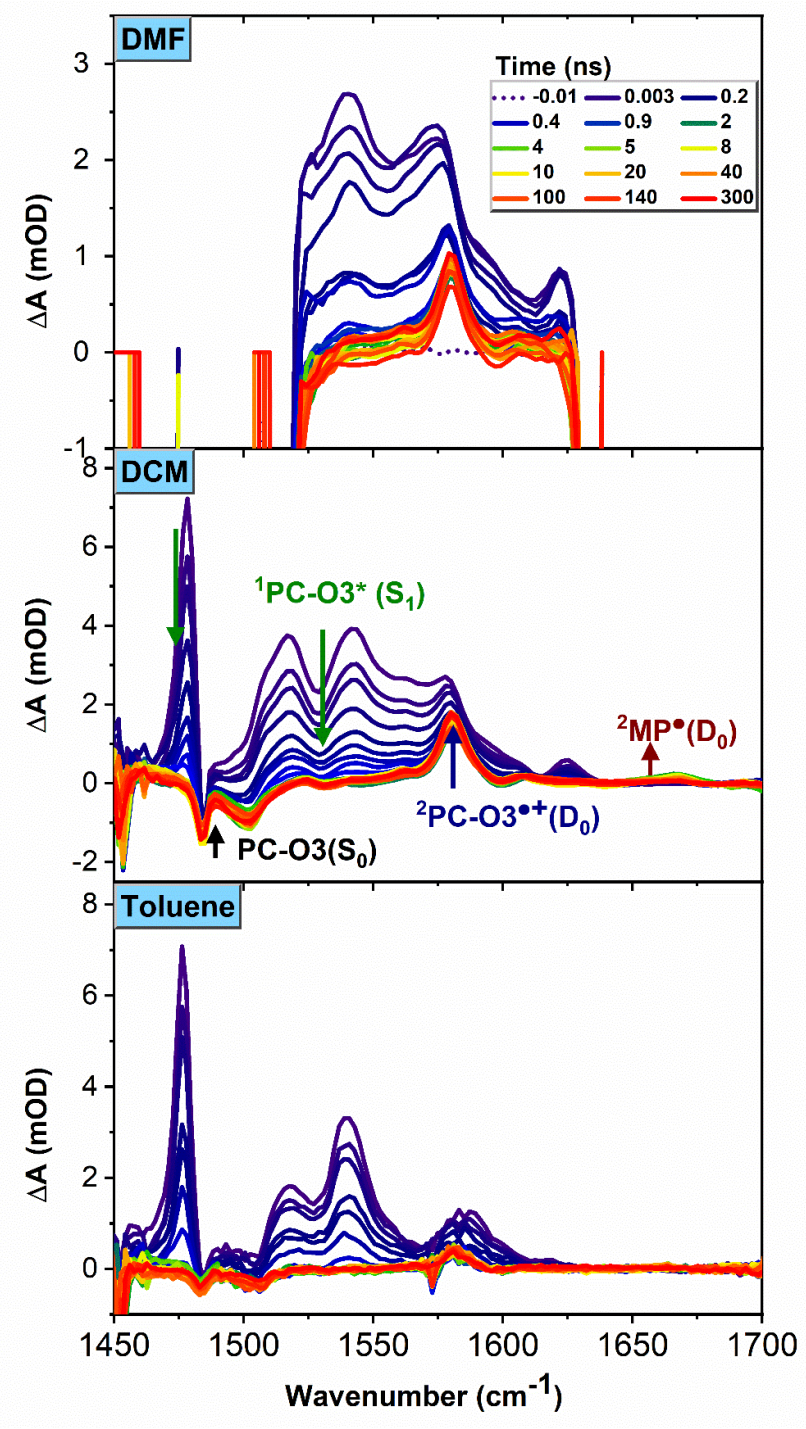

Figure E25. *TVAS measurements for PC-O3 (1.0 mM) with 0.8 M MBP in DMF, DCM and toluene-d_8 using a pathlength of 100 μm. Arrows show the directions of change of the IR bands and are colour coded to the labels of the corresponding IR bands.*

7.4.2.7 TEAS Measurement of PC-O3 with MBP

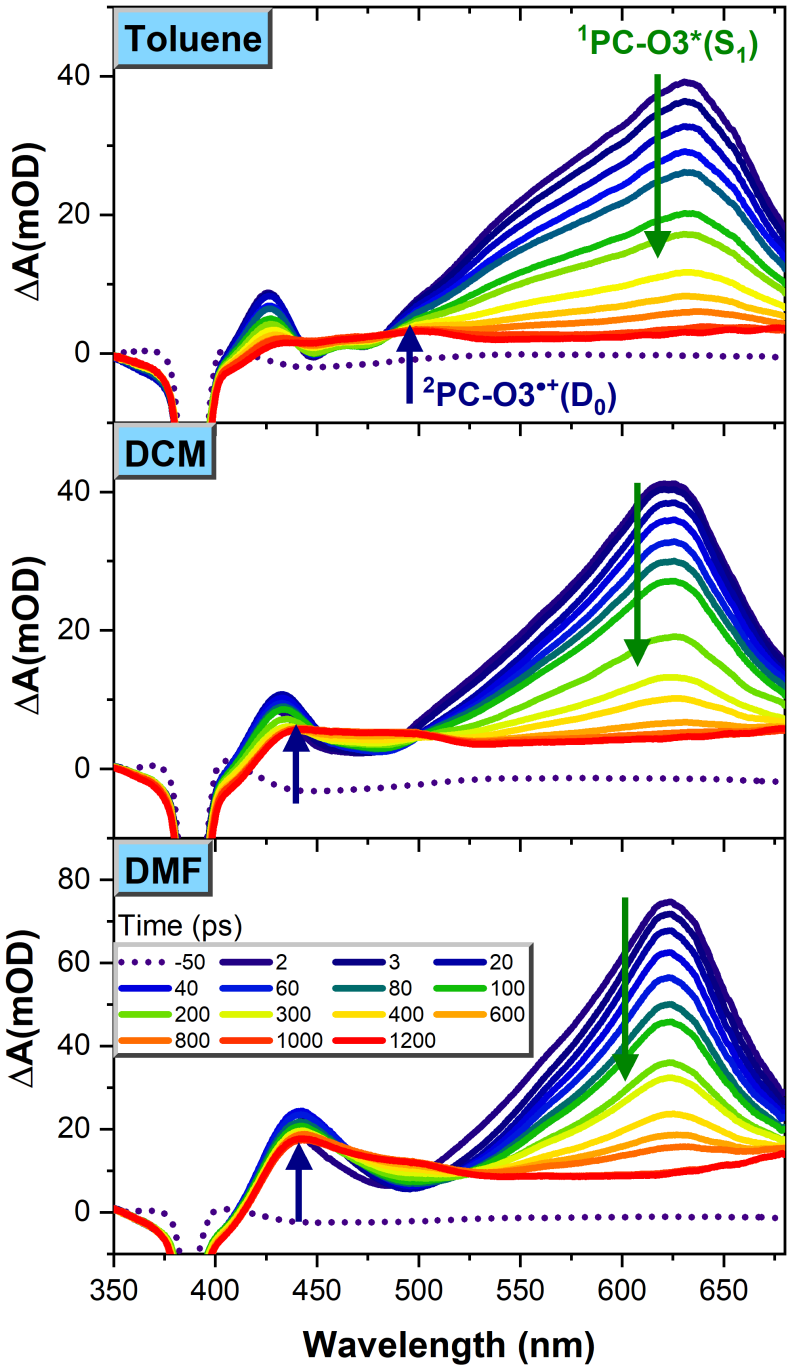

Figure E26. *TEAS measurements for PC-O3 (1.0 mM) with 2.0 M MBP in toluene, DCM and DMF using a pathlength of 380 μm. The dips centred at 389 nm result from pump-laser scatter detected in first order by the spectrometer. Arrows show the directions of change of the electronic absorption bands and are colour coded to the labels of the corresponding bands.*

7.4.2.8 TVAS Measurement of PC-S with MBP

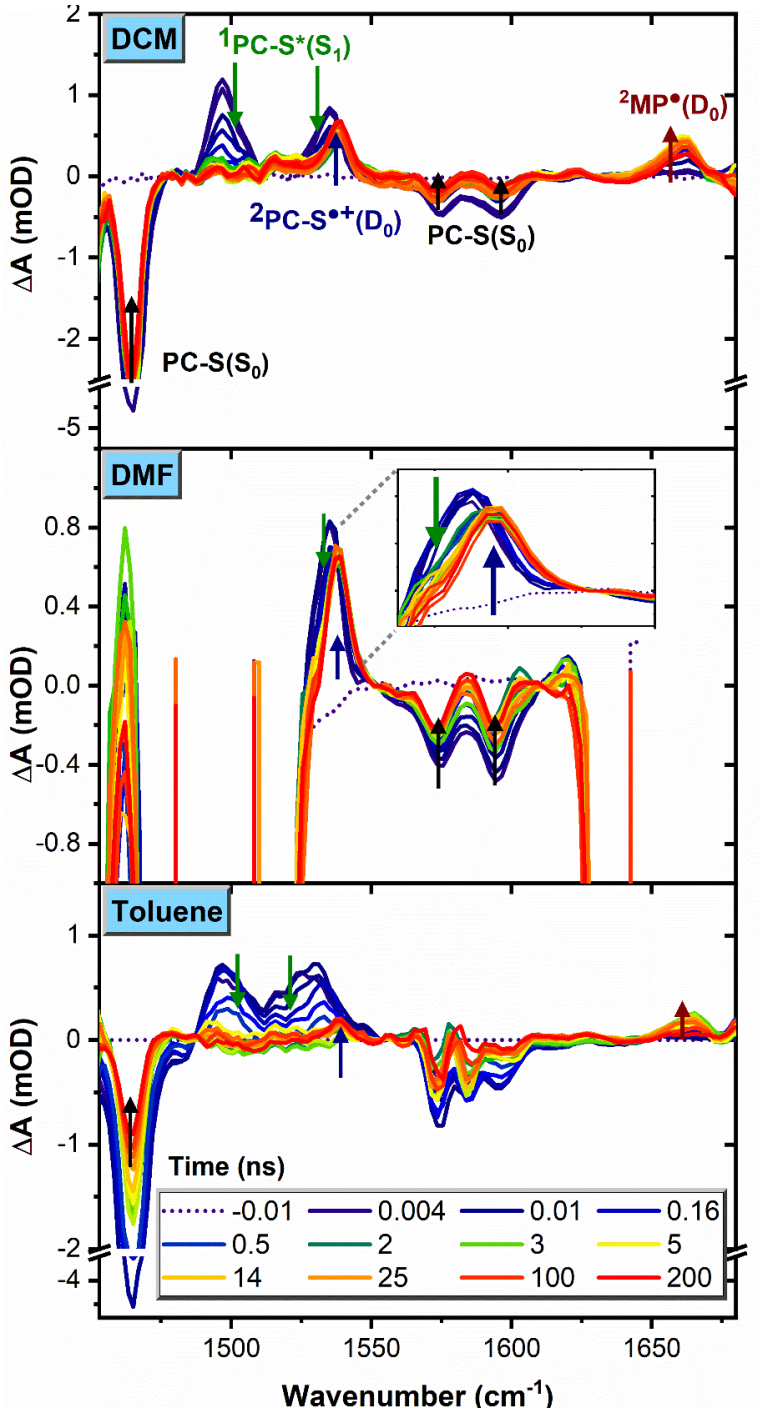

Figure E27. *TVAS measurements for PC-S (7.5 mM) with 0.8 M MBP in DCM, DMF and toluene-d_8 using a pathlength of 100 μm. Arrows show the directions of change of the IR bands and are colour coded to the labels of the corresponding IR bands.*

7.4.2.9 TEAS Measurement of PC-S with MBP

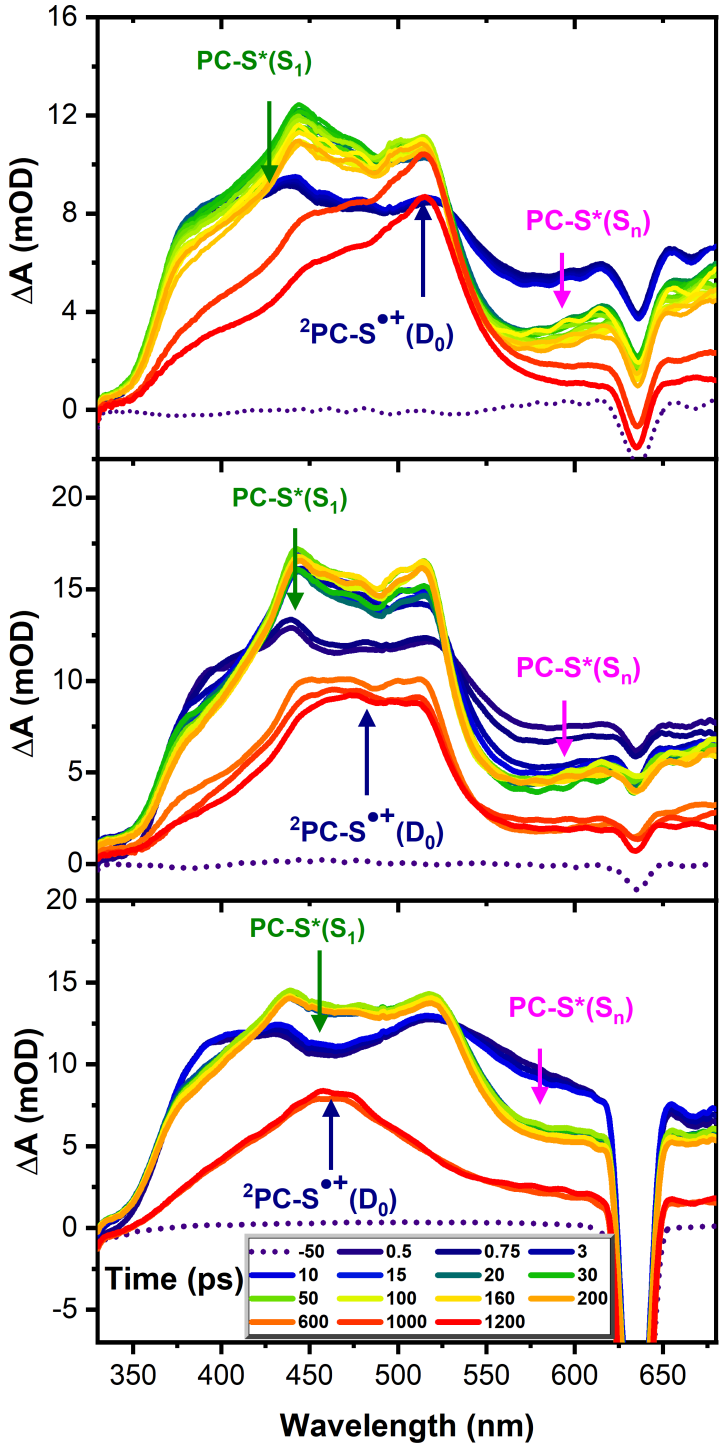

Figure E28. *TEAS measurements for PC-S (7.5 mM) with 2.0 M MBP in DMF, DCM and toluene using a pathlength of 380 µm. The dips centred at 636 nm result from pump-laser scatter detected in second order by the spectrometer (λ_{exc}=318 nm). Arrows show the directions of change of the electronic absorption bands and are colour coded to the labels of the corresponding bands.*

7.4.2.10 TEAS data and Kinetics for PC-S*(S_1) + MBP reaction in DMF

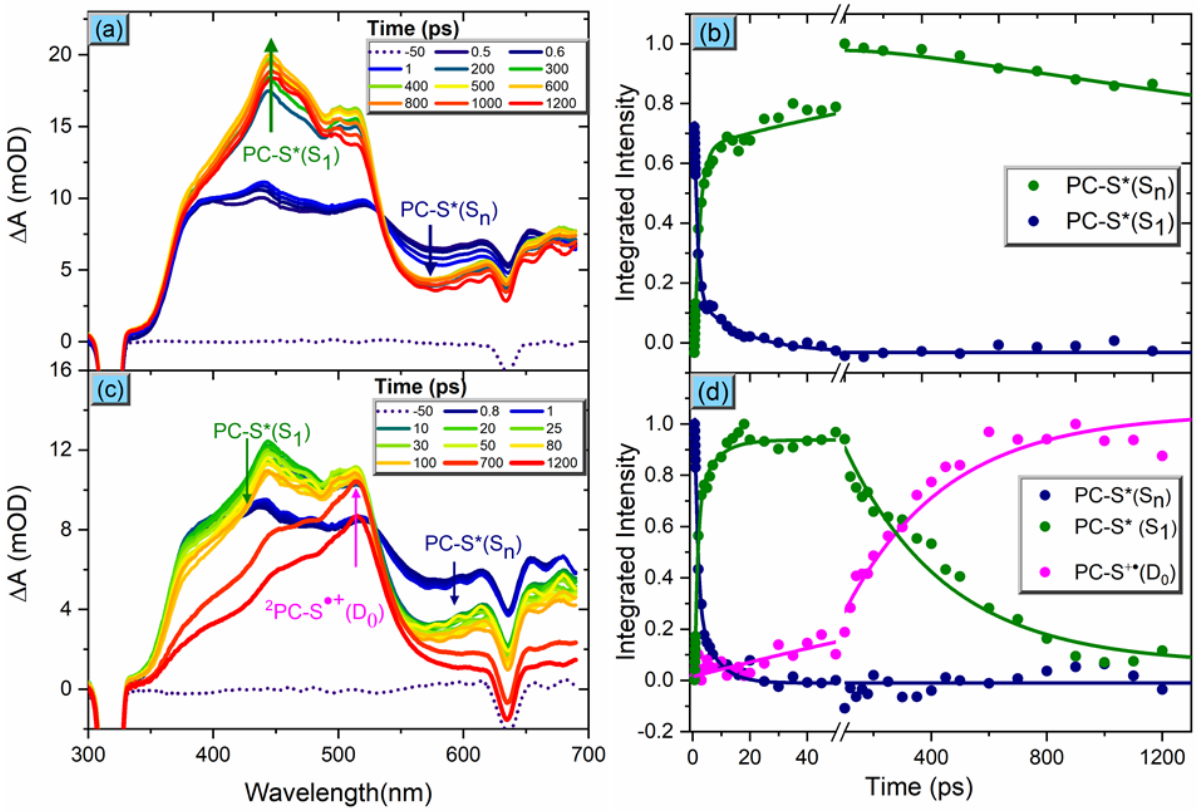

Figure E29. *TEAS measurements and corresponding kinetic fits for PC-S (7.5 mM) without and with MBP (2.0 M) in DMF. Panels (a) and (b) correspond to the TEAS measurements of PC-S in DMF, showing decay of a broad band for PC-S*(S_n) ESA and growth of a sharper band for PC*(S_1) ESA. The kinetic traces in panel (b) show the PC*(S_1) rising as PC*(S_n) decays. Panels (c) and (d) correspond to TEAS measurements with MBP added to the PC-S solution in DMF. A new peak can be seen arising with a maximum at ~515 nm, which we assign to the $PC^{\bullet+}$(D_0) cation. The kinetic traces in panel (d) show the PC-$S^{\bullet+}$(D_0) trace rising as PC-S*(S_1) decays. In panels (a) and (b) the sharp fall-off in ΔA below 360 nm reflects the onset of absorption by the PC (λ_{exc}=318 nm). The dips at 636 nm arise from pump scatter detected on the second order by the spectrometer*

7.4.2.11 Basis Function Fits for TEAS data in DMF

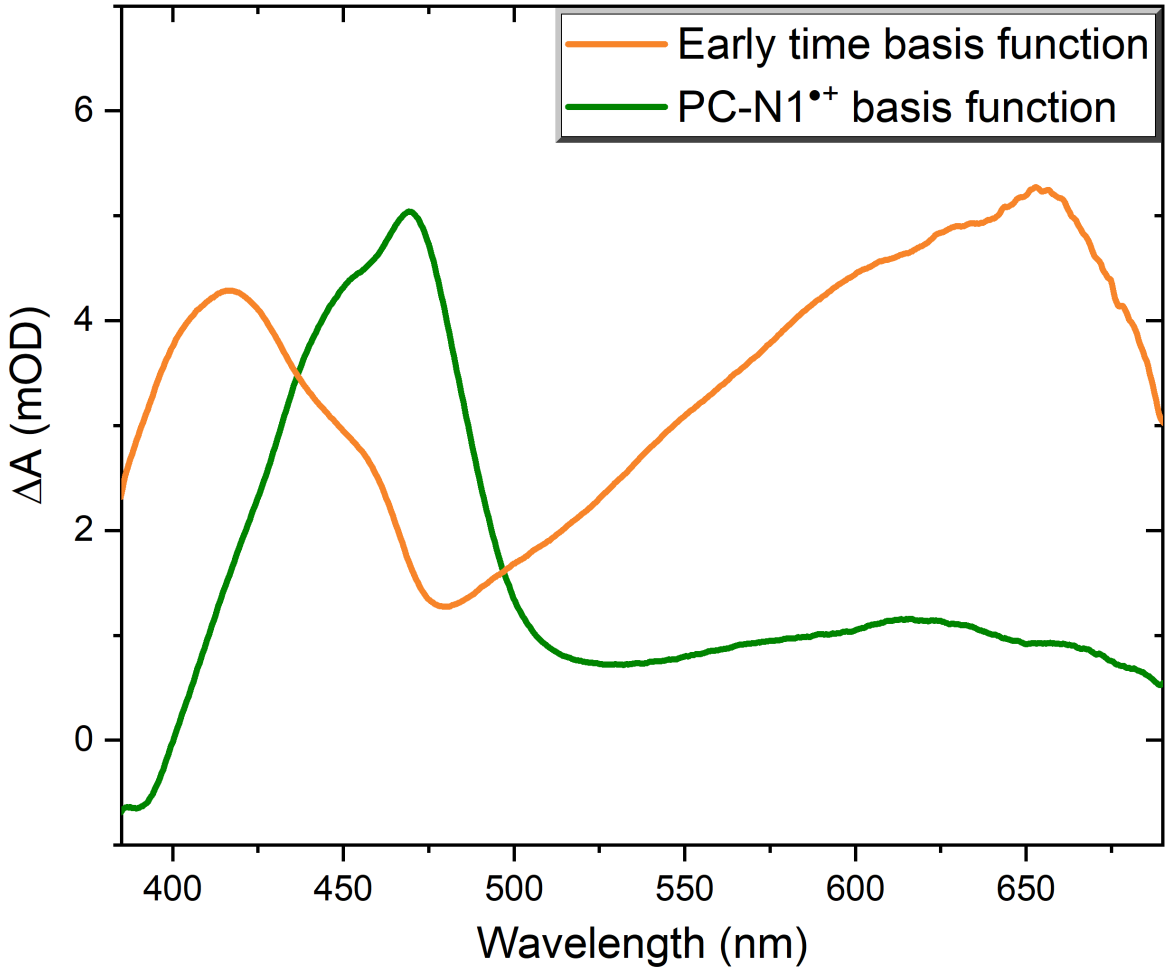

Figure E30. *Basis functions used to fit the TEAS data for PC-N1 with methyl 2-bromopropionate (MBP) in DMF. The TEA spectra can be satisfactorily decomposed using only these two basis functions. The basis function characterizing PC-N1*(S_1) absorption spectra (ochre) is chosen as the early time spectrum at 50 ps in the TEAS data without MBP. The basis function for PC-N1$^{\bullet+}$ (green) is obtained by taking a late time spectrum at 1200 ps from the TEAS data when all other transient species have decayed, and the spectrum resembles the steady state absorption spectrum of PC-N1$^{\bullet+}$ shown in Figure E2.*

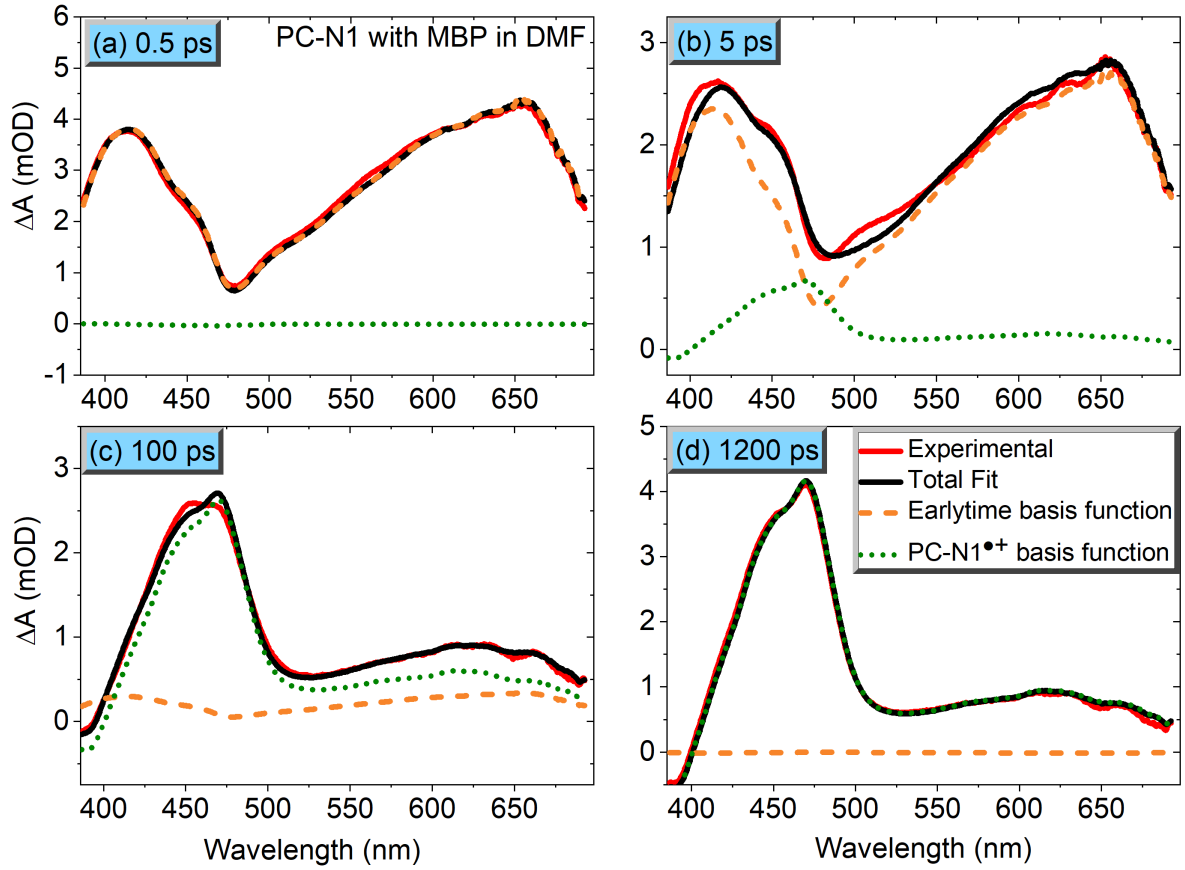

Figure E31. *Progression of the fit to the TEAS data using the basis functions shown in Figure E31 for 4.2 mM PC-N1 with 2 M MBP in N,N-dimethylformamide at early (a and b), intermediate (c) and late times (d). The early-time basis function is represented by the ochre dashed lines and the late-time PC-N1•+ basis function is shown by the green dotted lines. The total fits are shown by solid black lines and are compared with the experimentally recorded spectra which are plotted as solid red lines.*

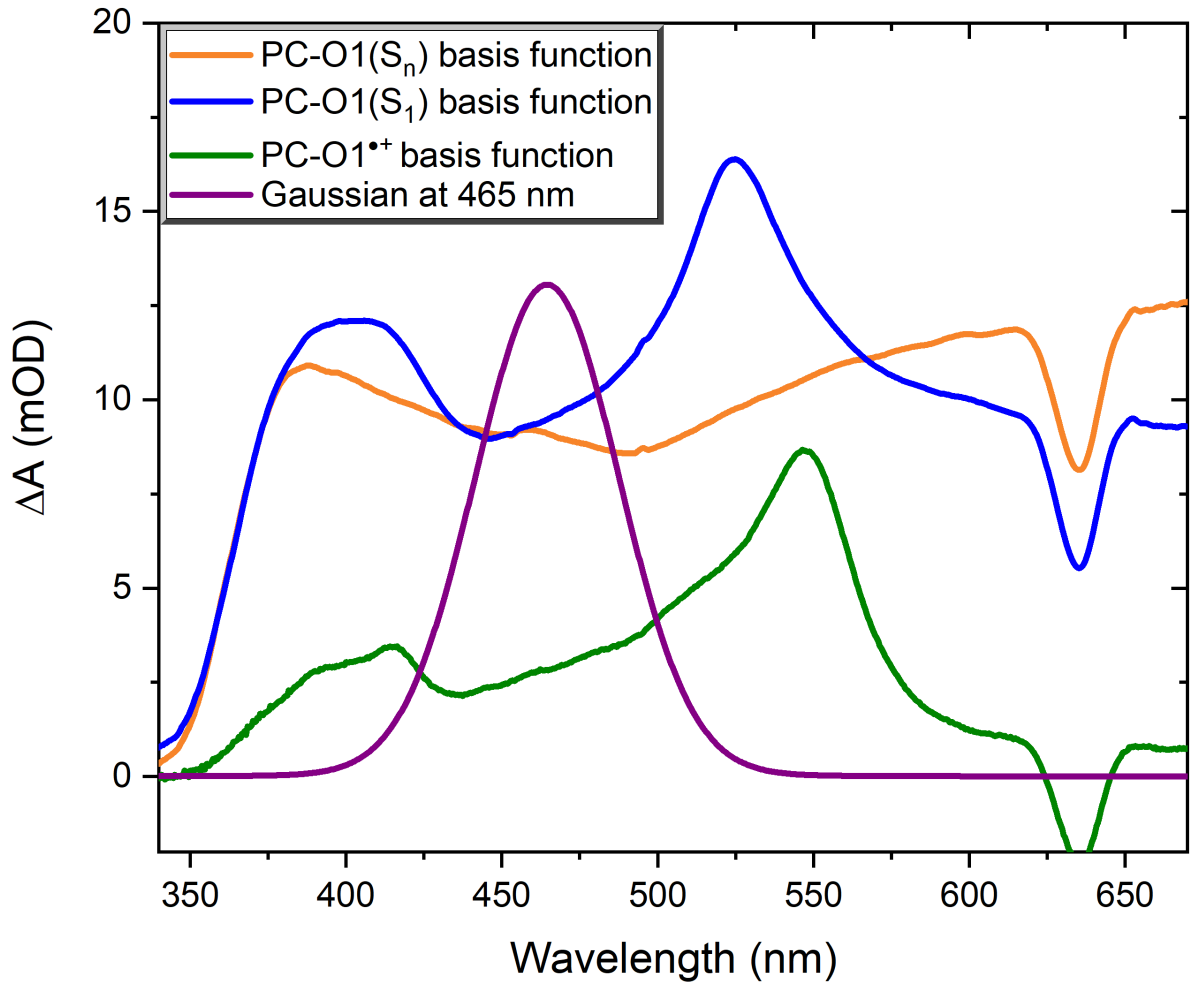

Figure E32. *Basis functions used to fit the TEAS data for PC-O1 with methyl 2-bromopropionate (MBP) in DMF. The TEA spectra can be satisfactorily decomposed using four basis functions. The basis function characterizing PC-O1*(S_n) absorption spectra (ochre) is chosen as the early time spectrum at 500 fs in the TEAS data. The spectrum shown in blue is assigned to PC-O1*(S_1) absorption and is taken from a middle-time spectrum (40 ps) in the TEAS data. The basis function for PC-O1$^{\bullet+}$ (green) is obtained by taking a late time spectrum at 1300 ps from the TEAS data for 1.5 M MBP when all other transient species have decayed, and the spectrum resembles the steady-state absorption spectrum of PC-O1$^{\bullet+}$ shown in Figure E2. The fourth basis function (purple) is a Gaussian function centred at 465 nm, which is assigned to the PC-O1*(T_1) ESA. Note that for high concentration MBP data, this latter basis function is not required to fit the TEAS data because no PC-O1*(T_1) growth is observed.*

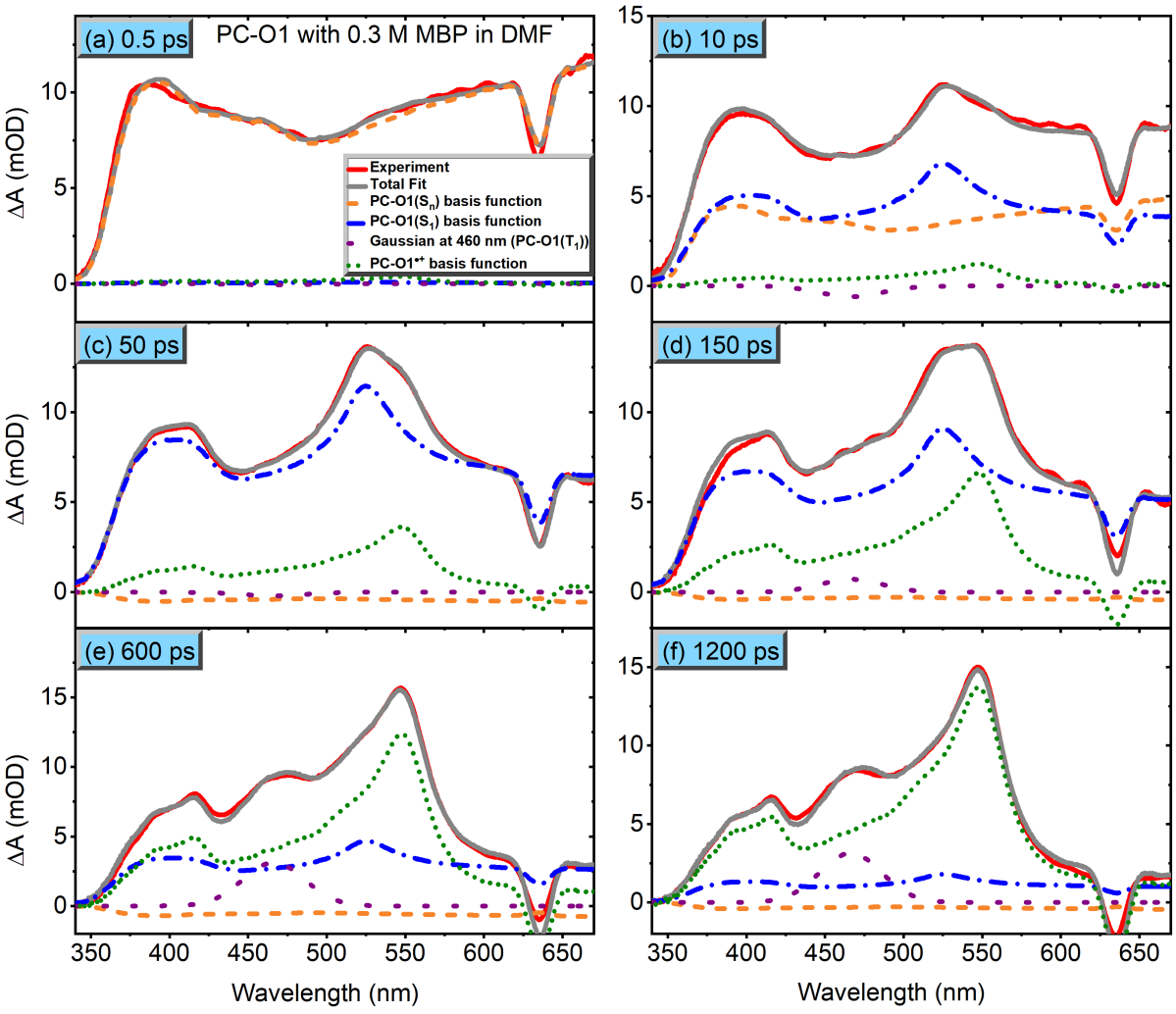

Figure E33. *Progression of the fit to the TEAS data using the basis functions shown in Figure E33 for 3.2 mM PC-O1 with 0.3 M MBP in N,N-dimethylformamide at early (a and b), intermediate (c, d) and late times (e, f). The PC-O1*(Sn) basis function is represented by ochre dashed lines, the PC-O1*(S1) basis function is shown in blue dashed-dotted lines, and the PC-O1•+ basis function is shown by green dotted lines. The Gaussian basis function which represents the absorption spectra of PC-O1*(T1) is shown by purple dotted lines. The total fits are shown by solid grey lines and are compared with the experimentally recorded spectra which are plotted as solid red lines. The decomposition of the spectra shows that the PC-O1(Sn) state which is formed upon photoexcitation decays rapidly to form PC-O1*(S1) state which simultaneously decays by either electron transfer to MBP, giving rise to the PC-O1•+ spectra, and by intersystem crossing to the triplet state as is evident by the rise of the Gaussian basis function.*

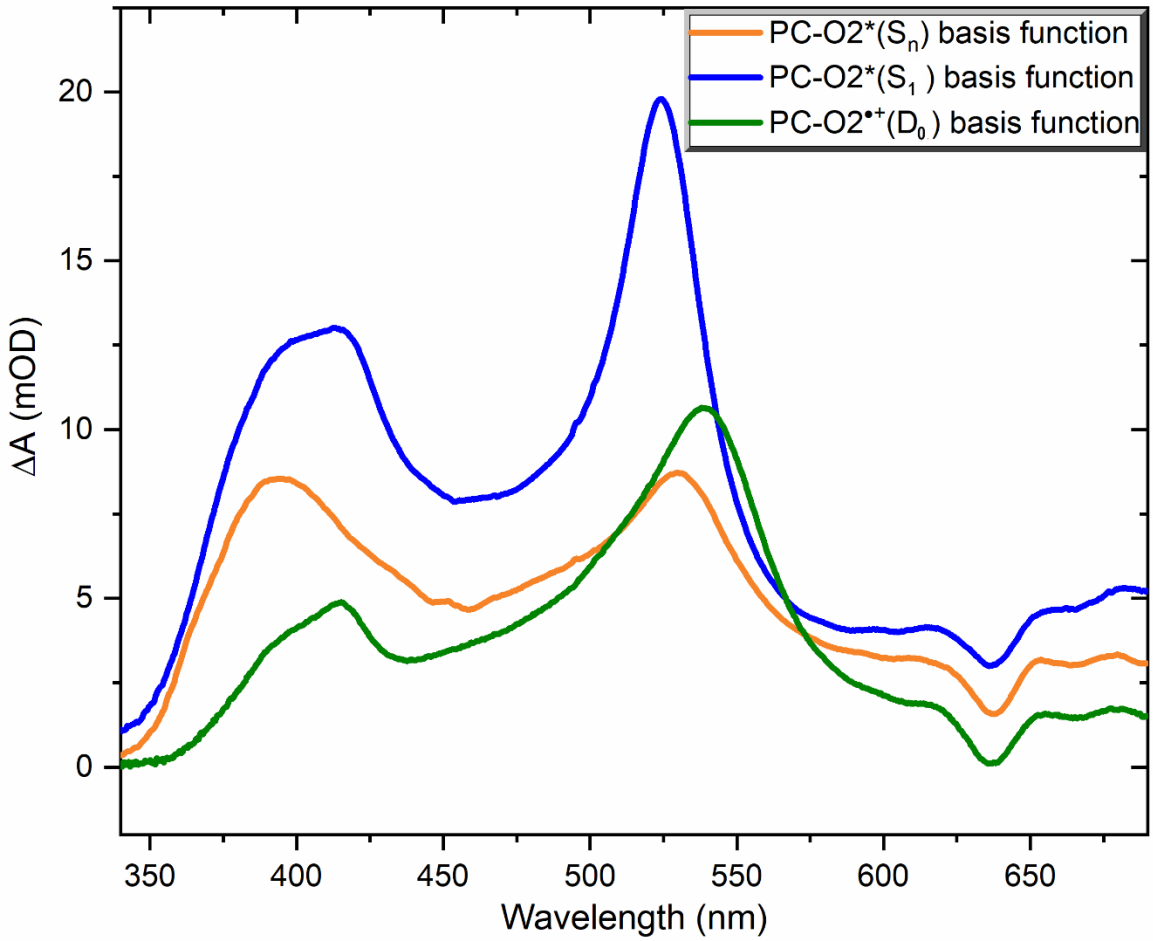

Figure E34. *Basis functions used to fit the TEAS data for PC-O2 with Methyl 2-bromopropionate (MBP) in DMF. The TEA spectra can be satisfactorily decomposed using three basis functions. The basis function characterizing PC-O2*(Sn) absorption spectra (ochre) is chosen as the early time spectrum at 400 fs in the TEAS data. The spectrum shown in blue is assigned to the PC-O2*(S1) absorption spectrum and is taken from a middle-time spectrum (100 ps) in the TEAS data without MBP. The basis function for PC-O1•+ (green) is obtained by taking a late time spectrum at 1300 ps from the TEAS data for PC-O2 with 2.0 M MBP when all other transient species have decayed by 1300 ps, and the spectrum resembles the steady state absorption spectrum of PC-O2•+ shown in Figure E2.*

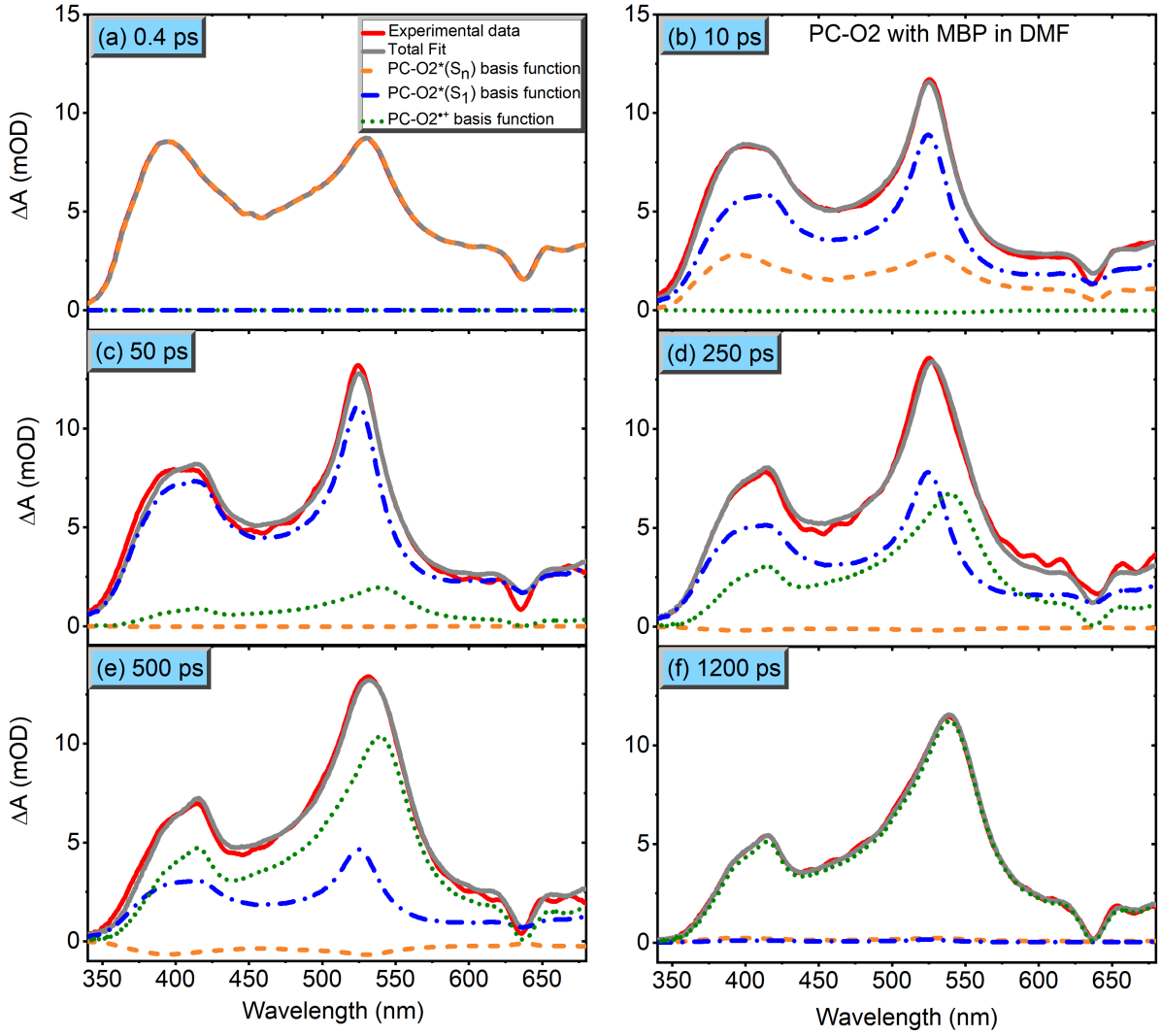

Figure E35. *Progression of the fit to the TEAS data using the basis functions shown in Figure E35 for 2.9 mM PC-O2 with 2.0 M MBP in N,N-dimethylformamide at early (a and b), intermediate (c, d) and late times (e, f). The PC-O2*(Sn) basis function is represented by ochre dashed lines, the PC-O2*(S1) basis function is shown by blue dashed-dotted lines, and the PC-O2•+ basis function is shown by green dotted lines. The total fits are shown by solid grey lines and are compared with the experimentally recorded spectra which are plotted as solid red lines. The decomposition of the spectra shows that the PC-O2(Sn) state which is formed upon photoexcitation decays rapidly to form PC-O2*(S1) which decays by electron transfer to MBP, giving rise to the PC-O2•+ spectra, and by relaxing back to the ground state.*

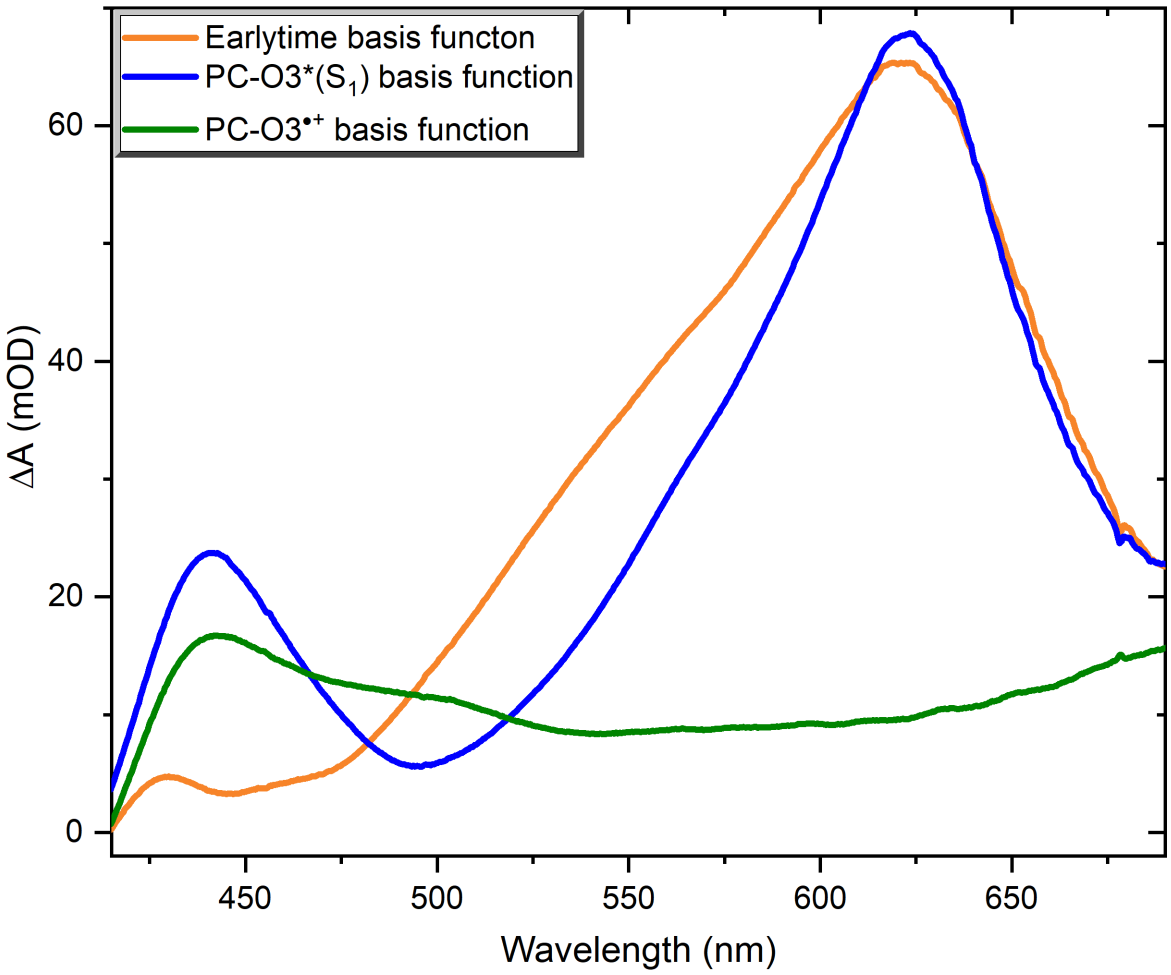

Figure E36. *Basis functions used to fit the TEAS data for PC-O3 with methyl 2-bromopropionate (MBP) in DMF. The TEA spectra can be satisfactorily decomposed using three basis functions. The basis function characterizing the vibrationally hot PC-O3*(S_1) absorption spectrum (ochre) is chosen as the early-time spectrum at 400 fs in the TEAS data. The spectrum shown in blue is assigned to the vibrationally cooled PC-O3*(S_1) state absorption spectrum and is taken from a middle-time spectrum (100 ps) in the TEAS data without MBP. The basis function for PC-O3$^{\bullet+}$ (green) is obtained by taking a late time spectrum at 1300 ps from the TEAS data for 2.0 M MBP data when all other transient species have decayed and, the spectrum resembles the absorption spectra of PC-O3$^{\bullet+}$ shown in Figure E2.*

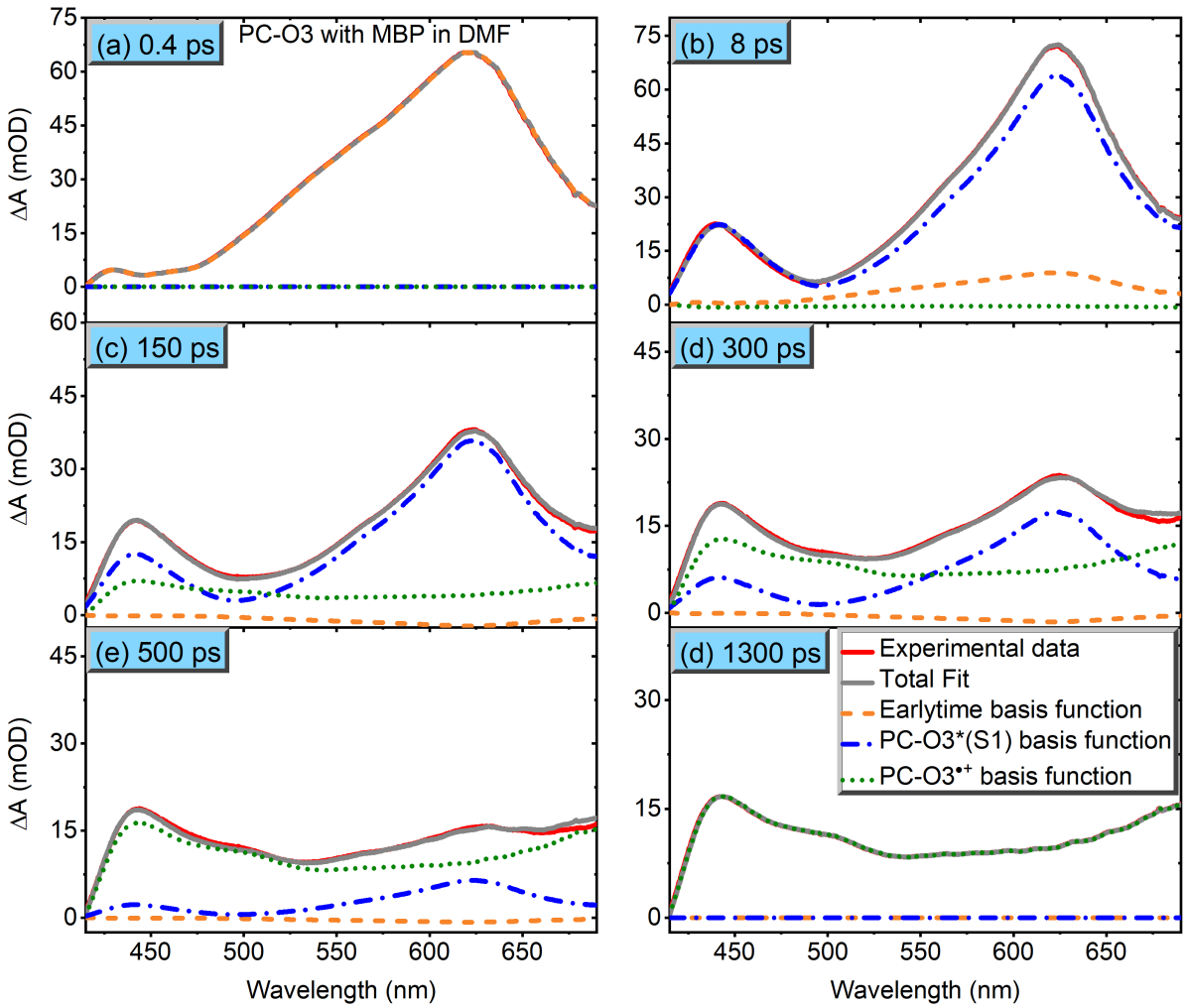

Figure E37. *Progression of the fit to the TEAS data using the basis functions shown in Figure E37 for 1.0 mM PC-O3 with 2.0 M MBP in N,N-dimethylformamide at early (a and b), intermediate (c, d) and late times (e, f). The early-time basis function is represented by ochre dashed lines, the vibrationally cooled PC-O3*(S1) basis function is shown by blue dashed-dotted lines, and the PC-O3•+ basis function is shown by green dotted lines. The total fits are shown by solid grey lines and are compared with the experimentally recorded spectra which are plotted as solid red lines. The decomposition of the spectra shows that the vibrationally hot PC-O3(S1) state which is formed upon photoexcitation decays rapidly to form vibrationally relaxed PC-O3*(S1) which decays by an electron transfer to MBP, giving rise to the PC-O3•+ spectra.*

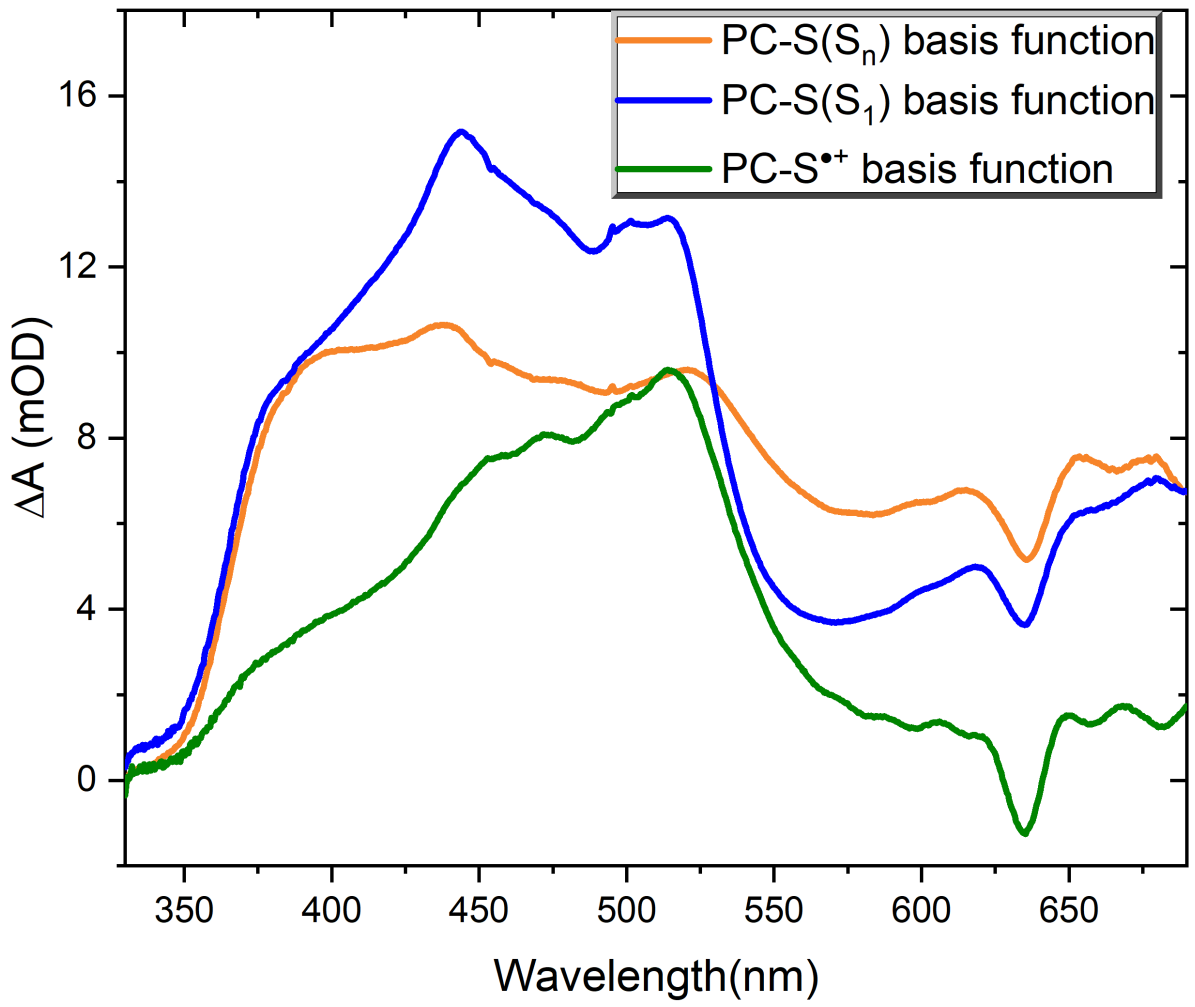

Figure E38. *Basis functions used to fit the TEAS data for PC-S with methyl 2-bromopropionate (MBP) in DMF. The TEA spectra can be satisfactorily decomposed using three basis functions. The basis function characterizing the PC-S*(S_n) absorption spectrum (ochre) is chosen as the early time spectrum at 500 fs in the TEAS data. The spectrum shown in blue is assigned to the PC-S*(S_1) absorption spectrum and is taken from a middle-time spectrum (40 ps) in the TEAS data. The basis function for PC-$S^{\bullet+}$ (green) is obtained by taking a late time spectrum at 1300 ps from the TEAS data for 2 M MBP data when all other transient species have decayed and the spectrum resembles the absorption spectrum of PC-$S^{\bullet+}$ shown in Figure E2.*

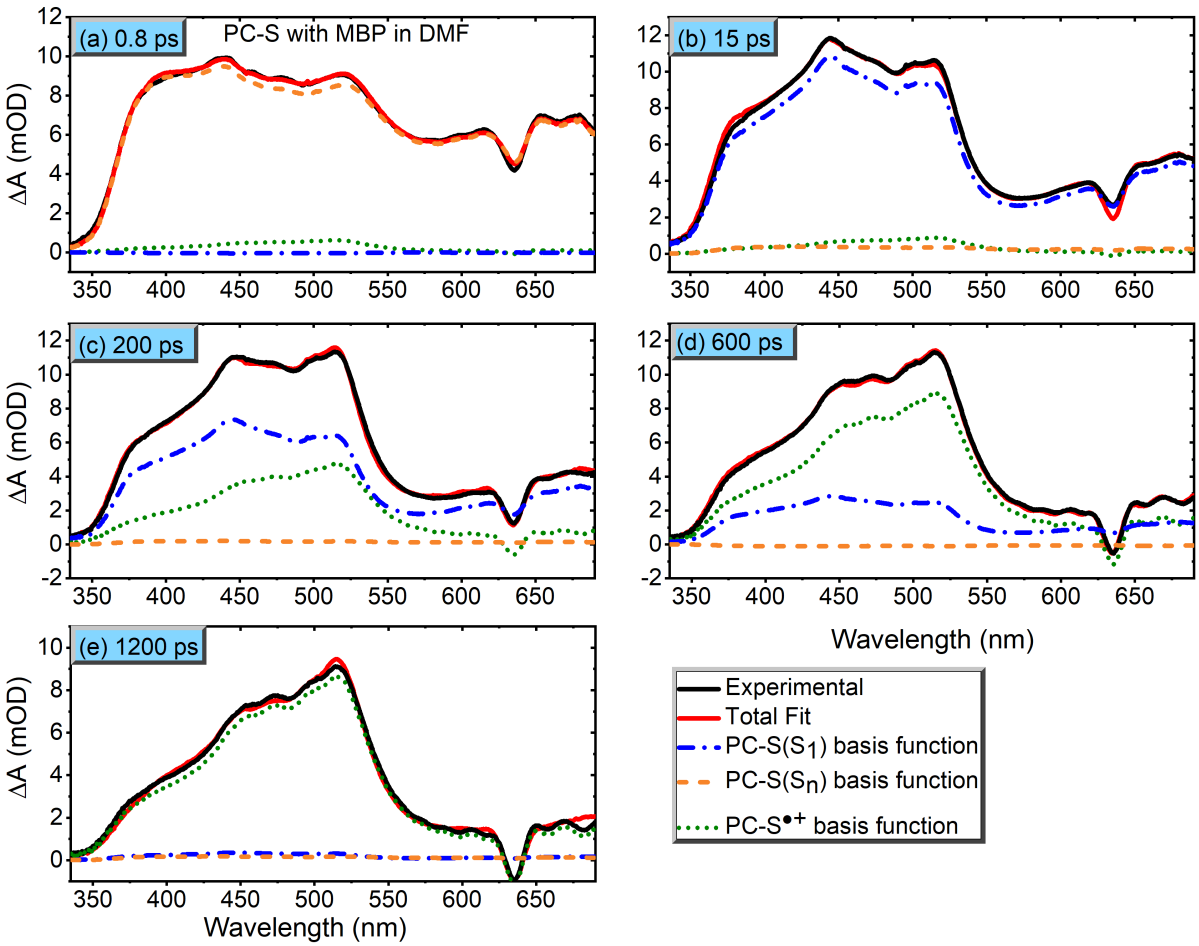

Figure E39. *Progression of the fit to the TEAS data using the basis functions shown in Figure E39 for 7.5 mM PC-S with 2 M MBP in N,N-dimethylformamide at early (a and b), intermediate (c) and late times (e, f). The PC-S*(Sn) basis function is represented by ochre dashed lines, the PC-S*(S1) basis function is shown by blue dashed-dotted lines, and the PC-S•+ basis function is shown by green dotted lines. The total fits are shown by solid black lines and are compared with the experimentally recorded spectra which are plotted as solid red lines. The decomposition of the spectra shows that the PC-S*(Sn) state which is formed upon photoexcitation decays rapidly to form PC-S*(S1) which decays by electron transfer to MBP, giving rise to the PC-S•+ spectra shown in green dotted lines.*

7.4.3 Chapter 5

7.4.3.1 Ethyl iodoacetate

7.4.3.1.1 40 mM ethyl iodoacetate

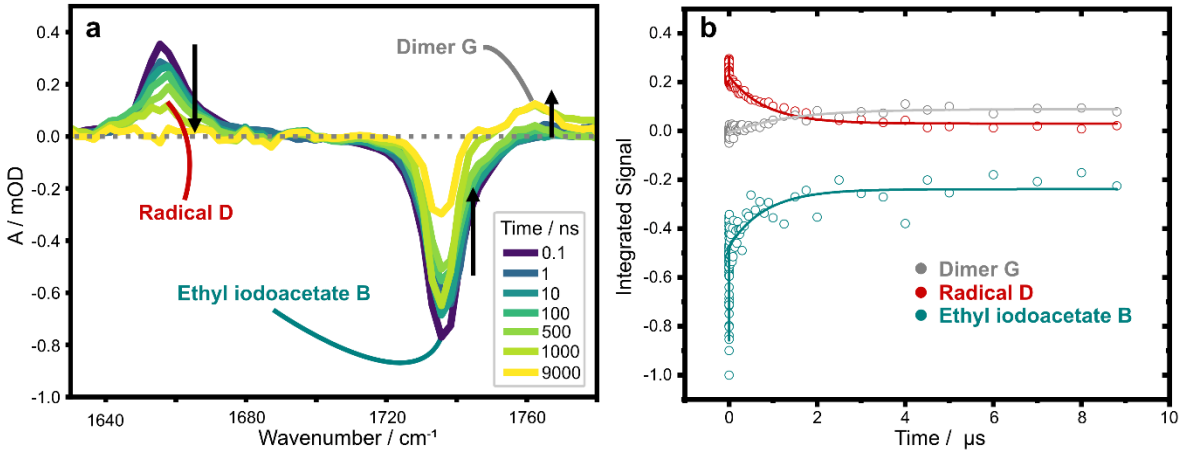

Figure E40. *TRIR measurement over the wavenumber range 1635-1770 cm^{-1} following pulsed excitation of an ethyl iodoacetate / THF solution at 280 nm. (a) TRIR spectra for ethyl iodoacetate (40 mM) in THF at time delays from 0.1 ns to 9 µs (b) The corresponding kinetic traces obtained by spectral decomposition. Solid lines superimposed on the Radical* ***D*** *and ethyl iodoacetate data are global fits with biexponential time constants of τ_1 = 26 ± 3 ps and τ_2 = 0.8 ± 0.1 µs. The solid line for dimer* ***G*** *is a single exponential fit with time constant τ_1 = 1.4 ± 0.2 µs.*

Figure E41 shows the TRIR spectrum of ethyl iodoacetate after excitation with a 280 nm pump pulse. Three spectral features were observed: (i) A transient absorption band at 1645 cm^{-1} assigned to the α-ethanoate radical (radical **D**) which decays to baseline as the radical undergoes termination reactions; (ii) A ground state bleach (GSB) assigned to the depletion of ethyl iodoacetate, which recovers because of termination reactions that reform ground state ethyl iodoacetate; (iii) a transient absorption band assigned to the dimer formed by reaction of pairs of radical **D**. For the radical **D** and ethyl iodoacetate absorptions, biexponential kinetics were observed with a global fit of both kinetic traces producing time constants τ_1 = 26 ± 3 ps and τ_2 = 0.8 ± 0.1 µs. We assign these time constants to primary and secondary geminate recombination, respectively.

7.4.3.2 BCB boronate

7.4.3.2.1 50 mM BCB boronate

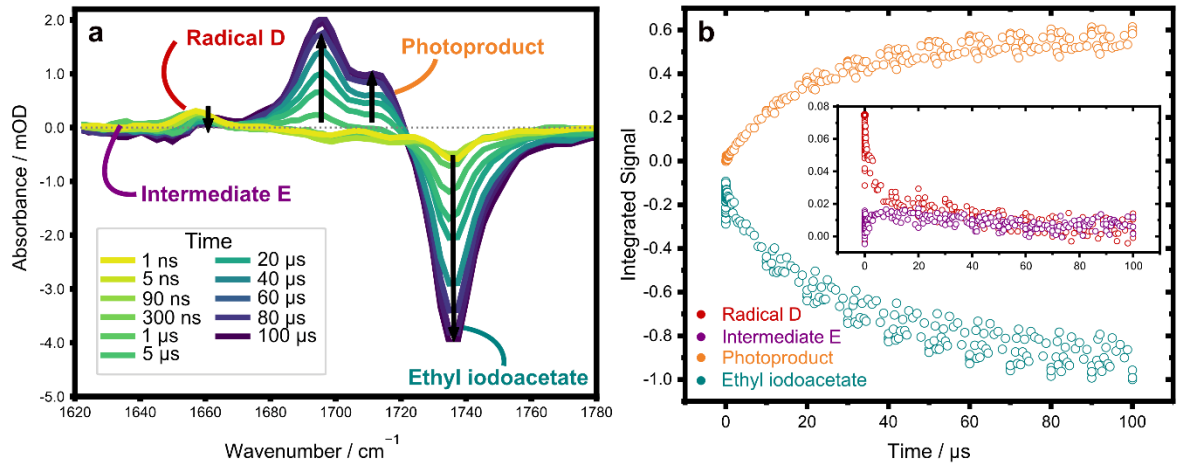

Figure E41. *TRIR measurement over the wavenumber range 1620-1780 cm^{-1} following pulsed excitation of an ethyl iodoacetate / BCB boronate / THF solution at 280 nm. (a) TRIR spectra for ethyl iodoacetate (40 mM) and BCB boronate (50 mM) in THF at time delays from 1 ns to 100 µs. (b) The corresponding kinetic traces obtained by spectral decomposition and band integration.*

7.4.3.2.2 70 mM BCB boronate

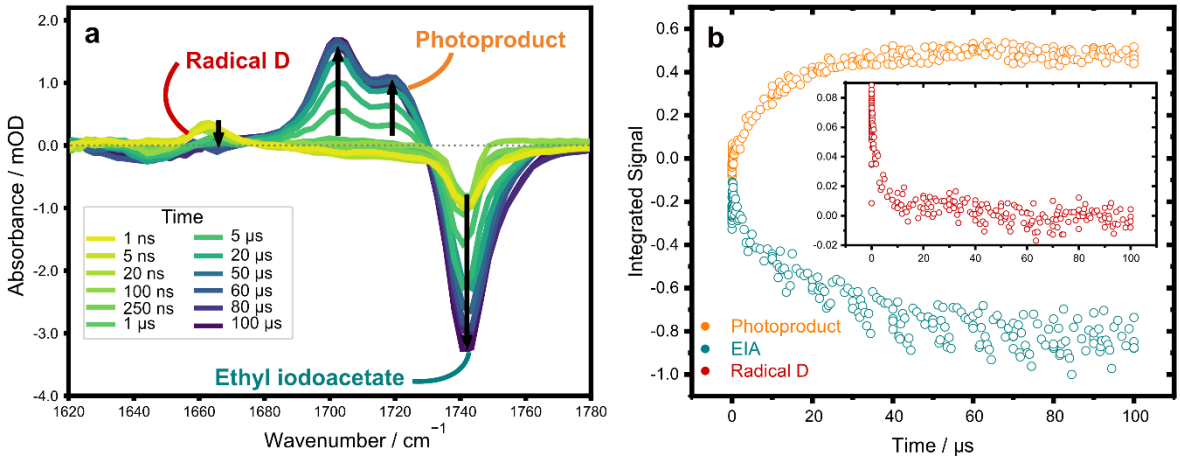

Figure E42. *TRIR measurement over the wavenumber range 1620-1780 cm^{-1} following pulsed excitation of an ethyl iodoacetate / BCB boronate / THF solution at 280 nm. (a) TRIR spectra for ethyl iodoacetate (40 mM) and BCB boronate (70 mM) in THF at time delays from 1 ns to 100 µs. (b) The corresponding kinetic traces obtained by spectral decomposition and band integration.*

7.4.3.3 Vinyl boronate

7.4.3.3.1 30 mM vinyl boronate

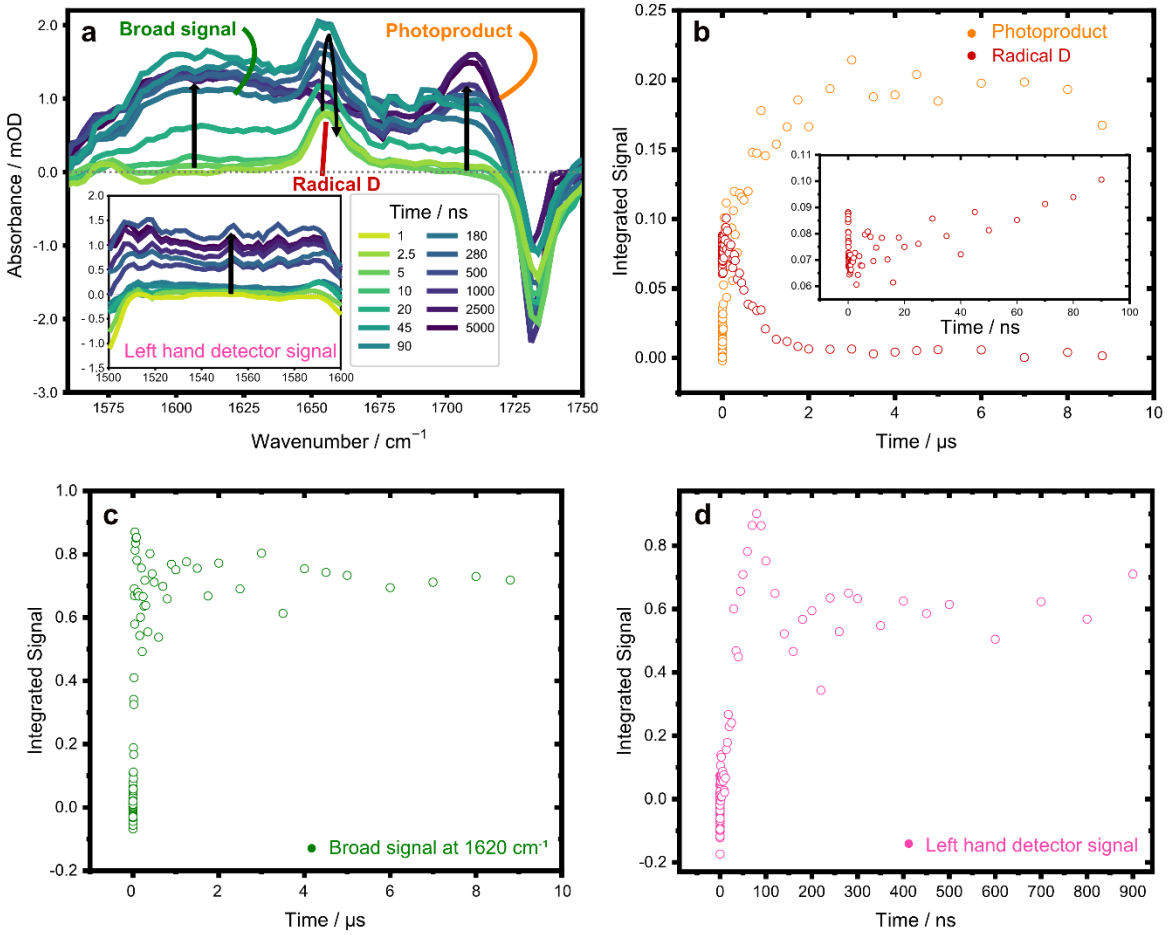

Figure E43. *TRIR measurement over the wavenumber range 1570-1750 cm^{-1} following pulsed excitation of an ethyl iodoacetate / Vinyl boronate / THF solution at 280 nm. (a) TRIR spectra for ethyl iodoacetate (40 mM) and Vinyl boronate (30 mM) in THF at time delays from 1 ns to 5 µs. (b) The corresponding kinetic traces for Radical **D** and Photoproduct **F'** obtained by spectral decomposition and band integration. (c) The corresponding kinetic traces for the broad signal centered at 1620 cm^{-1} (d) The corresponding kinetic traces for the signal on the left-hand detector (see text). Note the kinetics which show growth and partial decay. This behaviour is attributed to overlapping signals for Vinyl Intermediate **E** and Vinyl boronate photoproduct **F'** as can be seen from the calculated spectra in Figure E8 which show the vibrational bands for each species are predicted to overlap. The resulting time-dependent integrated band intensities would mimic the observed kinetics in panel d.*

The TRIR spectra shown in Figure E43 were measured using two simultaneous IR OPA probes, with the transmitted IR pulses analysed using two separate detectors we call the left-hand (LHD) and right-hand detector (RHD). As can be seen in **Figure E44a**, a broad feature stretches from 1500 cm^{-1} to 1600 cm^{-1} on the LHD, and 1560 cm^{-1} to 1725 cm^{-1} on the RHD. We attribute this feature to the overlap of two absorption bands: one is from intermediate **E**, whose expected kinetics are growth then decay; and the other is from the product, whose kinetics would show growth. The resulting observed kinetics from the overlap of these two

absorption bands would be growth followed by a partial decay which evens out as the growing absorption of the product nullifies the decay of absorption by intermediate **E**. **Figure E43b** and **c** show the kinetics of the broad signals on the LHD and RHD, with the observed rapid growth followed by incomplete decay consistent with our expectations for the two overlapping bands.

7.4.3.3.2 40 mM vinyl boronate

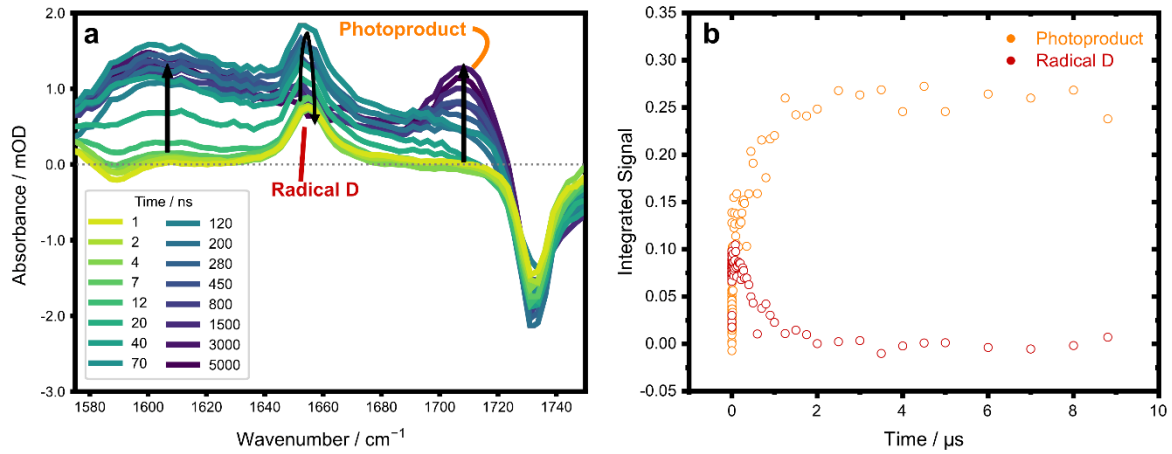

Figure E44. *TRIR measurement over the wavenumber range 1580-1740 cm^{-1} following pulsed excitation of an ethyl iodoacetate / Vinyl boronate / THF solution at 280 nm. (a) TRIR spectra for ethyl iodoacetate (40 mM) and Vinyl boronate (40 mM) in THF at time delays from 1 ns to 5 µs. (b) The corresponding kinetic traces for Radical **D** and Photoproduct **F'** obtained by spectral decomposition.*

7.4.3.3.3 50 mM vinyl boronate

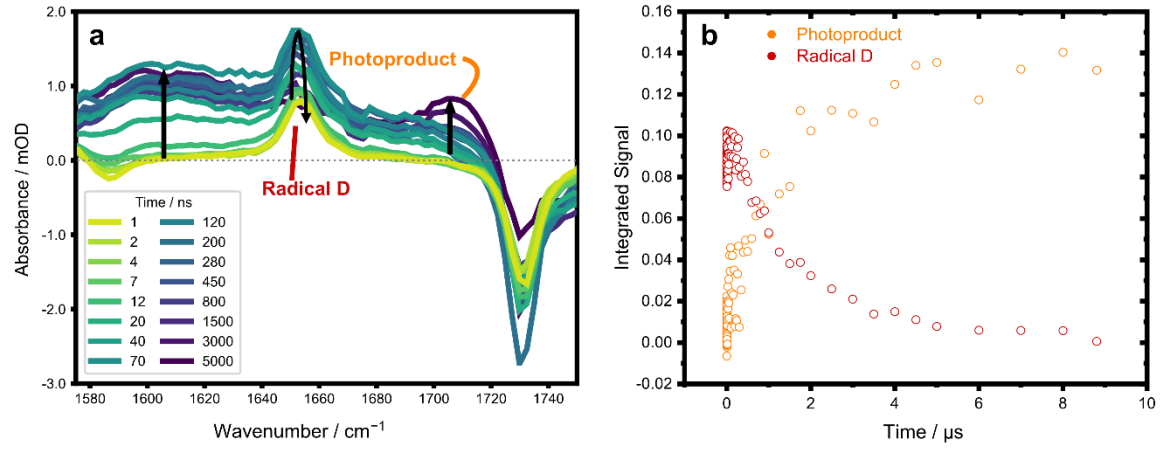

Figure E45. *TRIR measurement over the wavenumber range 1580-1740 cm^{-1} following pulsed excitation of an ethyl iodoacetate / Vinyl boronate / THF solution at 280 nm. (a) TRIR spectra for ethyl iodoacetate (40 mM) and Vinyl boronate (50 mM) in THF at time delays from 1 ns to 5 µs. (b) The corresponding kinetic traces for Radical **D** and Photoproduct **F'** obtained by spectral decomposition and band integration.*

7.4.3.4 Spectral Decomposition

Figure E46 illustrates the methods we use to decompose TRIR spectra into spectral components with individual kinetic behaviour, performed with the in-house software package KOALA.[11] Multiple Gaussian functions are chosen to mimic spectral components in the time evolving spectra, and examples at various time points throughout the time series can be seen in Figure E46. The close correspondence between the experimental data and the total fit in Figure E46 supports our choice of Gaussian functions. The integrated intensities of these decaying and growing Gaussian functions are plotted to obtain the kinetic traces shown in Figure E40, Figure E41, Figure E42, Figure E43, Figure E44, and Figure E45.

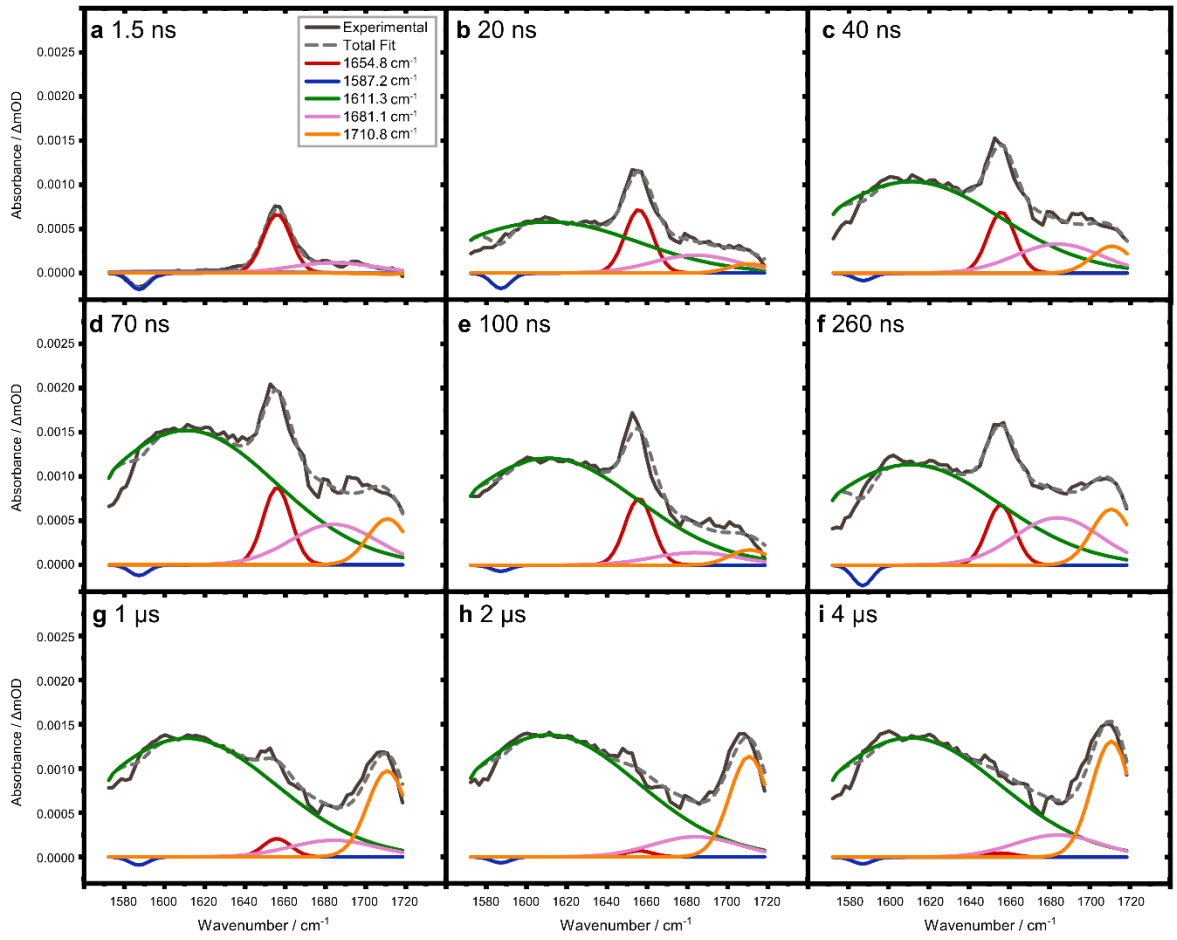

Figure E46. *Progression of the fit using Gaussian functions centred at wavenumbers indicated in the legend inset in frame a for vinyl boronate in THF at early (a, b and c), intermediate (d, e and f) and later times (g, h and i). The total fit is shown by the dashed grey line, and the recorded spectra are plotted as solid black lines. The red Gaussian centred at 1654 cm^{-1} represents radical **D** absorption; the blue Gaussian centred at 1587 cm^{-1} represents a GSB assigned to the boronate; the green Gaussian centred at 1611 cm^{-1} and the pink Gaussian centred at 1681 cm^{-1} represent the overlapping features of intermediate **E** and vinyl boronate photoproduct **F'**; finally, the orange Gaussian centred at 1710 cm^{-1} represents a further feature assigned to the reaction product.*

7.5 Kinetic Fits

7.5.1 Kinetic Fits for the PC* + MBP Reaction

7.5.1.1 Kinetic fits for PC-N1*(S_1) + MBP in DCM

7.5.1.1.1 Exponential Fitting

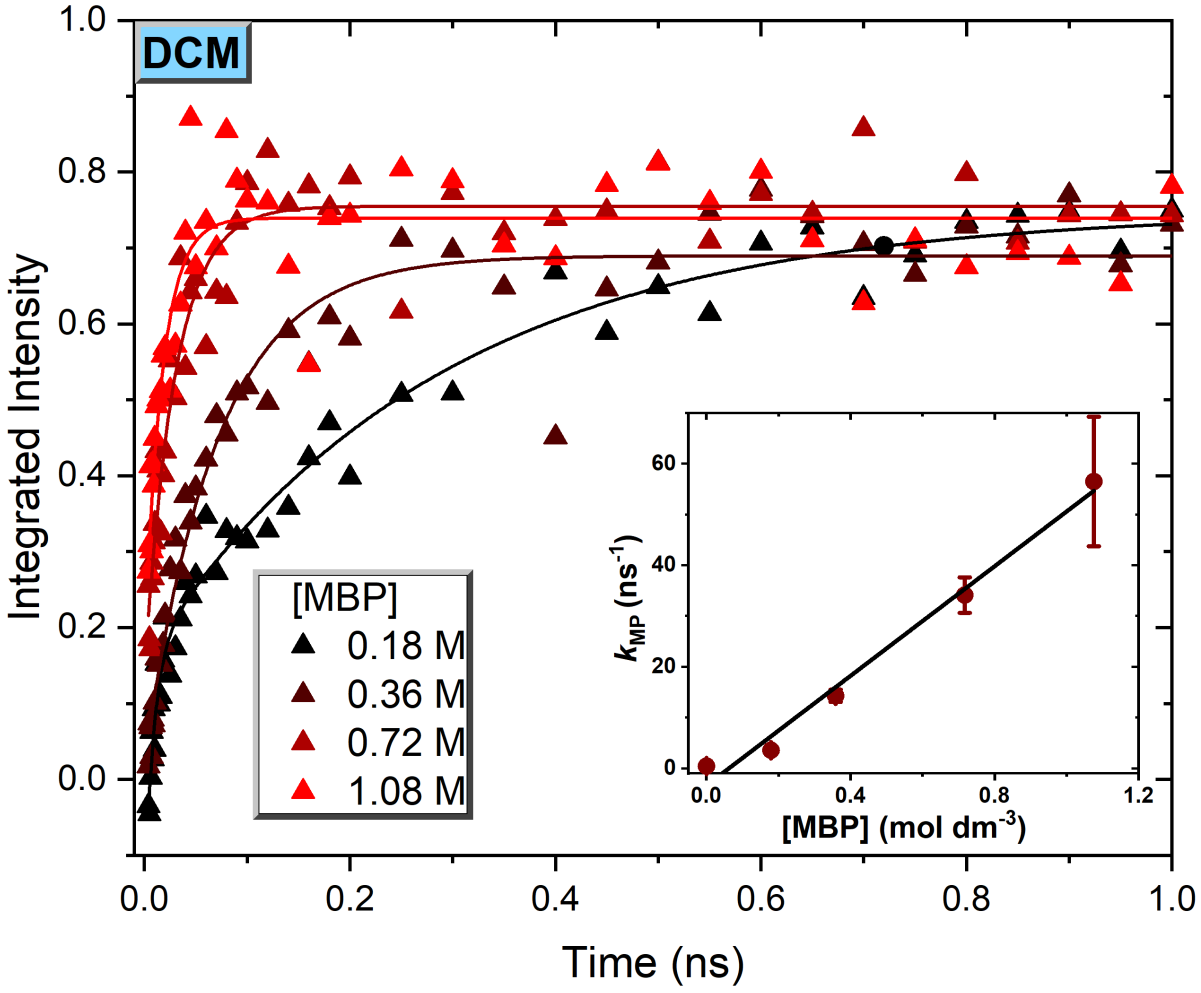

Figure E47. *Kinetic traces (triangles) showing rates of rise of the 2MP•(D0) band in the TVAS measurements by electron transfer from PC-N1*(S1) to MBP in DCM. Solid lines are single exponential fits to each data curve. Rate coefficients obtained from these fits are plotted against MBP concentration in the inset. The gradient of the linear fit to these points gives the rate coefficient for electron transfer,* $\boldsymbol{k_{ET} = (4.9 \pm 0.3) \times 10^{10}\ M^{-1}s^{-1}}$ *in DCM. The intercept in the kinetic plot in the inset is set to 1/lifetime of the PC-N1*(S1) in DCM in the absence of MBP. The kinetic model is explained in the main text. Note that the kET value is three times higher than the diffusion limited rate coefficient which in DCM is estimated to be* $1.5 \times 10^{10}\ M^{-1}s^{-1}$ *at 20 °C.*[12]

7.5.1.1.2 Fitting to the Smoluchowski model

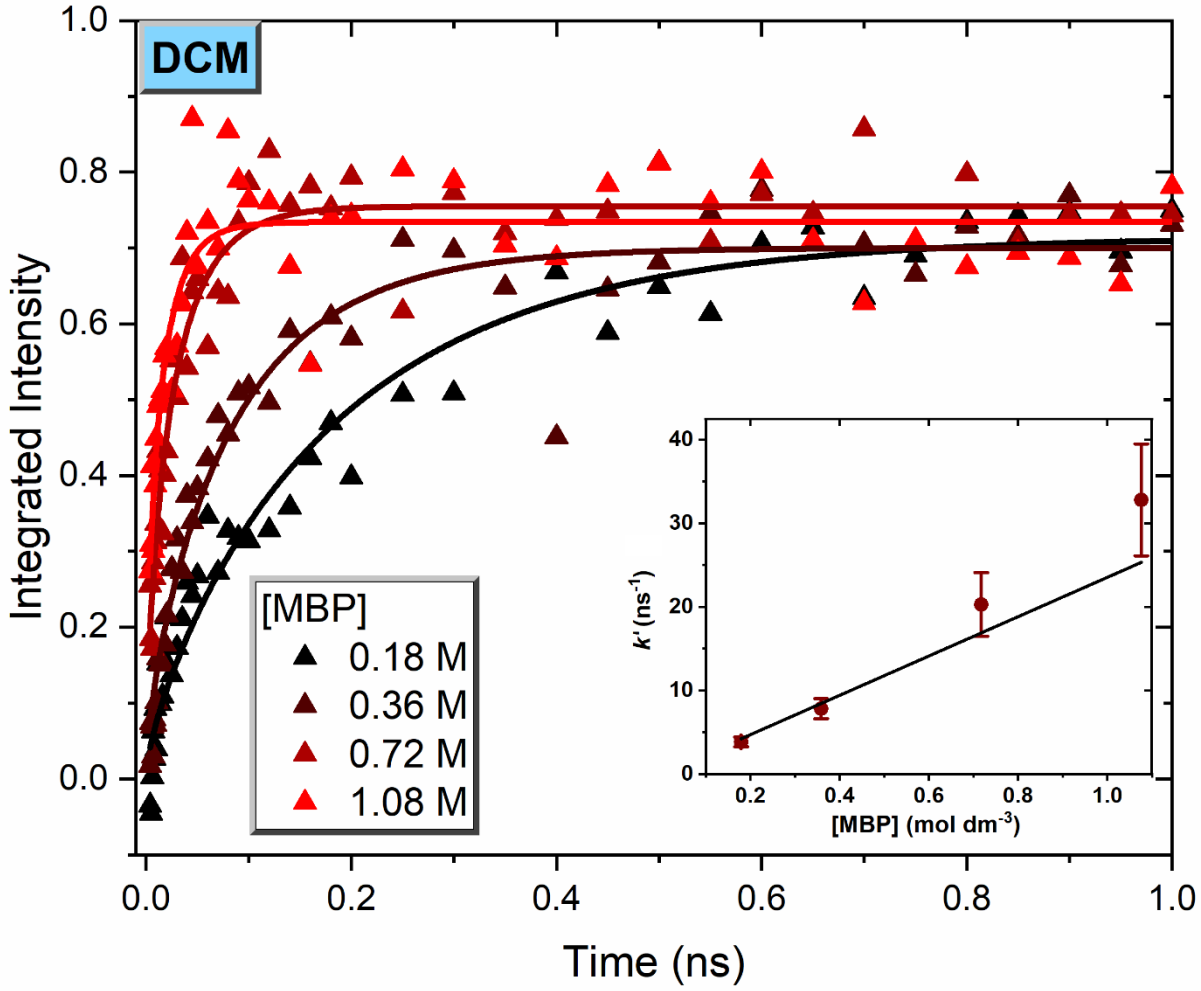

***Figure E48**. Kinetic traces (triangles) showing growth of the MP•(D$_0$) band in the TVAS measurements of the electron transfer from PC-N1*(S$_1$) to MBP in DCM. Solid lines are fits to each kinetic data set using the Smoluchowski model. Rate coefficients obtained from these fits are plotted against MBP concentration in the inset. The gradient of the linear fit to these points (weighted by the individual one standard error uncertainties derived from the exponential fits) gives the rate coefficient for electron transfer, $\boldsymbol{k_{ET} = (2.4 \pm 0.2) \times 10^{10} M^{-1} s^{-1}}$ in DCM. Note that the k_{ET} value obtained by the Smoluchowski model used here is closer to the estimated diffusion limited rate coefficient in DCM of $1.5 \times 10^{10}\ M^{-1}s^{-1}$ at 20 °C,[12] compared to the single exponential fit shown in Figure E13.*

7.5.1.2 Kinetic fits for PC-N1*(S_1) + MBP in toluene-d_8

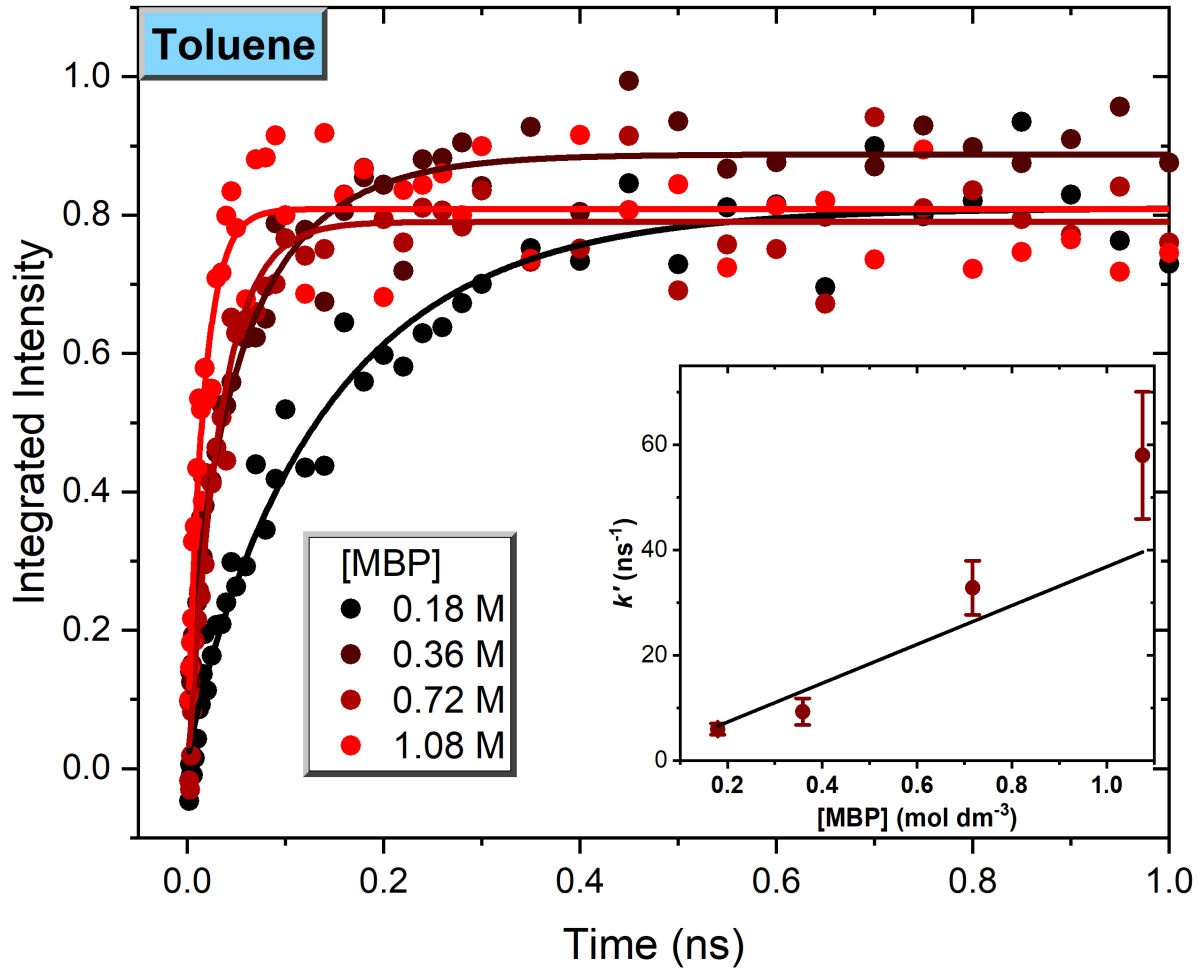

Figure E49. *Kinetic traces (triangles) showing growth of the MP•(D$_0$) band in the TVAS measurements of the electron transfer from PC-N1*(S$_1$) to MBP in toluene-d$_8$. Solid lines are fits to each kinetic data set using the Smoluchowski model. Rate coefficients obtained from these fits are plotted against MBP concentration in the inset. The gradient of the linear fit to these points (weighted by the individual one standard error uncertainties derived from the exponential fits) gives the rate coefficient for electron transfer,* $\boldsymbol{k_{ET} = (3.8 \pm 0.6) \times 10^{10} M^{-1} s^{-1}}$ *in toluene. Note that the* k_{ET} *value obtained here is similar to the estimated diffusion limited rate coefficient in toluene of* $1.1 \times 10^{10}\ M^{-1}s^{-1}$ *at 20 °C.*[12]

7.5.1.3 Kinetic fits for the reaction of PC-O1*(S_1) + MBP in toluene

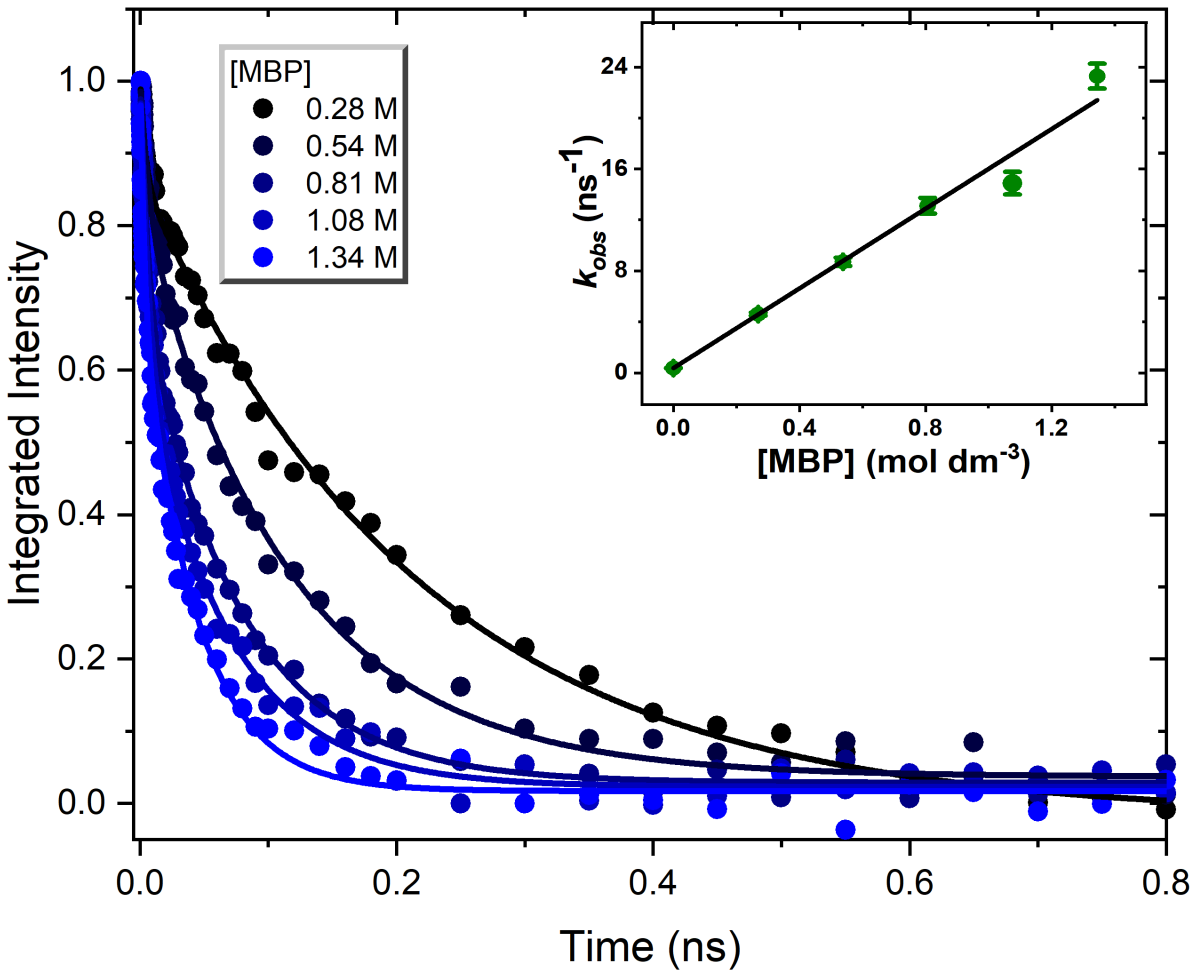

Figure E50. *Kinetic traces (circles) showing rates of decay of the ^{1}PC-O1*(S_1) band in the TEAS measurements by electron transfer to MBP in toluene. Solid lines are single exponential fits to each data curve. Pseudo first order rate coefficients obtained from these fits are plotted against MBP concentration in the inset. The gradient of the linear fit to these points (weighted by the individual one standard error uncertainties derived from the exponential fits) gives the rate coefficient for electron transfer,* $\boldsymbol{k_{ET} = (1.56 \pm 0.05) \times 10^{10}\ M^{-1}s^{-1}}$ *in toluene. The intercept in the kinetic plot in the inset is set to 1/lifetime of the PC-O1*(S_1) in toluene obtained through TVAS measurements in the absence of MBP. The kinetic model is explained in the main text. Note that the* k_{ET} *value is close to the diffusion limited rate coefficient which in toluene is estimated to be* $1.1 \times 10^{10}\ M^{-1}s^{-1}$ *at 20 °C.*[12]

7.5.1.4 Kinetic fits for the reaction of PC-O1*(S_1) + MBP in DCM

7.5.1.4.1 Single exponential fit

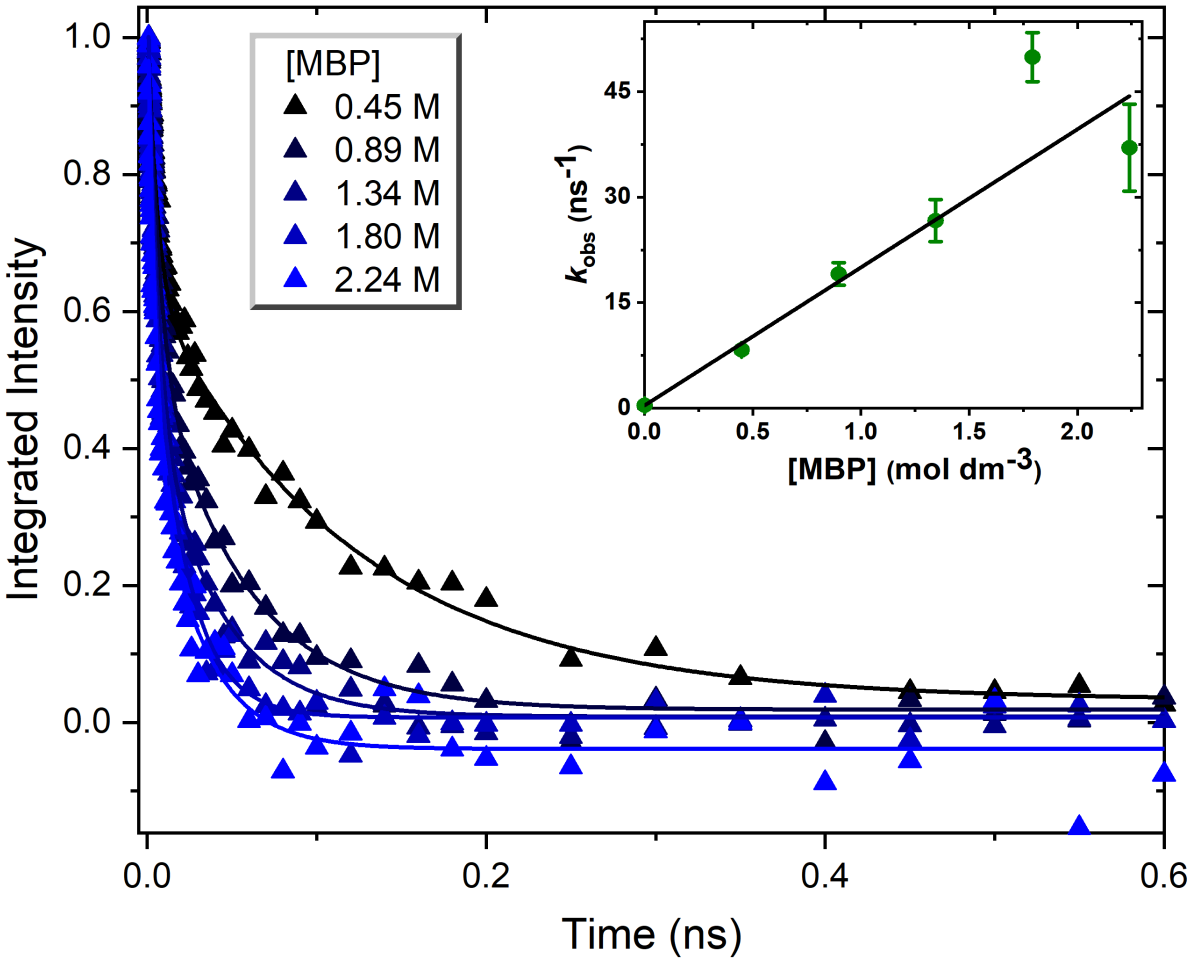

Figure E51. *Kinetic traces (triangles) showing rates of decay of the ^{1}PC-O1*(S_1) band in the TEAS measurements by electron transfer to MBP in DCM. Solid lines are single exponential fits to each data curve. Pseudo first order rate coefficients obtained from these fits are plotted against MBP concentration in the inset. The gradient of the linear fit to these points (weighted by the individual one standard error uncertainties derived from the exponential fits) gives the rate coefficient for electron transfer, $\boldsymbol{k_{ET} = (2.0 \pm 0.2) \times 10^{10} M^{-1} s^{-1}}$ in DCM. The intercept in the kinetic plot in the inset is set to 1/lifetime of the PC-O1*(S_1) in DCM obtained through TVAS measurements in the absence of MBP. The kinetic model is explained in the main text. Note that the value is close to the diffusion limited rate coefficient which in DCM is estimated to be* $1.5 \times 10^{10}\ M^{-1}s^{-1}$ *at 20 °C.*[12]

7.5.1.4.2 Fitting to Smoluchowski model

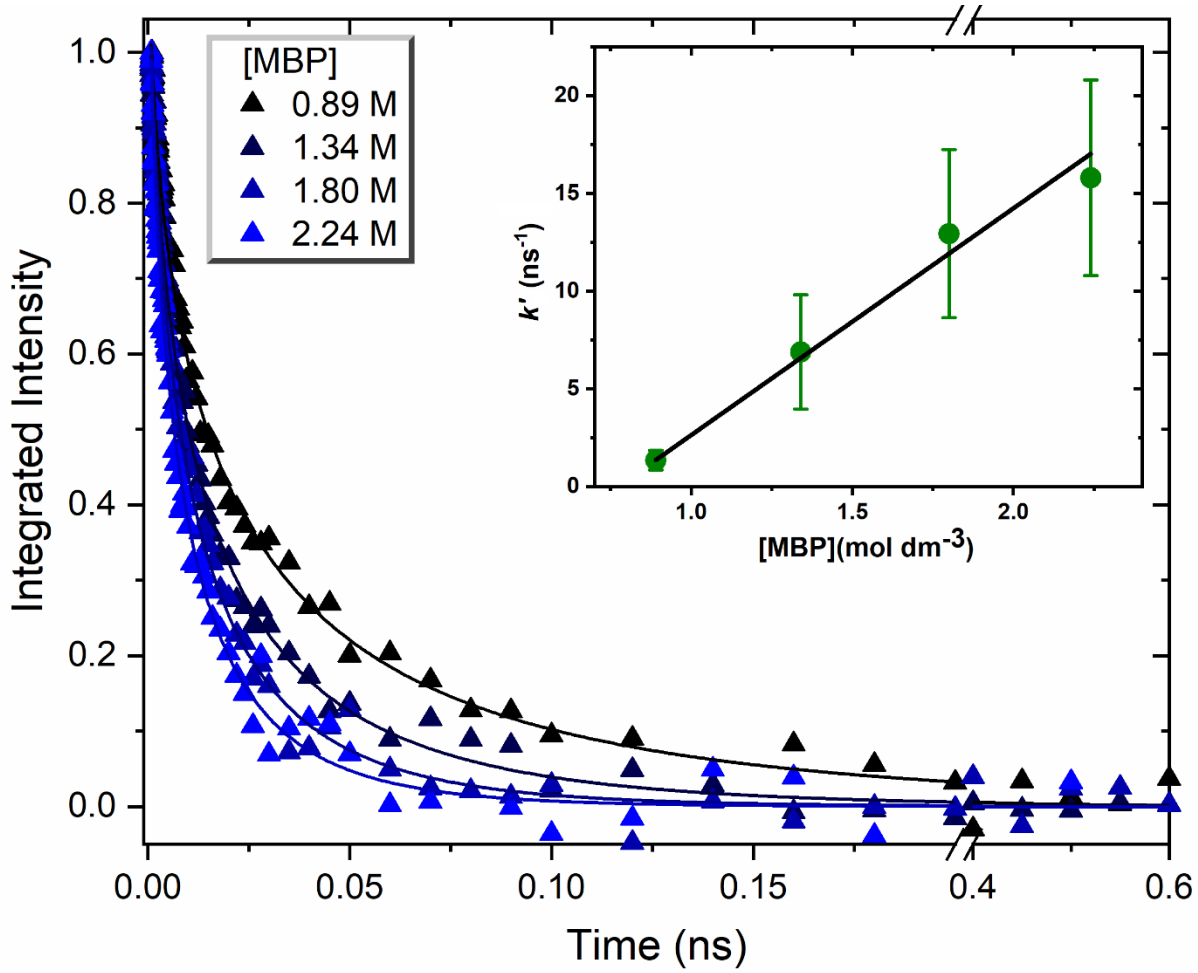

Figure E52. *Kinetic traces (triangles) showing rates of decay of the ^{1}PC-O1*(S_1) band in the TEAS measurements by electron transfer to MBP in DCM. Solid lines are fits to each kinetic data set using the Smoluchowski model. Rate coefficients obtained from these fits are plotted against MBP concentration in the inset. The gradient of the linear fit to these points (weighted by the individual fitting errors) gives the rate coefficient for electron transfer,* $\boldsymbol{k_{ET} = (1.2 \pm 0.1) \times 10^{10} M^{-1} s^{-1}}$ *in DCM. Note that the* k_{ET} *value obtained here is close to the value obtained by a single exponential fitting method used in Figure E17. Both values are similar to the estimated diffusion limited rate coefficient in DCM of* $1.5 \times 10^{10}\ M^{-1}s^{-1}$ *at 20 °C.*[12]

7.5.1.5 Kinetic fits for the reaction of PC-O1*(S_1) + MBP in DMF

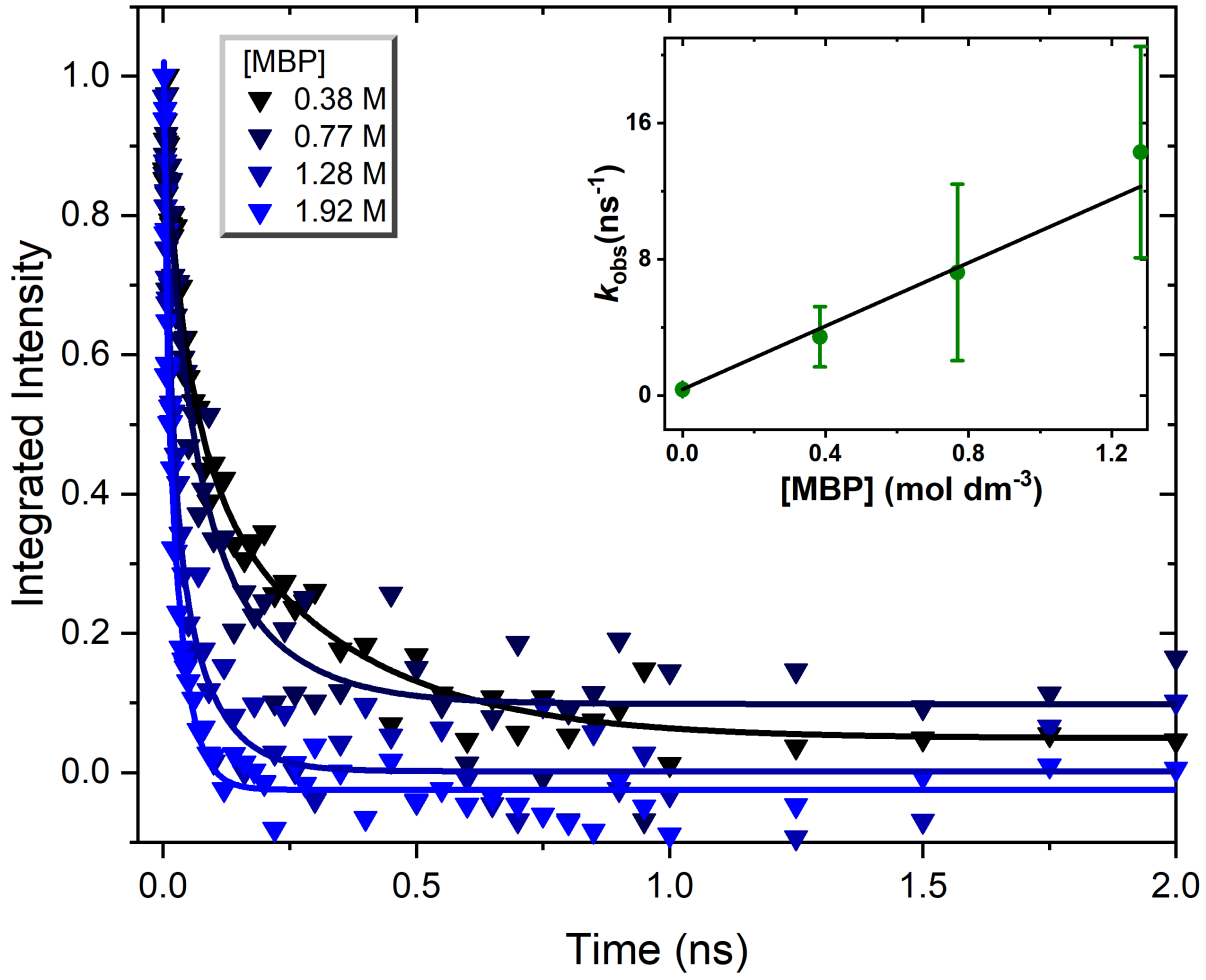

Figure E53. *Kinetic traces (inverted triangles) showing rates of decay of the ^{1}PC-O1*(S_1) band in the TVAS measurements by electron transfer to MBP in DMF. Solid lines are biexponential fits to each kinetic trace. The slower of the rate coefficients obtained from these fits are plotted against MBP concentration in the inset. The gradient of the linear fit to these points (weighted by the individual one standard error uncertainties derived from the exponential fits) gives the rate coefficient for diffusive electron transfer, $\boldsymbol{k_{ET} = (9.3 \pm 0.9) \times 10^9\ M^{-1}s^{-1}}$ in DMF. The intercept in the kinetic plot in the inset is set to 1/lifetime of the PC-O1*(S_1) in DMF obtained through TVAS measurements in the absence of MBP. The kinetic model is explained in the main text. Note that the value is close to the diffusion limited rate coefficient which in DMF is estimated to be* $7.6 \times 10^9\ M^{-1}s^{-1}$ *at 20 °C.*[12]

7.5.1.6 Kinetic fits for the reaction of PC-O2*(S_1) + MBP in DCM

7.5.1.6.1 Single exponential decay of PC-O2(S_1) state*

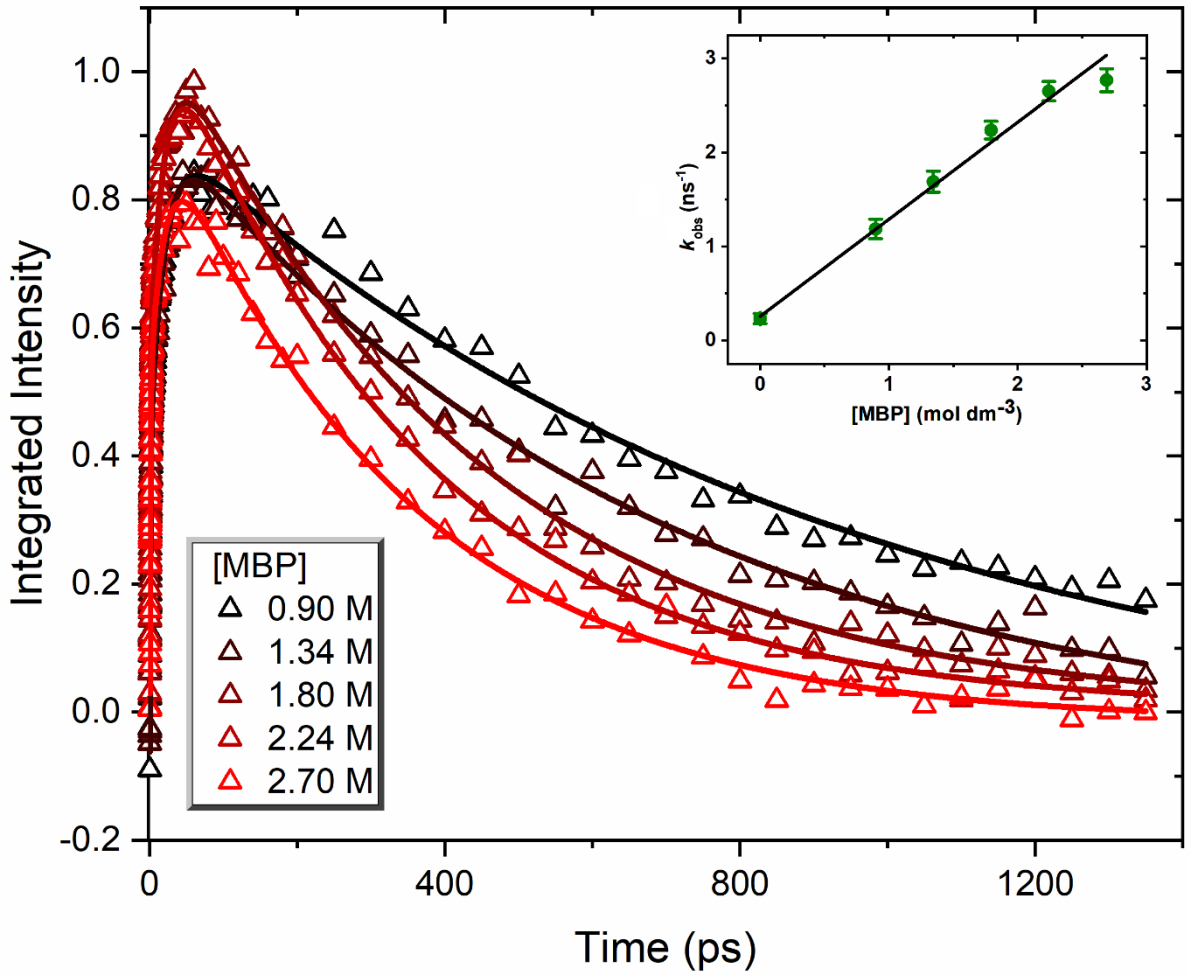

Figure E54. *Kinetic traces (hollow triangles) showing rates of decay of the ^{1}PC-O2*(S_1) band in the TEAS measurements by electron transfer to MBP in DCM. Solid lines are biexponential fits to each data curve, with a rising and a decaying component; the rising component shows the growth of S_1 from S_n state through internal conversion. The rate coefficients obtained for the fits to the decay of PC-O2*(S_1) are plotted against MBP concentration in the inset. The gradient of the linear fit to these points (weighted by the individual one standard error uncertainties derived from the exponential fits) gives the rate coefficient for electron transfer, $\boldsymbol{k_{ET} = (1.0 \pm 0.1) \times 10^9\ M^{-1}\ s^{-1}}$ in DCM. The intercept in the kinetic plot in the inset is set to 1/lifetime of the PC-O2*(S_1) in DCM obtained through TVAS measurements in the absence of MBP. Note that the k_{ET} value is smaller by an order of magnitude than the diffusion limited rate coefficient which in DCM is estimated to be $1.5 \times 10^{10}\ M^{-1}s^{-1}$ at 20 °C.*[12]

7.5.1.6.2 Single exponential rise of MP• radical band

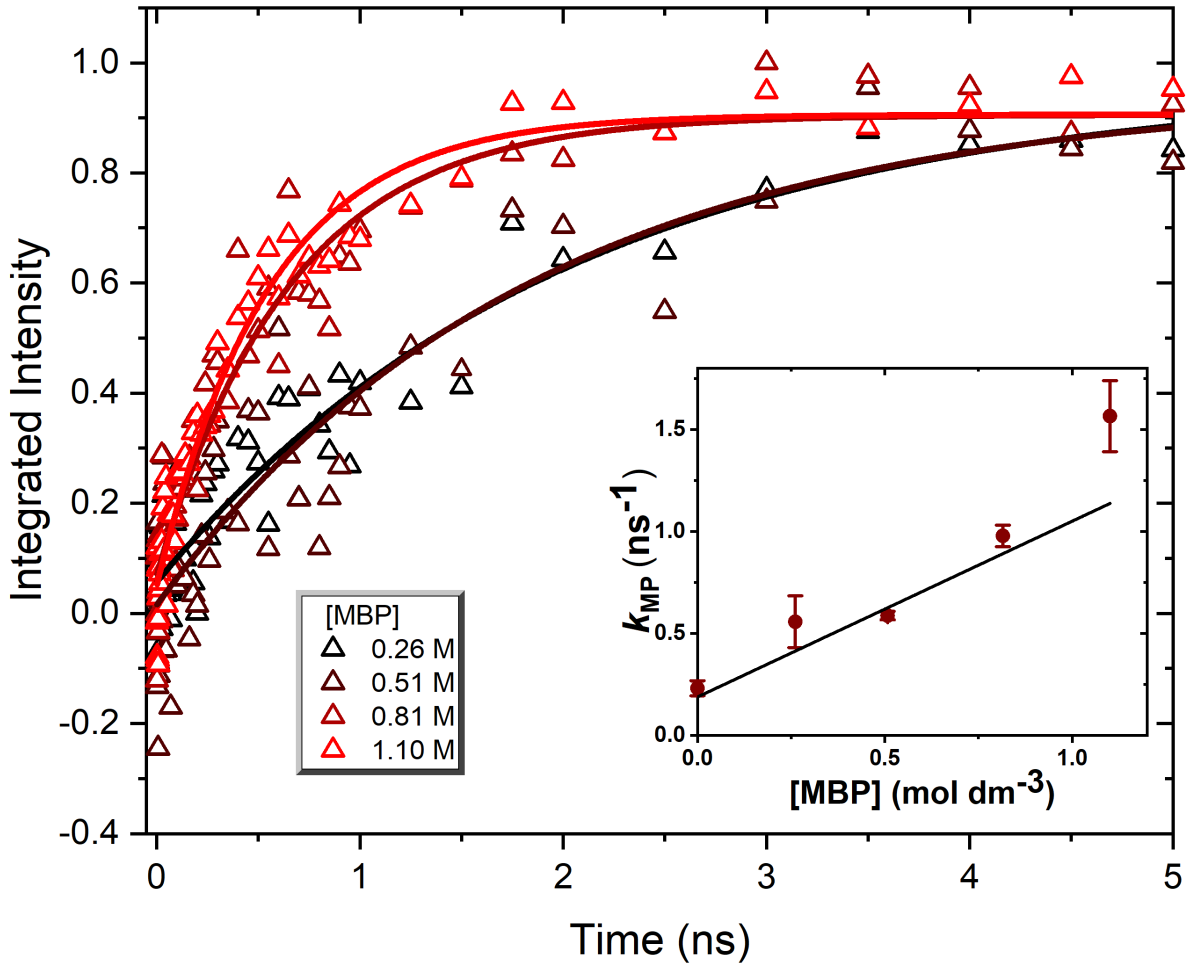

Figure E55. *Kinetic traces (hollow triangles) showing rates of rise of the ^{2}MP•(D_0) band in the TVAS measurements by electron transfer from PC-O2*(S_1) to MBP in DCM. Solid lines are single exponential fits to each data curve. The inset shows a plot of rate coefficient for each kinetic trace plotted against the corresponding MBP concentration. The gradient of the linear fit to these points (weighted by the individual one standard error uncertainties derived from the exponential fits) gives the rate coefficient for diffusive electron transfer,* $\boldsymbol{k_{ET} = (8.6 \pm 1.5) \times 10^8\ M^{-1}s^{-1}}$ *in DCM. The intercept in the kinetic plot in the inset is close to the 1/lifetime value of the PC-O2*(S_1) in DCM obtained through TVAS measurements in the absence of MBP. The kinetic model is explained in the main text. Note that the k_{ET} value obtained matches the k_{ET} value within error limits obtained from analysing the S_1 decay shown in Figure E20. We are confident therefore that the electron transfer at these MBP concentrations mostly happens from the PC*(S_1) state. It is also smaller by an order of magnitude than the estimated diffusion limited rate coefficient for DCM of* $1.5 \times 10^{10}\ M^{-1}s^{-1}$ *at 20 °C.*[12]

7.5.1.7 Kinetic fits for the reaction of PC-O2*(S_1) + MBP in DMF

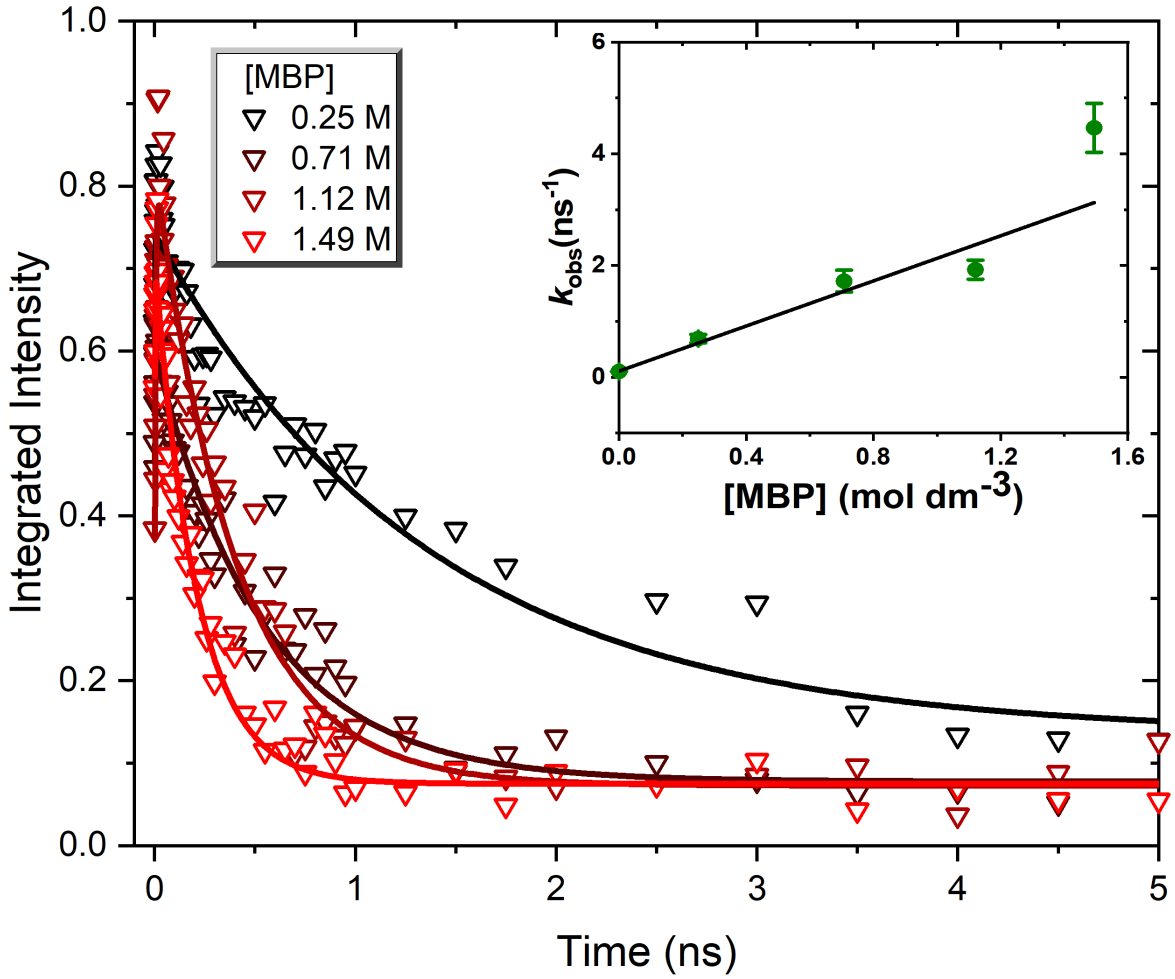

Figure E56. *Kinetic traces (hollow inverted triangles) showing rates of decay of the ^{1}PC-O2*(S_1) band in the TVAS measurements by electron transfer to MBP in DMF. Solid lines are bi-exponential fits to each kinetic trace, with the initial fast rising component resulting from vibrational cooling in the S_1 state. The slower decaying time coefficient is used to determine the rate coefficient for electron transfer. The inset shows a plot of rate coefficients for each kinetic trace plotted against the corresponding MBP concentration. The gradient of the linear fit to these points (weighted by the individual one standard error uncertainties derived from the exponential fits) gives the rate coefficient for bimolecular electron transfer, $\boldsymbol{k_{ET} = (2.3 \pm 0.3) \times 10^9\ M^{-1}s^{-1}}$ in DMF. The intercept in the kinetic plot in the inset is close to the 1/lifetime value of the PC-O2*(S_1) in DMF obtained through TVAS measurements in the absence of MBP. The kinetic model is explained in the main text. Note that the k_{ET} value is smaller than the diffusion limited rate coefficient, which in DMF is estimated to be $7.6 \times 10^9\ M^{-1}s^{-1}$ at 20 °C.*[12]

7.5.1.8 Kinetic fits for the reaction of PC-O2*(S_1) + MBP in toluene-d_8

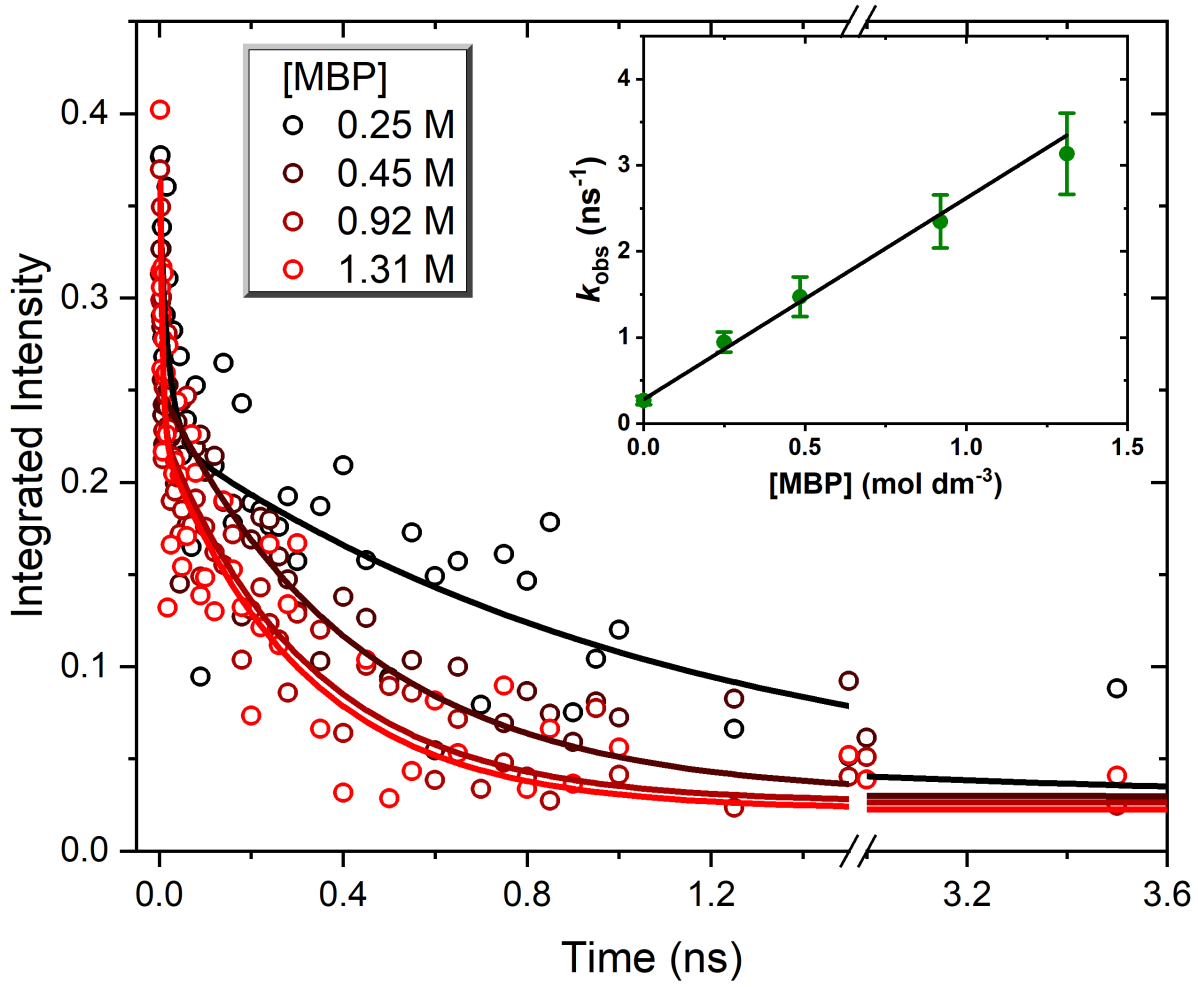

Figure E57. *Kinetic traces (hollow circles) showing rates of decay of the ^{1}PC-O2*(S_1) band in the TVAS measurements by electron transfer to MBP in toluene-d_8. Solid lines are bi-exponential fits to each kinetic data curve. The faster decaying component could result from vibrational cooling in the S_1 state or relaxation of hot S_1 molecules to S_0. The rate coefficient obtained from the slower decaying component is used to determine the rate coefficient for electron transfer. The inset shows a plot of the rate coefficients for each kinetic trace plotted against the corresponding MBP concentration. The gradient of the linear fit to these points (weighted by the individual one standard error uncertainties derived from the exponential fits) gives the rate coefficient for diffusive electron transfer, $\boldsymbol{k_{ET} = (2.0 \pm 0.3) \times 10^9\ M^{-1}s^{-1}}$ in toluene-d_8. The intercept in the kinetic plot in the inset is close to the 1/lifetime value of the PC-O2*(S_1) in toluene obtained through TVAS measurements in the absence of MBP. Note that the k_{ET} value is almost an order of magnitude smaller than the diffusion limited rate coefficient which in toluene is estimated to be* $1.1 \times 10^{10}\ M^{-1}s^{-1}$ *at 20 °C.*[12]

7.5.1.9 Kinetic fits for the reaction of ^{3}PC-O2*(T_1) + MBP in toluene-d_8

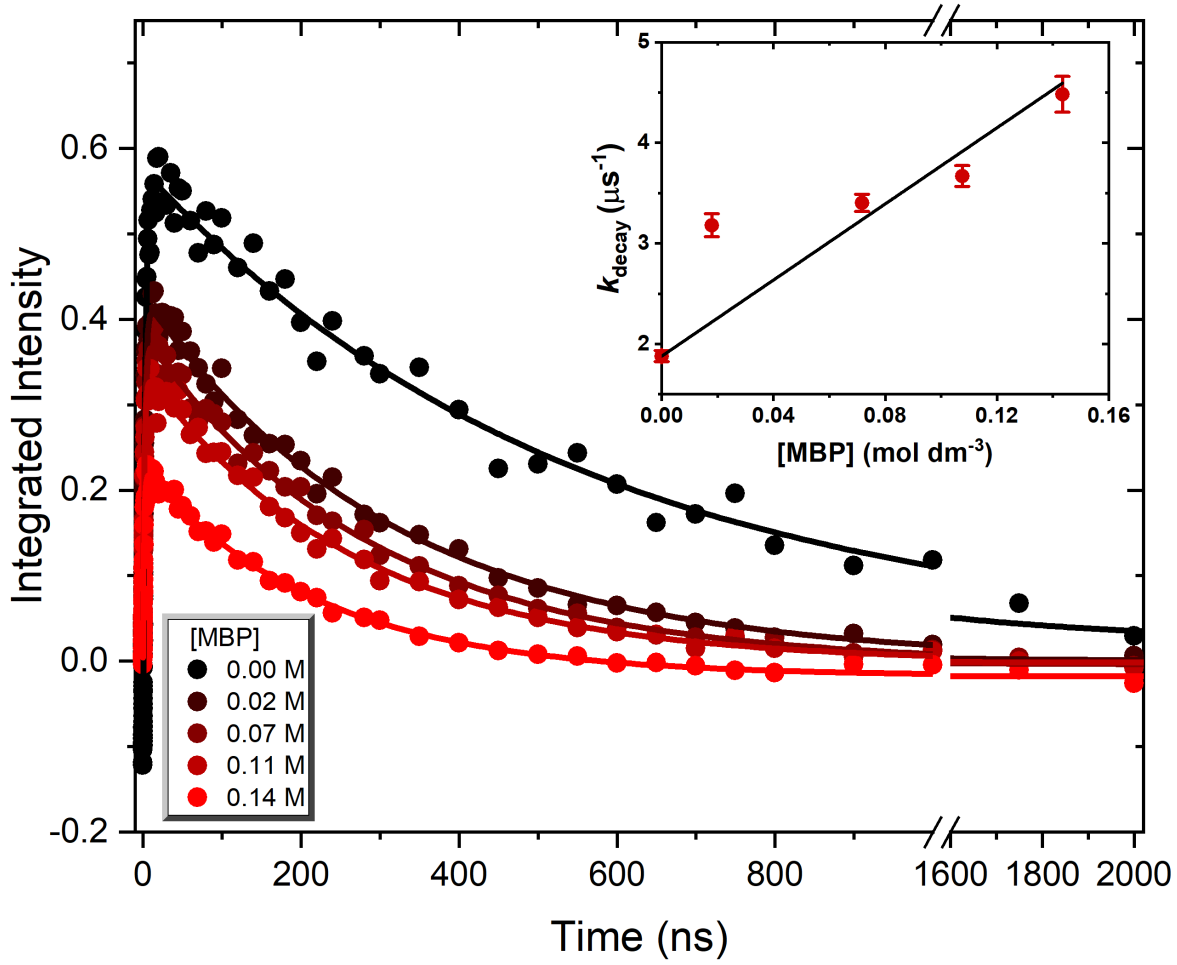

Figure E58. *Kinetic traces (circles) showing rates of decay of the ^{3}PC-O2*(T_1) band in the TVAS measurements by electron transfer to MBP in toluene-d_8. Solid lines are bi-exponential fits to each kinetic trace. The larger rate coefficient from the fast-rising part of the curve can be assigned to the growth of T_1 state population from the PC*(S_1) state through ISC, and the smaller rate coefficient arising from the slower decaying component is used to determine the rate coefficient for electron transfer from the T_1 state. The inset shows a plot of rate coefficients for each kinetic trace plotted against the corresponding MBP concentration. The gradient of the linear fit to these points (weighted by the individual one standard error uncertainties derived from the exponential fits) gives the rate coefficient for diffusive electron transfer, $\boldsymbol{k_{ET} = (2.0 \pm 0.3) \times 10^7\ M^{-1}s^{-1}}$ in toluene-d_8. The intercept in the kinetic plot in the inset is close to the 1/lifetime value of the PC-O2*(T_1) in toluene obtained through TVAS measurements in the absence of MBP. The kinetic model is explained in the main text. Note that the $\boldsymbol{k_{ET}}$ value is three orders of magnitude smaller than the diffusion limited rate coefficient which in toluene is $1.1 \times 10^{10}\ M^{-1}s^{-1}$ at 20 °C and two orders of magnitude smaller than reaction from the PC*(S_1) state.*[12]

7.5.1.10 Kinetic fits for the reaction of PC-O3*(S_1) + MBP in toluene-d_8

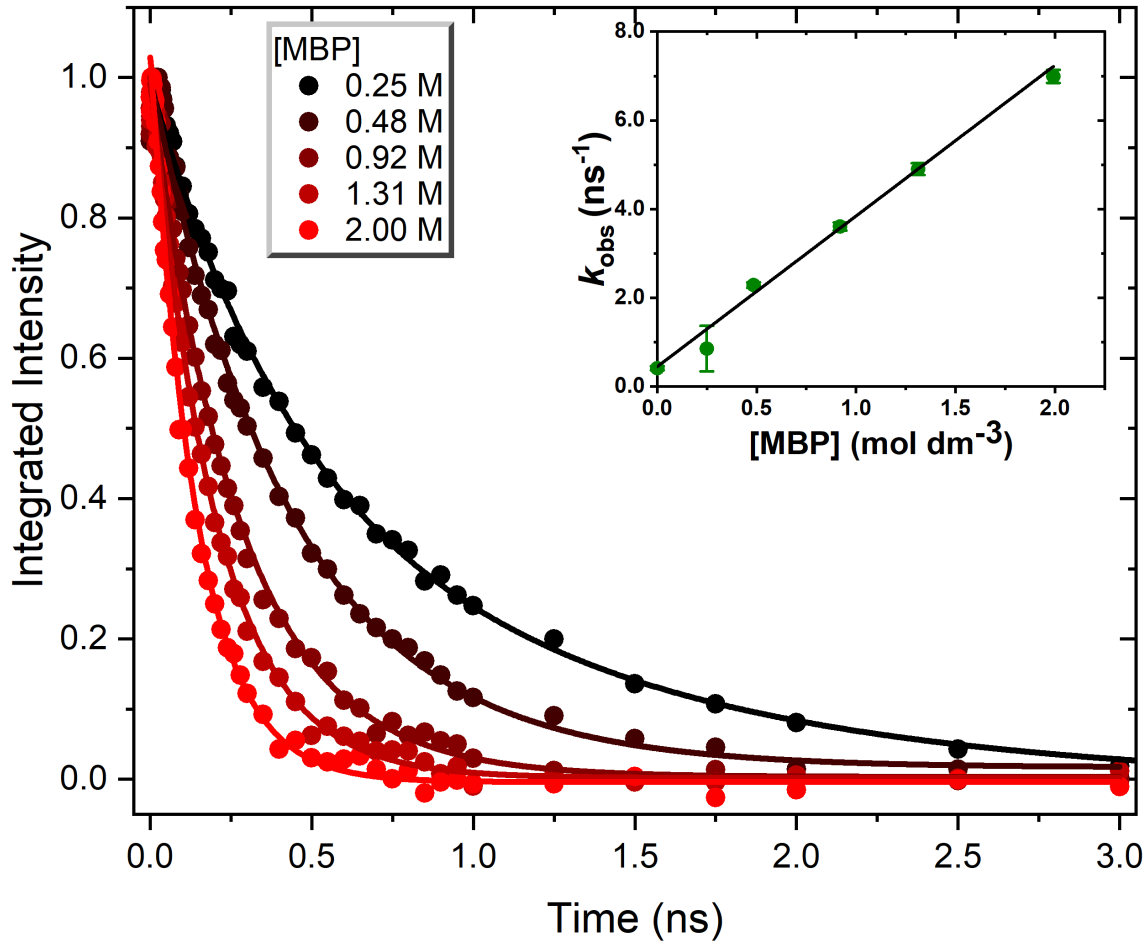

Figure E59. *Kinetic traces (circles) showing rates of decay of the PC-O3*(S_1) band in the TVAS measurements by electron transfer to MBP in toluene-d_8. Solid lines are single exponential fits to each kinetic data curve. Rate coefficients obtained from these fits are plotted against MBP concentration in the inset. The gradient of the linear fit to these points (weighted by the individual one standard error uncertainties derived from the exponential fits) gives the rate coefficient for electron transfer,* $\boldsymbol{k_{ET} = (1.8 \pm 0.1) \times 10^9\ M^{-1}s^{-1}}$ *in toluene-d_8. The intercept in the kinetic plot in the inset is set to 1/lifetime of the PC-O3*(S_1) obtained through TVAS measurements in toluene-d_8 in the absence of MBP. Note that the value is an order of magnitude smaller than the diffusion limited rate coefficient which in toluene is estimated to be* $1.1 \times 10^{10}\ M^{-1}s^{-1}$ *at 20 °C.*[12]

7.5.1.11 Kinetic fits for the reaction of PC-O3*(S_1) + MBP in DCM

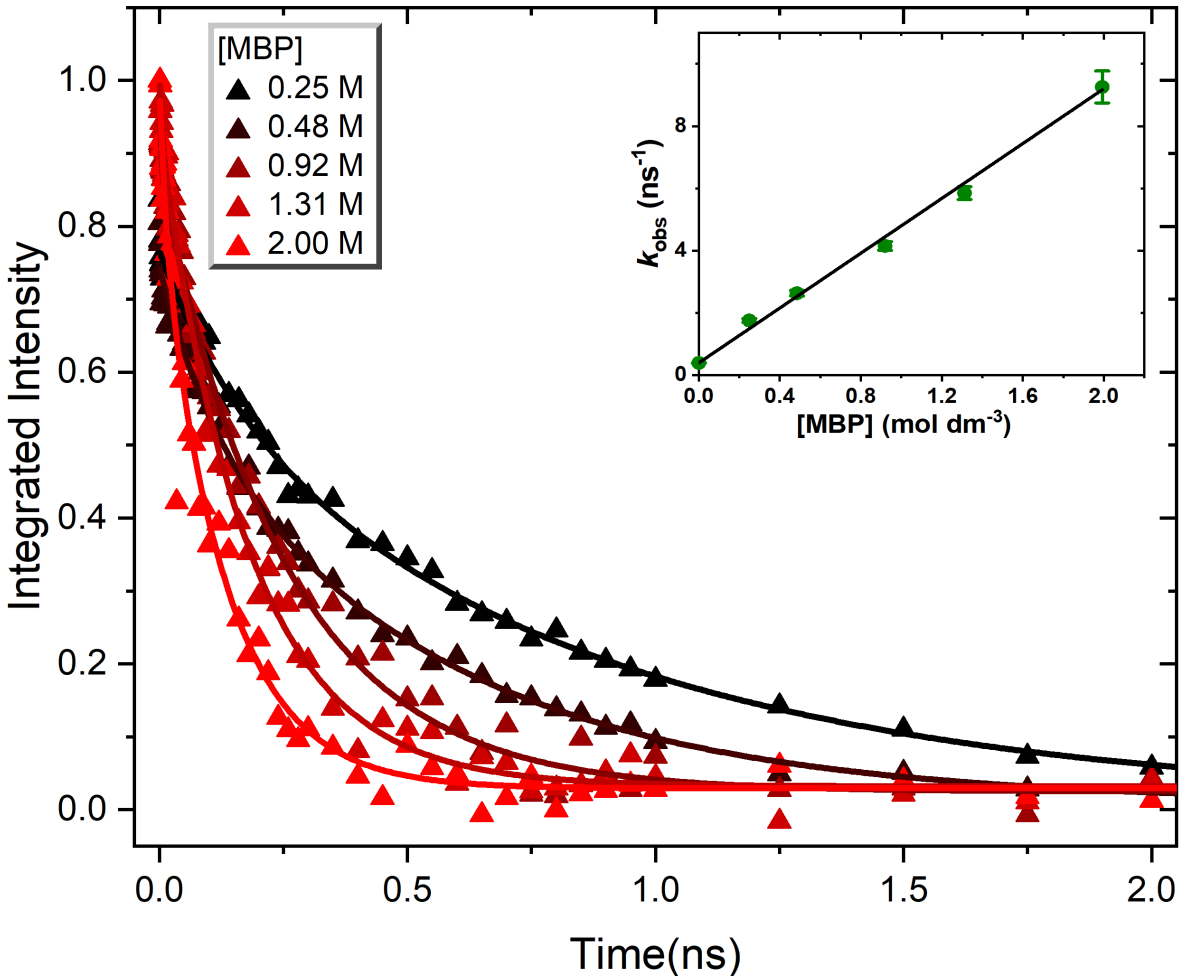

Figure E60. *Kinetic traces (triangles) showing rates of decay of the PC-O3*(S_1) band in the TVAS measurements by electron transfer to MBP in DCM. Solid lines are single exponential fits to each data curve. Rate coefficients obtained from these fits are plotted against MBP concentration in the inset. The gradient of the linear fit to these points (weighted by the individual one standard error uncertainties derived from the exponential fits) gives the rate coefficient for electron transfer,* $\boldsymbol{k_{ET} = (4.1 \pm 0.2) \times 10^9\ M^{-1}s^{-1}}$ *in DCM. The intercept in the kinetic plot in the inset is set to 1/lifetime of the PC-O3*(S_1) obtained through TVAS measurements in DCM the absence of MBP. Note that the value is smaller than the diffusion limited rate coefficient which in toluene is estimated to be* $1.5 \times 10^{10}\ M^{-1}s^{-1}$ *at 20 °C.*[12]

7.5.1.12 Kinetic fits for the reaction of PC-O3*(S_1) + MBP in DMF

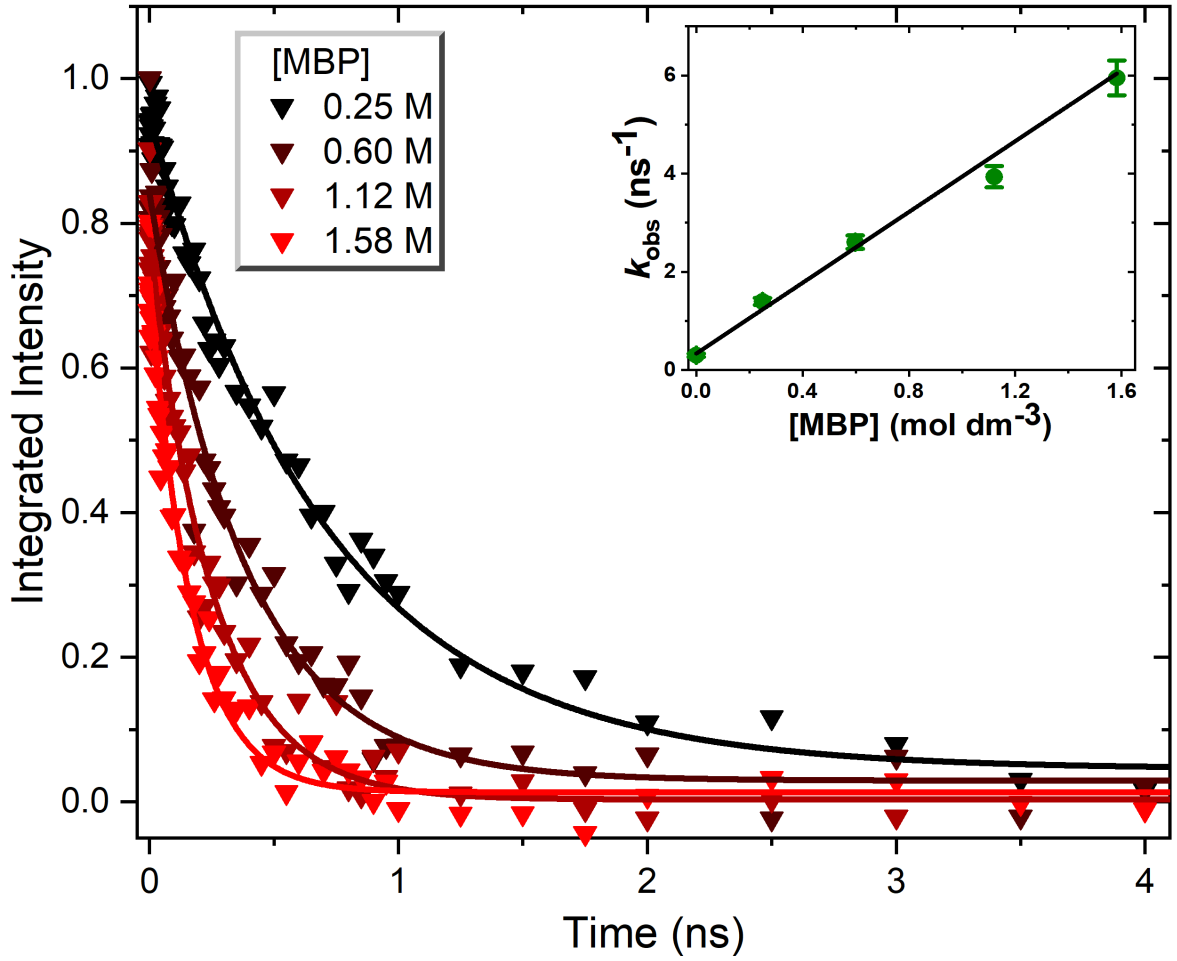

Figure E61. *Kinetic traces (inverted triangles) showing rates of decay of the PC-O3*(S_1) band in the TVAS measurements by electron transfer to MBP in DMF. Solid lines are single exponential fits to each data curve. Rate coefficients obtained from these fits are plotted against MBP concentration in the inset. The gradient of the linear fit to these points (weighted by the individual one standard error uncertainties derived from the exponential fits) gives the rate coefficient for electron transfer,* $\boldsymbol{k_{ET} = (3.6 \pm 0.2) \times 10^9\ M^{-1}s^{-1}}$ *in DMF. The intercept in the kinetic plot in the inset is set to 1/lifetime of the PC-O3*(S_1) obtained through TVAS measurements in DMF in the absence of MBP. Note that the value is smaller than the diffusion limited rate coefficient, which in DMF is estimated to be* $7.6 \times 10^9\ M^{-1}s^{-1}$ *at 20 °C.*[12]

7.5.1.13 Kinetic fit for PC-S*(S_1) + MBP in toluene-d_8

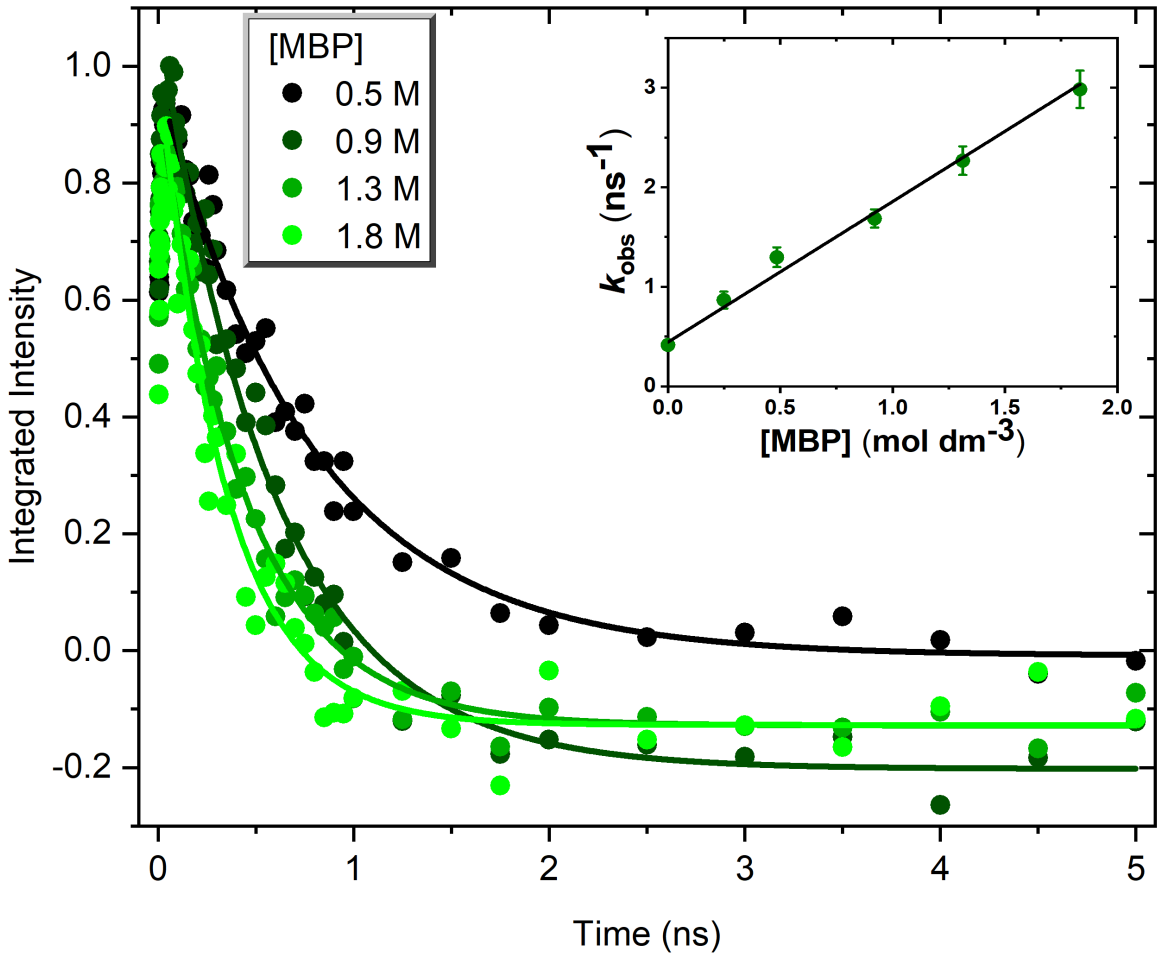

Figure E62. *Kinetic traces (circles) showing rates of decay of the PC-S*(S_1) band in the TVAS measurements by electron transfer to MBP in toluene-d_8. Solid lines are single exponential fits to each data curve. Rate coefficients obtained from these fits are plotted against MBP concentration in the inset. The gradient of the linear fit to these points (weighted by the individual one standard error uncertainties derived from the exponential fits) gives the rate coefficient for electron transfer,* $\boldsymbol{k_{ET} = (1.4 \pm 0.1) \times 10^9\ M^{-1}s^{-1}}$ *in toluene-d_8. The intercept in the kinetic plot in the inset is set to 1/lifetime of the PC-S*(S_1) in toluene-d_8 obtained through TVAS measurements in the absence of MBP. Note that the value is an order of magnitude smaller than the diffusion limited rate coefficient which in toluene is estimated to be* $1.1 \times 10^{10}\ M^{-1}s^{-1}$ *at 20 °C.*[12]

7.5.1.14 Kinetic fit for PC-S*(S_1) + MBP in DMF

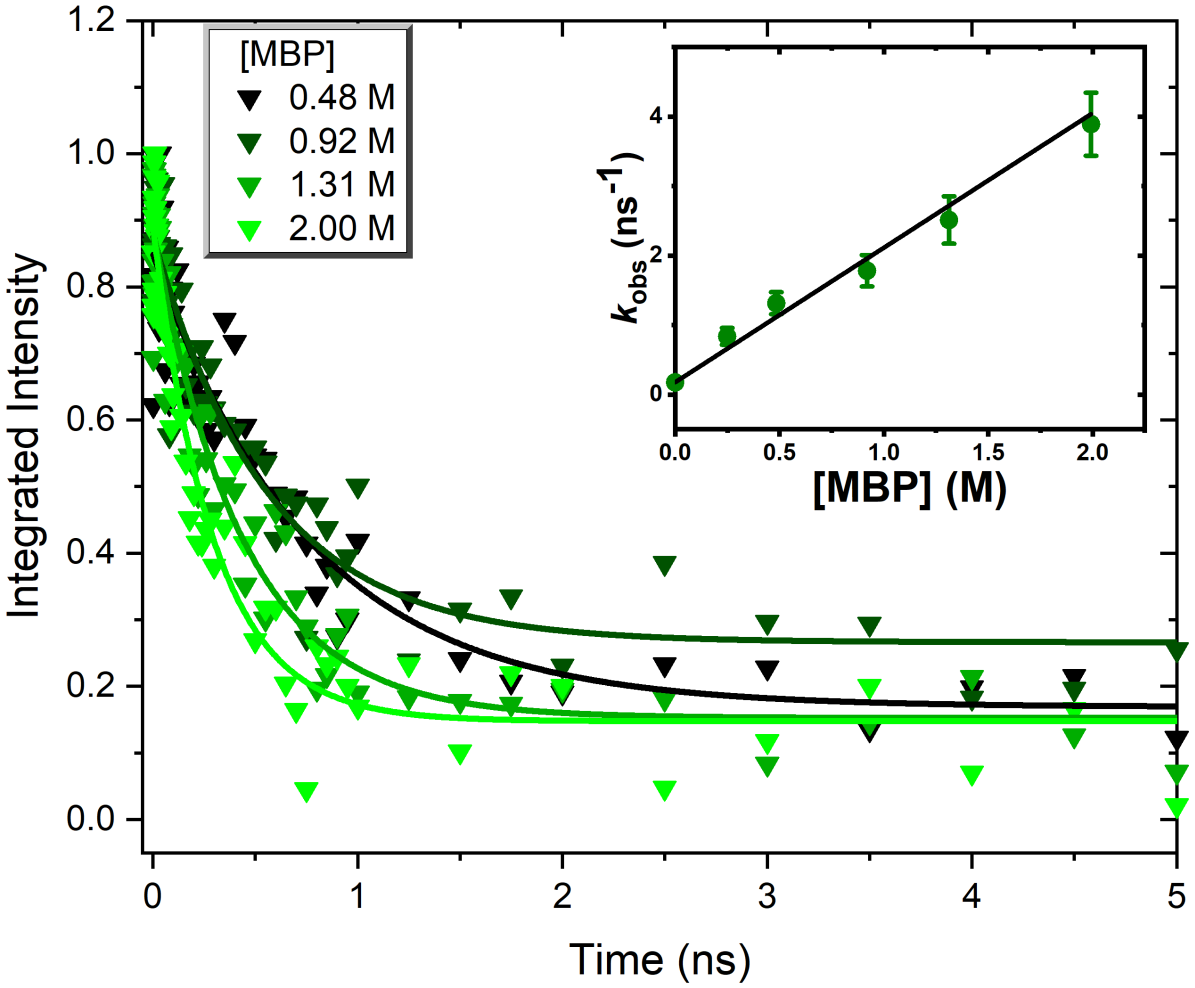

Figure E63. *Kinetic traces (circles) showing rates of decay of the PC-S*(S_1) band in the TVAS measurements by electron transfer to MBP in N,N-dimethylformamide. Solid lines are single exponential fits to each data curve. Rate coefficients obtained from these fits are plotted against MBP concentration in the inset. The gradient of the linear fit to these points (weighted by the individual one standard error uncertainties derived from the exponential fits) gives the rate coefficient for electron transfer,* $\boldsymbol{k_{ET} = (1.9 \pm 0.1) \times 10^9\, M^{-1}s^{-1}}$ *in DMF. The intercept in the kinetic plot in the inset is set to 1/lifetime of the PC-S*(S_1) *in DMF obtained through TVAS measurements in the absence of MBP. Note that the value is an order of magnitude smaller than the diffusion limited rate coefficient which in toluene is estimated to be* $7.6 \times 10^9\, M^{-1}s^{-1}$ *at 20 °C.*[12]

7.5.2 Decay of MP• Radical Band

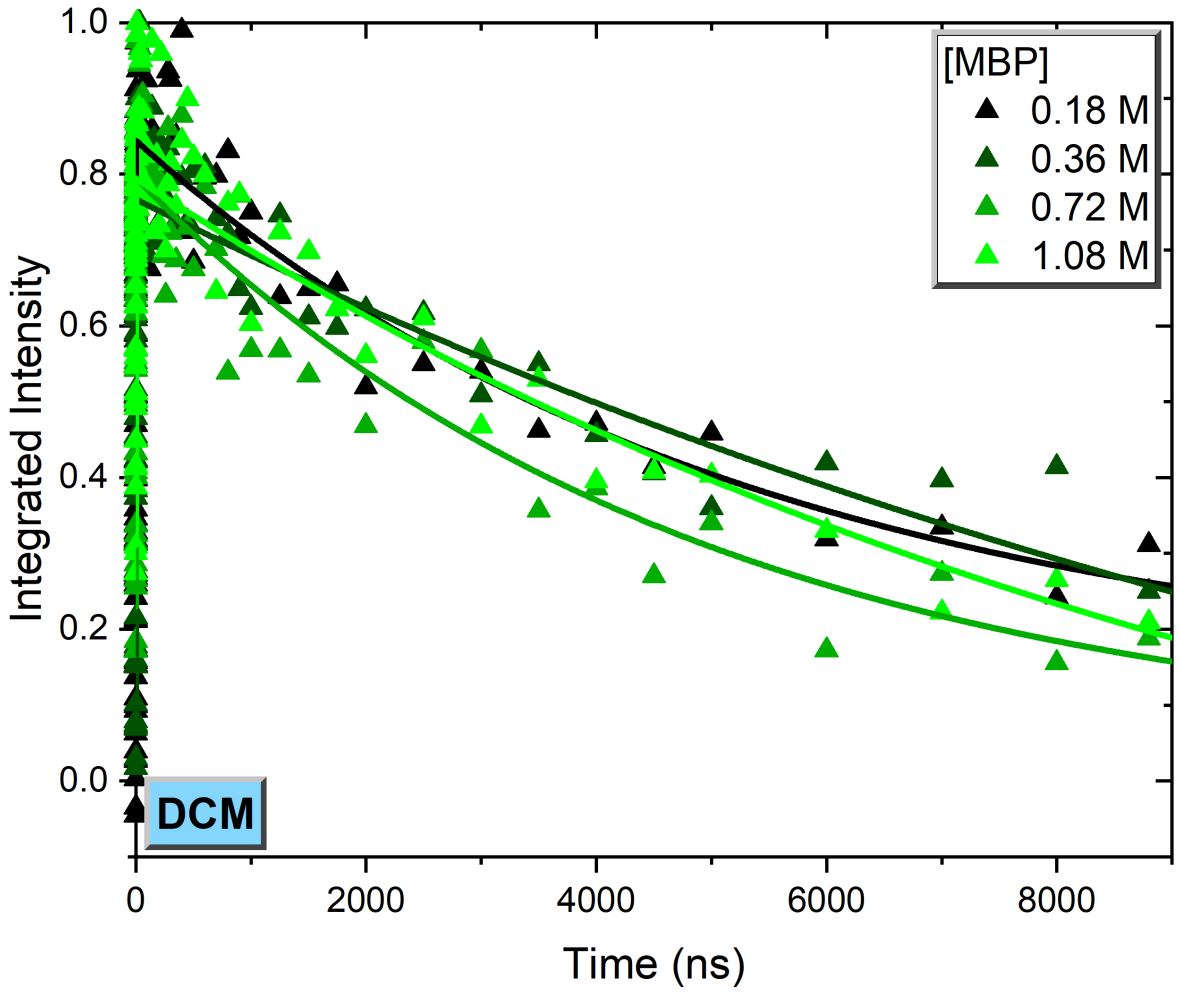

Figure E64. *Kinetic traces (triangles) showing rates of decay of the MP• band in TVAS measurements with PC-N1 and MBP in DCM over extended times (10-10000 ns). The rate of decay of the MP• band does not depend systematically on the increasing concentration of MBP (between 0.25 and 1.6 M). Solid lines are bi-exponential fits to each data curve with the faster rising part corresponding to the formation of the MP• band by electron transfer and the decay of the band assigned to reaction with dissolved oxygen. The decay time constant varies from system to system depending on the amount of dissolved oxygen, with a non-purged system having a decay time constant of ~300 ns and N_2-purged system showing times constants varying from 3000 to 5000 ns. The kinetic model is explained in the main text. Note that in both cases the difference between the timescales for the rising and decaying components is 3 orders of magnitude.*

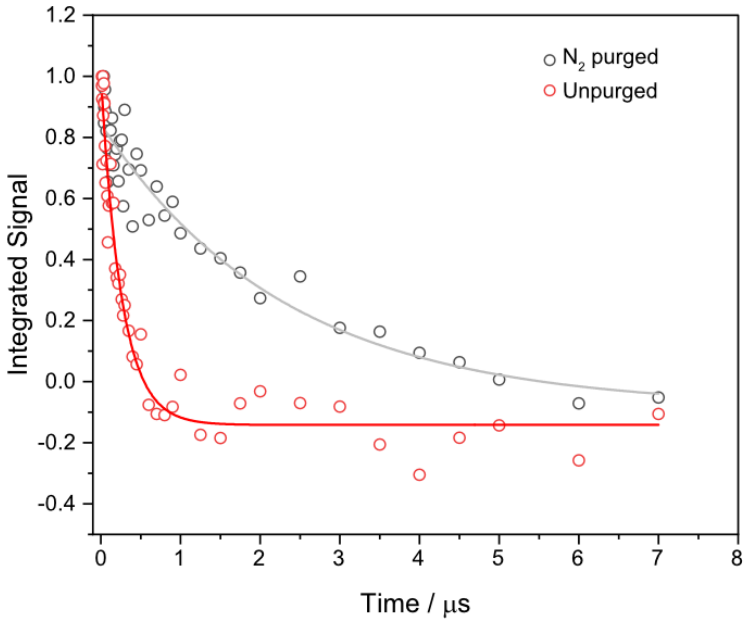

Figure E65. *Rates of decay of $^2MP^•(D_0)$ radicals in a N_2 purged vs unpurged system. Both data sets are for a solution of PCBN (4.2 mM) and MBP (0.2 M), either purged with N_2 for approximately 45 mins (grey) or not purged (red). The radical decays faster in an unpurged system where oxygen is present. Solid lines are single exponential fits and the corresponding time constants are τ = 2.3 ± 0.4 μs (N_2 purged) and τ = 260 ± 22 ns (unpurged).*

7.5.3 Sensitivity Analysis

Here we looked to test the sensitivity of the outputted rate coefficients to the choice of input value for k_1' as this represents a fixed value in the least squares fit performed in Chapter 5.

Table E1. *Sensitivity analysis performed on the chosen input value of k_1' to test the consequences for values of selected rate coefficients retrieved from the fits.*

		k_1' input (M^{-1} s^{-1})			
		1.38E+11	*3.03E+11*	*4.68E+11*	**Standard error of the fits**
Fitted rate coefficients (M^{-1} s^{-1} or s^{-1})	k_1	1.45E+09	1.48E+09	1.00E+09	1.54E+08
	k_3	1.29E+09	1.85E+09	1.50E+09	1.64E+08
	k_4	1.46E+06	3.52E+05	2.74E+06	6.89E+05

Table E1 shows that the values of k_1 and k_3 do not vary significantly with the chosen inputted value of k_1'. However, this is not the case for k_4 which increases in value with choices of k_1' that differ from the preferred value input to the fits. Thus, the current fitted value of k_4 is better thought of as a lower limit to the true value.

7.6 Computational Methods

7.6.1 Chapter 3

Computational characterizations of the ground and excited state properties of the PCs were performed using Gaussian 09 software.[13] Geometries and harmonic vibrational frequencies of the ground electronic states of the photocatalysts were computed using restricted Kohn-Sham density functional theory. The pure hybrid-GGA functional PBE0 was used with a polarized and augmented double-zeta basis set 6-31+G(d) (6d,7f). Solvent effects for toluene, DCM and DMF were included by implicit simulation of solvation as a continuous polarizable medium using the total solute density model (SMD).[14,15,16] The PBE0 functional long-range London dispersion interactions were simulated with Grimme's D3 dispersion correction, supplemented by the Becke-Johnson damping function (GD3BJ).[17,18] Vertical transition energies, oscillator strengths and excitation amplitudes were computed with time-dependent density functional theory (TD-DFT) using the Coulomb attenuated variant of the B3LYP functional (CAM-B3LYP).[19,20] _ENREF_40 CAM-B3LYP was used with the 6-311++G(2d,p) basis set and non-equilibrium SMD solvation to characterize the excited electronic states of the photocatalyst in the Franck-Condon region.

7.6.2 Chapter 5

Calculations were performed using the Gaussian09 suite of programmes.[13] For transition states, geometries were optimised with the DFT method using the M06-2X functional as implemented in Gaussian. The standard 6-311G(d,p) basis set was used for H, B, C, O, while the LANL2DZ basis set with an effective core potential was used for I. All calculations were carried out using the PCM model of solvation with tetrahydrofuran as the solvent.[21] All geometry optimizations were full, with no restrictions. All stationary points located in the potential energy hypersurface were characterized as minima (no imaginary frequencies) or as transition states (one and only one imaginary frequency) by vibrational analysis. The analysis also provided zero-point vibrational energy corrections and thermal corrections to various thermodynamic properties. The transition state was further confirmed by IRC calculations. For the calculation of IR vibrational frequencies, the LANL2DZ basis set and the functional B3LYP were preferred because this method better predicted the observed IR vibrational wavenumbers.

7.7 References

1. Lewis-Borrell L, Sneha M, Bhattacherjee A, Clark IP, Orr-Ewing AJ. Mapping the Multi-Step Mechanism of a Photoredox Catalyzed Atom-Transfer Radical Polymerization Reaction by Direct Observation of the Reactive Intermediates. *Chem Sci* 2020, **11**(17)**:** 4475-4481.

2. Theriot JC, Lim C-H, Yang H, Ryan MD, Musgrave CB, Miyake GM. Organocatalyzed atom transfer radical polymerization driven by visible light. *Science* 2016, **352**(6289)**:** 1082-1086.

3. Koyama D, Dale HJA, Orr-Ewing AJ. Ultrafast Observation of a Photoredox Reaction Mechanism: Photoinitiation in Organocatalyzed Atom-Transfer Radical Polymerization. *J Am Chem Soc* 2018, **140**(4)**:** 1285-1293.

4. Liu N, Wang B, Chen W, Liu C, Wang X, Hu Y. A general route for synthesis of N-aryl phenoxazines via copper(i)-catalyzed N-, N-, and O-arylations of 2-aminophenols. *RSC Adv* 2014, **4**(93)**:** 51133-51139.

5. McCarthy BG, Pearson RM, Lim C-H, Sartor SM, Damrauer NH, Miyake GM. Structure-Property Relationships for Tailoring Phenoxazines as Reducing Photoredox Catalysts. *J Am Chem Soc* 2018, **140**(15)**:** 5088-5101.

6. Pan X, Lamson M, Yan J, Matyjaszewski K. Photoinduced Metal-Free Atom Transfer Radical Polymerization of Acrylonitrile. *ACS Macro Lett* 2015, **4**(2)**:** 192-196.

7. Silvi M, Aggarwal VK. Radical Addition to Strained σ-Bonds Enables the Stereocontrolled Synthesis of Cyclobutyl Boronic Esters. *J Am Chem Soc* 2019, **141**(24)**:** 9511-9515.

8. Fawcett A, Biberger T, Aggarwal VK. Carbopalladation of C–C σ-bonds enabled by strained boronate complexes. *Nat Chem* 2019, **11**(2)**:** 117-122.

9. Guo L, Noble A, Aggarwal VK. α-Selective Ring-Opening Reactions of Bicyclo[1.1.0]butyl Boronic Ester with Nucleophiles. *Angew Chem Int Ed* 2021, **60**(1)**:** 212-216.

10. Silvi M, Sandford C, Aggarwal VK. Merging Photoredox with 1,2-Metallate Rearrangements: The Photochemical Alkylation of Vinyl Boronate Complexes. *J Am Chem Soc* 2017, **139**(16)**:** 5736-5739.

11. Grubb MP, Orr-Ewing AJ, Ashfold MNR. KOALA: A program for the processing and decomposition of transient spectra. *Rev Sci Instrum* 2014, **85**(6)**:** 064104.

12. Marco Montalti AC, Luca Prodi, M. Teresa Gandolfi. *Handbook of Photochemistry*, Third edn. Taylor & Francis Group: Boca Raton, FL, 2006.

13. Frisch MJ, Trucks GW, Schlegel HB, Scuseria GE, Robb MA, Cheeseman JR*, et al.* Gaussian 09. Gaussian Inc., Wallingford CT; 2009.

14. Marenich AV, Cramer CJ, Truhlar DG. Universal Solvation Model Based on Solute Electron Density and on a Continuum Model of the Solvent Defined by the Bulk Dielectric Constant and Atomic Surface Tensions. *J Phys Chem B* 2009, **113**(18)**:** 6378-6396.

15. Miertuš S, Scrocco E, Tomasi J. Electrostatic Interaction of a Solute with a Continuum. A Direct Utilizaion of Ab Initio Molecular Potentials for the Prevision of Solvent Effects. *Chem Phys* 1981, **55**(1)**:** 117-129.

16. Tomasi J, Mennucci B, Cammi R. Quantum Mechanical Continuum Solvation Models. *Chem Rev* 2005, **105**(8)**:** 2999-3094.

17. Goerigk L, Grimme S. Efficient and Accurate Double-Hybrid-Meta-GGA Density Functionals—Evaluation with the Extended GMTKN30 Database for General Main Group Thermochemistry, Kinetics, and Noncovalent Interactions. *J Chem Theor Comp* 2011, **7**(2)**:** 291-309.

18. Grimme S, Antony J, Ehrlich S, Krieg H. A Consistent and Accurate Ab Initio Parametrization of Density Functional Dispersion Correction (DFT-D) for the 94 Elements H-Pu. *J Chem Phys* 2010, **132**(15)**:** 154104.

19. Yanai T, Tew DP, Handy NC. A New Hybrid Exchange–Correlation Functional using the Coulomb-Attenuating Method (CAM-B3LYP). *Chem Phys Lett* 2004, **393**(1)**:** 51-57.

20. Peach MJG, Benfield P, Helgaker T, Tozer DJ. Excitation Energies in Density Functional Theory: An Evaluation and a Diagnostic Test. *J Chem Phys* 2008, **128**(4)**:** 044118.

21. Fasano V, Winter N, Noble A, Aggarwal VK. Divergent, Stereospecific Mono- and Difluoromethylation of Boronic Esters. *Angew Chem Int Ed* 2020, **59**(22)**:** 8502-8506.